GEOMAR
Helmholtz-Zentrum für Ozeanforschung Kiel

IODP
INTEGRATED OCEAN DRILLING PROGRAM

Preservation of geochemical proxies in foraminifera during carbonate diagenesis in sediments of the eastern equatorial Pacific

Janett Voigt
2015

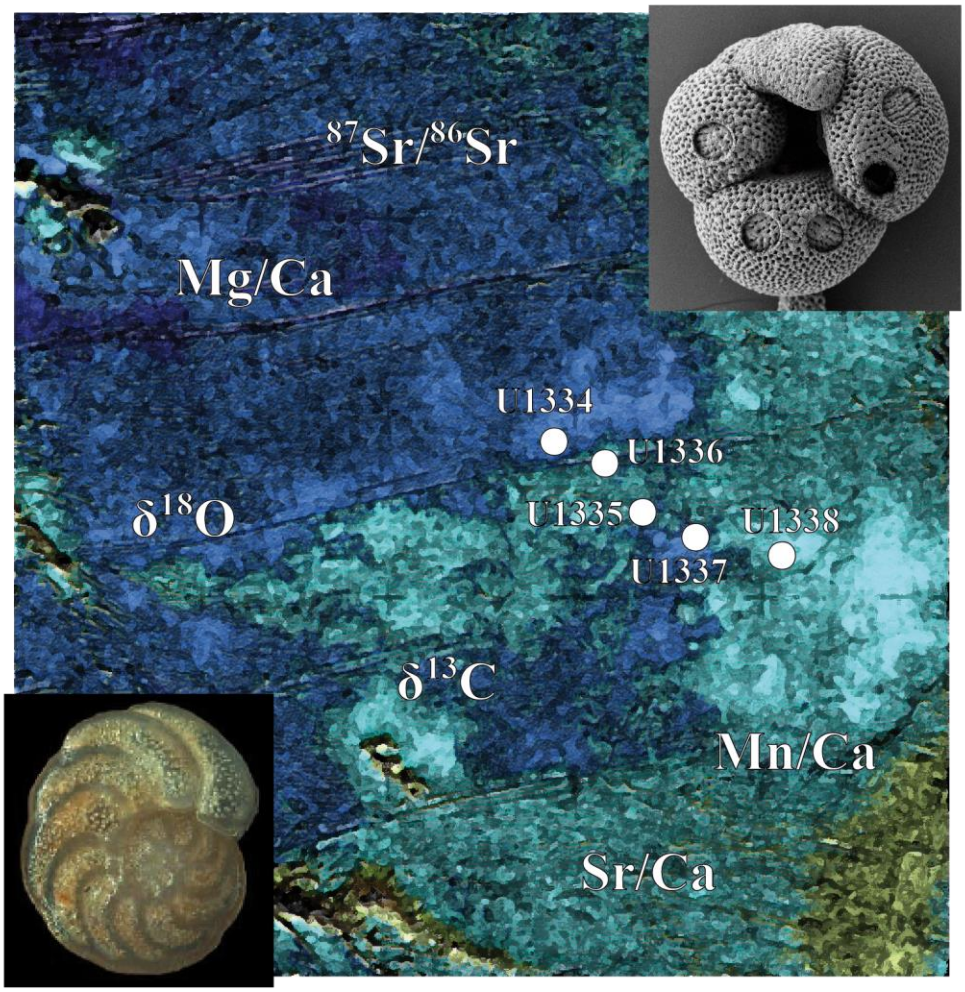

Dissertation

Cover:

Map of the eastern equatorial Pacific, modified from Pälike et al. (2010)

Light microscope image of *Cibicidoides wuellerstorfi*, from Holbourn A., Hendersen A. S. and Macleod N. (2013) *Atlas of benthic foraminifera*. Wiley-Blackwell, Chichester

Preservation of geochemical proxies in foraminifera during carbonate diagenesis in sediments of the eastern equatorial Pacific

Erhaltung geochemischer Proxies in Foraminiferen während der Karbonatdiagenese in Sedimentkernen des östlichen äquatorialen Pazifiks

Dissertation

zur Erlangung des akademischen Grades

Dr. rer. nat.

der Mathematisch-Naturwissenschaftlichen Fakultät

der Christian-Albrecht-Universität zu Kiel

vorgelegt von

Janett Voigt

Kiel, 2015

Erster Gutachter: Prof. Dr. Martin Frank

Zweiter Gutachter: Prof. Dr. Heiko Pälike

Tag der Disputation: 18. Juni 2015

Zum Druck genehmigt: 18. Juni 2015

gez. Prof. Dr. Wolfgang J. Duschl, Dekan

Erklärung

Hiermit erkläre ich gemäß § 8, dass ich die vorliegende Abhandlung, abgesehen von der Beratung durch meinen Betreuer, nach Inhalt und Form selbstständig erarbeitet habe und keine anderen, als die von mir aufgeführten, Quellen und Hilfsmittel verwendet wurden. Diese Arbeit ist unter Einhaltung der Regeln guter wissenschaftlicher Praxis der Deutschen Forschungsgemeinschaft entstanden und wurde weder in Auszügen noch in ganzer Form an einer anderen Stelle im Rahmen eines Prüfungsverfahrens eingereicht.
Teile dieser Arbeit sind bereits in Fachzeitschriften veröffentlicht, wurden zur Veröffentlichung eingereicht oder sind in Vorbereitung eingereicht zu werden.

Kiel, den 18.06.2015

Janett Voigt

Summary

The elemental and isotopic composition of calcitic foraminiferal tests, deposited in marine carbonate sediments, forms the backbone of palaeoceanography. The geochemical signature of the tests records numerous environmental parameters and is the basis of our knowledge about the global climate system in the recent geologic past. These data are vital for our understanding of the global carbon cycle and the role of atmospheric CO_2 in driving climatic changes. However, ancient microfossils, such as foraminifera, are normally altered after deposition by a process replacing the original biogenic calcite by secondary, inorganic calcite. This recrystallisation process is still not well understood. In order to reliably apply the proxy data obtained from these foraminiferal tests, it is therefore important to quantify changes in the elemental and isotopic composition of foraminiferal tests as a consequence of recrystallisation.

In the frame of this thesis, a multi-component study of pore waters, bulk carbonates and foraminiferal tests from selected time intervals of sediments from the Integrated Ocean Drilling Program Expedition 320/321 Pacific Equatorial Age Transect (PEAT) was conducted to investigate the consequences and processes involved in carbonate diagenesis. These sediments of similar age and initial composition have been subjected to different diagenetic histories and thus form a natural diagenesis laboratory.

Although bulk carbonate diagenesis is relatively well understood from the study of Sr concentrations and radiogenic Sr isotope ratios of sediments and pore waters, the results of this thesis reveal important additional complexity. Radiogenic Sr isotopes of bulk carbonates and associated pore waters analysed in sediments of the PEAT sites indicate rapid recrystallisation given that the radiogenic $^{87}Sr/^{86}Sr$ ratios are indistinguishable from contemporaneous seawater values. The Sr isotope signatures of bulk carbonates from Site U1336 are lower than contemporaneous seawater in sediments older than 20 Ma, which suggests a late phase of recrystallisation not observed in previous studies at other sites. Further, stable Sr isotopes from the carbonate-rich PEAT sediments were investigated during diagenesis for the first time. The results clearly document a stable Sr isotope fractionation process during recrystallisation at Site U1336. Besides the radiogenic Sr isotope measurements, further parameters such as Sr^{2+} concentration in pore waters and Sr/Ca in bulk carbonates indicate that the sediments of Site U1336 were extensively altered, most likely caused by an inferred higher geothermal gradient driving recrystallisation.

In the second part of the study, the focus was on the preservation of geochemical proxies in foraminiferal tests as the implications of recrystallisation for the elemental composition of such tests is still not well documented. To compare specific time intervals between the different sites of the Pacific Equatorial Age Transect, it was necessary to establish a benthic foraminiferal stable isotope record for Site U1336 to precisely constrain intervals within the middle Miocene (16-13 Ma). This middle Miocene record is compared to existing high resolution records from Sites U1337 and U1338 nearby. The middle Miocene is characterised by recurrent carbon isotope maxima events, known as the Monterey Carbon Isotope Excursion. Despite the extensive recrystallisation of Site U1336 bulk carbonates, the carbon isotope events can clearly be identified in our record and the absolute values and amplitudes of the $\delta^{13}C$ and $\delta^{18}O$ signatures agree well with those from the neighbouring Sites U1337 and U1338. Furthermore, the U1336 isotope data show clear correspondence to long (400 kyr) and short (100 kyr) eccentricity cycles.

Element/Ca ratios of the planktonic foraminifera *Dentoglobigerina venezuelana* were analysed for specific target intervals using a laser ablation ICP-MS depth profiling technique. Results reveal that ancient tests exhibit intratest Mg/Ca and Mn/Ca heterogeneity comparable to modern foraminifera. However, decreasing Sr/Ca ratios across the tests, in particular in specimens from the older time intervals (> 20 Ma), indicate pronounced recrystallisation. The highest proportion of altered tests is found at Site U1336 reflecting the intense recrystallisation also observed for bulk carbonates. Additionally, SEM images confirm the results of laser ablation analyses showing increasing alteration of the tests with age. Nevertheless, Mg/Ca heterogeneity is still preserved in the tests and average Mg/Ca values are comparable to modern foraminifera suggesting that much of the original Mg/Ca signal is retained and that the data can be used for reliable temperature reconstructions.

Our benthic foraminiferal record provides a direct comparison between the preservation of planktonic and benthic foraminiferal tests for the middle Miocene time interval (16-13 Ma) and demonstrates that benthic foraminifera can be reliably used for paleoceanographic studies of these carbonate-rich sediments, whereas planktonic foraminifera are more prone to recrystallisation.

Kurzfassung

Eine der wichtigsten Grundlagen für paläo-ozeanographische Rekonstruktionen sind Spurenelementverhältnisse und Isotopenzusammensetzungen der Kalzitschalen von Foraminiferen, die in marinen Sedimenten abgelagert wurden. Unser heutiges Wissen über das globale Klimasystem der Erdgeschichte basiert auf Informationen über zahlreiche Umweltparameter, die in der geochemischen Signatur der Schalen enthalten sind. Solche Daten sind essentiell, um den Einfluss des globalen Kohlenstoffkreislaufs und des atmosphärischen CO_2 auf Klimaveränderungen zu verstehen. Foraminiferenschalen verändern sich jedoch chemisch nach der Ablagerung, indem der biogene Kalzit durch sekundären anorganischen Kalzit ersetzt wird. Der dabei ablaufende Rekristallisierungsprozess ist bisher nicht ausreichend verstanden. Daher ist es erforderlich, durch Rekristallisierung hervorgerufene Veränderungen in der elementaren und isotopischen Zusammensetzung der Foraminiferenschalen zu quantifizieren, um die Proxydaten der Schalen verlässlich nutzen zu können.

Im Rahmen dieser Arbeit wurden Porenwasser, Gesamtkarbonat und Foraminiferenschalen ausgewählter Zeitabschnitte der Sedimentkerne der Integrated Ocean Drilling Program Expedition 320/321 Pacific Equatorial Age Transect (PEAT) auf die Auswirkungen der Karbonatdiagenese untersucht. Die Sedimente haben ähnliche Alter und Zusammensetzung, wurden aber durch Änderungen der Oberflächenproduktivität und der Sedimentbedingungen unterschiedlich diagenetisch verändert und stellen damit ein natürliches Karbonatdiageneselabor dar.

Die Sedimentdiagenese ist mittels Sr-Konzentrationen und radiogenen Sr-Isotopen der Karbonatfraktion und der Porenwasser relativ gut untersucht, jedoch zeigt diese Studie weitere wichtige Einflüsse auf. Die radiogenen Sr-Isotope des Gesamtkarbonats und der Porenwasser der PEAT-Sedimente weisen auf eine schnelle Rekristallisation hin, da sich die radiogenen $^{87}Sr/^{86}Sr$-Verhältnisse nicht von der Meerwassersignatur unterscheiden. In Sedimenten, die älter als 20 Mio. Jahre sind, sind die radiogenen Sr-Verhältnisse des Kerns U1336 geringer als die Seewassersignatur, was eine spätere Rekristallisierungsphase vermuten lässt, die bisher nirgends beobachtet wurde. Desweiteren wurden erstmals stabile Sr-Isotope karbonatreicher Sedimente gemessen, die einen Fraktionierungsprozess der stabilen Sr-Isotope der Station U1336 während des Rekristallisierungsprozesses belegen. Außerdem deuten die Sr-Konzentration der Porenwasser und die Sr/Ca-Verhältnisse

der Karbonatfraktion darauf hin, dass die Sedimente der Station U1336 stark verändert wurden, vermutlich aufgrund eines hohen geothermalen Gradienten.

Im zweiten Teil der Studie wurde die Erhaltung geochemischer Proxydaten der Foraminiferenschalen untersucht, da die Auswirkungen der Rekristallisation auf die Elementzusammensetzung der Schalen bisher kaum belegt sind. Ein Ziel der Studie war es, spezifische Zeitabschnitte der einzelnen PEAT-Stationen zu vergleichen. Daher war es erforderlich, stabile Isotope ($\delta^{18}O$, $\delta^{13}C$) benthischer Foraminiferen der Station U1336 zu messen, um die Stratigraphie dieses Kerns für das mittlere Miozän (16-13 Mio. Jahre) präzise bestimmen zu können. Das mittlere Miozän zeichnet sich durch periodische Maxima der Kohlenstoffisotope aus, bekannt als Monterey Carbon Isotope Excursion. Diese Maxima können eindeutig in den Isotopendaten dieser Studie identifiziert werden und die Absolutwerte und Amplituden der $\delta^{18}O$ und $\delta^{13}C$ Signaturen stimmen sehr gut mit den benachbarten Lokationen U1337 und U1338 überein, obwohl nur die Karbonate von Kern U1336 stark rekristallisiert sind.

Mittels einer Laserablations-ICP-MS-Tiefenprofiltechnik wurden Spurenelementverhältnisse (Mg/Ca, Sr/Ca, Mn/Ca) der planktischen Foraminiferenart *Dentoglobigerina venezuelana* für spezifische Zeitabschnitte analysiert. Die Ergebnisse zeigen, dass die fossilen Schalen eine Heterogenität der Mg/Ca und Mn/Ca-Verhältnisse innerhalb der Schalen aufweisen, die vergleichbar mit rezenten Foraminiferen ist. Allerdings verringern sich die Sr/Ca-Verhältnisse in den Querschnitten der Schalen systematisch, insbesondere für Proben, die älter als 20 Mio. Jahre sind, was auf verstärkte Rekristallisierung schließen lässt. Der größte Anteil rekristallisierter Schalen ist beim Kern U1336 zu finden, was die intensive Rekristallisierung der Karbonate dieser Station widerspiegelt. Zusätzlich deuten Rasterelektronenaufnahmen darauf hin, dass die Rekristallisierung der Schalen mit zunehmendem Alter voranschreitet. Dennoch blieb die Heterogenität der Mg/Ca-Verhältnisse erhalten und die Mg/Ca-Durchschnittswerte sind vergleichbar mit denen rezenter Foraminiferen, was die Erhaltung der ursprünglichen Mg/Ca-Verhältnisse nahe legt und somit eine verlässliche Temperaturrekonstruktion zulässt.

Unsere Ergebnisse ermöglichen einen direkten Vergleich der Erhaltung von planktischen und benthischen Foraminiferenschalen für das mittlere Miozän und zeigen, dass benthische Foraminiferen zuverlässige Daten für paläo-ozeanographische Studien liefern, während planktische Foraminiferen anfälliger gegenüber Rekristallisierungsprozessen sind.

Abbreviations

CCD	carbonate compensation depth
CM	carbon (isotope) maximum
$\delta^{13}C$	stable carbon isotopes
$\delta^{18}O$	stable oxygen isotopes
$\delta^{88/86}Sr$	stable strontium isotopes
DSDP	Deep Sea Drilling Program
EMP	electron microprobe
F, F-2	final (F), antepenultimate (F-2) chamber of a foraminiferal test
γ	rate at which the recrystallisation rate changes with depth
GRA	gamma ray attenuation
IAPSO	International Association for the Physical Sciences of the Ocean
ICP-AES	inductively coupled plasma atomic emission spectroscopy
IODP	Integrated Ocean Drilling Program
JCp-1	Japan carbonate reference material coral (*Porites* sp.)
JCt-1	Japan carbonate reference material giant clam (*Tridacna gigas*)
kyr	thousand years
LA-ICP-MS	laser ablation inductively coupled plasma mass spectrometry
λ	background recrystallisation rate at depth
Ma	million years ago
mbsf	metres below seafloor
MC-ICP-MS	multi collector inductively coupled plasma mass spectrometry
Mi-1, Mi-3	Miocene glaciation 1 (at 22.8 Ma) and 3 (at 13.9 Ma)
MMCO	middle Miocene climate optimum
Myr(s)	million year(s)
NanoSIMS	nanoscale secondary ion mass spectrometry
NIST	National Institute of Standards and Technology
ODP	Ocean Drilling Program
Oi-1, Oi-2b	Oligocene glaciation 1 (at ~34 Ma) and 2b (at ~27 Ma)
OKA	carbonatite standard from the Oka complex, Canada
Ω	calcite saturation state
PEAT	Pacific Equatorial Age Transect
POM	primary organic membrane
R^2	correlation coefficient

RDS 1σ, 2σ	relative standard deviation, doubled relative standard deviation
(r)mcd	(revised) metres composite depth
rpm	rounds per minute
SEM	scanning electron microscope
$^{87}Sr/^{86}Sr$	radiogenic strontium isotopes
STDEV	standard deviation
TIMS	thermal ionisation mass spectrometry
TOC	total organic carbon
VPDB	Vienna Pee Dee Belemnite

I. Introduction

I.1 Motivation

The geochemical signature of the calcite tests of foraminifera records various environmental parameters providing a key tool in palaeoceanography. Foraminiferal tests, preserved in marine sediments, are widely used to reconstruct oceanic and climatic conditions in the past including seawater temperature and global ice volume (e.g., Lear et al., 2000; Zachos et al., 2001b, 2008) as well as atmospheric carbon dioxide concentrations (e.g., Pagani et al., 1999; Pearson and Palmer, 2000; Foster et al., 2012). Such studies helped to understand key climate events in the past and have greatly improved our knowledge of the workings of the global climate system. However, ancient foraminiferal tests are often altered after deposition by recrystallisation, during which the original biogenic calcite is replaced by secondary (inorganic) calcite. This normally results in significant changes in stable isotope composition and element/Ca ratios of recrystallised foraminifera, which bias the interpretation of palaeo-temperatures and the climate of the past (e.g., Pearson et al., 2001; Sexton et al., 2006). Therefore, it is very important to better understand the process of recrystallisation and to quantify the extent of recrystallisation as well as its impact on geochemical proxies. The recrystallisation of bulk carbonate is well documented based on studies of Sr concentrations and Sr isotope ratios of the sediments and co-existing pore waters (e.g., Baker et al., 1982; Elderfield et al., 1982; Gieskes et al., 1986; Richter and DePaolo, 1987; Richter and Liang, 1993; Fantle and DePaolo, 2006). However, the implications for the reliability of foraminiferal proxy data are still unclear, but several studies suggested that foraminiferal tests react differently to bulk carbonates during recrystallisation and retain much of their original geochemical signal (e.g., Hampt and Delaney, 1997; Kozdon et al., 2013).

Deep sea sediment cores of the equatorial Pacific are ideal to study key climate events in the past and the effects of recrystallisation. The tropical Pacific is not significantly influenced by seasonal variability and thus offers stable climatic conditions only affected by global climate changes. Sediments recovered by IODP Expedition 320/321 Pacific Equatorial Age Transect (PEAT) provide a continuous

Cenozoic record, unrivalled for completeness and temporal resolution (Pälike et al., 2010), based on which key climate events in the equatorial Pacific can be studied. Additionally, the sediments have been recovered along an age transect, in which sediments of similar age and initial composition have been subjected to different diagenetic histories. Therefore, these sediments are ideal for the study of recrystallisation and the preservation of geochemical proxies in foraminifera.

I.2 Foraminifera

Foraminifera are abundant and cosmopolitan protozoa, which evolved during the Cambrian (e.g., Brady, 1884; Murray, 1897; Cushman, 1911; Bé and Tolderlund, 1971; Bé, 1977). The amount of extant species is still not fully constrained but is reported to be between 2185 (Murray, 2007) and 8714 (World Foraminifera Database) and 1864 fossil species have been described so far (World Foraminifera Database). Only 45 of these extant species are planktonic, whereas the majority lives on or in the sediment. Foraminifera build tests of various shapes, which are composed of organic material (allogromiids), agglutinated sediment particles (astrorhiziids, textulariids, lituoliids, trochamminiids), aragonite (robertiniids, involutiniids), calcite (milioliids, carteriniids, spirilliniids, lageniids, buliminiids, rotaliids, globogeriniids) or silica (silicoloculiniids) (Sen Gupta, 2002). Based on test morphology, 15 extant orders of foraminifera have been described, of which 7 precipitate calcitic carbonate tests (Sen Gupta, 2002). As most of the species precipitate carbonate tests, they contribute about 1.4 billion tons $CaCO_3$ per year to the global carbonate production corresponding to ~25 % of the total marine carbonate production (Schiebel, 2002; Langer, 2008). The calcifying species precipitate either high-Mg calcite (> 7 mole % Mg) or low-Mg calcite (< 5 mole % Mg) (Erez, 2003). The milioliids are the only order that builds high-Mg tests with values ranging between 100 mmol/mol and 150 mmol/mol (Toyofuku et al., 2000). Most of the hyaline species precipitate low-Mg calcite and the Mg/Ca values of modern foraminifera range between 1-10 mmol/mol for planktonic and 0.5-20 mmol/mol for benthic species (e.g., Rosenthal et al., 1997; Russell et al., 2004; Elderfield et al., 2006; Raitzsch et al., 2010; Filipsson et al., 2010). Foraminifera secrete their tests from seawater and therefore incorporate the geochemical signature of the water mass, in which they calcify. Thus, the tests are an excellent archive for the

reconstruction of past seawater conditions (e.g., Murray, 1897; Pfleger, 1948; Arrhenius, 1952; Bé and Tolderlund, 1971).

I.3 Proxies in foraminiferal tests

The elemental and isotopic compositions of the calcite tests of foraminifera are used as proxies that record different environmental parameters, which are themselves not recorded directly and are widely used to reconstruct oceanic and climatic conditions in the past. The following is not a complete list of proxies generally applied, but describes the proxies used in this thesis.

Since the pioneering work of Urey (1947), McCrea (1950), Epstein et al. (1953) and Emiliani (1954, 1955), stable carbon and oxygen isotopes ($\delta^{13}C$ and $\delta^{18}O$) of foraminiferal tests have become one of the most important tools in paleoceanography. Stable oxygen isotopes are linked to the global hydrological cycle and the $\delta^{18}O$ of seawater (retained in foraminiferal tests) reflects global ice volume and temperature (e.g., Emiliani, 1955; McCrea, 1950; Shackleton and Opdyke, 1973; Shackleton and Kennett, 1975). In addition, $\delta^{18}O$ records allow estimating past sea level changes due to the close correlation between $\delta^{18}O$ and ice-volume (e.g., Chappell and Shackleton, 1986; Shackleton, 1987; Rohling et al., 1998). The $\delta^{18}O$ of planktonic foraminifera provide information about precipitation and run-off (e.g., Spielhagen and Erlenkeuser, 1994; Rohling and Bigg, 1998; Wang et al., 1999). The $\delta^{18}O$ signal is also widely used as a stratigraphic tool to correlate deep sea sedimentary records globally and is integrated with biostratigraphy and palaeo-magnetic reversals (e.g., Savin et al., 1975; Shackleton and Kennett, 1975; Imbrie et al., 1984, 1992; Zachos et al., 2001b, 2008; Lisiecki and Raymo, 2005). In contrast, the foraminiferal $\delta^{13}C$ signal is influenced by global shifts in terrestrial vegetation, large-scale burial of organic material, primary productivity and deep water circulation (e.g., Belanger et al., 1981; Vincent and Berger, 1985; Wright et al., 1992; Derry and France-Lanord, 1996; Köhler and Fischer, 2004) and thus reflect changes in the global carbon cycle. $\delta^{13}C$ data are also used as water mass tracers and to reconstruct palaeo-productivity (e.g., Shackleton, 1977a; Woodruff and Savin, 1989, 1991; Wright et al., 1991; Schmiedl and Mackensen, 1997). However, possible biases for $\delta^{18}O$ and $\delta^{13}C$ arise from the photosynthetic production of organic carbon

and its decay (e.g., McConnaughey, 1989; Spero and Lea, 1993), ontogeny (e.g., Ravelo and Fairbanks, 1995; Spero and Lea, 1996) and metabolism (e.g., Erez, 1978; Spero and Lea, 1993, 1996) as well as the carbonate ion concentration of seawater (e.g., Spero et al., 1997).

Moreover, element/Ca ratios offer a variety of proxies for numerous environmental parameters. One of the most important and most applied of these proxies is Mg/Ca. The incorporation of Mg^{2+} is primarily controlled by temperature. Numerous culture experiments and core top studies have indicated an exponential relationship between the foraminiferal Mg/Ca ratio and the temperature of the seawater, in which they calcify (e.g., Nürnberg et al., 1995, 1996; Rosenthal et al., 1997, 2002; Bemis et al., 1998; Lea et al., 1999; Lear et al., 2000, 2002; Dekens et al., 2002; Anand et al., 2003). Therefore, Mg/Ca ratios record past seawater temperatures. Using paired measurements of Mg/Ca ratios and $\delta^{18}O$, palaeo-salinity (e.g., Lea et al., 1999; Elderfield and Ganssen, 2000; Schmidt et al., 2004; Shevenell et al., 2004) and ice-volume corrected seawater temperatures can be estimated (e.g., Mashiotta et al., 1999; Lea et al., 2000; Lear et al., 2000; Rosenthal et al., 2000). Another widely applied proxy is Sr/Ca, which is used to determine the Sr concentration of past seawater that varies on million year time scales (e.g., Graham et al., 1982; Stoll et al., 1999; Lear et al., 2003a) and in conjunction with the marine evolution of radiogenic Sr isotopes ($^{87}Sr/^{86}Sr$) long-term stratigraphies can be established (e.g., DePaolo and Ingram, 1985; Koepnick et al., 1985; DePaolo, 1986; Hodell and Woodruff, 1994; Hodell et al., 2007). Sr has a long residence time (~2.5 Myrs) compared to the ocean mixing time, thus it is homogenously distributed in seawater at any time in the geological past (e.g., Richter and DePaolo, 1988; Veizer, 1989). Therefore and due to the fact that Sr is directly incorporated into carbonates from seawater, it provides a reliable stratigraphic tool (e.g., Koepnick et al., 1985; Hodell and Woodruff, 1994). Since the radiogenic Sr signature in seawater is mainly controlled by the riverine input from continental weathering products, $^{87}Sr/^{86}Sr$ and also Sr/Ca, determined either on bulk carbonate samples or foraminifera, allow the estimation of past continental weathering intensity (Raymo et al., 1988; Edmond, 1992; Raymo and Ruddimann, 1992; Lear et al., 2003b; Krabbenhöft et al., 2010). In addition, Sr/Ca and $^{87}Sr/^{86}Sr$ are reliable indicators of diagenetic alteration of the

sediment and are used to estimate the preservation of sediments and the foraminifera contained in them (e.g., Baker et al., 1982; Delaney, 1989; Brown and Elderfield, 1996; Kozdon et al., 2013). Furthermore, Mn/Ca ratios, originating from overgrowths and coatings, also indicate alteration of sediments and foraminifera given that high amounts of Mn^{2+} are incorporated into Mn-Fe oxides and Mn-carbonates under reducing conditions in the sediment column (e.g., Boyle, 1983; Pingitore et al., 1988; Regenberg et al., 2007; Pena et al., 2005, 2008).

All the above mentioned proxies have been applied to bulk carbonates as well, which mainly consist of coccolithophorids, calcifying photoautotrophic algae. The bulk carbonates record the same climatic conditions as foraminifera and are widely used in particular in old sediments (e.g., Baker et al., 1982; Koepnick et al., 1985; Pingitore, 1988; Schrag et al., 1995; Wade and Pälike, 2004), although Mg/Ca ratios of bulk carbonates are mainly controlled by alteration of the sediment instead of temperature (e.g., Delaney, 1989; Delaney and Linn, 1993; Higgins and Schrag, 2012).

I.4 Climate of the Oligocene and Miocene

The early studies of Shackleton (1974, 1977b) provided first insights into the climate of the past. Hays et al. (1976) and Imbrie (1982) built on this work and linked changes in $\delta^{18}O$ to changes in orbital insolation. These pioneering efforts opened an entire new field and with this, we started to understand the forcing of Earth's climate on geological timescales.

I.4.1 Climate and orbital cyclicity of the Oligicene

The Oligocene marked the establishment of the icehouse world following the warm greenhouse climate of the Paleocene and Eocene (e.g., Miller et al., 1991; Zachos et al., 2008). The onset of the Oligocene is represented by a brief but intense cooling at ~34 Ma when the first large continental ice sheets formed on Antarctica (Figure 1) (Miller et al., 1991; Zachos et al., 1997, 2001b; Coxall et al., 2005). This event is thought to have involved a re-organisation of climate and ocean conditions, which is also evident in an ~1 km drop of the carbonate compensation depth (CCD; the depth where the rate of calcite supply equals the dissolution rate and no calcite

accumulates) (Zachos et al., 2001b; Pälike et al., 2006b). Benthic foraminiferal $\delta^{18}O$ values increased by > 1 ‰ during the cooling (Miller et al., 1991; Zachos et al., 1997, 2001a, 2001b; Wade and Pälike, 2004; Pälike et al., 2006b) and stayed high (≥ ~2.5 ‰) afterwards (Zachos et al., 2001b; Wade and Pälike, 2004; Pälike et al., 2006b) indicating the first permanent ice sheets on Antarctica and cold deep water temperatures of ~4°C compared to the warm temperatures of the Eocene (up to ~12°C) (Zachos et al., 2001b). This colder climate included a few short-term glaciations, of which the one at ~26.8 Ma (termed Oi-2b or cycle 67_{Oi}; Miller et al.,1991; Wade and Pälike, 2004) exhibit the highest $\delta^{18}O$ values throughout the entire Oligocene (Wade and Pälike, 2004, 2005; Pälike et al., 2006b). As indicated by a decline of the $\delta^{18}O$ to < 2 ‰ after 27-26 Ma, the ice sheet decreased until ~23.6 Ma when the $\delta^{18}O$ values increased again and culminated in the Mi-1 glaciation at ~22.8 Ma at the Oligocene/Miocene boundary (Figure 1) (Zachos et al., 2001a, 2001b; Pälike et al., 2006b).

The $\delta^{18}O$ and $\delta^{13}C$ values exhibit a strong coherence with the long eccentricity (400 kyr) and the 1.2 Myrs obliquity cycles through the entire Oligocene (Zachos et al., 1997, 2001a, 2001b; Wade and Pälike, 2004; Pälike et al., 2006a, 2006b). This strong correspondence with the 400 kyr band has been described as the “heartbeat” of the Oligocene (Pälike et al., 2006b). The $\delta^{18}O$ variability also shows a close correlation with short eccentricity (100 kyr), whereas the $\delta^{13}C$ data exhibit pronounced obliquity cycles (40 kyr) (Zachos et al., 1997, 2001a, 2001b; Wade and Pälike, 2004; Pälike et al., 2006a, 2006b). Several lines of evidence indicate that the brief but prominent glaciations during the Oligocene (Oi-1, Oi-2b), but also including the Mi-1 and Mi-3 (mid-Miocene cooling at 13.9 Ma), were triggered by obital cyclicity (e.g., Zachos et al., 2001a, 2001b; Wade and Pälike, 2004; Pälike et al., 2006b). It has been suggested that a low obliquity amplitude mode prevailing before and during the glaciation pre-conditioned the climate, including a drawdown of atmospheric CO_2 close to a climatic threshold, whereas the onset of these glaciations were triggered by eccentricity (minima in 400 kyr cycle) (Zachos et al., 2001a; Wade and Pälike, 2004; Coxall et al., 2005; DeConto and Pollard, 2003; Pälike et al., 2006a, 2006b). The drawdown of atmospheric CO_2 and a heavier $\delta^{13}C$ record coinciding with those glaciations suggest that the global carbon cycle was involved in these climate

changes (e.g., Zachos et al., 2001a, 2001b; Wade and Pälike, 2004; Pälike et al., 2006b).

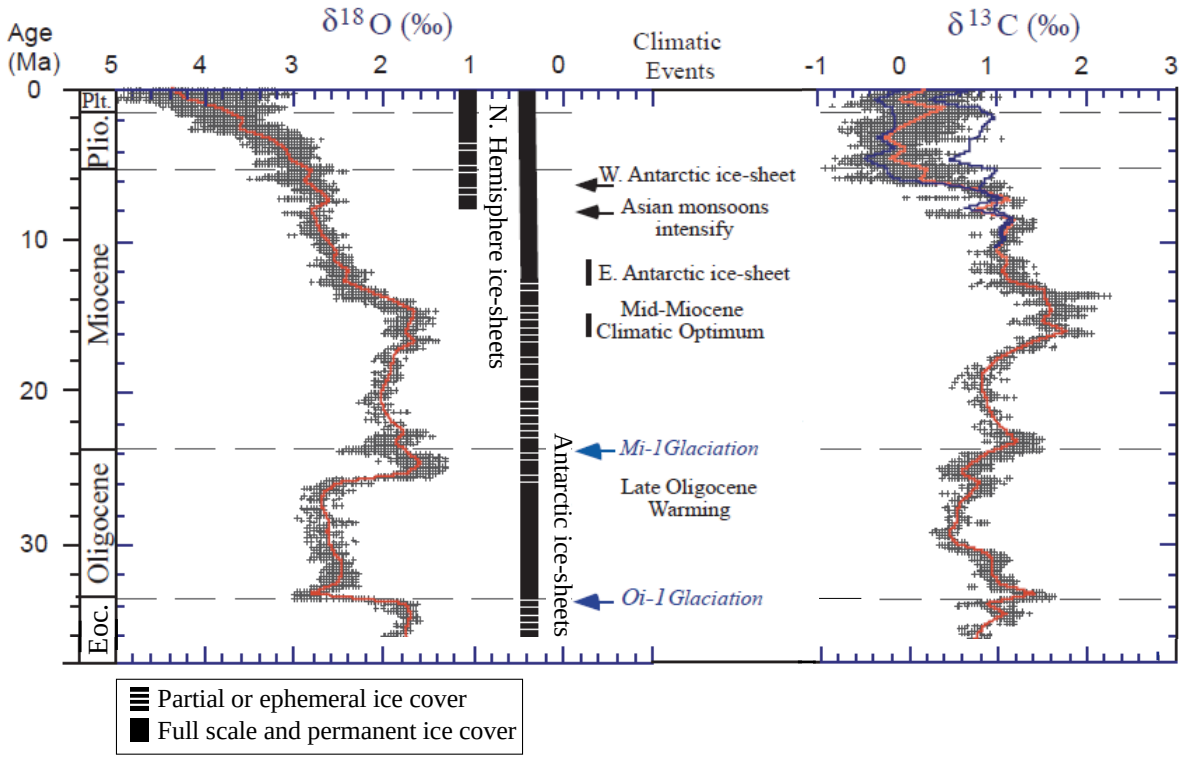

Figure 1. Compilation of global deep sea oxygen and carbon isotope records (modified after Zachos et al., 2001b). The blue curves in the $\delta^{13}C$ record show data from the Atlantic. The vertical bars represent ice volume in each hemisphere relative to the last glacial maximum. The dashed bar illustrates partial ice cover (≤ 50 % of present ice coverage) and the full bar represents close to maximum ice cover (> 50 % of present ice coverage). Climatic key events are shown as well.

I.4.2 Climate of the early and middle Miocene

The onset of the Miocene at 22.8 Ma was marked by a prominent but transient glaciation (Mi-1) similar to the Oi-1 and was accompanied by an ~1 ‰ increase of the benthic foraminiferal $\delta^{18}O$ values (Miller et al., 1991; Zachos et al., 1997, 2001a, 2001b; Wade and Pälike, 2004; Pälike et al., 2006b). After the Mi-1 glaciation, the Cenozoic cooling trend continued, but was interrupted by an extended warm period from ~17 to 14.7 Ma termed the Middle Miocene Climate Optimum (MMCO) (Figure 1) (e.g., Flower and Kennett, 1993; Holbourn et al., 2005, 2007). The MMCO was characterised by relatively low benthic $\delta^{18}O$ values (< 2 ‰) indicating a minimum ice volume (e.g., Holbourn et al., 2007). One characteristic feature of the middle Miocene are the prominent maxima in $\delta^{13}C$ of the “Monterey Carbon Isotopic Excursion” (e.g., Vincent and Berger, 1985; Holbourn et al., 2007), which were

closely linked to the 400 kyr long eccentricity cycles (e.g., Woodruff and Savin, 1991; Shevenell et al., 2004; Holbourn et al., 2005, 2007, 2014). Periodic increases in organic carbon burial probably caused the $\delta^{13}C$ maxima and resulted in reduced atmospheric CO_2 levels and global cooling (Vincent and Berger, 1985; Woodruff and Savin, 1991; Flower and Kennett, 1993, 1994). The highest $\delta^{13}C$ values are found within the carbon maxima (CM) events 3b, 4 and 6 (Woodruff and Savin, 1991; Holbourn et al., 2005, 2007, 2014; Tian et al., 2013). The onset of the carbon isotope excursion CM 4a is represented by a peak warmth event at ~15.6 Ma and was associated with a sharp decrease in $\delta^{13}C$ (Holbourn et al., 2005, 2007, 2014; Tian et al., 2013). After ~14.7 Ma, the benthic $\delta^{18}O$ values increased gradually indicating the continuation of the long-term cooling trend (Figure 1) (Zachos et al., 2001b; Holbourn et al., 2005, 2007, 2014). This cooling trend culminated in an intense increase of the benthic $\delta^{18}O$ signature (~1 ‰) between 13.9-13.7 Ma and marked the onset of the global Miocene cooling (Mi-3), which has been attributed to Antarctic ice-sheet expansion and deep water cooling (Figure 1) (e.g., Shackleton and Kennett, 1975; Miller et al., 1991; Woodruff and Savin, 1991; Flower and Kennett, 1994; Holbourn et al., 2005, 2007). This cooling was associated with the onset of event CM 6, during which the $\delta^{13}C$ values increased significantly (e.g., Woodruff and Savin, 1991; Holbourn et al., 2005, 2007, 2014).

I.4.3 Link between $\delta^{18}O$ and $\delta^{13}C$ and climate feedbacks during the middle Miocene

The benthic $\delta^{18}O$ and $\delta^{13}C$ data co-varied during the middle Miocene until the Mi-3 glaciation (e.g., Holbourn et al., 2005, 2007, 2014; Tian et al., 2013). This relationship between the $\delta^{18}O$ and $\delta^{13}C$ records suggest that global ice volume and deep water temperature changes were largely associated with changes in the global carbon cycle (e.g., Vincent and Berger, 1985; Flower and Kennett, 1993, 1994; Pälike et al., 2006b; Kirtland Turner, 2014). This interval of strong coherence between benthic $\delta^{18}O$ and $\delta^{13}C$ data appears to have been orbitally paced and was possibly linked via a carbon cycle feedback loop involving climate, weathering, carbonate preservation and atmospheric CO_2 (e.g., Vincent and Berger, 1985; Flower and Kennett, 1994; Zachos et al., 2008, 2010; Ma et al., 2011; Kirtland Turner, 2014). Considering the long-term variation (~400 kyr), a negative weathering feedback has

been suggested, which controlled the atmospheric CO_2 and temperature (e.g., Ma et al., 2011; Kirtland Turner, 2014). This means, at high temperatures weathering rates are high resulting in enhanced nutrient supply (and possible labile organic material) to the ocean and thus in carbonate dissolution. Weathering and carbonate dissolution consume CO_2, which consequently reduces the atmospheric CO_2 and leads to cooling. Such cooling, in turn, results in decreasing weathering rates and less CO_2 removal by weathering, which then increases temperatures and closes the feedback loop. Nevertheless, the increased sequestration of organic carbon, modulated by the low eccentricity frequency (400 kyr), was responsible for the carbon isotope events of the Monterey Excursion, but possibly included other internal feedback mechanisms (Woodruff and Savin, 1991; Flower and Kennett, 1993, 1994; Ma et al., 2011). During the long-term cooling trend from ~14.7 Ma onwards, atmospheric CO_2 declined (e.g., Foster et al., 2012), possibly reaching values close to an internal climate threshold, which consequently initiated the global cooling and was triggered by a change in the orbital cyclicity (e.g., Pälike et al., 2006b; Kirtland Turner, 2014). Similar to the prominent glaciations Oi-1, Oi-2b and Mi-1, the amplitude in the obliquity was low at ~13.8 Ma and a minimum in the long eccentricity probably triggered the mid-Miocene cooling. Two main mechanisms, although not mutually exclusive, have been hypothesised to have caused the mid-Miocene cooling event. The ocean circulation hypothesis suggests that the continued opening of the Drake Passage strengthened the Antarctic Circumpolar Current and thermally isolated the Antarctic continent (Shackleton and Kennett, 1975; Woodruff and Savin, 1991; Flower and Kennett, 1994; Shevenell et al., 2004). This change in ocean circulation led to a better ventilation of the deep Pacific (e.g., Woodruff and Savin, 1991; Wright et al., 1992; Holbourn et al., 2007) and increased upwelling in the equatorial Pacific (Holbourn et al., 2014; Tian et al., 2014). The CO_2 hypothesis, on the other hand, proposed that the episodic (400 kyr paced) increases in organic carbon burial (intensified by increased upwelling) resulted in a drawdown of atmospheric CO_2 and led to further cooling during Southern Hemisphere insolation minima via a positive climate feedback (Vincent and Berger, 1985; Flower and Kennett, 1994; Pagani et al., 1999; Holbourn et al., 2005, 2007, 2014). The cooling reduced the supply of organic carbon to the ocean (Zachos et al., 2010; Kirtland Turner, 2014) and supported the build-up of continental ice sheets, lowered sea level and increased the erosion of organic-rich

sediments from formerly marginal seas (Vincent and Berger, 1985), which subsequently decreased the benthic $\delta^{13}C$ from ~13.8 Ma onwards.

I.4.4 Climate of the late middle Miocene to present

Since the onset of Antarctic ice sheet growth at ~13.9 Ma, the Miocene climate gradually cooled further (Figure 1) including a series of incremental steps seen in the benthic $\delta^{18}O$ records (e.g., Westerhold et al., 2005; Holbourn et al., 2013). The most prominent step in the $\delta^{18}O$ data is observed at ~13.1 Ma, which corresponds to the Mi-4 event (Miller et al., 1991), and smaller cooling events are recognised at ~11.8, 10.6, 9.9, 9.0, ~6.2, and 5.5 Ma (e.g., Hodell et al., 2001; Westerhold et al., 2005; Billups et al., 2008; Cooke et al., 2008; Holbourn et al., 2013). These smaller cooling events indicate smaller-scale expansions of the ice sheet and/or further cooling of deep water masses (Holbourn et al., 2013). The cooling trend was interrupted by a short intense warming at ~10.8-10.7 Ma, which seems to be a global feature as it is recognised, for instance, in the records of two subtropical sites in the South China Sea (Holbourn et al., 2013) and the eastern South Atlantic (Westerhold et al., 2005). This peak warmth period is believed to be orbitally triggered (Holbourn et al., 2013). Nevertheless, the Antarctic ice sheet became more stable after the expansions at ~13.9 and 13.1 Ma, which is evident in the low variability of the benthic $\delta^{18}O$ data, and was possibly caused by a combination of several factors including the further isolation of Antarctica, colder deep water temperatures, and decreased moisture flux from low latitudes (e.g., Wright et al., 1991; Holbourn et al., 2013). Long eccentricity cycles (400 kyr) are prominent in the $\delta^{13}C$ record from 16.4-5 Ma (e.g., Holbourn et al., 2013; Kirtland Turner, 2014) and short eccentricity (100 kyr) and obliquity cycles are recognised in both, $\delta^{18}O$ and $\delta^{13}C$ data indicating that orbital forcing largely controlled the evolution of the climate (e.g., Westerhold et al., 2005; Holbourn et al., 2013).

At ~3.3 Ma, permanent ice sheets were established on Greenland marking the onset of the Northern Hemisphere glaciation (Figure 1) (e.g., Zachos et al., 2001b; Lisiecki and Raymo, 2005) and the transition into the ice age mode of the modern climate at ~2.7 Ma (e.g., Raymo, 1994; Tiedemann et al., 1994; Shackleton et al., 1995). The waxing and waning of the ice sheets in the period between 5.3 and ~0.9 Ma was

dominated by the obliquity band and since then the short eccentricity cycles have been most prominent (e.g., Shackleton and Opdyke, 1973; Imbrie et al., 1992; Raymo, 1994; Tiedemann et al., 1994; Lisiecki and Raymo, 2005).

I.5 Objectives

We investigated carbonate recrystallisation on selected sediment cores of IODP Expedition 320/321 Pacific Equatorial Age Transect (PEAT) in the eastern equatorial Pacific. The sediment successions have been recovered along an age transect and are of similar age and initial composition, but have been subjected to different diagenetic histories resulting from variable subsidence, sedimentation rates (Figure 2), productivity and geothermal gradients (Pälike et al., 2010). Thus, these sediments are well suited for the study of recrystallisation.

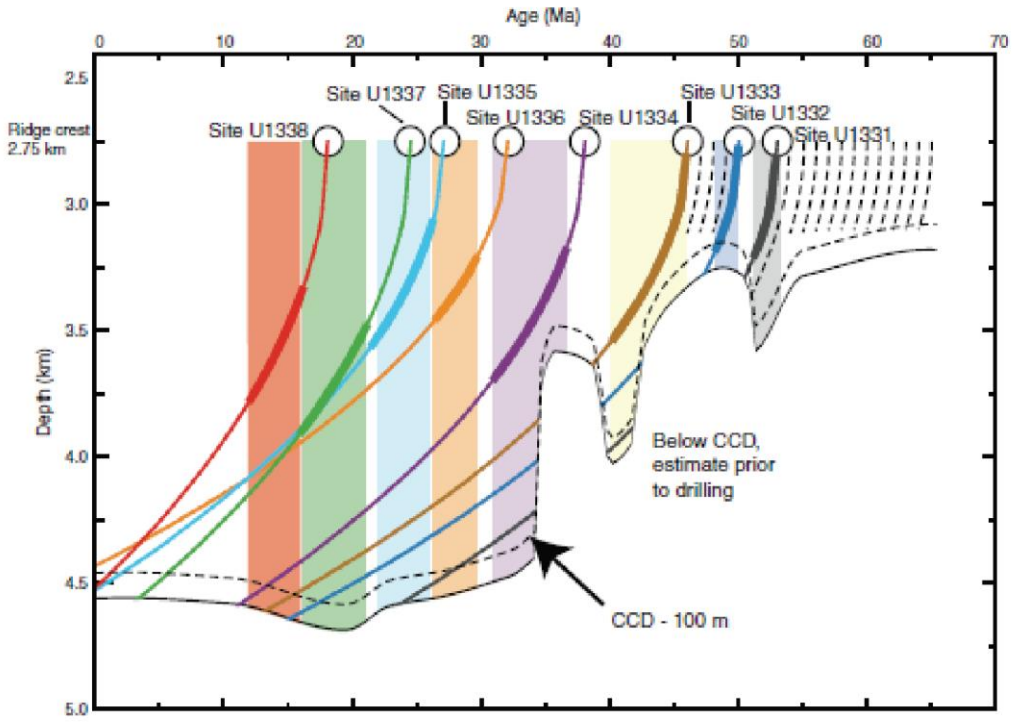

Figure 2. Subsidence curves of the PEAT sites based on the carbonate compensation depth (CCD) history (from Pälike et al., 2010). Coloured boxes represent the time interval when each site was at the equator. Coloured subsidence lines mark the time intervals when carbonate deposition was expected meaning that the sites were above the CCD. Subsidence curves were determined by using a subsidence parameter calculated from estimated basement age of the PEAT sites and their present-day depth.

One objective of this study was to quantify down-core carbonate diagenesis at the PEAT site sediments by analysing bulk carbonates and associated pore waters (Chapter 1). Having identified the extent of recrystallisation in the bulk carbonates, foraminiferal tests deposited during specific climatic key events were analysed to investigate their preservation state and the impact of recrystallisation on different geochemical proxies and on the validity of the conclusions drawn from them. In particular, element/Ca ratios of planktonic foraminiferal tests were measured using micro-analytical techniques (laser ablation ICP-MS, electron microprobe) to study the intratest chemistry of different tests from the same sample and compare the different sites (Chapter 3). Another objective was to establish a middle Miocene benthic foraminiferal stable isotope stratigraphy of one specific PEAT site (U1336) to test the reliability of past benthic stable isotope records (Chapter 2).

I.6 Research questions and outline

This thesis comprises a multi-component study of recrystallisation in eastern equatorial Pacific sediments from the IODP Expedition 320/321 in which bulk carbonates, pore waters as well as foraminiferal tests from specific time intervals were analysed to investigate the extent of recrystallisation on different geochemical proxies.

The following research questions are addressed in the Chapters 1-3:

- How fast did recrystallisation occur and how open was the system?
- Which factors mainly influence recrystallisation – age, sedimentation rate, carbonate saturation state of the bottom water, lithology or geothermal gradient?
- How variable is the preservation state between different individual foraminiferal tests and species from the same sediment sample and how does the preservation state change over time?
- Are benthic foraminifera better preserved than planktonic ones?
- What is the impact of recrystallisation on different geochemical proxy signatures, such as $\delta^{18}O$, $\delta^{13}C$, Mg/Ca, Sr/Ca, and Mn/Ca, and how are the interpretations affected?

Outline of the publication and manuscripts

Chapter 1: Bulk carbonates and associated pore waters were investigated concerning their degree of recrystallisation down-core. The analyses mainly focussed on the behaviour of Sr and its isotopes: Sr^{2+} concentrations of pore waters; Sr/Ca, $^{87}Sr/^{86}Sr$, and $\delta^{88/86}Sr$ of both, pore waters and bulk carbonates. In this study, stable Sr isotopes were for the first time used as a proxy in carbonate-rich deep sea sediments.

Chapter 2: A benthic foraminiferal stable isotope stratigraphy of the middle Miocene was established for Site U1336 focussing on the “Monterey Carbon Isotope Excursion”. This record was compared to existing stable isotope records of neighbouring Sites U1337 and U1338.

Chapter 3: Laser ablation ICP-MS derived element/Ca ratio depth profiles through test walls of the planktonic foraminifera *Dentoglobigerina venezuelana* were obtained for specific time intervals of the PEAT sites. Individual tests were analysed to investigate the variability of preservation of specimens of the same sediment samples. Additionally, SEM images helped to constrain the preservation state of the tests.

References

Anand P., Elderfield H., and Conte M. H. (2003) Calibration of Mg/Ca thermometry in planktonic foraminifera from a sediment trap time-series. *Paleoceanography* **18**, 1050, doi:10.1029/2002PA000846.

Arrhenius G. (1952) Sediment cores from the East Pacific. *Reports of the Swedish Deep-Sea Expedition, 1947-1948*. 5, 1-228.

Baker P. A., Gieskes J. M., and Elderfield H. (1982) Diagenesis of carbonates in deep-sea sediments-evidence from Sr/Ca ratios and interstitial dissolved Sr^{2+} data. *J. Sediment. Petrol.* **52**, 71-82.

Bé A. W. H. (1977) An ecological, zoogeographic and taxonomic review of recent planktonic foraminifera. In: *Oceanic Micropaleontology* 1 (eds. A. T. S. Ramsay). Academic Press, London. pp. 1-100.

Bé A. W. H. and Tolderlund D. S. (1971) Distribution and ecology of living planktonic foraminifera in surface waters of the Atlantic and Indian Oceans. In: *The Micropaleontology of Oceans* (eds. B. M. Funnell and W. R. Riedel). Cambridge University Press, Cambridge. pp. 105-149.

Bé A. W. H., Hemleben C., Anderson O. R., and Spindler M. (1979) Chamber formation in planktonic Foraminifera. *Micropaleontology* **25**, 294-307.

Belanger P. E., Curry W. B., and Matthews R. K. (1981) Core-top evaluation of benthic foraminiferal isotopic ratios for paleo-oceanographic interpretations. *Paleogeogr. Paleoclimatol. Paleoecol.* **33**, 205-220.

Bemis B. E., Spero H., Bijima J., and Lea D. W. (1998) Reevaluation of the oxygen isotopic composition of planktonic foraminifera: experimental results and revised paleotemperature equations. *Paleoceanography* **13**, 150-160.

Bender M. L., Lorens R. B., and Williams D. F. (1975) Sodium, magnesium, and strontium in the tests of planktonic foraminifera. *Micropaleontology* **21**, 448-459.

Billups K., Kelly C., and Pierce E. (2008) The late Miocene to early Pliocene climate transition in the Southern Ocean. *Paleogeogr. Paleoclimatol. Paleoecol.* **267**, 31-40.

Boyle E. A. (1981) Cadmium, zinc, copper, and barium in foraminifera tests. *Earth Planet. Sci. Lett.* **53**, 11-35.

Boyle E. A. (1983) Manganese carbonate overgrowths on foraminifera tests. *Geochim. Cosmochim. Acta* **47**, 1815-1819.

Boyle E. A. (1988) Cadmium: Chemical tracer of deepwater paleoceanography. *Paleoceanography* **3**, 471-489.

Boyle E. A. and Keigwin L. D. (1985) Comparison of Atlantic and Pacific paleochemical records for the last 215,000 years: changes in deep ocean circulation and chemical inventories. *Earth Planet. Sci. Lett.* **76**, 135-150.

Brady H. B. (1884) Report on the foraminifera dredged by H.M.S. *Challenger* during the years 1873-1876. In: *Report on the Scientific Results of the Voyage of H.M.S. Challenger, during the years 1873-1876, Zoology* 9 (eds. J. Murray). Neill and Company, Edinburgh. pp. 1-814.

Brown S. J. and Elderfield H. (1996) Variation in Mg/Ca and Sr/Ca ratios of planktonic foraminifera caused by postdepositional dissolution: Evidence of shallow Mg-dependent dissolution. *Paleoceanography* **11**, 543-551.

Chappell J. and Shackleton N. J. (1986) Oxygen isotopes and sea-level. *Nature* **324**, 137-140.

Cooke P. J., Nelson C. S., and Crundwell M. P. (2008) Miocene isotope zones, paleotemperatures, and carbon maxima events at intermediate water-depth, Site 593, Southwest Pacific, New Zealand. *New Zeal. J. Geol. Geop.* **51**, 1-22.

Coxall H. K., Wilson P. A., Palike H., Lear C. H., and Backman J. (2005) Rapid stepwise onset of Antarctic glaciation and deeper calcite compensation in the Pacific Ocean. *Nature* **433**, 53-57.

Cushman J. A. (1911) A Monograph of the Foraminifera of the North Pacific Ocean. Part II - Textulariidae. *Bull. USNM* **71**, 1-108.

DeConto R. M. and Pollard D. (2003) Rapid Cenozoic glaciation of Antarctica induced by declining atmospheric CO_2. *Nature* **421**, 245-249.

Dekens P. S., Lea D. W., Pak D. K., and Spero H. J. (2002) Core top calibration of Mg/Ca in tropical foraminifera: Refining paleotemperature estimation. *Geochem. Geophys. Geosyst.* **3**, 1022, doi:10.1029/2001GC000200.

Delaney M. L. (1989) Temporal changes in interstitial water chemistry and calcite recrystallization in marine sediments. *Earth Planet. Sci. Lett.* **95**, 23-37.

Delaney M. L. and Boyle E. A. (1986) Lithium in foraminifera shells: Implication for high-temperature hydrothermal circulation fluxes and oceanic crustal generation rates. *Earth Planet. Sci. Lett.* **80**, 91-105.

Delaney M. L. and Linn L. J. (1993) Interstitial water and bulk calcite chemistry, Leg 130, and calcite recrystallization. In: *Proc. ODP. Sci. Res.* 130 (eds. W. H. Berger, L. W. Kroenke, T. R. Janecek, et al.). Ocean Drilling Program, pp. 561-572.

Delaney M. L., Bé A. W. H., and Boyle E. A. (1985) Li, Sr, Mg, and Na in foraminiferal calcite shells from laboratory culture, sediment traps, and sediment cores. *Geochim. Cosmochim. Acta* **49**, 1327-1341.

DePaolo D. J. (1986) Detailed record of the Neogene Sr isotopic evolution of seawater from DSDP Site 590B. *Geology* **14**, 103-106.

DePaolo D. J. and Ingram B. L. (1985) High-Resolution Stratigraphy with Strontium Isotopes. *Science* **227**, 938-941.

Derry L. A. and France-Lanord C. (1996) Neogene growth of the sedimentary organic carbon reservoir. *Paleoceanography* **11**, 267-275.

Edmond J. M. (1992) Himalayan Tectonics, Weathering Processes, and the Sr Isotope Record in Marine Limestones. *Science* **258**, 1594-1597.

Elderfield H. and Ganssen G. (2000) Past temperature and $\delta^{18}O$ of surface ocean waters inferred from foraminiferal Mg/Ca ratios. *Nature* **405**, 442-445.

Elderfield H., Gieskes J. M., Baker P. A., Oldfield R. K., Hawkesworth C. J., and Miller R. (1982) $^{87}Sr/^{86}Sr$ and $^{18}O/^{16}O$ ratios, interstitial water chemistry and diagenesis in deep-sea carbonate sediments of the Ontong Java Plateau. *Geochim. Cosmochim. Acta* **46**, 2259-2268.

Elderfield H., Yu J., Anand P., Kiefer T., and Nyland B. (2006) Calibrations for benthic foraminiferal Mg/Ca paleothermometry and the carbonate ion hypothesis. *Earth Planet. Sci. Lett.* **250**, 633-649.

Emiliani C. (1954) Temperatures of Pacific Bottom Waters and Polar Superficial Waters during the Tertiary. *Science* **119**, 853-855.

Emiliani C. (1955) Pleistocene temperatures. *J. Geol.* **63**, 538-578.

Epstein S., Buchsbaum R., Lowenstam H. A., and Urey H C. (1953) Revised carbonate-water isotopic temperature scale. *Geol. Soc. Am. Bull.* **64**, 1315-1326.

Erez J. (1978) Vital effect on stable-isotope composition seen in foraminifera and coral skeletons. *Nature* **273**,199-202.

Erez J. (2003) The source of ions for biomineralization in foraminifera and their implications for paleoceanographic proxies. *Rev. Mineral. Geochem.* **54**, 115-149.

Fantle M. S. and DePaolo D. J. (2006) Sr isotopes and pore fluid chemistry in carbonate sediment of the Ontong Java Plateau: Calcite recrystallization rates and evidence for a rapid rise in seawater Mg over the last 10 million years. *Geochim. Cosmochim. Acta* **70**, 3883-3904.

Filipsson H. L., Bernhard J. M., Lincoln S. A., and McCorkle D. C. (2010) A culture-based calibration of benthic foraminiferal paleotemperature proxies: $\delta^{18}O$ and Mg/Ca results. *Biogeosciences* **7**, 1335-1347.

Flower B. P. and Kennett J. P. (1993) The middle Miocene ocean/climate transition: High-resolution oxygen and carbon isotopic records from DSDP Site 588A, southwest Pacific. *Paleoceanography* **8**, 811-843.

Flower B. P. and Kennett J. P. (1994) The middle Miocene climatic transition: East Antarctic ice sheet development, deep ocean circulation and global carbon cycling. *Paleogeogr. Paleoclimatol. Paleoecol.* **108**, 537-555.

Foster G. L., Lear C. H., and Rae J. W. B. (2012) The evolution of pCO_2, ice volume and climate during the middle Miocene. *Earth Planet. Sci. Lett.* **341-344**, 243-254.

Gieskes J. M., Elderfield H. and Palmer M. R. (1986) Strontium and its isotopic composition in interstitial waters of marine carbonate sediments. *Earth Planet. Sci. Lett.* **77**, 229-235.

Graham D. W., Bender M. L., Williams D. F., and Keigwin L. D. (1982) Strontium-calcium ratios in Cenozoic planktonic foraminifera. *Geochim. Cosmochim. Acta* **46**, 1281-1292.

Hampt G. and Delaney M. L. (1997) Influences on calcite Sr/Ca records from Ceara Rise and other regions: Distinguishing ocean history and calcite recrystallization. In: *Proc. ODP, Sci. Res.* 154 (eds. N.J. Shackleton, W.B. Curry, C. Richter, and T.J. Bralower). Ocean Drilling Program, pp. 491-500.

Hathorne E. C. and James R. H. (2006) Temporal record of lithium in seawater: A tracer for silicate weathering? *Earth Planet. Sci Lett.* **246**, 393-406.

Hay W. W. (1985) Potential errors in estimates of carbonate rock accumulating through geologic time. In: *The Carbon Cycle and Atmospheric CO_2: Natural Variations Archean to Present* (eds. E. T. Sundquist and W. S. Broecker). Amer. Geophys. Union Geophys. Monogr. 32. pp. 573-583.

Hays J. D., Imbrie J., and Shackleton N. J. (1976) Variations in the Earth's Orbit: Pacemaker of the Ice Ages. *Science* **194**; 1121-1132.

Hayward, B. W. (2015) World Foraminifera Database. developed by VLIZ, Flanders Marine Institute. available online at http://www.marinespecies.org/foraminifera/.

Hemleben C., Bé A. W. H., Anderson O. R., and Tuntivate S. (1977) Test morphology, organic layers and chamber formation of the planktonic foraminifer *Globorotalia menardii* (d'Orbigny). *J. Foramin. Res.* **7**, 1-25.

Hemleben C., Anderson O. R., Berthold W., and Spindler M. (1986) Calcification and chamber formation in Foraminifera - a brief overview. In: *Biomineralization in Lower Plants and Animals* (eds. B. S. C. Leadbeater and R. Riding). Clarenton Press. pp. 237-249.

Hemleben C., Spindler M., and Anderson O. R. (1989) *Modern Planktonic Foraminifera*. Springer Verlag, Berlin.

Higgins J. A. and Schrag D. P. (2012) Records of Neogene seawater chemistry and diagenesis in deep-sea carbonate sediments and pore fluids. *Earth Planet. Sci. Lett.* **357-358**, 386-396.

Hodell D. A. and Woodruff F. (1994) Variations in the strontium isotopic ratio of seawater during the Miocene: Stratigraphic and geochemical implications. *Paleoceanography* **9**, 405-426.

Hodell D. A., Mueller P. A., and Garrido J. R. (1991) Variations in the strontium isotopic composition of seawater during the Neogene. *Geology* **19**, 24-27.

Hodell D. A., Curtis J. H., Sierro F. J., and Raymo M. E. (2001) Correlation of late Miocene to early Pliocene sequences between the Mediterranean and North Atlantic. *Paleoceanography* **16**, 164-178.

Hodell D. A., Kamenov G. D., Hathorne E. C., Zachos J. C., Röhl U., and Westerhold T. (2007) Variations in the strontium isotope composition of seawater during the Paleocene and early Eocene from ODP Leg 208 (Walvis Ridge). *Geochem. Geophys. Geosyst.* **8**, Q09001, doi:10.1029/2007GC001607.

Holbourn A., Kuhnt W., Schulz M., and Erlenkeuser H. (2005) Impacts of orbital forcing and atmospheric carbon dioxide on Miocene ice-sheet expansion. *Nature* **438**, 483-487.

Holbourn A., Kuhnt W., Schulz M., Flores J.-A., and Andersen N. (2007) Orbitally-paced climate evolution during the middle Miocene "Monterey" carbon-isotope excursion. *Earth Planet. Sci. Lett.* **261**, 534-550.

Holbourn A., Kuhnt W., Clemens S., Prell W., and Andersen N. (2013) Middle to late Miocene stepwise climate cooling: Evidence from a high-resolution deep water isotope curve spanning 8 million years. *Paleoceanography* **28**, 688-699.

Holbourn A., Kuhnt W., Lyle M., Schneider L., Romero O., and Andersen N. (2014) Middle Miocene climate cooling linked to intensification of eastern equatorial Pacific upwelling. *Geology* **42**, 19-22.

Hönisch B. and Hemming N. G. (2005) Surface ocean pH response to variations in pCO_2 through two full glacial cycles. *Earth Planet. Sci. Lett.* **236**, 305-314.

Imbrie J. (1982) Astronomical theory of the ice ages: A brief historical review. *Icarus* **50**, 408-422.

Imbrie J., Hays J. D., Martinson D. G., McIntyre A., Mix A. C., Morley J. J., Pisias N. G., Prell W. L., and Shackleton N. J. (1984) The orbital theory of Pleistocene climate: support from a revised chronology of the marine $\delta^{18}O$ record. In: *Milankovitch and Climate* (eds. A. Berger, et al.). D. Reidel, Hingham, Massachusetts. pp. 269-305.

Imbrie J., Boyle E. A., Clemens S. C., et al. (1992) On the structure and origin of major glaciation cycles. 1. Linear responses to Milankovitch forcing. *Paleoceanography* **7**, 701-738.

Kirtland Turner S. (2014) Pliocene switch in orbital-scale carbon cycle/climate dynamics. *Paleoceanography* **29**, 1256-1266.

Koepnick R. B., Burke W. H., Denison R. E., Hetherington E. A., Nelson H. F., Otto J. B., and Waite L. E. (1985) Construction of the seawater $^{87}Sr/^{86}Sr$ curve for the Cenozoic and Cretaceous: Supporting data. *Chem. Geol., Isot. Geosci. Sec.* **58**, 55-81.

Köhler P. and Fischer H. (2004) Simulating changes in the terrestrial biosphere during the last glacial/interglacial transition. *Global Planet. Change* **43**, 33-55.

Kozdon R., Kelly D. C., Kitajima K., Strickland A., Fournelle J. H., and Valley J. W. (2013) In situ $\delta^{18}O$ and Mg/Ca analyses of diagenetic and planktic foraminiferal calcite preserved in a deep-sea record of the Paleocene-Eocene thermal maximum. *Paleoceanography* **28**, 517-528.

Krabbenhöft A., Eisenhauer A., Böhm F., et al. (2010) Constraining the marine strontium budget with natural strontium isotope fractionations ($^{87}Sr/^{86}Sr^*$, $\delta^{88/86}Sr$) of carbonates, hydrothermal solutions and river waters. *Geochim. Cosmochim. Acta* **74**, 4097-4109.

Kroenke L. W., Berger W. H., Janecek T. R., et al. (1991) Site 807. In: *Proc. ODP. Init. Repts.* 130 (eds. W. H. Berger, L. W. Kroenke, T. R. Janecek, et al.). Ocean Drilling Program, pp. 369-493.

Langer M. R. (2008) Assessing the contribution of foraminiferan protists to global ocean carbonate production. *J. Eukaryot. Microbiol.* **55**, 163-169.

Lea D. W. and Boyle E. A. (1989) Barium content of benthic foraminifera controlled by bottom water composition. *Nature* **338**, 751-753.

Lea D. W. and Spero H. J. (1992) Experimental determination of barium uptake in shells of the planktonic foraminifera *Orbulina universa* at 22°C. *Geochim. Cosmochim. Acta* **56**, 2673-2680.

Lea D. W. and Spero H. J. (1994) Assessing the reliability of paleochemical tracers: barium uptake in the shells of planktonic foraminifera. *Paleoceanography* **9**, 445-452.

Lea D. W., Mashiotta T. A., and Spero H. J. (1999) Controls on magnesium and strontium uptake in planktonic foraminifera determined by live culturing. *Geochim. Cosmochim. Acta* **63**, 2369-2379.

Lea D. W., Pak D. K., and Spero H. J. (2000) Climate Impact of Late Quaternary Equatorial Pacific Sea Surface Temperature Variations. *Science* **289**, 1719-1724.

Lear C. H., Elderfield H., and Wilson P. A. (2000) Cenozoic Deep-Sea Temperatures and Global Ice Volumes from Mg/Ca in Benthic Foraminiferal Calcite. *Science* **287**, 269-272.

Lear C. H., Rosenthal Y., and Slowey N. (2002) Benthic foraminiferal Mg/Ca-paleothermometry: A revised core-top calibration. *Geochim. Cosmochim. Acta* **66**, 3375-3387.

Lear C. H., Elderfield H., and Wilson P. A. (2003a) A Cenozoic seawater Sr/Ca record from benthic foraminiferal calcite and its application in determining global weathering fluxes. *Earth Planet. Sci. Lett.* **208**, 69-84.

Lear C. H., Rosenthal Y., and Wright J. D. (2003b) The closing of a seaway: ocean water masses and global climate change. *Earth Planet. Sci. Lett.* **210**, 425-436.

Lisiecki L. E. and Raymo M. E. (2005) A Pliocene-Pleistocene stack of 57 globally distributed benthic $\delta^{18}O$ records. *Paleoceanography* **20**, PA1003, doi:10.1029/2004PA001071.

Lyle M., Wilson P. A., Janecek T. R., et al. (2002) Site 1218. In: *Proc. ODP. Init. Repts.* 199 (eds. P. A. Wilson, M. Lyle, and J. V. Firth). Ocean Drilling Program, pp. 1-126.

Ma W. T., Tian J., Li Q. Y., and Wang P. X. (2011) Simulation of long eccentricity (400-kyr) cycle in ocean carbon reservoir during Miocene climate optimum: Weathering and nutrient response to orbital change. *Geophys. Res. Lett.* **38**, L10701, doi:10.1029/2011GL047680.

Martin P. A., Lea D. W., Mashiotta T. A., Papenfuss T., and Sarnthein M. (1999) Variation of foraminiferal Sr/Ca over Quaternary glacial-interglacial cycles: Evidence for changes in mean ocean Sr/Ca?. *Geochem. Geophys. Geosyst.* **1**, 1004, doi:10.1029/1999GC000006.

Mashiotta T. A., Lea D. W., and Spero H. J. (1997) Experimental determination of cadmium uptake in shells of the planktonic foraminifera *Orbulina universa* and *Globigerina bulloides*: Implications for surface water paleoreconstructions. *Geochim. Cosmochim. Acta* **61**, 4053-4065.

Mashiotta T. A., Lea D. W., and Spero H. J. (1999) Glacial-interglacial changes in subantarctic sea surface temperature and $\delta^{18}O$-water using foraminiferal Mg. *Earth Planet. Sci. Lett.* **170**, 417-432.

McConnaughey T. (1989) ^{13}C and ^{18}O isotopic disequilibrium in biological carbonates: I. Patterns. *Geochim. Cosmochim. Acta* **53**, 151-162.

McCrea J. M. (1950) On the isotopic chemistry of carbonates and a paleotemperature scale. *J. Chem. Phys.* **18**, 849-857.

Miller K. G., Wright J. D., and Fairbanks R. G. (1991) Unlocking the ice house: Oligocene-Miocene oxygen isotopes, eustasy, and margin erosion. *J. Geophys. Res.* **96**, 6829-6848.

Murray J. (1897) On the distribution of the pelagic foraminifera at the surface and on the floor of the oceans. *Nat. Sci.* **11**, 17-27.

Murray J. W. (2007) Biodiversity of living benthic foraminifera: How many species are there? *Mar. Micropaleontol.* **64**, 163-176.

Nürnberg D. (1995) Magnesium in tests of *Neogloboquadrina pachyderma* sinistral from high Northern and Southern latitudes. *J. Foramin. Res.* **25**, 350-368.

Nürnberg D., Bijma J., and Hemleben C. (1996) Assessing the reliability of magnesium in foraminiferal calcite as a proxy for water mass temperature. *Geochim. Cosmochim. Acta* **60**, 803-814.

Oberhänsli H. (1992) Planktonic foraminifers as tracers of ocean currents in the eastern South Atlantic. *Paleoceanography* **7**, 607-632.

Pagani M., Arthur M. A., and Freeman K. H. (1999) Miocene evolution of atmospheric carbon dioxide. *Paleoceanography* **14**, 273-292.

Pälike H., Frazier J., and Zachos J. C. (2006a) Extended orbitally forced palaeoclimatic records from the equatorial Atlantic Ceara Rise. *Quaternary Sci. Rev.* **25**, 3138-3149.

Pälike H., Norris R. D., Herrle J. O., Wilson P. A., Coxall H. K., Lear C. H., Shackleton N. J., Tripati A. K., and Wade B. S. (2006b) The Heartbeat of the Oligocene Climate System. *Science* **314**, 1894-1898.

Pälike H., Lyle M., Nishi H., Raffi I., Gamage K., Klaus A., and the Expedition 320/321 Scientists (2010) *Proc. IODP*, 320/321: Tokyo (Integrated Ocean Drilling Program Management International, Inc.).

Pearson P. N. and Palmer M. R. (2000) Atmospheric carbon dioxide concentrations over the past 60 million years. *Nature* **406**, 695-699.

Pearson P. N., Ditchfield P. W., Singano J., Harcourt-Brown K. G., Nicholas C. J., Olsson R. K., Shackleton N. J., and Hall M. A. (2001) Warm tropical sea surface temperatures in the Late Cretaceous and Eocene epochs. *Nature* **413**, 481-487.

Pena L. D., Calvo E., Cacho I., Eggins S., and Pelejero C. (2005) Identification and removal of Mn-Mg-rich contaminant phases on foraminiferal tests: Implications for Mg/Ca past temperature reconstructions. *Geochem. Geophys. Geosyst.* **6**, Q09P02, doi:10.1029/2005GC000930.

Pena L. D., Cacho I., Calvo E., Pelejero C., Eggins S., and Sadekov A. (2008) Characterization of contaminant phases in foraminifera carbonates by electron microprobe mapping. *Geochem. Geophys. Geosyst.* **9**, Q07012, doi:10.1029/2008GC002018.

Peterson L. C. and Prell W. L. (1985) Carbonate preservation and rates of climatic change: An 800 kyr record from the Indian Ocean. In: *The Carbon Cycle and Atmospheric CO_2: Natural Variations Archean to Present* (eds. E. T. Sundquist and W. S. Broecker). Amer. Geophys. Union Geophys. Monogr. 32. pp. 251-269.

Pfleger F. B. (1948) Foraminifera of a submarine core from the Caribbean Sea. *Göteborgs Kungliga Vetenskaps-och Vitterhets-samhälles Handlingar* 6B, 5, 3-9.

Pingitore N. E., Eastman M. P., Sandidge M., Oden K., and Freiha B. (1988) The coprecipitation of Manganese(II) with calcite: an experimental study. *Mar. Chem.* **25**, 107-120.

Raitzsch M., Dueñas-Bohórquez A., Reichart G.-J., de Nooijer L. J., and Bickert T. (2010) Incorporation of Mg and Sr in calcite of cultured benthic foraminifera: impact of calcium concentration and associated calcite saturation state. *Biogeosciences* **7**, 869-881.

Ravelo A. C. and Fairbanks R. G. (1995) Carbon isotopic fractionation in multiple species of planktonic foraminifera from core-tops in the tropical Atlantic. *J. Foramin. Res.* **25**, 53-74.

Raymo M. E. (1994) The initiation of Northern Hemisphere glaciation. *Annu. Rev. Earth Pl. Sc.* **22**, 353-383.

Raymo M. E. and Ruddiman W. F. (1992) Tectonic forcing of late Cenozoic climate. *Nature* **359**, 117-122.

Raymo M. E., Ruddiman W. F., and Froelich P. N. (1988) Influence of late Cenozoic mountain building on ocean geochemical cycles. *Geology* **16**, 649-653.

Regenberg M., Nürnberg D, Schönfeld J, and Reichart G.-J. (2007) Early diagenetic overprint in Caribbean sediment cores and its effect on the geochemical composition of planktonic foraminifera. *Biogeosciences* **4**, 957-973.

Richter F. M. and DePaolo D. J. (1987) Numerical models for diagenesis and the Neogene Sr isotopic evolution of seawater from DSDP Site 590B. *Earth Planet. Sci. Lett.* **83**, 27-38.

Richter F. M. and DePaolo D. J. (1988) Diagenesis and Sr isotopic evolution of seawater using data from DSDP 590B and 575. *Earth Planet. Sci. Lett.* **90**, 382-394.

Richter F. M. and Liang Y. (1993) The rate and consequences of Sr diagenesis in deep-sea carbonates. *Earth Planet. Sci. Lett.* **117**, 553-565.

Rohling E. J. and Bigg G. R. (1998) Paleosalinity and $\delta^{18}O$: a critical assessment. *J. Geophys. Res.* **103**, 162-165.

Rohling E. J., Fenton M., Jorissen F. J., Bertrand P., Ganssen G., and Caulet J. P. (1998) Magnitudes of sea-level lowstands of the past 500,000 years. *Nature* **394**, 162-165.

Rosenthal Y. and Lohmann G. P. (2002) Accurate estimation of sea surface temperatures using dissolution-corrected calibrations for Mg/Ca paleothermometry. *Paleoceanography* **17**, 1044, doi:10.1029/2001PA000749.

Rosenthal Y., Boyle E. A., and Slowey N. (1997) Temperature control on the incorporation of Mg, Sr, F, and Cd into benthic foraminiferal shells from Little Bahama Bank: Prospects for thermocline paleoceanography. *Geochim. Cosmochim. Acta* **61**, 3633-3643.

Rosenthal Y., Lohmann G. P., Lohmann K. C., and Sherrell R. M. (2000) Incorporation and preservation of Mg in *Globigerinoides sacculifer*: Implications for reconstructing the temperature and $\delta^{18}O$ of seawater. *Paleoceanography* **15**, 135-145.

Russell A. D., Hönisch B., Spero H. J., and Lea D. W. (2004) Effects of seawater carbonate ion concentration and temperature on shell U, Mg, and Sr in cultured planktonic foraminifera. *Geochim. Cosmochim. Acta* **68**, 4347-4361.

Sanyal A., Hemming N. G., Broecker W.S., Lea D. W., Spero H. J., and Hanson G. N. (1996) Oceanic pH control on the boron isotopic composition of foraminifera: Evidence from culture experiments. *Paleoceanography* **11**, 513-517.

Savin S. M., Douglas R. G., and Stehli F. G. (1975) Tertiary marine paleotemperatures. *Geol. Soc. Am. Bull.* **86**, 1499-1510.

Schiebel R. (2002) Planktic foraminiferal sedimentation and the marine calcite budget. *Glob. Biogeochem. Cycle* **16**, 1065, doi:10.1029/2001GB001459.

Schmidt M. W., Spero H. J., and Lea D. W. (2004) Links between salinity variation in the Caribbean and North Atlantic thermohaline circulation. *Nature* **428**, 160-163.

Schmiedl G. and Mackensen A. (1997) Late Quaternary paleoproductivity and deep water circulation in the eastern South Atlantic Ocean: Evidence from benthic foraminifera. *Paleogeogr. Paleoclimatol. Paleoecol.* **130**, 43-80.

Schrag D. P., DePaolo D. J., and Richter F. M. (1995) Reconstructing past sea-surface temperatures – Correcting for diagenesis of bulk marine carbonate. *Geochim. Cosmochim. Acta* **59**, 2265-2278.

Sen Gupta B. K. (2002) Introduction to modern foraminifera and Systematics of modern foraminifera. In: *Modern foraminifera* (eds. B. K. Sen Gupta). Kluwer Academic Publishers, Dordrecht. pp. 3-36.

Sexton P. F., Wilson P. A., and Pearson P. N. (2006) Microstructural and geochemical perspectives on planktic foraminiferal preservation: "Glassy" versus "Frosty". *Geochem. Geophys. Geosyst.* **7**, 1-29.

Shackleton N. J. (1974) Attainment of isotopic equilibrium between ocean water and the benthonic foraminifera genus *Uvigerina*: isotopic changes in the ocean during the last glacial. *CNRS, Colloques Internationals* **219**, 203-209.

Shackleton N. J. (1977a) $\delta^{13}C$ in *Uvigerina*: tropical rainforest history and the equatorial Pacific carbonate dissolution cycles. In: *Fate of Fossil Fuel CO_2 in the Oceans* (eds. N. Anderson and A. Malahof). Plenum, New York. pp. 401-427.

Shackleton N. J. (1977b) The oxygen isotopic stratigraphic record of the late Pleistocene. *Philos. T. R. Soc. Lon. B* **280**, 169-182.

Shackleton N. J. (1987) Oxygen isotopes, ice volume and sea-level. *Quaternary Sci. Rev.* **6**, 183-190.

Shackleton N. J. and Kennett J. P. (1975) Paleotemperature history of the Cenozoic and the initiation of Antarctic glaciation: Oxygen and carbon analyses in DSDP Sites 277, 279, and 281. In: *DSDP Init. Repts.* 29 (eds. J. P. Kennett, et al.). Deep Sea Drilling Project, pp. 743-755.

Shackleton N. J. and Opdyke N. D. (1973) Oxygen isotope and paleomagnetic stratigraphy of equatorial Pacific core V28-238: Oxygen isotope temperatures and ice volumes on a 10^5 year and 10^6 year scale. *Quaternary Res.* **3**, 39-55.

Shackleton N. J., Hall M. A., and Pate D. (1995) Pliocene stable isotope stratigraphy of ODP Site 846. In: *Proc. ODP. Sci. Res.* 138 (eds. L. Mayer, N. Pisias, T. Janecek, et al.). Ocean Drilling Program, pp. 337-355.

Shevenell A. E., Kennett J. P., and Lea D. W. (2004) Middle Miocene Southern Ocean Cooling and Antarctic Cryosphere Expansion. *Science* **305**, 1766-1770.

Spero H. J. and Lea D. W. (1993) Intraspecific stable isotope variability in the planktonic foraminifer *Globigerinoides sacculifer*: results from laboratory experiments. *Mar. Micropaleontol.* **22**, 221-234.

Spero H. J. and Lea D. W. (1996) Experimental determination of stable isotope variability in *Globigerina bulloides*: implications for paleoceanographic reconstructions. *Mar. Micropaleontol.* **28**, 231-246.

Spero H. J., Bijima J., Lea D. W., and Bemis B. E. (1997) Effect of seawater carbonate concentration on foraminiferal carbon and oxygen isotopes. *Nature* **390**, 497-500.

Spielhagen R. F. and Erlenkeuser H (1994) Stable oxygen and carbon isotopes in planktic foraminifers from Arctic Ocean surface sediments: Reflection of the low salinity surface water layer. *Mar. Geol.* **119**, 227-250.

Spivack A. J., You C.-F., and Smith H. J. (1993) Foraminiferal boron isotope ratios as a proxy for surface ocean pH over the past 21 Myr. *Nature* **363**, 149-151.

Stoll H. M., Schrag D. P., and Clemens S. C. (1999) Are seawater Sr/Ca variations preserved in quaternary foraminifera?. *Geochim. Cosmochim. Acta* **63**, 3535-3547.

Tian J., Yang M., Lyle M. W., Wilkens R., and Shackford J. K. (2013) Obliquity and long eccentricity pacing of the Middle Miocene climate transition. *Geochem. Geophys. Geosyst.* **14**, 1740-1755.

Tian J., Ma W., Lyle M. W., and Shackford J. K. (2014) Synchronous mid-Miocene upper and deep oceanic $\delta^{13}C$ changes in the east equatorial Pacific linked to ocean cooling and ice sheet expansion. *Earth Planet. Sci. Lett.* **406**, 72-80.

Tiedemann R., Sarnthein M., and Shackleton N. J. (1994) Astronomic timescale for the Pliocene Atlantic $\delta^{18}O$ and dust flux records of ODP Site 659. *Paleoceanography* **9**, 619-638.

Toyofuku T., Kitazato H., Kawahata H., Tsuchiya M., and Nohara N. (2000) Evaluation of Mg/Ca thermometry in foraminifera: Comparison of experimental results and measurements in nature. *Paleoceanography* **15**, 456.464.

Urey H. C. (1947) The thermodynamic properties of isotopic substances. *J. Chem. Soc.* **1**, 562-581.

Veizer J. (1989) Strontium isotopes in seawater through time. *Annu. Rev. Earth Planet. Sci.* **17**, 141-167.

Vincent E. and Berger W. H. (1985) Carbon dioxide and polar cooling in the Miocene: The Monterey hypothesis. In: *The Carbon Cycle and Atmospheric CO_2: Natural Variations Archean to Present* (eds. E. T. Sundquist and W. S. Broecker). Amer. Geophys. Union Geophys. Monogr. 32. pp. 455-468.

Wade B. S. and Pälike H. (2004) Oligocene climate dynamics. *Paleoceanography* **19**, PA4019, doi:10.1029/2004PA001042.

Wade B. S. and Pälike H. (2005) Data report: Oligocene paleoceanography of the equatorial Pacific Ocean: Planktonic and benthic foraminifer stable isotope results from Site 1218. In: *Proc. ODP. Sci. Res.* 199 (eds. P. A. Wilson, M. Lyle, and J. V. Firth). Ocean Drilling Program, pp. 1-12.

Wang L., Sarnthein M., Erlenkeuser H., Grimalt J., Grootes P., Heilig S., Ivanova E., Kienast M., Pelejero C., and Pflaumann U. (1999) East Asian monsoon climate during the Late Pleistocene: high-resolution sediment records from the South China Sea. *Mar. Geol.* **156**, 245-284.

Westerhold T., Bickert T., and Röhl U. (2005) Middle to late Miocene oxygen isotope stratigraphy of ODP site 1085 (SE Atlantic): New constrains on Miocene climate variability and sea-level fluctuations. *Palaeogeogr. Palaeoclimatol. Palaeoecol.* **217**, 205-222.

Woodruff F. and Savin S. M. (1989) Miocene deepwater oceanography. *Paleoceanography* **4**, 87-140.

Woodruff F. and Savin S. (1991) Mid-Miocene isotope stratigraphy in the deep sea: High resolution correlations, paleoclimatic cycles, and sediment preservation. *Paleoceanography* **6**, 755-806.

Wright J. D, Miller K. G., and Fairbanks R. G. (1991) Evolution of deep-water circulation: Evidence from the late Miocene Southern Ocean. *Paleoceanography* **6**, 275-290.

Wright J. D., Miller K. G., and Fairbanks R. G. (1992) Early and middle Miocene stable isotopes: Implication for deepwater circulation and climate. *Paleoceanography* **7**, 357-389.

Zachos J. C., Flower B. P., and Paul H. (1997) Orbitally paced climate oscillations across the Oligocene/Miocene boundary. *Nature* **388**, 567-571.

Zachos J. C., Shackleton N. J., Revenaugh J. S., Palike H., and Flower B. P. (2001a) Climate Response to Orbital Forcing Across the Oligocene-Miocene Boundary. *Science* **292**, 274-278.

Zachos J., Pagani M., Sloan L., Thomas E., and Billups K. (2001b) Trends, Rhythms, and Aberrations in Global Climate 65 Ma to Present. *Science* **292**, 686-693.

Zachos J. C., Dickens G. R., and Zeebe R. E. (2008) An early Cenozoic perspective on greenhouse warming and carbon-cycle dynamics. *Nature* **451**, 279-283.

Zachos J. C., McCarren H., Murphy B., Röhl U., and Westerhold T. (2010) Tempo and scale of late Paleocene and early Eocene carbon isotope cycles: Implications for the origin of hyperthermals. *Earth Planet. Sci. Lett.* **299**, 242-249.

II. Publications and manuscripts

Declaration of my contribution to the following chapters:

Chapter 1:

Publication: Voigt J., Hathorne E. C., Frank M., Vollstaedt H., and Eisenhauer A. (2015) Variability of carbonate diagenesis in equatorial Pacific sediments deduced from radiogenic and stable Sr isotopes. *Geochim. Cosmochim. Acta* **148**, 360-377

Statement:
I prepared the bulk sediment samples for analysis, performed the chemical separation of bulk carbonate and pore water samples and measured the element/Ca ratios and the radiogenic Sr isotope ratios ($^{87}Sr/^{86}Sr$). Measurements of the stable Sr isotopes ($\delta^{88/86}S$) were carried out by myself and Ana Kolevica. Florian Böhm, Volker Liebetrau, and Jan Fietzke helped with the discussion of the stable Sr. I interpreted the data, wrote the manuscript and all co-authors and 4 external reviewers helped to improve and revise the manuscript.

Chapter 2:

Manuscript: Voigt J., Hathorne E. C., Holbourn A., and Frank M. Minimal influence of recrystallisation on middle Miocene benthic foraminiferal stable isotope stratigraphy in the eastern equatorial Pacific. *Paleoceanography* (in review), 2015PA002822

Statement:
Benthic foraminifera were picked by myself and a student assistant. I prepared and cleaned the foraminiferal tests. The stable carbon and oxygen isotope composition of the tests was measured by Lulzim Haxhiaj, Kirstin Werner, Christelle Not, Andrea Bodenbinder, Ed Hathorne, Fynn Wulf and by myself. I interpreted the data and wrote the manuscript. Ann Holbourn and Ed Hathorne helped with discussing the data and their interpretation. All co-authors helped improving and revising the manuscript.

Chapter 3:

Manuscript to be submitted: Voigt J., Hathorne E. C., Frank M., and Fietzke J., Variable preservation of geochemical proxy data in recrystallised planktonic foraminifera.

Statement:

Planktonic foraminifera were picked by myself and the sample preparation, including cleaning, was performed by myself. Laser ablation ICP-MS derived element/Ca ratios were measured by myself with technical assistance of Jan Fietzke and Ed Hathorne. SEM images were taken by Petra Witte and myself at MARUM, Bremen. The first set of SEM images was discussed with Jeroen Groeneveld and he helped with their interpretation. Nico Glock helped me with embedding the samples in epoxy. Electron microprobe measurements were carried out by myself with technical assistance of Mario Thöner. Ed Hathorne contributed to discussing the data and their interpretation. I wrote the chapter and Martin Frank and Ed Hathorne helped improving the draft.

Chapter 1

Variability of carbonate diagenesis in equatorial Pacific sediments deduced from radiogenic and stable Sr isotopes

Janett Voigt[a,*], Ed C. Hathorne[a], Martin Frank[a], Hauke Vollstaedt[a,1] and Anton Eisenhauer[a]

[a]GEOMAR Helmholtz Centre for Ocean Research Kiel, Wischhofstr. 1-3, 24148 Kiel, Germany

[1]Present address: Center for Space and Habitability and Institute of Geological Sciences, University of Bern, Baltzerstr. 1+3, 3012 Bern, Switzerland

*Corresponding author, e-mail address: jvoigt@geomar.de

Published in: Geochimica et Cosmochimica Acta 148 (2015) 360–377. doi:10.1016/j.gca.2014.10.001

Abstract

The recrystallisation (dissolution-precipitation) of carbonate sediments has been successfully modelled to explain profiles of pore water Sr concentration and radiogenic Sr isotope composition at different locations of the global ocean. However, there have been few systematic studies trying to better understand the relative importance of factors influencing the variability of carbonate recrystallisation. Here we present results from a multi-component study of recrystallisation in sediments from the Integrated Ocean Drilling Program (IODP) Expedition 320/321 Pacific Equatorial Age Transect (PEAT), where sediments of similar initial composition have been subjected to different diagenetic histories.

The PEAT sites investigated exhibit variable pore water Sr concentration gradients with the largest gradients in the youngest sites. Radiogenic Sr isotopes suggest recrystallisation was relative rapid, consistent with modelling of other sediment columns, as the $^{87}Sr/^{86}Sr$ ratios are indistinguishable (within 2σ uncertainties) from contemporaneous seawater $^{87}Sr/^{86}Sr$ ratios. Bulk carbonate leachates and

associated pore waters of Site U1336 have lower $^{87}Sr/^{86}Sr$ ratios than contemporaneous seawater in sediments older than 20.2 Ma most likely resulting from the upward diffusion of Sr from older recrystallised carbonates. It seems that recrystallisation at Site U1336 may still be on-going at depths below 102.5 rmcd (revised metres composite depth) suggesting a late phase of recrystallisation. Furthermore, the lower Sr/Ca ratios of bulk carbonates of Site U1336 compared to the other PEAT sites suggest more extensive diagenetic alteration as less Sr is incorporated into secondary calcite. Compared to the other PEAT sites, U1336 has an inferred greater thermal gradient and a higher carbonate content. The enhanced thermal gradient seems to have made these sediments more reactive and enhanced recrystallisation.

In this study we investigate stable Sr isotopes from carbonate-rich deep sea sediments for the first time. Pore water $\delta^{88/86}Sr$ increases with depth (from 0.428 to values reaching up to 0.700 ‰) at Site U1336 documenting an isotope fractionation process during recrystallisation. Secondary calcite preferentially incorporates the lighter Sr isotope (^{86}Sr) leaving pore waters isotopically heavy. The $\delta^{88/86}Sr$ values of the carbonates themselves show more uniform values with no detectable change with depth. Carbonates have a much higher Sr content and total Sr inventory than the pore waters meaning pore waters are much more sensitive to fractionation processes than the carbonates. The $\delta^{88/86}Sr$ results indicate that pore water stable Sr isotopes have the potential to indicate the recrystallisation of carbonate sediments.

1. Introduction

The elemental and isotopic compositions of carbonate microfossils in marine sediments are widely used to reconstruct oceanic and climatic conditions (i.e. temperature, salinity, etc.) in the past (e.g., Zachos et al., 2001, 2008). However, carbonate sediments, mainly coccolithophorid and foraminifera microfossils, are normally altered by recrystallisation during which the original biogenic calcite is replaced by secondary (inorganic) calcite. Significant changes in stable isotope ($\delta^{13}C$ and $\delta^{18}O$) and Mg/Ca ratios of recrystallised planktonic foraminifera have been identified, which can lead to biased palaeo-temperatures and to misinterpretations of

palaeo-climate (Pearson et al., 2001; Sexton et al., 2006). It is thus essential to better understand the variability of recrystallisation and thereby help to constrain the reliability of proxy data from different sedimentary sections.

The recrystallisation of bulk carbonate sediments has been extensively studied and differences in isotope and element/Ca ratios between altered and well-preserved sediments have been found (e.g., Elderfield et al., 1982; Schrag et al., 1995; Hampt Andreasen and Delaney, 2000). During the recrystallisation of relatively Sr-rich biogenic carbonates Sr^{2+} is released to the pore waters causing the Sr concentration to increase with depth (Baker et al., 1982; Elderfield and Giekes, 1982; Stout, 1985; Gieskes et al., 1986; Richter and DePaolo, 1987, 1988; Richter and Liang, 1993; Richter, 1993, 1996; Fantle and DePaolo, 2006). To a first order, the slope of the Sr concentration increase indicates the rate of dissolution and re-precipitation or recrystallisation (Richter and DePaolo, 1988). Pore water Sr concentrations and $^{87}Sr/^{86}Sr$ ratios have been used as fitting parameters to constrain models of carbonate recrystallisation (e.g., Baker et al., 1982; Richter and DePaolo, 1987, 1988; Richter and Liang, 1993; Fantle and DePaolo, 2006). Such models estimate the recrystallisation rate, which is defined as the Sr flux from the solid to the fluid (Richter and DePaolo, 1987), by accounting for diffusion, advection and reaction between fluid and solid while adjusting constants to match the observed pore water Sr^{2+} profile (Richter and Liang, 1993; Richter, 1996; Fantle and DePaolo, 2006). All these previous studies show that recrystallisation rates decrease exponentially with increasing depth and age (Baker et al., 1982; Richter and Liang, 1993; Fantle and DePaolo, 2006). Recrystallisation rates are also influenced by sedimentation rates, temperature gradients, lithology and the carbonate saturation state of the overlying bottom waters (Richter and Liang, 1993; Hampt-Andreasen and Delaney, 2000). However, the relative importance of these factors for the recrystallisation rate is not well constrained.

Here we investigate recrystallisation by measuring $^{87}Sr/^{86}Sr$ and element/Ca ratios of bulk carbonates and associated pore waters of selected sites of the IODP Expedition 320/321 Pacific Equatorial Age Transect (PEAT) in the eastern equatorial Pacific (Figure 1). The sediment cores are of similar initial composition at a particular age but have been subjected to different diagenetic histories resulting from variable

subsidence, sedimentation rates (Figure 2) and geothermal gradients. Therefore, these sediments are well suited for the study of recrystallisation.

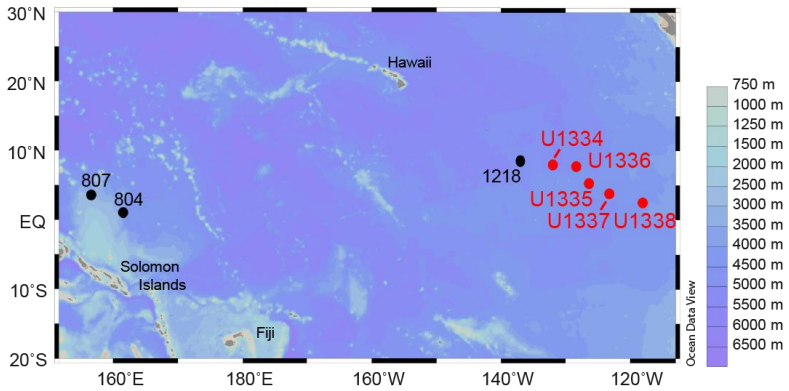

Figure 1. Map of equatorial Pacific showing the location of PEAT sites (Pälike et al., 2010) investigated in this study in red and ODP Sites 804, 807 (Kroenke et al., 1991) and 1218 (Lyle et al., 2002).

For the first time, we investigate the stable Sr isotope compositions of carbonate-rich deep sea sediments and their associated pore waters to constrain recrystallisation. By measuring paired radiogenic ($^{87}Sr/^{86}Sr$) and stable ($\delta^{88/86}Sr$) Sr isotopes (Krabbenhöft et al., 2009), natural mass-dependent stable isotope fractionation occurring in the environment can be determined (e.g., Krabbenhöft et al., 2010; Böhm et al., 2012). Recently, stable Sr isotope fractionation has been investigated for biogenic carbonates and inorganic calcite and this suggests a -0.12 to -0.25 ‰ fractionation between the solid and solution can occur (Krabbenhöft et al., 2010; Böhm et al., 2012; Raddatz et al., 2013).

2. Materials and Methods

2.1 Site description

The sites investigated are U1334 to U1338 spanning the late Eocene until present. Sediment cores were recovered during the IODP Expedition 320/321 and site locations and basic coring data are summarised in Table 1 (Pälike et al., 2010). All depths reported here for the PEAT Sites U1334, U1336, U1337 and U1338 are in revised metres composite depth (rmcd) (Westerhold et al., 2012; Wilkens et al.,

2013) and for Site U1335 depth is given in metres composite depth (mcd) (Pälike et al., 2010).

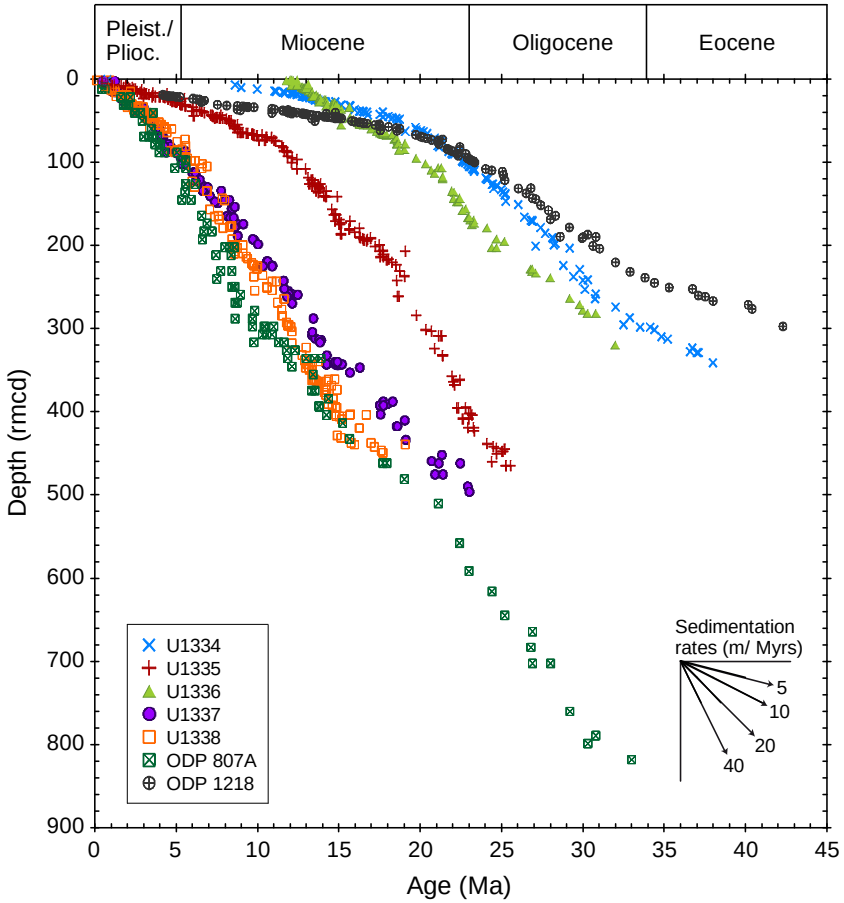

Figure 2. Sedimentation rates of PEAT sites; age is plotted against revised metres composite depth (rmcd), from Pälike et al. (2010). Revised composite depths are from Westerhold et al. (2012) and Wilkens et al. (2013). ODP Sites 807 (Kroenke et al., 1991) is shown in metres below seafloor (mbsf) and 1218 (Lyle et al., 2002) in metres composite depth (mcd). Both sites were adjusted to the PEAT age scale.

The sedimentary sequences represent a continuous Cenozoic record of the equatorial Pacific recovered along an age transect, where different sites were located within a 2° band north and south of the equator for different time intervals (Pälike et al., 2010). The sites were located in the equatorial high productivity zone at different time periods as the Pacific plate moved away from East Pacific Rise. All PEAT sites are relatively carbonate-rich ranging from 40.1 to 97.8 % $CaCO_3$ within the ooze sections (Figure S1). Low carbonate content is found in opal-rich layers at Sites U1335, U1337 and U1338, reaching < 1 % $CaCO_3$ in places at Site U1337. Generally, the sites consist of nanno- and microfossil ooze with only minor amounts of clay in the top of the sediment sequences. This is most pronounced at Sites U1334

and U1336, where a clay layer accumulated since the site subsided below the carbonate compensation depth (CCD) around 12 Ma (Pälike et al., 2010; Pälike et al., 2012). All other sites are at present still above the CCD (Pälike et al., 2010; Pälike et al., 2012), the depth where the rate of calcite supply equals the dissolution rate resulting in no calcite accumulation.

Table 1. Details of the investigated PEAT Sites (for further information see Pälike et al., 2010).

Site	Geographic location	Water depth (m)	Sediment thickness (m)[a]	Age of underlying crust (Ma)
U1334	7°59.998'N 131°58.408'W	4799	~285	~38
U1335	5°18.735'N 126°17.002'W	4328	~420	~26
U1336	7°42.067'N 128°15.253'W	4286	~174	~32
U1337	3°50.007'N 123°12.356'W	4461	~450	~24
U1338	2°30.469'N 117°58.178'W	4200	~413	~18

[a] All Sites, except Site U1336, were drilled to the basement. The sediment thickness represents the total drilling depth below seafloor to the basalt basement.

Porosity decreases in several steps down hole as a function of compaction from 64 to 91 % in the upper sections to about 47-54 % near the basement (Figure S2) (Pälike et al., 2010). The ooze-chalk transition at each site is located at different depths due to different sedimentation rates and is found at 273.5 rmcd at Site U1334, at 393.4 mcd at Site U1335, at 347.6 rmcd at Site U1337 and at 343.1 rmcd at Site U1338 (Pälike et al., 2010). Site U1336B consists only of ooze since sections deeper than 191.9 rmcd were not drilled (Pälike et al., 2010).

The geothermal gradients vary significantly between the PEAT sites. Sites U1334, U1337 and U1338 have similar geothermal gradients of 33.0°C km^{-1}, 32.4°C km^{-1} and 34.4°C km^{-1}, respectively (Pälike et al., 2010). Site U1335 has the lowest geothermal gradient of only 7.4°C km^{-1} (Pälike et al., 2010). Unfortunately, no *in-situ* temperature measurements were conducted at Site U1336 because of time constraints, but pore water Mg^{2+}, Ca^{2+} and K^{+} suggest that this site is relatively reactive and by inference subject to a relatively high thermal gradient (see Section 4.1).

Pore water profiles of Sites U1334, U1335 and U1338 show rather uniform values for Mg^{2+} and Ca^{2+} (Table S1 contains pertinent pore water data, compiled from Pälike et al., 2010). At Site U1336 Ca^{2+} concentrations increase with depth and show a sharp increase at 147.6 rmcd, whereas the Mg^{2+} concentrations decrease with depth and show an enhanced gradient of the decrease at the same depth. At Site U1337 many pore water profiles, but not Mg^{2+} and Ca^{2+} values, are offset either side of a chert layer at 263 rmcd (Table S1, see also Section 4.1, Pälike et al., 2010).

Data from Ocean Drilling Program (ODP) Sites 1218, 804 and 807 are compared to the PEAT sites. Detailed information for Site 1218 can be found in Lyle et al. (2002) and for Sites 804 and 807 in Kroenke et al. (1991). ODP Site 1218 is also located in the eastern equatorial Pacific about 380 km northwest of Site U1334. The top of the sediment core comprises 52 m of radiolarian clay with a nannofossil ooze and chalk section below (Lyle et al., 2002). This clay layer, similar to Site U1334, reflects the subsidence of this site below the CCD at around 12 Ma (Lyle et al., 2002; Pälike et al., 2012). The porosity of Site 1218 declines down hole from 88 to 48 %. The pore water Ca^{2+} concentrations increase from seawater-like 11 mM to 14 mM at the basement while Mg^{2+} concentrations decrease from 54 to 49 mM (Table S1, Lyle et al., 2002).

ODP Sites 804 and 807 are located in the western equatorial Pacific on the Ontong Java Plateau. The sediments of these sites are carbonate-rich nannofossil oozes and chalk with up to 93 % $CaCO_3$ (Delaney and Linn, 1993; Kroenke et al., 1991). Porosity decreases from 70 to 72 % in the uppermost sections of the sediments to about 57 % at the basement of Site 804 and to 52 % at the basement of Site 807 (Kroenke et al., 1991). The pore water Ca^{2+} increases with depth until the basement from 11 to 21-22 mM at both sites and Mg^{2+} decreases with depth from 53 to 42 mM at Site 804 and to 38 mM at Site 807 (Table S1, Kroenke et al., 1991).

2.2 Pore water extraction and sediment leaching

Pore waters were extracted directly after core recovery on board the *JOIDES Resolution* by either the standard IODP technique whole-round squeezing or inserting Rhizon samplers into the sediment core (see Pälike et al., 2010 for more details). Rhizon samples were not taken for all sites investigated but only for Sites

U1334, U1337 and U1338. At Site U1334 Rhizon and the squeezed whole-round samples were taken from different holes, which explains slight differences between the data. At Site U1337 both methods give identical results within the uncertainties (see Section 2.3 for reproducibility of International Association for the Physical Sciences of the Ocean (IAPSO) seawater measurements on board) (Pälike et al., 2010). Only pH measurements differ at Site U1337 probably because of the time Rhizon samples waited to be measured (Pälike et al., 2010). In general, squeezed whole round samples agree with Rhizon samples indicating both methods are suitable for the data of interest in this study.

Bulk sediment samples (squeeze cake samples; the remaining sediment following pore water extraction) were processed and analysed at GEOMAR. The samples were freeze dried and about 100 mg were ground for homogenisation. The powder was transferred into acid cleaned 50 ml centrifuge tubes and subjected to a modified leaching method after Kryc et al. (2003).

Sample powders were rinsed three times with 20 ml of deionized 18.2 MΩ water to remove the loosely-bound fraction and were then shaken for 30 min on a shaker table (140 rpm) before being centrifuged for 30 min (4000 rpm). Although the 18.2 MΩ water was slightly acidic (> pH 5.5), it was not observed to be aggressive. The supernatant was discarded. The carbonate fraction was dissolved with 20 ml of 0.1 M acetic acid buffered to pH 5 with sodium acetate. Samples were continuously agitated on a shaker table (125 rpm) for 18 h at room temperature before being centrifuged for about 30 min (4000 rpm) and the supernatant was transferred into acid cleaned Savillex® vials.

2.3 Elemental analysis

Pore water samples were measured for elemental composition on board the *JOIDES Resolution* by inductively coupled plasma atomic emission spectroscopy (ICP-AES) following established techniques (Gieskes et al., 1991; Murray et al., 2000; Pälike et al., 2010). To assess the precision of the ICP-AES technique, IAPSO seawater was measured multiple times. The relative standard deviation (RSD, 2σ) for the conservative elements in the IAPSO seawater during the shipboard analyses was ± 5.5 % for Mg^{2+}, 3.0 % for Ca^{2+}, 3.1 % for Sr^{2+} and 1.6 % for K^{+} (Pälike et al., 2010).

To determine the precision for Mn^{2+} and Fe^{2+} some pore waters were repeatedly measured and gave a reproducibility of 16 % RSD for Mn^{2+} and 6.6 % RSD for Fe^{2+} (Pälike et al., 2010). Alkalinity and pH of the pore waters were determined by Gran titration with a Brinkman pH electrode and Metrohm autotitrator (Pälike et al., 2010).

An aliquot of each bulk carbonate leachate was taken for determination of element/Ca ratios by inductively coupled plasma mass spectrometry (ICP-MS, Agilent 7500cx at GEOMAR) calibrated using multi-element standards made from high purity single element solutions. Uncertainties (2σ) estimated by repeated measurement of a sample are ± 2.13 % RSD for Mg/Ca ratios, 1.82 % for Sr/Ca ratios, 9.35 % for Mn/Ca ratios and 10.36 % for Fe/Ca ratios (see also Table S2 and figure captions).

2.4 Radiogenic and stable Sr isotope analysis

For multi collector inductively coupled plasma mass spectrometry (MC-ICP-MS) analysis of $^{87}Sr/^{86}Sr$ ratios, an aliquot of the carbonate leachates containing about 500 ng Sr or 100 µl of pore water were dried down, re-dissolved in 100 µl of 8 M HNO_3 and loaded onto chromatographic columns filled with 55 µl of Eichrom SrSpec resin (mesh size: 50-100 µm). The sample matrix was eluted with 8 M HNO_3 and Sr was collected in 1 ml 18.2 MΩ water.

$^{87}Sr/^{86}Sr$ ratios were measured on a *Nu Plasma* MC-ICP-MS. Data were acquired at a typical ^{88}Sr signal intensity of about 8 V and were corrected for mass bias with the $^{86}Sr/^{88}Sr$ ratio of 0.1194 (Nier, 1938) and the exponential law. As is standard practice with MC-ICP-MS, $^{87}Sr/^{86}Sr$ ratios of each analytical session were corrected to the accepted value of the standard SRM 987 = 0.710248 (McArthur and Howarth, 2004) to account for additional fractionation effects and instrument drift between sessions. The SRM 987 is distributed by the National Institute of Standards and Technology (NIST). Repeated measurements of the IAPSO seawater, subjected to the same chemistry as the samples, gave an average $^{87}Sr/^{86}Sr$ value of 0.709171 ± 0.000019 (2σ, n = 51).

Paired Sr isotope analyses ($^{87}Sr/^{86}Sr$, $\delta^{88/86}Sr$) followed the procedure from Krabbenhöft et al. (2009). Sample solutions containing about 1200 ng Sr were dried

down and re-dissolved in 2 ml of 8 M HNO_3 and split into two aliquots. One aliquot was spiked with a $^{87}Sr/^{84}Sr$ double spike. Sr separation from the sample matrix was performed as described above but using about 200 µl of the Eichrom SrSpec resin and the Sr was collected in 4 ml of 18.2 MΩ water. After separation solutions were dried down and 200 µl of 8 M HNO_3 and 100 µl of H_2O_2 (30 %) were added and heated at 80°C for at least 6 h to break down any residual resin or other organic material. Finally, the samples were dried down again and about 300 ng Sr loaded onto single Re filaments with H_3PO_4 and $TaCl_5$ activators.

Measurements were performed by thermal ionisation mass spectrometry (TIMS, Triton) at about 1400°C with a typical ^{88}Sr signal intensity of about 10 V. Spike correction and normalisation to the NIST SRM 987 ($^{88}Sr/^{86}Sr$ of 8.375209 (Nier, 1938) were carried out after Krabbenhöft et al. (2009) to calculate the $\delta^{88/86}Sr$ of the samples and reference materials. Simultaneously measured $^{87}Sr/^{86}Sr$ ratios were also corrected for mass bias using $^{86}Sr/^{88}Sr = 0.1194$ (Nier, 1938). Repeated measurement of the NIST SRM 987 standard gave an average $^{87}Sr/^{86}Sr = 0.710246 \pm 0.000022$ (2σ, n = 16). The $^{88}Sr/^{86}Sr$ ratios are reported in the common delta notation relative to the SRM 987: $\delta^{88/86}Sr$ (‰) = $[(^{88}Sr/^{86}Sr)_{sample}/(^{88}Sr/^{86}Sr)_{SRM\ 987} - 1] * 1000$. The IAPSO seawater was measured repeatedly and gave an average $\delta^{88/86}Sr$ of 0.381 ± 0.029 ‰ and $^{87}Sr/^{86}Sr$ of 0.709167 ± 0.000004 (2σ, n = 5, see also Table 2) consistent with published values (e.g., Fietzke and Eisenhauer, 2006; Krabbenhöft et al., 2009, 2010). Repeated measurement of the JCp-1 coral reference material gave an average $\delta^{88/86}Sr$ of 0.202 ± 0.027 ‰, and $^{87}Sr/^{86}Sr = 0.709168 \pm 0.000019$ (2σ, n = 10, Table 2) in good agreement with published data (Krabbenhöft et al., 2010). The analytical blank for the leaching procedure and chromatographic Sr separation including the 18.2 MΩ water, acidified on the ship identical to the pore water samples, were determined and contained 0.35 and 0.16 ng Sr, respectively, which is less than 0.1 % of the Sr amount in samples.

The analytical uncertainties for the pore water measurements were estimated using the IAPSO seawater and the reproducibility of the bulk carbonate analyses was estimated with the JCp-1.

3. Results

3.1 Pore water Sr concentration

The pore water Sr concentrations increase with depth from the sediment water interface to different extents at each site (Figure 3). The smallest increase is observed at Site U1334 and the greatest occurs at U1338. At most of the PEAT sites the Sr concentration then decreases towards seawater-like values (85 µM) near the basement. This decrease is consistent with relatively fresh seawater circulating through the basement (Pälike et al., 2010). Site U1334 exhibits a small increase with depth reaching maximum values of only 107 µM (Figure 3), which is still very close to seawater concentrations. The sampled section of U1336 does not show a Sr maximum but rather a continuous increase of the Sr concentration with depth, however with a significantly steeper slope below 137.3 rmcd (Figure 3). The lower section below 186.7 rmcd at Site U1336 was not sampled for pore waters because of time constraints during the expedition. Site U1338 shows the strongest increase of pore water Sr concentration with depth, as well as the highest Sr^{2+} values observed at PEAT sites of 400 µM (Figure 3). The peak Sr concentration of this site also occurs at the shallowest depth at about 221.1 rmcd below sea floor (Pälike et al., 2010).

3.2 $^{87}Sr/^{86}Sr$ ratios of pore waters

Pore water $^{87}Sr/^{86}Sr$ ratios of Sites U1334, U1335 and U1337 have generally more radiogenic (higher) $^{87}Sr/^{86}Sr$ ratios than seawater of contemporaneous age as reflected by marine carbonate sediments globally (McArthur et al., 2001) (Figure 4a, b, d, Table S3). The ratios decrease from 0.7092 to up to 0.7088 and then increase again towards the basement. Site U1336 pore waters exhibit less radiogenic (lower) $^{87}Sr/^{86}Sr$ ratios than contemporaneous seawater (McArthur et al., 2001) in sediments older than 14.7 Ma (below 32.5 rmcd) with a maximum difference of 0.000143 corresponding to 2.85 Myrs (Figure 4c). The pore water $^{87}Sr/^{86}Sr$ ratios of Site U1338 are close to contemporaneous seawater in sediments younger than 9.5 Ma and then increase with depth (Figure 4e).

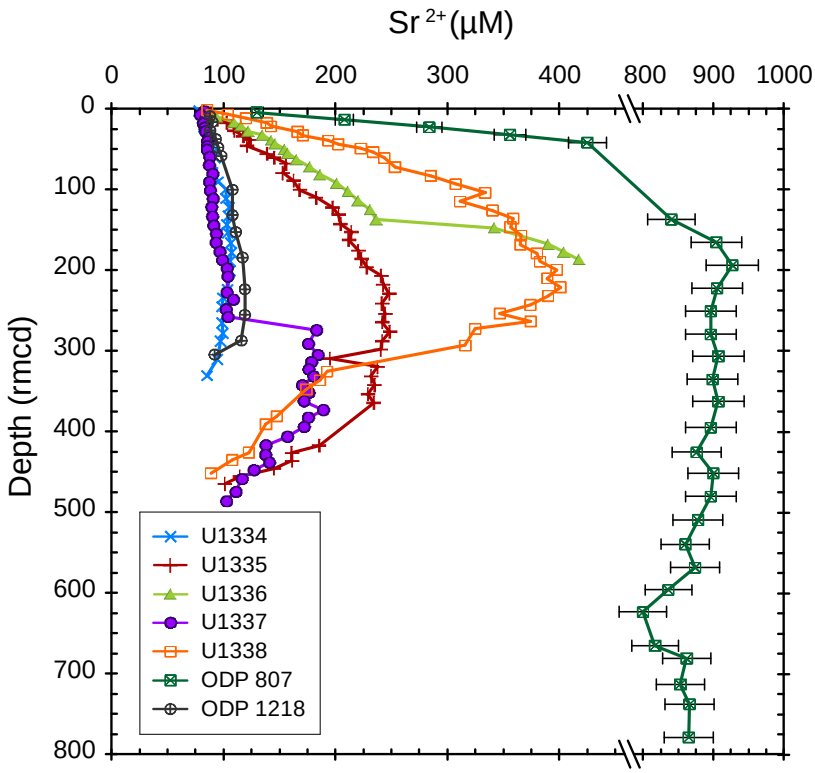

Figure 3. Pore water Sr concentrations for the PEAT sites investigated (Pälike et al., 2010) and ODP Sites 807 (Kroenke et al., 1991) and 1218 (Lyle et al., 2002) plotted against depth. Revised composite depths are from Westerhold et al. (2012) and Wilkens et al. (2013). Depth scale for ODP Site 807 is mbsf and for Site 1218 is mcd. Error bars of the PEAT sites at 2σ level are ± 3.06 % (Pälike et al., 2010) and for ODP Site 1218 are ± 4.8 % (Lyle et al., 2002). The errors for the PEAT sites and Site 1218 are as big as the symbol size. Error bars shown for ODP Site 807 at 2σ level are ± 4 % (Kroenke et al., 1991).

3.3 $^{87}Sr/^{86}Sr$ ratios ratio of bulk carbonate leachates

The $^{87}Sr/^{86}Sr$ ratios of the bulk carbonates decrease with depth from 0.7092 to 0.7077 and are generally in very good agreement (within 2σ uncertainties) with contemporaneous seawater (McArthur et al., 2001) (Figure 4, Table S3). However, the carbonate $^{87}Sr/^{86}Sr$ ratios of Site U1336 older than 20.2 Ma exhibit systematically less radiogenic values than contemporaneous seawater (Figure 4c).

The $^{87}Sr/^{86}Sr$ ratios of the bulk carbonates at Site U1335 are more radiogenic than contemporaneous seawater in places. This may result from turbidites observed in this core (Pälike et al., 2010) transferring younger sediments to greater depths (Figure 4b). These deviations towards younger seawater $^{87}Sr/^{86}Sr$ ratios occur between 7.1-9.2 Ma (45.5-60.3 mcd), 13.7-14.2 Ma (131-142.6 mcd) and 22.9-23.6 Ma (393-417.1 mcd), although shipboard sedimentology does not suggest

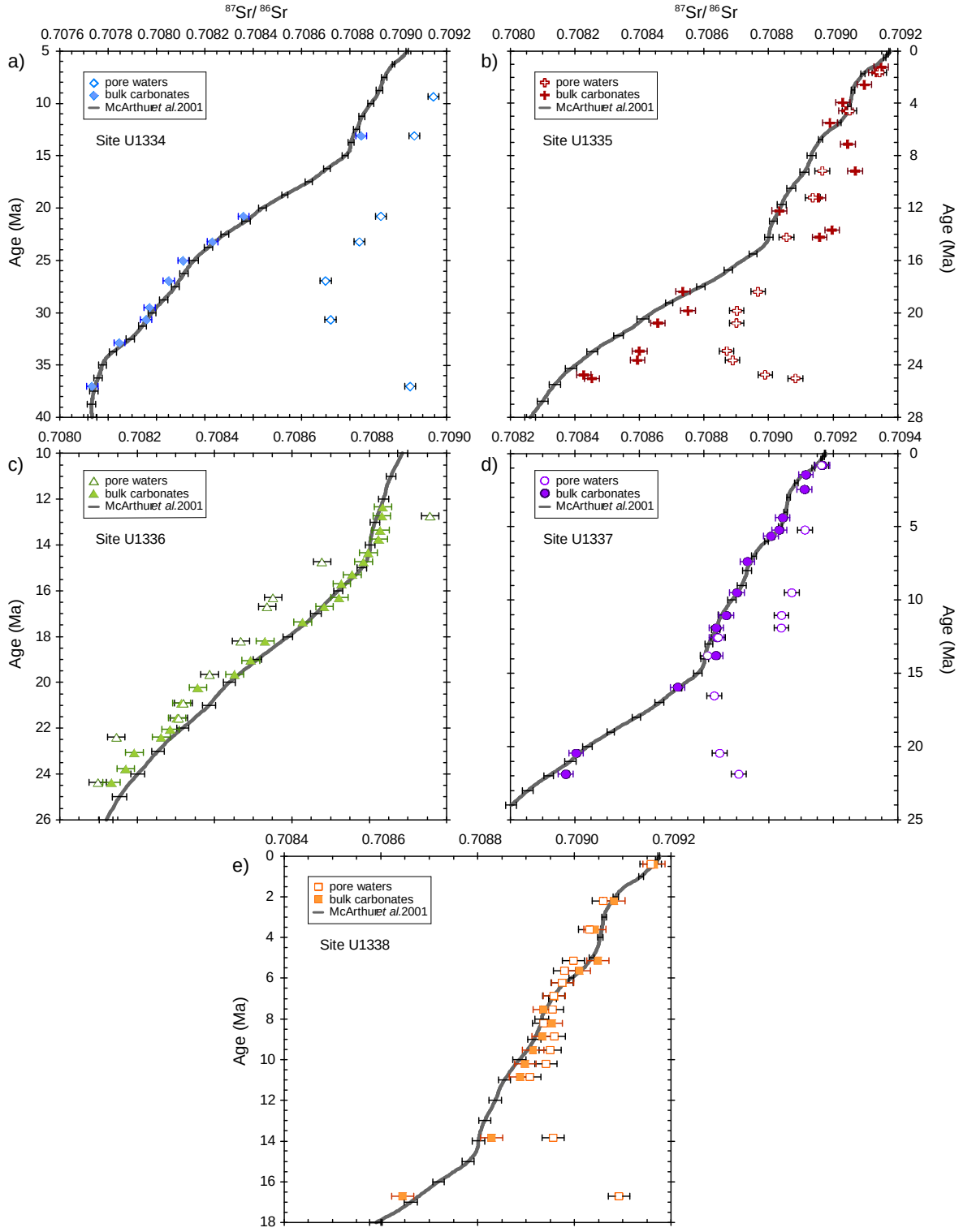

Figure 4. $^{87}Sr/^{86}Sr$ ratios of the PEAT sites investigated plotted versus age. The seawater Sr isotope curve is shown as a grey line (McArthur et al., 2001, LOWESS fit, version 3) and represents the contemporary seawater composition based on a compilation of 13 published sources for the shown ages. Error bars of the seawater Sr isotope curve represent the 2σ uncertainties of the data compiled by McArthur et al. (2001). Closed symbols represent bulk carbonate leachates and open symbols are pore water samples. Error bars for the PEAT sites denote the 2σ uncertainties of repeated measurements of IAPSO seawater. Please note the different scales for each panel. $^{87}Sr/^{86}Sr$ ratios of the PEAT sites are plotted against depth in Figures S6 and S7.

any gravity flows in sediments younger than 11.6 Ma (about 89 mcd). This site will not be discussed further regarding recrystallisation because of the disturbed sedimentation.

3.4 Element/Ca ratios of bulk carbonates

The Sr/Ca ratios of the bulk carbonates of the PEAT sites range from 1.23 to 2.96 mmol/mol (Figure 5a, Table S2). The Sr/Ca ratios of Site U1336 are generally lower than of the other PEAT sites (Figure 5a). The Sr/Ca ratios of Sites U1334, U1335, U1337 and U1338 fluctuate around 2 mmol/mol, interrupted by a transient increase between 8.9 and 11.1 Ma at Sites U1337 and U1338 (Figure 5a). The highest Sr/Ca value of Site U1338 of nearly 3 mmol/mol coincides with the maximum in the pore water Sr.

The Mg/Ca ratios of the bulk carbonates range from 1.0 to 32.2 mmol/mol (Figure 5b, Table S2). The Mg/Ca ratios fluctuate around 2-3.5 mmol/mol with a notable deviation between 8.2 and 9.5 Ma at Sites U1337 and U1338 (with the highest value reaching 32 mmol/mol) (Figure 5b) similar to the excursion in Sr/Ca (Figure 5a).

The Mn/Ca ratios of the bulk carbonates from the PEAT sites range from 0.01 to 14.11 mmol/mol with an excursion between 7.1 and 10.8 Ma at Sites U1335, U1337 and U1338 (Figure 5c, Table S2). These increases in carbonate Mn/Ca corresponded to intervals of increased dissolved Mn in pore waters (Figure 6, Table S1).

3.5 $\delta^{88/86}$Sr of pore waters and bulk carbonate leachates

Nine bulk carbonate and associated pore water couplets were chosen for the measurement of $\delta^{88/86}$Sr because both their bulk carbonate and pore water $^{87}Sr/^{86}Sr$ ratios either deviated from the seawater Sr isotope curve or there was a difference in $^{87}Sr/^{86}Sr$ between pore water and bulk carbonate (Figure 7a, Table 2). One sample (U1338A 18H3, 179 rmcd, 8.2 Ma; Table 2) represents a control sample as both the pore water and the bulk carbonate $^{87}Sr/^{86}Sr$ ratios did not deviate from contemporaneous seawater.

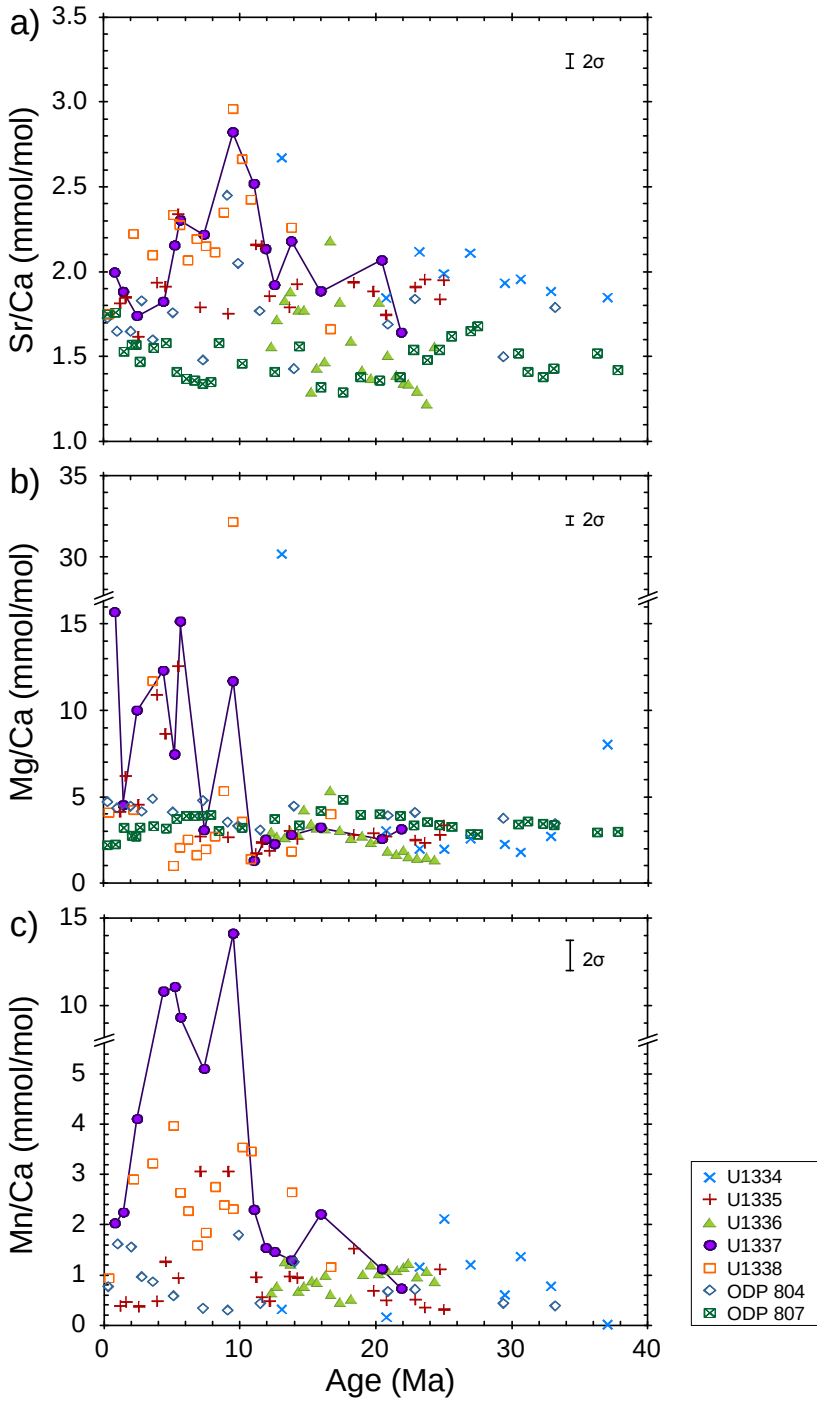

Figure 5. Sr/Ca a), Mg/Ca b) and Mn/Ca c) ratios of bulk carbonate leachates shown against age. Values from ODP Sites 804 and 807 are from Delaney and Linn (1993). Error bars represent the 2σ uncertainty estimates and were estimated from repeated measurements of one sample. High Sr/Ca and Mg/Ca values between 8 and 11 Ma at Sites U1337 and U1338 are probably related to high productivity events and the dissolution of carbonates (Lyle et al., 1995). This is supported by a low carbonate content (< 1 wt %) during this interval at Site U1337 (Pälike et al., 2010) (Figure S1, Table S2). The peak in Mg/Ca ratios may be caused by diagenetic overgrowths of Mg-rich carbonate (Boyle et al., 1983; Higgins and Schrag, 2012). Data plotted versus depth (rmcd) are shown in Figure S8.

The $\delta^{88/86}$Sr of pore waters analysed from Site U1338 and the shallowest sample of U1336 are relatively close to modern seawater values, whereas the analysed pore waters of Sites U1334, U1336 (except the shallowest sample) and U1337 exhibit heavier $\delta^{88/86}$Sr values compared to modern seawater (IAPSO = 0.381 ± 0.029 ‰, n = 5) (Figure 7, Table 2). Generally, the $\delta^{88/86}$Sr values of U1336 pore waters increase with depth and age (Figure 7, Table 2).

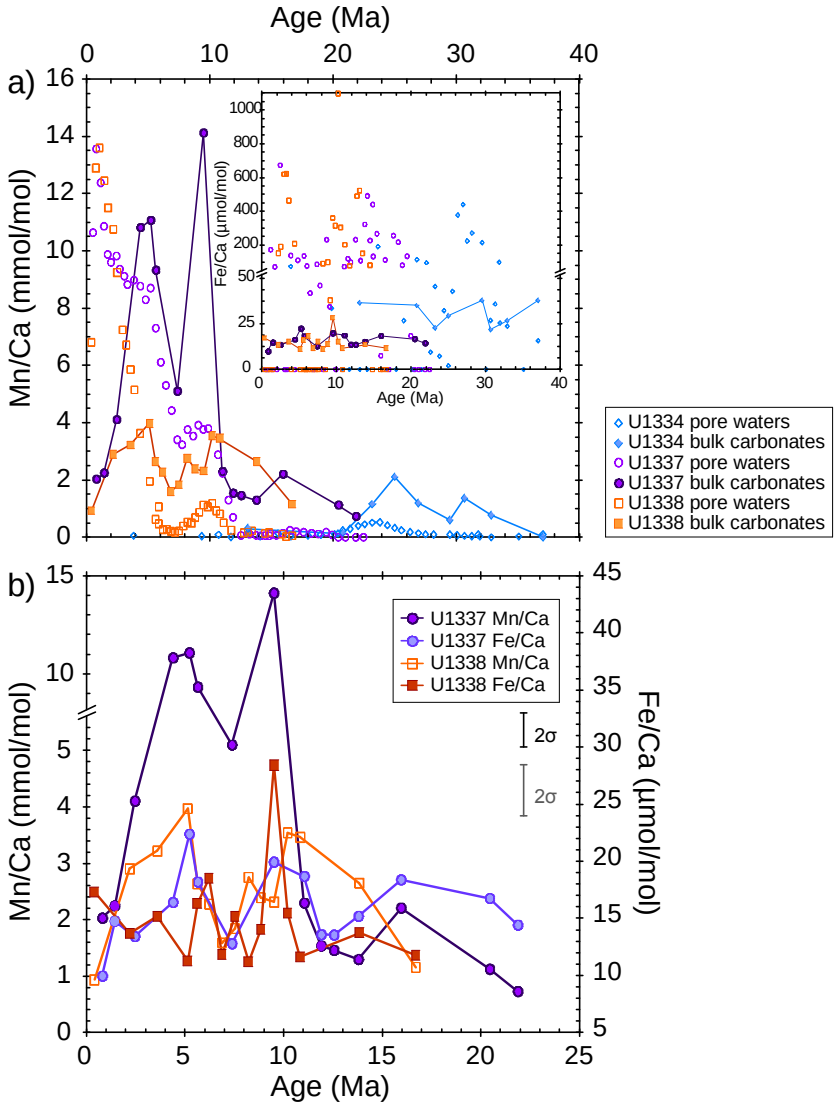

Figure 6. Mn/Ca a) and Fe/Ca insert) ratios of bulk carbonate leachates and pore waters of Sites U1334 (blue diamonds), U1337 (purple circles) and U1338 (orange squares) plotted against age. b) Bulk carbonate Mn/Ca and Fe/Ca of Site U1337 and U1338 plotted against age for direct comparison. Please note the different scale on the x-axis in a) and b). Closed symbols represent bulk carbonate leachates and open symbols are pore water samples. Data for pore waters are from Pälike et al. (2010). Error bars for Mn/Ca (black) and Fe/Ca (grey) represent the 2σ uncertainty estimates from repeated measurements of one sample. Mn/Ca and Fe/Ca ratios versus depth (rmcd) are illustrated in Figure S9.

The $\delta^{88/86}Sr$ values of the bulk carbonates do not show a trend with depth or age, ranging from 0.211 to 0.249 ‰ and are similar to modern carbonates (coral reference material JCp-1 = 0.202 ± 0.027 ‰, n = 10) (Figure 7, Table 2).

Table 2. $\delta^{88/86}Sr$ and $^{87}Sr/^{86}Sr$ values of bulk carbonate leachates and associated pore waters as well as standards measured by TIMS.

Sample	Depth	Age	Pore waters			Bulk carbonate leachates		
	rmcd	(Ma)	$^{87}Sr/^{86}Sr$	$\delta^{88/86}Sr$ (‰)	Sr^a (ppm)	$^{87}Sr/^{86}Sr$	$\delta^{88/86}Sr$ (‰)	Sr^b (ppm)
U1334A 30X3	330.64	37.04	0.709030	0.473	7.50	0.707739	0.217	1075
U1336B 2H5	9.78	12.73	0.708941	0.428	8.22	0.708829	0.245	1096
U1336B 6H2	50.36	16.30	0.708551	0.505	13.53	0.708707	0.231	1142
U1336B 12H3	113.79	20.90	0.708319	0.635	19.32	0.708321	0.235	1161
U1336B 13H3	125.04	21.56	0.708298	0.655	20.25	0.708298	0.241	1146
U1336B 20H3	186.67	24.36	0.708086	0.700	36.61	0.708137	0.211	1223
U1337A 26X3	258.03	11.91	0.709030	0.605	9.09	0.708840	0.240	1308
U1338A 18H3	179.03	8.22	0.708932	0.457	33.30	0.708935	0.249	1091
U1338B 36H3	359.44	13.84	0.708925	0.365	16.06	0.708822	0.230	1539
IAPSO seawater	-	-	0.709167 ±0.000004	0.381 ± 0.029	7.45	-	-	-
JCp-1 coral	-	-	-	-	-	0.709168 ±0.000019	0.202 ± 0.027	

The analytical uncertainties for the pore waters are comparable to those measured for IAPSO seawater reference material and the reproducibility of the bulk carbonates conforms to that of the JCp-1 coral reference material.

[a] The Sr content (ppm) of the pore waters was calculated from the Sr concentration reported from Pälike et al. (2010).

[b] The Sr content (ppm) of the bulk carbonates was calculated from the Sr/Ca ratio and the Ca content from this sample. The Ca content was estimated from the $CaCO_3$ content given by Pälike et al. (2010).

4. Discussion

4.1 Insights from pore water chemistry

Below the pore water Sr concentration maximum, a decrease with depth is observed for ODP Site 1218 (Lyle et al., 2002) and Sites U1334, U1335, U1337 and U1338

(Figure 3), where circulation of relatively modern seawater through the basement was inferred from various chemical species in the pore waters like Li^+ and sulphate (Baker et al., 1991; Pälike et al., 2010). This seawater in the basement has a lower Sr^{2+} concentration than the pore waters and the gradient causes diffusive exchange. A trend towards modern seawater values is also seen in the $^{87}Sr/^{86}Sr$ ratios of the pore waters (see Section 4.2). In the case of Site U1336 the lower section of the sediment was not sampled for pore waters.

A small increase in pore water Sr^{2+} may result from net carbonate dissolution in opal-rich layers, especially at Sites U1337 and U1338 (see Figure 24, Site U1338 in Pälike et al., 2010), but the overall Sr^{2+} trend for these sites reflects recrystallisation, diffusion and advection. The clay content of these sediments is low, but reactions with clay are clearly visible in the Li^+ profiles (not shown here, see Pälike et al., 2010). These differ from the corresponding Sr^{2+} and Mg^{2+} profiles suggesting clay mineral reactions have little influence on these elements here.

The small increase in Sr^{2+} at ODP Site 1218 (Figure 3) can possibly be explained by the age of the sediments. Site 1218 travelled out of the equatorial high productivity zone at around 28 Ma (Pälike et al., 2010) and below the CCD around 12 Ma resulting in low sedimentation rates thereafter. Therefore, the sediment layer younger than 28 Ma is thin and diffusion caused excess Sr^{2+} in the pore waters to be lost over time (e.g., Rudnicki et al., 2001; Richter and Liang, 1993; Edgar et al., 2013). Site U1334 is similar to Site 1218 and comprises the oldest sediment sampled of the investigated sites. It is therefore likely that the Sr originally released from the biogenic carbonates has been lost from the sediment over time and the recrystallisation, which decreases exponentially with sediment age (Richter and DePaolo, 1988; Richter and Liang, 1993; Richter, 1996; Fantle and DePaolo, 2006), has not kept up. Additional evidence for this is the radiogenic $^{87}Sr/^{86}Sr$ ratios of the pore waters of Site U1334, where diffusive exchange of Sr from seawater results in pore waters some 12.3 Myrs younger than seawater contemporaneous to the sediments in the upper 120 rmcd (see also Section 4.2). The fact that the pore water $^{87}Sr/^{86}Sr$ ratios are not the same as modern seawater suggests a small contribution of Sr from carbonate recrystallisation.

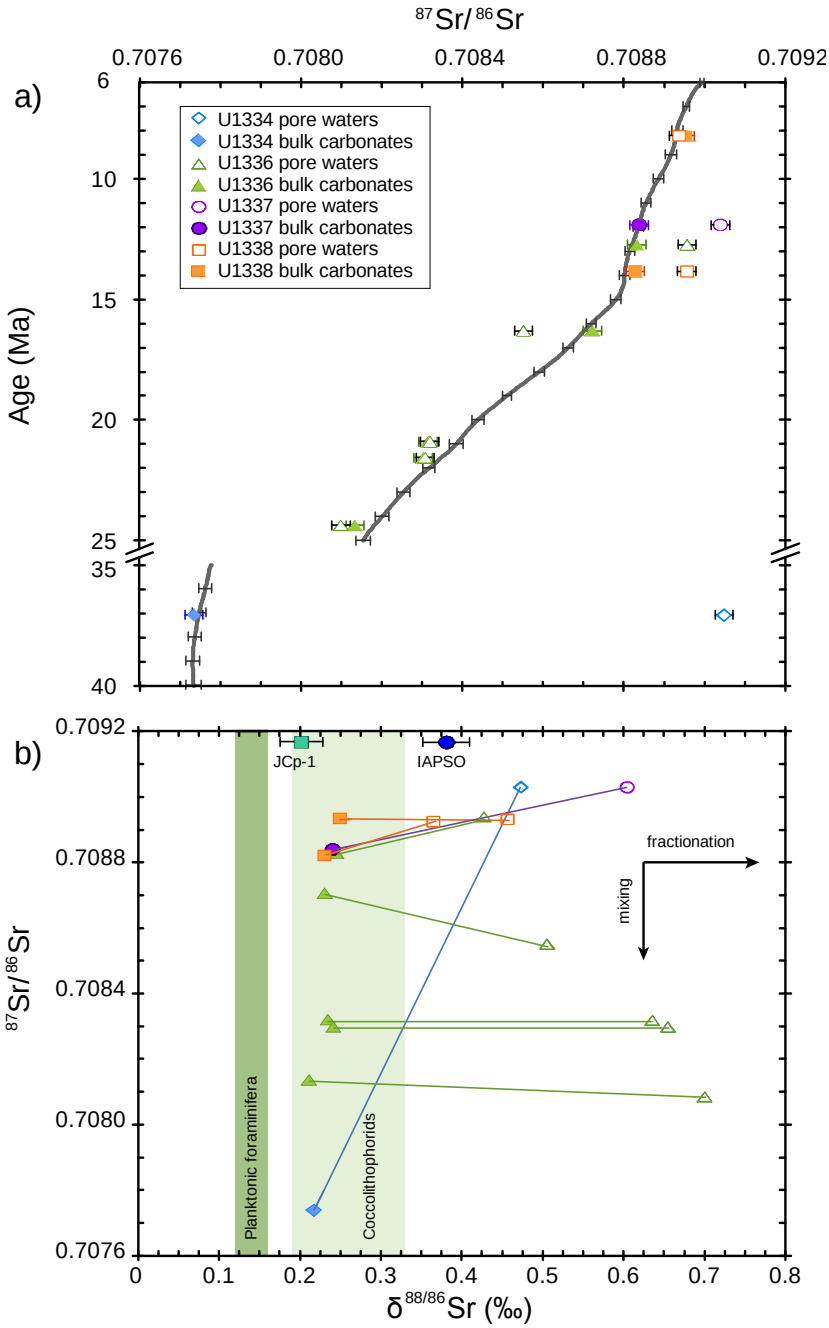

Figure 7. a) $^{87}Sr/^{86}Sr$ ratios of the selected bulk carbonate and associated pore water couplets plotted against age. b) Stable Sr ($\delta^{88/86}Sr$) isotopes of selected bulk carbonate leachates and their associated pore waters from Sites U1334 (blue diamonds), U1336 (green triangles), U1337 (purple circles) and U1338 (orange squares) plotted against the radiogenic Sr ratio ($^{87}Sr/^{86}Sr$). Bulk carbonates and associated pore waters are connected by a line. Closed symbols represent bulk carbonate leachates and open symbols are pore water samples. IAPSO seawater and JCp-1 coral reference material measurements are shown for comparison. The error bars for the IAPSO seawater represent the analytical uncertainties of the pore waters and the uncertainty of the JCp-1 represents those for the bulk carbonates. Coloured bars represent the $\delta^{88/86}Sr$ range of planktonic foraminifera and coccolithophorids (Krabbenhöft et al., 2010; Böhm et al., 2012). The depth and age for each bulk carbonate and associated pore water couplet is given in Table 2.

Although the upper part of the sediment sequence of Site U1337 (until 258 rmcd) is younger than at Site U1334, the observed Sr gradient is comparably low (Figure 3). Diffusive exchange with seawater seems to have been the dominant process (Richter and Liang, 1993) in this upper layer resulting in low Sr^{2+} concentrations and pore water $^{87}Sr/^{86}Sr$ ratios about 7 Myrs younger than seawater contemporaneous to the sediments, similar to those observed at Site U1334. Below 258 rmcd (11.9 Ma) the pore water Sr^{2+} concentration increases strongly (Figure 3). This sharp increase marks the onset of a chert layer (at 263 rmcd), which acts as an aquitard or a barrier to diffusion (Pälike et al., 2010). Ca^{2+}, Mg^{2+} and K^{+} profiles are not offset below the chert layer like Sr^{2+} (Figures S3 and S4, Table S1), but the former three species are mostly influenced by diffusive exchange with the basement (Lawrence et al., 1975; Gieskes, 1976; Rudnicki et al., 2001). Sr^{2+}, on the other hand, reflects reactions in the sediments, diffusive exchange and advection while other elements also influenced by reactions with the sediment, such as Li^{+}, Mn^{2+}, Fe^{2+}, and total alkalinity, are offset below the chert layer at Site U1337 (Table S1). The Sr released to the pore waters below that layer can thus only diffuse downwards to the relatively young seawater in the basement.

Site U1338 is located on the youngest basement of the PEAT transect (Pälike et al., 2010) and has the thickest sediment cover deposited from the Miocene to present (Figure 2). It exhibits the steepest pore water Sr^{2+} gradient (Figures 3 and 8) and therefore is likely to have the highest recrystallisation rates. Although diagenesis modelling for Site U1337 has not been conducted, the sediment accumulation rates and changes in porosity with depth (until the chert layer at 263 rmcd at U1337) (Figure S2) are very similar for U1338 and U1337, yet the pore water Sr^{2+} gradients differ by a factor of 16. This difference in Sr^{2+} gradients is most likely influenced by the chert layer at Site U1337 preventing Sr^{2+} from below diffusing upwards, but above the chert layer the difference in Sr^{2+} reflects different recrystallisation rates.

The increase in pore water Sr^{2+} concentration with sediment age is shown in Figure 8. It is likely that Site U1336 would have the deepest Sr^{2+} maximum of all sites, but the total length of the core was not sampled for pore waters. The pore water Sr^{2+} gradient (the slope of the regression lines in Figure 8) changes with depth at Site U1336 by a factor of 2.6. This change in the pore water Sr^{2+} gradient occurs

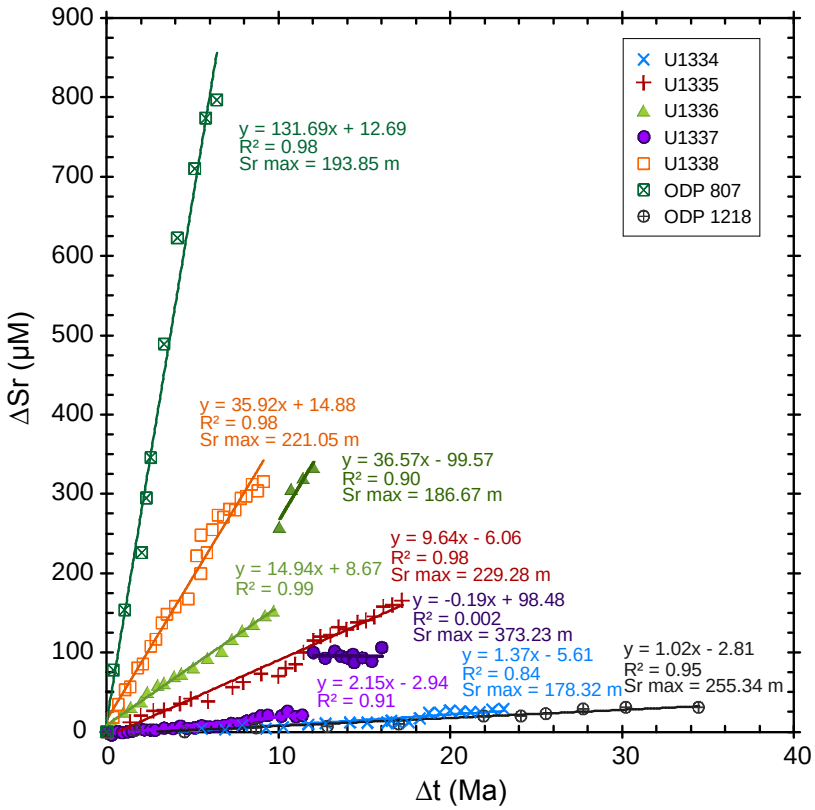

Figure 8. The change in pore water Sr^{2+} plotted against the change in age of the sediments sampled for waters. The Sr concentration of the shallowest sample was subtracted from the pore water concentration ($\Delta Sr = Sr^{2+}_{x} - Sr^{2+}_{top}$). Shown ΔSr^{2+} comprises concentrations from the top of the sediment section to the Sr^{2+} maximum depth (given in the plot), except for Site U1336, where all pore water Sr^{2+} values were used. Δt is the age of the core top set to zero for a better comparison between the sites ($\Delta t = t_x - t_{top}$). For Sites U1336 and U1337 two regression lines are shown as the rates change significantly below a layer of restricted diffusional exchange at these sites. The section below this aquitard layer is illustrated by a darker colour. Data for PEAT sites are from Pälike et al. (2010), for ODP Site 1218 from Lyle et al. (2002) and for ODP Site 807 from Kroenke et al. (1991) using the age model from the Initial Reports for the ODP sites (Lyle et al., 2002; Kroenke et al., 1991).

within a short section of decreased porosity, which could restrict the diffusive exchange of the pore water below and above (Gieskes and Lawrence, 1976; Rudnicki et al., 2001). Within this interval, between 137.7-142.5 rmcd, the porosity decreases to a mean value of 48.9 % compared to 59.6 and 59.9 % (mean of 5 m sections) below and above, respectively (Figure S2) (Pälike et al., 2010). This decrease in porosity is accompanied by a peak in total organic carbon content of 0.3 % at 135.1 rmcd causing a pronounced decline in alkalinity from 2.29 to 1.73 mM by organic material degradation. The decrease in alkalinity and the steeper Sr^{2+} slope suggests higher recrystallisation rates (Richter and DePaolo, 1988). These higher rates may be ascribed to higher temperatures likely at this site since it is located close (about 30 km) to the Clipperton Fracture Zone (Pälike et al., 2010). Although no

in-situ temperatures were measured at Site U1336, high gradients in pore water Mg/Ca and decreasing K^+ with depth suggest strong reactivity in the basement (Lawrence et al., 1975; Gieskes, 1976; Rudnicki et al., 2001), and comparison to other sites in the region, with negligible horizontal advection in the sediments, suggests a relatively strong thermal gradient for Site U1336 (Figure 9). This gradient may also have influenced the pore water profiles of Ca^{2+}, Mg^{2+} through reactions with the sediment (Higgins and Schrag, 2012) (Figure S3, see also Section 4.6). In contrast to Site U1337, the profiles of Ca^{2+} and Mg^{2+} change significantly across the aquitard along with sediment reactive elements like Sr^{2+}, Li^+ and total alkalinity (Figure S3, Table S1).

Overall, the pore water Sr^{2+} gradient reflects the reactivity to a first order (Figure 8). ODP Site 807 shows the steepest slope suggesting intense recrystallisation (Delaney and Linn, 1993). The highest pore water Sr^{2+} gradient values of the PEAT transect are observed at Sites U1336 and U1338. To account for variable sediment accumulation rates and vertical advection, sediment diagenesis at both Sites U1336 and U1338 has been simulated using a 1-D reactive transport model (Figure S5) (J. Higgins personal communication, 2014; supplementary information and Table S4). The numerical model used to simulate the sediment pore-fluid system is described in detail elsewhere (Higgins and Schrag, 2012). The diagenesis model results suggest Site U1336 is more recrystallised (37 % at the bottom of the core at 32 Ma) than Site U1338 (21 % at 18 Ma), although only the upper section of Site U1336 could be modelled since the deeper sediment was not sampled for pore waters. The upper sediment column at Site U1336 is more recrystallised, which largely results from the sediments having more time to recrystallise than those at Site U1338. The change in the Sr^{2+} gradient below the aquitard, not captured by the model, may be related to the restriction of diffusion, but the continued increase of Sr^{2+} with depth indicates further recrystallisation in the deeper part of the sediment column (see also Section 4.4).

4.2 Radiogenic Sr isotopes of pore waters and bulk carbonate leachates

The bulk carbonate $^{87}Sr/^{86}Sr$ ratios of Sites U1334, U1337, U1338 and the upper sediment column of U1336 (until about 102.5 rmcd, 20.2 Ma) are indistinguishable

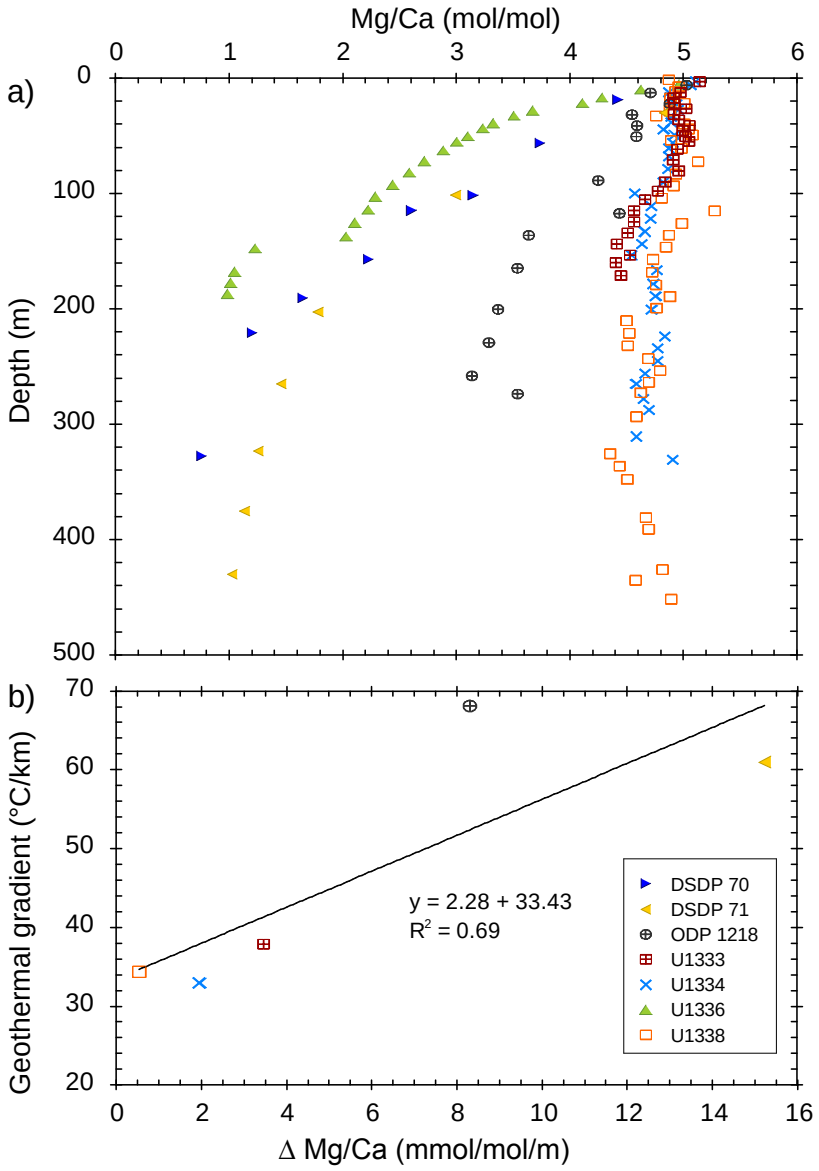

Figure 9. a) Pore water Mg/Ca ratios of Deep Sea Drilling Project (DSDP) Sites 70 (blue triangles) and 71 (yellow triangles) (Tracey et al., 1971), ODP Site 1218 (grey crossed circles) (Lyle et al., 2002), and PEAT Sites U1333 (red crossed squares), U1334 (blue crosses), U1336 (green triangles) and U1338 (orange open squares) (Pälike et al., 2010) plotted against depth. The pore water profiles of U1334 and U1338 represent the other PEAT sites investigated as the Mg/Ca profiles are consistent between all sites, except U1336. Depths for PEAT sites are given in rmcd from Westerhold et al. (2012) and Wilkens et al. (2013). Depth scale for DSDP Sites 70 and 71 is mbsf and for ODP Site 1218 is mcd. b) Pore water Mg/Ca gradient for the first 200 m of the same sites like in a), excluding DSDP Site 70 and U1336, plotted against the geothermal gradient. The pore water Mg/Ca gradient is illustrated for the first 200 m of the sediment column only for better comparison between sites. The gradient was calculated by subtracting the Mg/Ca ratio at surface from the Mg/Ca ratio at 200 m. The geothermal gradient for DSDP Site 71 was taken from Von Herzen et al. (1971). The geothermal gradient for Site 1218 was calculated using the *in-situ* temperature measurements (Lyle et al., 2002) and measured gradients for PEAT sites were taken from Pälike et al. (2010). Also shown is a linear regression for those sites to estimate the geothermal gradient for Site U1336 (78.8°C km^{-1}).

(within 2σ uncertainties) from contemporaneous seawater (McArthur et al., 2001) indicating that recrystallisation occurred relatively rapidly (within 1.5 Myrs) (Figure 4). This 1.5 Myrs is based on the analytical uncertainty of the $^{87}Sr/^{86}Sr$ measurements (2σ) converted to age using the McArthur et al. (2001) seawater Sr isotope curve. In sediments younger than 9.5 Ma, the pore waters of Site U1338 show good agreement with contemporaneous seawater (Figure 4e). All PEAT sites sampled to basement show increasing $^{87}Sr/^{86}Sr$ ratios (towards present-day values) of the pore waters with depth in the oldest parts of the cores confirming the circulation of relatively modern seawater through the basement (Figure 4a, b, d, e) (Baker et al., 1991). This trend in pore water $^{87}Sr/^{86}Sr$ ratios towards present-day values shows that the isotopic composition of pore waters can easily be changed by diffusive exchange with young seawater in the basement. It is difficult to change the $^{87}Sr/^{86}Sr$ ratios of bulk carbonates as they have a higher Sr content than pore waters (by a factor of > 100, see Table 2). Even in the deeper sediment sections with more radiogenic pore water $^{87}Sr/^{86}Sr$ ratios, the bulk carbonates have not incorporated detectable amounts of pore water Sr.

4.3 Elemental ratios of bulk carbonates

Sr/Ca ratios of bulk carbonates have been used to assess recrystallisation processes, as well as past changes in seawater chemistry (Baker et al., 1982; Delaney, 1989; Delaney and Linn, 1993). The Sr/Ca ratio is species-specific in foraminifera and coccoliths (Stout, 1985; Delaney, 1989; Reinhardt et al., 2000; Stoll and Schrag, 2000) and thus the Sr/Ca will reflect the main constituents when bulk carbonates are measured (Reinhardt et al., 2000). The Sr/Ca ratio is species dependent because of unique calcification processes and calcification rates (Elderfield et al., 1982; Stoll et al., 1999). Recent foraminifera exhibit Sr/Ca values of 1-2 mmol/mol (e.g., Rosenthal et al., 1997; Russell et al., 2004), whereas modern coccolithophorids have Sr/Ca ratios varying from 1.9 to 3.2 mmol/mol (Stoll et al., 2002).

Diagenetic alteration is generally accompanied by lower Sr/Ca ratios in bulk carbonates as less Sr is incorporated into secondary calcite (e.g., Baker et al., 1982; Delaney, 1989). ODP Site 807 is considered to be heavily recrystallised based on

Sr/Ca ratios (Delaney and Linn, 1993) and it has been suggested that equilibrium has been achieved between pore waters and carbonate sediments below 150 metres below seafloor (mbsf) (Fantle and DePaolo, 2006). By comparison, the generally lower Sr/Ca ratios of bulk carbonates of Site U1336, which are similar to those of Site 807, suggest more extensive diagenetic alteration compared to the other PEAT sites (Figure 5a). Site U1336 Sr/Ca decreases slightly with depth indicating further recrystallisation. In contrast, the bulk carbonate samples of Site U1334 exhibit higher Sr/Ca ratios suggesting a better preservation of sediments older than 20 Ma compared to Site U1336 and 807 (Figure 5a).

The Mg/Ca ratio can also be used for the assessment of diagenetic alteration with elevated values indicating recrystallisation (Delaney et al., 1989; Delaney and Linn, 1993). Mg/Ca ratios are also species-specific with values of 1-10 mmol/mol for most modern foraminifera (e.g., Rosenthal et al., 1997; Lea et al., 2000; Russell et al., 2004) and 0.1-0.2 mmol/mol for modern coccolithophorids (Stoll et al., 2002).

Recently, Higgins and Schrag (2012) proposed that the Mg content of recrystallised carbonates would be higher than the original bulk carbonate consisting mostly of low Mg/Ca coccoliths. The deepest bulk carbonate sample of Site U1334 (330.6 rmcd, 37 Ma) exhibits elevated Mg/Ca ratios indicating recrystallisation (Figure 5b, Table S2), but in general Site U1334 is less altered than Site U1336 based on Sr/Ca (Figure 5a). Site U1336 Mg/Ca decreases with depth in sediments older than 17.4 Ma (below 62.6 rmcd) (Figure 5b), whereas elevated ratios are reported for recrystallised carbonates (Delaney, 1989; Delaney and Linn, 1993). This may reflect the decrease of pore water Mg/Ca ratios with depth at Site U1336 (see Section 4.1) resulting from exchange with basement basalt.

Mn/Ca ratios can give valuable information about diagenetic changes with high values resulting from Mn-Fe oxyhydroxide or authigenic $MnCO_3$ coatings (Boyle, 1983; Franklin and Morse, 1983; Pena et al., 2005). Recent non-contaminated foraminifera (without coatings) have Mn/Ca ratios of 0.01-0.2 mmol/mol (Rosenthal et al., 1999; Harding et al., 2006).

Site U1337 and U1338 bulk carbonates exhibit higher Mn/Ca ratios than the other PEAT sites and show a peak at about 5 Ma. Correspondence between pore water and bulk carbonate Mn content suggests incorporation from pore water, enriched in Mn^{2+}, as Mn oxide phases are reduced (Figure 6a). Bulk carbonate Mn/Ca ratios could be biased towards higher values by partial leaching of Mn oxides, although all sites would be affected similarly as the same leaching method was applied throughout. However, the fact that the pore water Mn^{2+} peaks just above the carbonate Mn maxima at U1337 and U1338 suggests higher carbonate Mn/Ca ratios may be explained by Mn-carbonate overgrowths, such as kutnahorite ($Ca(Mn^{2+}, Mg^{2+})(CO_3)_2$) (Boyle, 1983; Pena et al., 2005). Bulk carbonate Mn/Ca values of U1336 increase slightly below 18.2 Ma (72 rmcd), which may also indicate authigenic carbonates and the incorporation of Mn into recrystallised calcites. The pore water Fe^{2+} at the PEAT sites is much higher than the values measured in the bulk carbonates and Fe/Ca ratios show no corresponding trends between pore water and bulk carbonates (insert of Figure 6a), supporting the formation of $MnCO_3$ phases rather than the dissolution of the ferromanganese oxides during the leaching process.

4.4 Persistent recrystallisation at Site U1336

In sediments older than 14.7 Ma (below 32.5 rmcd) pore waters of Site U1336 show lower $^{87}Sr/^{86}Sr$ ratios than contemporaneous seawater (Figure 4c). These lower ratios likely result from upward diffusion of Sr from older carbonates recrystallised deeper in the section. This Sr originating from older carbonates is also evident in bulk carbonates older than 20.2 Ma (Figure 4c) and suggests active recrystallisation further down in the sediment column.

Recrystallisation modelling performed at other locations (e.g., Richter and DePaolo, 1988; Richter and Liang, 1993) suggests that diagenetic changes in the $^{87}Sr/^{86}Sr$ ratio of bulk carbonates of this age should not be detectable as they would be on the same order of magnitude as the uncertainty of the measurements (about 30 ppm). However, recrystallisation is evident in the $^{87}Sr/^{86}Sr$ ratios of the bulk carbonates and associated pore waters of Site U1336 older than 20 Ma (Figure 4c). Previous studies at other locations suggested recrystallisation rates decrease exponentially with age

and depth (e.g., Baker et al., 1982; Richter and Liang, 1993; Fantle and DePaolo, 2006), but it seems that significant recrystallisation is still ongoing below 100 rmcd at Site U1336. Today, Site U1336 is located below the CCD resulting in the dissolution of carbonate sediments younger than 12 Ma. In general, recrystallisation modelling at other locations has produced the highest reaction rates for the uppermost 200 m (Hampt-Andreasen and Delaney, 2000; Fantle and DePaolo, 2006), corresponding to about 10 Myrs (Richter and Liang, 1993; Hampt-Andreasen and Delaney, 2000). At Site U1336 bulk carbonate $^{87}Sr/^{86}Sr$ ratios deviate from contemporaneous seawater in deeper sediments older than 20 Ma suggesting a late phase of recrystallisation (see Figures 8, 9a and Section 4.1). The recrystallisation coefficients of the model, determined by fitting the pore water properties, also indicate a higher background recrystallisation rate (λ) at Site U1336, as well as a smaller depth increment at which the rate of recrystallisation changes (γ) compared to Sites U1338 and 807 (Tables S4 and S5). Being located near the fracture zone, forced advection (Fantle et al., 2010) may have played a role in the high reactivity at Site U1336. However, without samples from the entire sediment column it is not possible to be more specific about what drives the enhanced reactivity observed at this site.

4.5 $\delta^{88/86}Sr$ of pore waters and bulk carbonates

The use of $\delta^{88/86}Sr$ ratios in geochemistry is novel and although only a few studies have been published, the $\delta^{88/86}Sr$ of modern planktonic foraminifera and coccolithophorids have been measured (Figure 7b: Krabbenhöft et al., 2010; Böhm et al., 2012). The bulk carbonate samples measured in this study are in good agreement with the range for coccolithophorids (Figure 7b), which are the main constituents of the bulk carbonates (Section 4.3). The $\delta^{88/86}Sr$ ratio of the bulk carbonate of the control sample (U1338A 18H3, Table 2) is in good agreement with the JCp-1 coral reference material, but the $\delta^{88/86}Sr$ value of the pore water is 0.076 ‰ higher than the IAPSO seawater (Figure 7b, Table 2).

The $\delta^{88/86}Sr$ of U1336 pore waters increase with depth and age (Figure 7b, Table 2). This increase is unlikely to derive from basalt or hydrothermal sources as these have lower $\delta^{88/86}Sr$ values ranging from 0.25 to 0.27 ‰ (Krabbenhöft et al., 2010). The increase in $\delta^{88/86}Sr$ with depth (depth is represented by decreasing $^{87}Sr/^{86}Sr$ ratios) at

Site U1336 (Figure 7b, Table 2) suggests that the recrystallisation of carbonates is associated with an isotopic fractionation process that enriches the pore waters in ^{88}Sr. This ^{88}Sr enrichment indicates that, although less Sr is incorporated into secondary calcite during recrystallisation, the lighter Sr isotope (^{86}Sr) is incorporated preferably leaving heavy pore waters behind. This lighter Sr needs to be locked away in a stable phase that is not dissolved again by further recrystallisation allowing the pore water $\delta^{88/86}Sr$ to evolve with recrystallisation. The pore waters of Site U1336 become increasingly isotopically fractionated with depth but show $^{87}Sr/^{86}Sr$ values similar to the associated carbonates suggesting the same Sr source. The $\delta^{88/86}Sr$ values of the carbonates do not change noticeably with depth and age since the carbonates have much higher concentrations and mass fraction of Sr than pore waters (by a factor of > 100, see Table 2). This results in pore waters being a much more sensitive indicator of isotope fractionation processes than carbonates. Thus, our first results of $\delta^{88/86}Sr$ from deep sea carbonate sediments indicate that stable Sr isotopes have the potential to identify recrystallised carbonate sediments by their pore water signals.

Precipitation of celestite ($SrSO_4$), as a possible phase of highly fractionated Sr, can be excluded since Site U1336 does not show any extensive consumption of SO_4^{2-} (Pälike et al., 2010) and solution simulations using PHREEQC Interactive Version 3.0.4 (Parkhust and Appelo, 2013) show that the investigated pore waters are undersaturated with respect to celestite.

Different studies have shown that isotope fractionation depends mainly on the precipitation rate of the carbonates and the crystal surface kinetics (e.g., Fantle and DePaolo, 2007; DePaolo, 2011; Böhm et al., 2012; Higgins and Schrag, 2012). The precipitation rate of secondary calcite during recrystallisation is very low and occurs near equilibrium, so no isotope fractionation is observed (Fantle and DePaolo, 2007; DePaolo, 2011; Böhm et al., 2012). Fantle and DePaolo (2007) pointed out that diffusional effects on Ca isotopes are within the analytical uncertainties. The same should be true for Sr isotopes as Böhm et al. (2012) demonstrated little fractionation at slow precipitation rates (approaching equilibrium) in laboratory experiments and natural systems. Recently, Chao et al. (2013) reported high pore water $\delta^{88/86}Sr$ values of 0.82 ‰ from mud volcanoes in the northern Chu-kou Fault, Taiwan similar

to those observed here at Site U1336. Although the chemical composition of the pore waters in this study is very different to those of the mud volcanoes, the isotope fractionation towards higher $\delta^{88/86}Sr$ ratios is the same and these authors demonstrated that calcite precipitation along the fluid path was the most likely cause for the heavy pore water $\delta^{88/86}Sr$ ratios.

Table 3. Calculated Sr data for coccolithophorid carbonates.

Sr/Ca ratio (mmol/mol)	Calculated Sr content (ppm)[a]	Sr content adjusted to mass ratio M (ppm)[b]	Calculated percentage of recrystallised Sr (%)[c]	Estimated $\delta^{88/86}Sr_{bulk\ carbonate}$ (‰)[d]
1.9	1487	2781	5.9	0.227
2.0	1565	2927	4.5	0.235
2.1	1644	3074	3.7	0.240
2.2	1722	3220	3.1	0.243
3.2	2505	4684	1.2	0.254

[a] The Sr content (ppm) was calculated from the Sr/Ca ratio given in the first column and the Ca content of sample U1336B 20H3 (Ca^{2+} = 358000 ppm).
[b] The calculated Sr content was multiplied by the mass ratio M of sample U1336B 20H3 which was calculated by $M = \rho_{solid} * (1 - \phi)/ (\rho_{fluid} * \phi)$ where ρ_{solid} is the density of the calcite with $\rho_{calcite}$ = 2.7 g/cm³ and ρ_{fluid} is the density of the seawater with $\rho_{seawater}$ = 1.025 g/cm³. The porosity ϕ of this sample is 58.5 % (Pälike et al., 2010) resulting in M = 1.87.
[c] The percentage of the recrystallised Sr input from recrystallisation was calculated using equation 1.
[d] The $\delta^{88/86}Sr$ of the recrystallised bulk carbonate was estimated by using equation 3.

A simple mass balance calculation can be used to estimate the amount of isotopically fractionated Sr that is needed to produce the measured pore water $\delta^{88/86}Sr$ values of Site U1336 (Equations 1-3, Tables 3 and S6). Such heavy pore waters could only be generated if Sr released from the carbonates, enriched in ^{88}Sr, had mixed with the initial pore water that had an assumed $\delta^{88/86}Sr$ value of seawater (0.381 ‰). Unfortunately, no seawater $\delta^{88/86}Sr$ data exist for the last 25 Myrs, but the $\delta^{88/86}Sr$ value of seawater could have changed by a maximum of 0.3 ‰ during such a period (Vollstaedt et al., 2014). However, such a change in seawater $\delta^{88/86}Sr$ does not significantly influence the amount of isotopically fractionated Sr required to produce the observed pore water $\delta^{88/86}Sr$. For simplicity, we assume that the initial bulk carbonate consisted of only coccolithophorids as coccolithophorids represent the main constituent of bulk carbonates. The Sr content of the initial carbonate was

estimated by the Sr/Ca range of modern coccolithophorids (1.9-3.2 mmol/mol, Stoll et al., 2002) taking into account the carbonate content of the deepest sample of U1336 (U1336B 20H3: Ca^{2+} = 358000 ppm, 89.5 wt % $CaCO_3$, Tables 3 and S6). The Sr/Ca ratios of modern coccolithophorids can be used since the seawater Sr/Ca ratio has not varied significantly over the last 30 Myrs (Sosdian et al., 2012). The calculated Sr content was adjusted to the mass ratio M of that sample (M = 1.87) to take the densities of pore water and calcite, as well as the porosity into account (Table 3). Then the fraction of isotopically fractionated Sr that is released from the bulk carbonates to the pore waters can be calculated by:

$$p_{\text{recrystallised input}} = Sr^{2+}_{PW} - Sr^{2+}_{SW} / Sr^{2+}_{\text{coccolithophorids}} - Sr^{2+}_{\text{bulk carbonate}} \quad (1)$$

where all Sr concentrations are given in ppm. The Sr^{2+}_{PW} is the Sr content of the pore water, Sr^{2+}_{SW} is the Sr concentration of seawater (7.45 ppm) and $Sr^{2+}_{\text{bulk carbonate}}$ is the Sr content of the measured bulk carbonate of sample U1336B 20H3 (Table S6). The calculated percentage ranges from 5.9 to 1.2 % for low and high Sr content coccolithophorid carbonates (Table 3). The $\delta^{88/86}Sr$ value of this recrystallised Sr contribution from the bulk carbonates (coccolithophorids) was calculated for the deepest U1336 pore water measured giving a $\delta^{88/86}Sr_{\text{recrystallised input}}$ of 0.78 ‰ using:

$$\delta^{88/86}Sr_{\text{recrystallised input}} = ((Sr^{2+}_{PW} * \delta^{88/86}Sr_{PW}) - (Sr^{2+}_{SW} * \delta^{88/86}Sr_{SW}))/(Sr^{2+}_{PW} - Sr^{2+}_{SW}) \quad (2)$$

where $\delta^{88/86}Sr_{PW}$ is the stable Sr ratio of the pore water sample U1336B 20H3 (Table S6) and $\delta^{88/86}Sr_{SW}$ is the seawater ratio ($\delta^{88/86}Sr_{IAPSO}$ = 0.381 ‰). The $\delta^{88/86}Sr$ of the recrystallised bulk carbonate can then be estimated by the following equation using the determined $\delta^{88/86}Sr_{\text{recrystallised input}}$ and the $\delta^{88/86}Sr$ of recent coccolithophorids ($\delta^{88/86}Sr$ = 0.26 ‰; Krabbenhöft et al., 2010):

$$\delta^{88/86}Sr_{\text{bulk carbonate}} = \delta^{88/86}Sr_{\text{coccolithophorid}} - (x * \delta^{88/86}Sr_{\text{recrystallised input}}) / 1 - x \quad (3)$$

where x is the fraction of isotopically fractionated Sr that is released during recrystallisation (see Equation 1). The obtained $\delta^{88/86}Sr$ ratios range from 0.227 to 0.254 ‰ for low and high Sr content coccolithophorid carbonate (Table 3). The average of the measured U1336 $\delta^{88/86}Sr_{\text{bulk carbonate}}$ = 0.233 ‰ lies within this range, attesting to the validity of our calculations and is also in agreement with the average $\delta^{88/86}Sr$ = 0.22 ‰ of the major calcifying species (Krabbenhöft et al., 2010). A starting

Sr/Ca ratio of 2.0 mmol/mol fits best and results in a recrystallised Sr contribution of the bulk carbonates of 4.5 % and $\delta^{88/86}Sr_{bulk\ carbonate}$ = 0.235 ‰. This Sr/Ca ratio is in accordance with the average of Sr/Ca ratios measured for Sites U1337 and U1338, which are better preserved than U1336 suggesting that the initial Sr/Ca ratio of Site U1336 may have been similar.

Assuming that the initial bulk carbonate had an average Sr content corresponding to a Sr/Ca ratio of about 2.0-2.1 mmol/mol, the release of about 5 % of strongly isotopically fractionated Sr during recrystallisation would be sufficient to produce the high $\delta^{88/86}Sr$ values of the pore waters. This suggests the $\delta^{88/86}Sr$ of the carbonates remain unaffected because of their much higher Sr concentrations (with lower $\delta^{88/86}Sr$) compared to the pore waters. The determined recrystallised Sr input ($\delta^{88/86}Sr_{recrystallised\ input}$ = 0.78 ‰) is similar for all analysed pore waters older than 20 Ma, which may indicate a correlation of the isotope fractionation process with the late phase of recrystallisation observed (see Section 4.4).

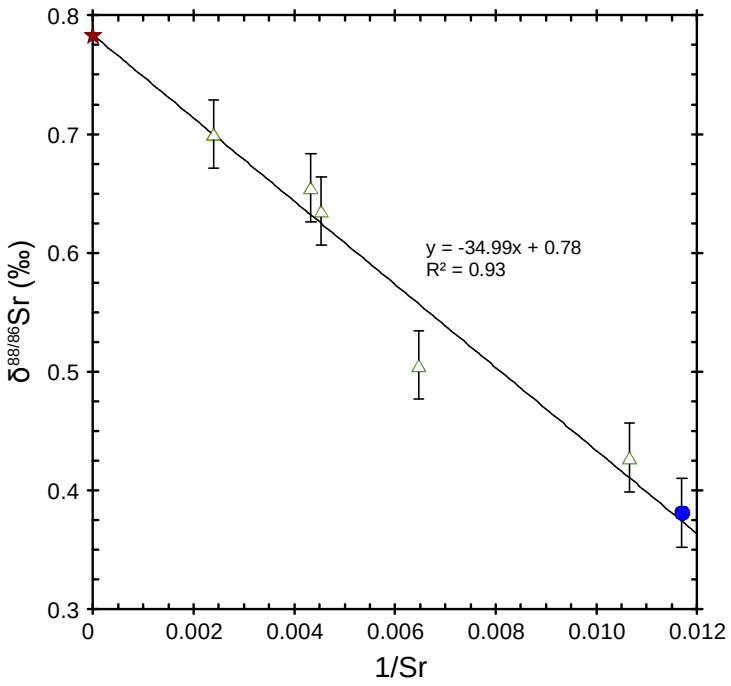

Figure 10. Inverse of the Sr concentration of Site U1336 pore waters (open green triangles) plotted against $\delta^{88/86}Sr$. The end members for the mixing line are also illustrated: Seawater (IAPSO) (blue cycle) and the $\delta^{88/86}Sr$ value of the recrystallised Sr input (red star). Data for the U1336 Sr concentration are from Pälike et al. (2010).

Diffusive transport in the pore water is most likely responsible for the relatively high $\delta^{88/86}$Sr signal in the younger part of the sediments as a consequence of a mixing gradient between two end members. Figure 10 shows a mixing relationship between the $\delta^{88/86}$Sr and the inverse Sr concentration of the pore waters. The intercept of this mixing line with $\delta^{88/86}$Sr reveals a source with the same $\delta^{88/86}$Sr as calculated for the purely recrystallised Sr contribution of the bulk carbonate. The intercept of the mixing line with the inverse Sr concentration gives the seawater Sr concentration as the second end member. The fact that the end members of the mixing relationship are seawater and the recrystallised Sr input validates our calculations.

4.6 Factors influencing recrystallisation

Different factors are believed to influence recrystallisation including sedimentation rates, subsidence, carbonate saturation state of the bottom water and geothermal gradients (Richter and Liang, 1993; Hampt Andreasen and Delaney, 2000). Today, all PEAT sites investigated are below the lysocline, the depth horizon, where the rate of dissolution of carbonates significantly increases. The lysocline and the CCD have varied over time and were much shallower in the Eocene and deepened drastically at the Eocene-Oligocene boundary and during the early Oligocene, coinciding with the onset of ice sheet growth (e.g., Pälike et al., 2012). When a site subsides below the CCD depends on the rate of subsidence and the age of the crust. Sites U1334 and U1336 subsided below the CCD at around 12 Ma, whereas the other sites are still above the CCD (Pälike et al., 2012), but a direct effect of this on the recrystallisation of carbonates at the PEAT sites is unclear. Additionally, although Site U1336 and ODP Site 807 have both experienced intense recrystallisation, Site 807 is still above the CCD, suggesting the saturation state of the overlying bottom water is not a primary control on carbonate recrystallisation. The calcite saturation of the pore waters is even more important for early diagenesis given that undersaturated pore waters tend to dissolve the carbonates and high amounts of organic matter lead to reducing sediments during the remineralisation of organic matter. The total organic carbon (TOC) content of the PEAT sites varies between < 0.03 and 0.72 % and is highest in the youngest, rapidly accumulated sediments at Sites U1337 and U1338. Such values compare well with benthic lander data from the area (TOC: 0.10-0.99 %) (Berelson et al., 1990; Hammond et al., 1996) suggesting the pore waters have

calcite saturation values between $\Omega = 0.76\text{-}1.36$ during early diagenesis and are undersaturated below the CCD (calculated with the carbonate system calculation software CO2SYS from Lewis and Wallace (1998) using the nutrient and carbonate data from Jahnke et al. (1982) and Berelson et al. (1990)).

Sedimentation rates at the PEAT sites do not seem to influence recrystallisation given that sedimentation rates systematically decrease when a site travelled out of the high productivity area (± 2°) at the equator. Therefore, Sites U1337 and U1338, as the youngest sites, show the highest sedimentation rates, but recrystallisation appears to have been different at these sites.

The lithology of each sedimentary section is also believed to have an impact on recrystallisation, with clay-rich sediments reported to be better preserved than carbonate-rich ones (Hampt Andreasen and Delaney, 2000). All PEAT sites investigated are relatively carbonate-rich (Figure S1, Table S2), but the extent of recrystallisation seems to be related to the carbonate content. The better preserved Site U1337 has on average lower $CaCO_3$ contents with 61.7 % (in the ooze sections) compared to Site U1338 with 71.2 % (Pälike et al., 2010). Site U1334 shows a slightly higher value than U1338 with 74.4 % and is less well preserved compared to Sites U1337 and U1338 (Pälike et al., 2010). Site U1336 has the highest carbonate content reaching 87.3 % (Pälike et al., 2010) and is extensively recrystallised, similar to ODP Site 807 with an even higher $CaCO_3$ content of 93 % (Kroenke et al., 1991).

The inferred strong geothermal gradient is likely important for the reactivity of the sediment at Site U1336 (see Section 4.1) and the remarkable extent of persistent carbonate recrystallisation. This is most likely due to the proximity (30 km) of Site U1336 to the Clipperton Fracture Zone (Pälike et al., 2010), making the location useful for the study of recrystallisation even if it is a relatively rare case.

5. Conclusion

The pore water Sr concentrations of the PEAT sites increase with depth due to dissolution of carbonates and the release of Sr from the carbonates to the pore waters during recrystallisation. The $^{87}Sr/^{86}Sr$ ratios of bulk carbonate leachates

generally suggest that recrystallisation occurred relatively rapidly (within 1.5 Myrs) as the values are indistinguishable (within 2σ uncertainties) from contemporaneous seawater (McArthur et al., 2001).

The Sr/Ca ratios of the bulk carbonates of Site U1336 are generally lower than those of the other PEAT sites investigated and decrease with depth suggesting more extensive recrystallisation at this site.

In sediments older than 20.2 Ma a late phase of recrystallisation is observed at Site U1336 as the $^{87}Sr/^{86}Sr$ ratios of bulk carbonate leachates and associated pore waters exhibit lower values than contemporaneous seawater. These lower ratios indicate the incorporation of Sr dissolved from older carbonates.

For the first time we document $\delta^{88/86}Sr$ fractionation during recrystallisation of deep sea carbonates. Pore water $\delta^{88/86}Sr$ values increase with depth at Site U1336 suggesting an isotope fractionation process during recrystallisation, where the secondary calcite preferentially incorporates light Sr (^{86}Sr) thus enriching the pore waters in ^{88}Sr. The lighter Sr isotope (^{86}Sr) enriched phase appears to be locked away in a stable phase not released by further recrystallisation. Mass balance calculations show that only a small amount of Sr in the carbonates (1-6 %) must fractionate during recrystallisation to produce the high $\delta^{88/86}Sr$ values of the pore waters. Therefore, our first $\delta^{88/86}Sr$ results indicate that stable Sr isotopes have the potential to identify recrystallised sediments by their pore water signals. The combination of several Sr parameters (Sr^{2+}, Sr/Ca, $^{87}Sr/^{86}Sr$, $\delta^{88/86}Sr$) indicates that the bulk carbonates of Site U1336 are extensively altered, compared to the other PEAT sites investigated, and also show a late phase of recrystallisation at this more reactive site. Our data suggest a strong geothermal gradient is the primary driver of extensive carbonate recrystallisation at this location.

Acknowledgements

This work was funded by the German Science Foundation, DFG, HA 5751/1-1 and HA 5751/2-1 (PEAT). We thank Ana Kolevica, Silke and Folkmar Hauff for laboratory assistance and technical support for the stable Sr isotope measurements. Discussion with Florian Böhm, Jan Fietzke and Volker Liebetrau helped to improve the manuscript. John Higgins kindly provided insights from diffusion reaction modelling. The suggestions of associate editor Silke Severmann and two anonymous reviewers greatly improved the manuscript. We especially thank Matthew Fantle for extensive comments, which considerably improved the manuscript.

References

Baker P. A., Gieskes J. M., and Elderfield H. (1982) Diagenesis of carbonates in deep-sea sediments – evidence from Sr/Ca ratios and interstitial dissolved Sr^{2+} data. *J. Sediment. Petrol.* **52**, 71-82.

Baker P.A., Stout P.M., Kastner M., and Elderfield H., (1991) Largescale lateral advection of seawater through oceanic crust in the central equatorial Pacific. *Earth Planet. Sci. Lett.* **105**, 522-533.

Berelson W. M., Hammond D. E., O'Neill D., Xu X-M., Chin C., and Zukin J. (1990) Benthic fluxes and pore water studies from sediments of the central equatorial north Pacific: Nutrient diagenesis. *Geochim. Cosmochim. Acta* **54**, 3001-3012.

Böhm F., Eisenhauer A., Tang J., Dietzel M., Krabbenhöft A., Kisakürek B., and Horn C. (2012) Strontium isotope fractionation of planktic foraminifera and inorganic calcite. *Geochim. Cosmochim. Acta* **93**, 300-314.

Boyle E. A. (1983) Manganese carbonate overgrowths on foraminifera tests. *Geochim. Cosmochim. Acta* **47**, 1815-1819.

Chao H.-C., You C.-F., Liu H.-C. and Chung C.-H. (2013) The origin and migration of mud volcano fluids in Taiwan: Evidence from hydrogen, oxygen, and strontium isotopic compositions. *Geochim. Cosmochim. Acta* **114**, 29-51.

Delaney M. L. (1989) Temporal changes in interstitial water chemistry and calcite recrystallization in marine sediments. *Earth Planet. Sci. Lett.* **95**, 23-37.

Delaney M. L. and Linn L. J. (1993) Interstitial water and bulk calcite chemistry, Leg 130, and calcite recrystallization. In: *Proc. ODP. Sci. Results* 130 (eds. W. H. Berger, L. W. Kroenke, T. R. Janecek, et al.). Ocean Drilling Program, pp. 561-572.

DePaolo D. J. (2011) Surface kinetic model for isotopic and trace element fractionation during precipitation of calcite from aqueous solutions. *Geochim. Cosmochim. Acta* **75**, 1039-1056.

Edgar K. M., Pälike H., and Wilson P. A. (2013) Testing the impact of diagenesis on the $\delta^{18}O$ and $\delta^{13}C$ of benthic foraminiferal calcite from a sediment burial depth transect in the equatorial Pacific. *Paleoceanography* **28**, 468-480.

Elderfield H. and Gieskes J. M. (1982) Sr isotopes in interstitial waters of marine sediments from Deep Sea Drilling Project cores. *Nature* **300**, 493-497.

Elderfield H., Gieskes J. M., Baker P. A., Oldfield R. K., Hawkesworth C. J., and Miller R. (1982) $^{87}Sr/^{86}Sr$ and $^{18}O/^{16}O$ ratios, interstitial water chemistry and diagenesis in deep-sea carbonate sediments of the Ontong Java Plateau. *Geochim. Cosmochim. Acta* **46**, 2259-2268.

Fantle M. S. and DePaolo D. J. (2006) Sr isotopes and pore fluid chemistry in carbonate sediment of the Ontong Java Plateau: Calcite recrystallization rates and evidence for a

rapid rise in seawater Mg over the last 10 million years. *Geochim. Cosmochim. Acta* **70**, 3883-3904.

Fantle M. S. and DePaolo D. J. (2007) Ca isotopes in carbonate sediment and pore fluid from ODP Site 807A: The Ca^{2+}(aq)-calcite equilibrium fractionation factor and calcite recrystallization rates in Pleistocene sediments. *Geochim. Cosmochim. Acta* **71**, 2524-2546.

Fantle M. S., Maher K. M. and DePaolo D. J. (2010) Isotopic approaches for quantifying the rates of marine burial diagenesis. *Rev. Geophys.* **48**, RG3002, doi:10.1029/2009RG000306.

Fietzke J. and Eisenhauer A. (2006), Determination of temperature-dependent stable strontium isotope ($^{88}Sr/^{86}Sr$) fractionation via bracketing standard MC-ICP-MS. *Geochem. Geophys. Geosyst.* **7**, Q08009, doi:10.1029/2006GC001243.

Franklin M. L. and Morse J. W. (1983) The interaction of manganese(II) with the surface of calcite in dilute solutions and seawater. *Mar. Chem.* **12**, 241-254.

Gieskes J. M. (1976) Interstitial water studies, Leg 33, Deep Sea Drilling Project. *Init. Repts*. *DSDP* **33**, 563-570.

Gieskes J. M. and Lawrence J. R. (1976) Interstitial water studies, Leg 35, Deep Sea Drilling Project. *Init. Repts. DSDP* **35**, 407-424.

Gieskes J. M., Elderfield H. and Palmer M. R. (1986) Strontium and its isotopic composition in interstitial waters of marine carbonate sediments. *Earth Planet. Sci. Lett.* **77**, 229-235.

Gieskes J. M., Gamo T., and Brumsack H. (1991) Chemical methods for interstitial water analysis aboard *JOIDES Resolution. ODP Tech. Note* 15.

Hammond D. E., McManus J., Berelson W. M., Kilgore T. E., and Pope R. H. (1996) Early diagenesis of organic material in equatorial Pacific sediments: stoichiometry and kinetics. *Deep-Sea Res. II* **43**, 1365-1412.

Hampt Andreasen G. and Delaney M. L. (2000) Bulk calcite size fraction distribution and Sr/Ca composition for deep-sea sediments at selected age horizons. *Mar. Geol.* **169**, 185-205.

Harding D. J., Arden J. W., and Rickaby R. E. M. (2006) A method for precise analysis of trace element/calcium ratios in carbonate samples using quadrupole inductively coupled plasma mass spectrometry. *Geochem. Geophys. Geosyst.* **7**, Q06003, doi:10.1029/2005GC001093.

Higgins J. A. and Schrag D. P. (2012) Records of Neogene seawater chemistry and diagenesis in deep-sea carbonate sediments and pore fluids. *Earth Planet. Sci. Lett.* **357-358**, 386-396.

Jahnke R., Heggie D., Emerson S., and Grundmanis V. (1982) Pore waters of the central Pacific Ocean: nutrient results. *Earth Planet. Sci. Lett.* **61**, 233-256.

Krabbenhöft A., Fietzke J., Eisenhauer A., Liebetrau V., Böhm F., and Vollstaedt H. (2009) Determination of radiogenic and stable strontium isotope ratios ($^{87}Sr/^{86}Sr$; $\delta^{88/86}Sr$) by thermal ionization mass spectrometry applying an $^{87}Sr/^{84}Sr$ double spike. *J. Anal. At. Spectrom.* **24**, 1267-1271.

Krabbenhöft A., Eisenhauer A., Böhm F., et al. (2010) Constraining the marine strontium budget with natural strontium isotope fractionations ($^{87}Sr/^{86}Sr^*$, $\delta^{88/86}Sr$) of carbonates, hydrothermal solutions and river waters. *Geochim. Cosmochim. Acta* **74**, 4097-4109.

Kroenke L. W., Berger W. H., Janecek T. R., et al. (1991) Site 807. In: *Proc. ODP. Init. Repts.* 130 (eds. W. H. Berger, L. W. Kroenke, T. R. Janecek, et al.). Ocean Drilling Program, pp. 369-493.

Kryc K. A., Murray R. W., and Murray D. W. (2003) Elemental fractionation of Si, Al, Ti, Fe, Ca, Mn, P, and Ba in five marine sedimentary reference materials: results from sequential extractions. *Anal. Chim. Acta* **487**, 117-128.

Lawrence J. R., Gieskes J. M., and Broecker W. S. (1975) Oxygen isotope and cation composition of DSDP pore waters and the alteration of Layer II basalts. *Earth Planet. Sci. Lett.* **27**, 1-10.

Lea D. W., Pak D. K., and Spero H. J. (2000) Climate Impact of Late Quaternary Equatorial Pacific Sea Surface Temperature Variations. *Science* **289**, 1719-1724.

Lewis E. and Wallace D. W. R. (1998) Program developed for CO_2 system calculations. ORNL/CDIAC-105. Carbon Dioxide Information Analysis Center, Oak Ridge National Laboratory, U.S. Department of Energy.

Lyle M., Dadey K. A., and Farrell J. W. (1995) The late Miocene (11-8 Ma) eastern Pacific carbonate crash: Evidence for reorganization of deep-water circulation by the closure of the Panama Gateway. In: *Proc. ODP. Sci. Results* 138 (eds. N. G. Pisias, L. A. Mayer, T. R. Janecek, et al.). Ocean Drilling Program, pp. 821-838.

Lyle M., Wilson P. A., Janecek T. R., et al. (2002) Site 1218. In: *Proc. ODP. Init. Repts.* 199 (eds. P. A. Wilson, M. Lyle and J. V. Firth). Ocean Drilling Program.

McArthur J. M., Howarth R. J., and Baily T. R. (2001) Strontium isotope stratigraphy: LOWESS version 3: best fit to the marine Sr-isotope curve for 0-509 Ma and accompanying look-up table for deriving numerical age. *J. Geol.* **109**, 155-170.

McArthur J. M. and Howarth R. J. (2004) Strontium isotope stratigraphy. In: *A Geologic Time Scale* (eds. F. M. Gradstein, J. G. Ogg and A. G. Smith). Cambridge University Press, Cambridge, pp. 96-105.

Murray R. W., Miller D. J., and Kryc K. A. (2000) Analysis of major and trace elements in rocks, sediments, and interstitial waters by inductively coupled plasma-atomic emission spectrometry (ICP-AES). *ODP Tech. Note* 29.

Nier A. O. (1938) The isotopic constitution of strontium, barium, bismuth, thallium and mercury. *Phys. Rev.* **5**, 275-278.

Pälike H., Lyle M., Nishi H., Raffi I., Gamage K., Klaus A., and the Expedition 320/321 Scientists (2010) *Proc. IODP*, 320/321: Tokyo (Integrated Ocean Drilling Program Management International, Inc.).
Available at http://publications.iodp.org/proceedings/320_321/32021toc.htm

Pälike H., Lyle M. W., Nishi H., et al. (2012) A Cenozoic record of the equatorial Pacific carbonate compensation depth. *Nature* **488**, 609-614.

Parkhurst D. L. and Appelo C. A. J. (2013) Description of input and examples for PHREEQC version 3 – A computer program for speciation, batch-reaction, one-dimensional transport, and inverse geochemical calculations: U.S. Geological Survey Techniques and Methods, book 6, chap. A43, 497 p.

Pearson P. N., Ditchfield P. W., Singano J., Harcourt-Brown K. G., Nicholas C. J., Olsson R. K., Shackleton N. J., and Hall M. A. (2001) Warm tropical sea surface temperatures in the Late Cretaceous and Eocene epochs. *Nature* **413**, 481-487.

Pena L. D., Calvo E., Cacho I., Eggins S., and Pelejero C. (2005) Identification and removal of Mn-Mg-rich contaminant phases on foraminiferal tests: Implications for Mg/Ca past temperature reconstructions. *Geochem. Geophys. Geosyst.* **6**, Q09P02, doi:10.1029/2005GC000930.

Raddatz J., Liebetrau V., Rüggeberg A., Hathorne E., Krabbenhöft A., Eisenhauer A., Böhm F., Vollstaedt H., Fietzke J., Lopez Correa M., Freiwald A., and Dullo W-Chr. (2013) Stable Sr-isotope, Sr/Ca, Mg/Ca, Li/Ca and Mg/Li ratios in the scleractinian cold-water coral *Lophelia pertusa*. *Chem. Geol.* **352**, 143-152.

Reinhardt E. G., Cavazza W., Patterson R. T., and Blenkinsop J. (2000) Differential diagenesis of sedimentary components and the implication for strontium isotope analysis of carbonate rocks. *Chem. Geol.* **164**, 331-343.

Richter F. M. (1993) Fluid flow in deep-sea carbonate: estimates based on porewater Sr. *Earth Planet. Sci. Lett.* **119**, 133-141.

Richter F. M. (1996) Models for the coupled Sr-sulfate budget in deep-sea carbonates. *Earth Planet. Sci. Lett.* **141**,199-211.

Richter F. M. and DePaolo D. J. (1987) Numerical models for diagenesis and the Neogene Sr isotopic evolution of seawater from DSDP Site 590B. *Earth Planet. Sci. Lett.* **83**, 27-38.

Richter F. M. and DePaolo D. J. (1988) Diagenesis and Sr isotopic evolution of seawater using data from DSDP 590B and 575. *Earth Planet. Sci. Lett.* **90**, 382-394.

Richter F. M. and Liang Y. (1993) The rate and consequences of Sr diagenesis in deep-sea carbonates. *Earth Planet. Sci. Lett.* **117**, 553-565.

Rosenthal Y., Boyle E. A., and Slowey N. (1997) Temperature control on the incorporation of magnesium, strontium, fluorine, and cadmium into benthic foraminiferal shells from Little Bahama Bank: Prospects for thermocline paleoceanography. *Geochim. Cosmochim. Acta* **61**, 3633-3643.

Rosenthal Y., Field M. P., and Sherrell R. M. (1999) Precise determination of element/calcium ratios in calcareous samples using sector field inductively coupled plasma mass spectrometry. *Anal. Chem.* **71**, 3248-3253.

Rudnicki M. D., Wilson P. A., and Anderson W. T. (2001) Numerical models of diagenesis, sediment properties, and pore fluid chemistry on a paleoceanographic transect: Blake Nose, Ocean Drilling Program Leg 171B. *Paleoceanography* **16**, 563-575.

Russell A. D., Hönisch B., Spero H. J., and Lea D. W. (2004) Effects of seawater carbonate ion concentration and temperature on shell U, Mg, and Sr in cultured planktonic foraminifera. *Geochim. Cosmochim. Acta* **68**, 4347-4361.

Schlitzer R. (2012) Ocean Data View. available online at http://odv.awi.de.

Schrag D. P., DePaolo D. J., and Richter F. M. (1995) Reconstructing past sea-surface temperatures – Correcting for diagenesis of bulk marine carbonate. *Geochim. Cosmochim. Acta* **59**, 2265-2278.

Sexton P. F., Wilson P. A., and Pearson P. N. (2006) Microstructural and geochemical perspectives on planktic foraminiferal preservation: "Glassy" versus "Frosty". *Geochem. Geophys. Geosyst.* **7**, 1-29.

Sosdian S. M., Lear C. H., Tao K., Grossman E. L., O'Dea A., and Rosenthal Y. (2012) Cenozoic seawater Sr/Ca evolution. *Geochem. Geophys. Geosyst.* **13**, Q10014, doi:10.1029/2012GC004240.

Stoll H. M., Schrag D. P., and Clemens S. C. (1999) Are seawater Sr/Ca variations preserved in quaternary foraminifera? *Geochim. Cosmochim. Acta* **63**, 3535-3547.

Stoll H. M. and Schrag D. P. (2000) Coccolith Sr/Ca as a new indicator of coccolithophorid calcification and growth rate. *Geochem. Geophys. Geosyst.* **1**, 1-24.

Stoll H. M., Rosenthal Y., and Falkowski P. (2002) Climate proxies from Sr/Ca of coccolith calcite: Calibrations from continuous culture of Emiliania huxleyi. *Geochim. Cosmochim. Acta* **66**, 927-936.

Stout P. M. (1985) Interstitial water chemistry and diagenesis of biogenic sediments from the eastern equatorial Pacific, Deep Sea Drilling Project Leg 85. In: *Init. Repts. DSDP* 85 (eds. L. Mayer, E. Theyer, et al.). Deep Sea Drilling Project, pp. 805-820.

Tracey J. I., Sutton G. H., Nesteroff W. D. et al. (1971) *Proc. DSDP. Init. Repts.* 8 In: *DSDP Init. Repts.* 8 (eds. J. I. Tracey, G. H. Sutton, W. D. Nesteroff, et al.). Deep Sea Drilling Project.

Vollstaedt H., Eisenhauer A., Wallmann K., Böhm F., Fietzke J., Liebetrau V., Krabbenhöft A., Farkas J., Tomasovych A., Raddatz J., and Veizer J. (2014) The Phanerozoic $\delta^{88/86}$Sr record of seawater: New constraints on past changes in oceanic carbonate fluxes. *Geochim. Cosmochim. Acta* **128**, 249-265.

Von Herzen R. P., Fiske R. J., and Sutton G. H. (1971) Geothermal measurements on Leg 8. In: *DSDP Init. Repts.* 8 (eds. J. I. Tracey, G. H. Sutton, W. D. Nesteroff, et al.). Deep Sea Drilling Project, pp. 837-849.

Westerhold T., Röhl U., Wilkens R., et al. (2012) Revised composite depth scales and integration of IODP Sites U1331-U1334 and ODP Sites 1218-1220. In: *Proc. IODP,* 320/321: Tokyo (eds. H. Pälike, et al.) (Integrated Ocean Drilling Program Management International, Inc.). doi:10.2204/iodp.proc.320321.201.2012.

Wilkens R. H., Dickens G. R., Tian J., Backman J., and the Expedition 320/321 Scientists (2013) Revised composite depth scales for Sites U1336, U1337, and U1338. In: *Proc. IODP,* 320/321: Tokyo (eds. H. Pälike, et al.) (Integrated Ocean Drilling Program Management International, Inc.). doi:10.2204/iodp.proc.320321.209.2013.

Zachos J., Pagani M., Sloan L., Thomas E., and Billups K. (2001) Trends, rhythms, and aberrations in global climate 65 Ma to present. *Science* **292**, 686-693.

Zachos J. C., Dickens G. R., and Zeebe R. E. (2008) An early Cenozoic perspective on greenhouse warming and carbon-cycle dynamics. *Nature* **451**, 279-283.

Table S1. Pore water data from squeezed whole-round samples of the PEAT sites, compiled from Pälike et al. (2010).

U1334A												
Sample	Depth (rmcd)	Age (Ma)	pH	Alkalinity (mM)	SO_4^{2-} (mM)	Ca^{2+} (mM)	Mg^{2+} (mM)	Sr^{2+} (µM)	Mn^{2+} (µM)	Fe^{2+} (µM)	K^{+} (mM)	Li^{+} (µM)
1H-2, 145-150	2.95	3.84	7.58	2.73	28.4	10.3	52.4	78.0	0.56	0.74	10.6	25.3
1H-4, 145-150	5.95	9.36	7.62	2.83	28.6	10.6	53.5	82.6	0.44	0.36	11.2	25.0
2H-2, 145-150	12.02	10.72	7.66	3.00	28.2	10.7	52.3	80.8	0.93	BDL	11.0	25.9
2H-5, 145-150	16.52	11.73	7.65	3.32	28.4	10.8	52.5	86.7	0.14	BDL	11.2	22.6
3H-2, 145-150	22.62	13.10	7.62	3.04	28.2	10.7	52.7	82.6	1.63	BDL	11.1	21.7
3H-5, 145-150	27.12	14.11	7.62	3.00	26.3	10.7	53.0	84.5	0.39	BDL	11.0	21.2
4H-2, 145-150	33.63	15.58	7.61	3.16	28.5	11.0	54.0	87.6	1.46	2.11	11.4	20.7
4H-5, 145-150	38.13	16.59	7.60	3.18	27.5	11.0	53.9	88.8	0.47	BDL	11.4	20.5
5H-2, 145-150	44.42	18.00	7.52	3.00	27.6	11.0	53.1	89.7	0.69	BDL	11.5	20.4
5H-5, 145-150	48.92	19.01	7.52	3.13	26.5	10.8	53.1	89.7	1.06	0.29	11.2	19.9
6H-2, 145-150	56.08	20.16	7.58	3.22	25.4	10.9	53.2	89.7	1.01	BDL	11.0	19.3
6H-5, 145-150	60.58	20.41	7.54	3.23	25.1	10.9	53.1	92.6	1.49	BDL	11.4	19.6
7H-3, 140-150	67.52	20.79	7.48	3.23	25.2	11.3	55.0	88.9	2.75	1.29	10.8	19.0
8H-3, 140-150	78.66	21.41	7.48	3.26	24.4	10.8	52.7	90.3	3.23	BDL	10.5	18.1
9H-3, 140-150	90.32	22.06	n.d.	n.d.	26.2	10.9	52.5	95.2	4.31	1.04	10.9	18.2
10H-3, 140-150	99.91	22.60	7.45	3.17	26.8	11.4	52.2	102.2	5.15	0.11	11.2	17.5
11H-3, 140-150	111.02	23.21	7.26	3.24	25.0	11.2	52.8	102.5	5.70	0.51	11.2	17.1
12H-3, 140-150	121.75	23.81	7.51	3.33	25.5	11.4	53.9	105.1	5.97	0.08	11.5	16.8
13H-4, 140-150	133.04	24.44	7.63	3.26	26.6	11.4	53.3	104.2	4.77	0.37	11.3	16.0
14H-3, 140-150	143.53	25.02	7.51	3.41	26.1	11.5	53.2	103.0	3.76	0.02	11.3	15.8
15H-3, 140-150	153.56	25.58	7.41	3.61	25.7	11.4	52.0	103.5	2.79	0.49	11.0	15.6
16H-3, 140-150	166.16	26.28	7.57	3.50	24.6	11.0	52.6	106.5	1.92	4.17	11.2	17.3
17H-3, 140-150	178.32	26.96	7.89	3.15	24.4	11.0	52.2	107.0	1.52	4.85	11.3	17.4
18H-3, 140-150	188.7	27.53	7.81	3.36	25.5	11.2	53.4	105.5	1.16	2.52	11.3	16.6
19H-3, 140-150	200.44	28.19	7.42	3.29	25.2	11.1	52.6	105.9	1.00	3.03	11.2	15.7
20H-3, 140-150	224.06	29.50	7.47	4.02	24.5	10.7	51.8	103.9	1.03	2.30	10.8	16.7
21H-3, 140-150	234.26	30.07	7.42	3.62	24.2	11.0	52.4	99.6	0.67	BDL	10.4	15.6
22H-3, 140-150	245.06	30.67	7.52	3.69	25.6	11.0	52.4	99.0	0.55	0.30	10.5	15.7

Table S1. Continued

U1334A												
Sample	Depth (mcd)	Age (Ma)	pH	Alkalinity (mM)	SO_4^{2-} (mM)	Ca^{2+} (mM)	Mg^{2+} (mM)	Sr^{2+} (µM)	Mn^{2+} (µM)	Fe^{2+} (µM)	K^+ (mM)	Li^+ (µM)
23X-3, 140-150	256.02	31.28	7.60	3.38	25.9	11.3	52.6	101.5	0.38	0.41	10.6	15.8
24X-2, 140-150	265.1	31.78	7.53	3.34	25.9	11.4	52.4	98.7	1.01	1.12	10.7	15.7
25X-3, 140-150	277.93	31.94	7.51	3.24	25.5	11.0	51.2	99.3	0.30	0.28	10.4	16.9
26X-3, 140-150	287.64	32.88	7.51	3.38	24.7	10.9	51.2	97.4	BDL	0.26	10.7	19.0
28X-3, 140-150	310.5	35.09	7.48	3.19	27.6	11.4	52.2	94.3	0.32	BDL	10.3	26.4
30X-3, 140-150	330.64	37.04	7.57	3.07	27.2	10.8	52.9	85.6	1.16	0.17	10.1	29.9

n.d.: not determined; BDL: below detection limit (0.1µM for Mn^{2+}; 0.02 µM for Fe^{2+}; 1.2 µM for Sr^{2+})

U1335A												
Sample	Depth (mcd)	Age (Ma)	pH	Alkalinity (mM)	SO_4^{2-} (mM)	Ca^{2+} (mM)	Mg^{2+} (mM)	Sr^{2+} (µM)	Mn^{2+} (µM)	Fe^{2+} (µM)	K^+ (mM)	Li^+ (µM)
1H-2, 145-150	3.09	1.23	7.53	2.77	25.8	10.0	50.4	82.4	33.91	BDL	10.7	24.8
1H-4, 145-150	6.09	1.64	7.54	2.65	27.9	10.5	50.7	88.8	37.93	5.72	10.7	23.7
2H-2, 145-150	12.86	2.58	7.54	2.65	25.8	10.1	50.8	94.7	43.82	BDL	10.8	22.8
2H-5, 145-150	17.36	3.21	7.52	2.78	26.6	10.4	50.8	102.9	36.91	BDL	10.8	22.3
3H-2, 145-150	22.66	3.94	7.54	2.79	27.1	10.3	50.9	109.0	33.14	BDL	10.8	22.5
3H-5, 145-150	27.16	4.56	7.54	2.80	26.0	10.5	51.1	109.8	29.59	0.55	10.8	21.4
4H-2, 145-150	33.89	5.50	7.75	2.81	26.7	10.5	51.0	117.7	18.96	BDL	10.8	21.0
4H-5, 145-150	38.39	6.12	7.52	2.84	26.2	10.5	50.9	124.4	13.75	1.05	11.4	20.8
5H-2, 145-150	45.52	7.11	7.48	2.92	25.4	9.9	50.9	120.9	6.62	BDL	10.7	19.8
6H-2, 145-150	55.84	8.54	7.52	2.92	26.7	10.4	51.0	138.8	4.59	0.53	10.6	18.9
6H-5, 145-150	60.34	9.17	7.89	2.96	25.6	10.5	50.7	145.3	7.71	0.26	10.7	18.5
7H-3, 140-150	67.89	10.21	7.50	2.97	27.0	10.8	50.0	156.2	12.77	0.26	10.7	18.7
8H-3, 140-150	79.49	11.21	7.48	3.02	25.4	10.2	49.9	152.8	7.66	BDL	10.5	16.3
9H-3, 145-150	88.67	11.65	7.47	2.97	26.2	10.4	49.9	162.6	3.32	1.81	10.7	15.3
10H-3, 145-150	100.40	12.21	7.42	3.40	23.6	10.4	50.0	168.1	1.18	1.53	10.7	14.9
11H-2, 140-150	110.16	12.68	7.40	3.24	24.7	10.7	50.4	182.7	0.62	3.46	10.7	14.4
12H-3, 140-150	122.39	13.27	7.42	3.13	25.5	10.8	50.1	197.6	0.45	3.88	10.6	13.3
13H-3, 140-150	131.04	13.68	7.63	3.39	24.9	10.8	47.9	202.9	0.50	5.43	10.6	12.9
14H-3, 140-150	142.60	14.24	7.42	3.20	25.0	10.9	49.6	204.7	0.52	6.26	10.7	11.9

Table S1. Continued

U1335A												
Sample	Depth (mcd)	Age (Ma)	pH	Alkalinity (mM)	SO_4^{2-} (mM)	Ca^{2+} (mM)	Mg^{2+} (mM)	Sr^{2+} (µM)	Mn^{2+} (µM)	Fe^{2+} (µM)	K^+ (mM)	Li^+ (µM)
15H-3, 140-150	152.65	14.72	7.40	3.33	24.9	10.8	47.9	214.3	0.57	5.73	10.5	11.6
16H-3, 140-150	162.65	15.20	7.57	6.50	25.5	11.0	48.1	212.0	0.93	5.23	10.6	10.5
17H-3, 140-150	175.80	15.83	7.50	3.30	24.9	11.1	47.7	220.4	1.52	6.23	10.7	10.2
18H-3, 140-150	185.77	16.31	7.44	3.38	25.5	11.0	47.8	223.1	2.78	2.80	10.7	9.3
19H-3, 140-150	196.11	16.81	7.46	3.35	23.5	11.4	47.3	228.0	4.32	0.31	10.5	9.2
20H-3, 140-150	207.03	17.33	7.47	3.31	24.8	11.3	47.9	240.8	4.69	1.06	10.8	8.7
21H-3, 140-150	217.92	17.85	7.42	3.11	23.2	11.2	47.4	242.6	3.09	1.54	10.7	8.1
22H-3, 140-150	229.28	18.40	7.24	3.13	25.2	10.5	44.4	248.1	2.06	1.98	10.5	8.0
23H-3, 140-150	241.22	18.49	7.51	3.09	25.0	11.3	47.1	241.7	1.24	3.79	10.7	8.3
24H-3, 140-150	253.93	18.86	7.43	3.22	22.9	11.4	47.9	244.4	0.76	2.98	10.8	6.9
25H-3, 140-150	264.57	19.17	7.44	3.49	24.9	11.1	47.4	241.8	0.82	2.34	10.5	6.4
26H-3, 140-150	275.94	19.50	7.46	3.35	23.2	11.6	48.0	248.6	0.71	4.30	10.6	5.6
27H-3, 140-150	287.74	19.85	7.44	3.26	23.1	11.3	48.0	241.8	0.61	3.15	10.7	5.6
28H-3, 140-150	298.08	20.15	7.42	3.26	23.2	11.1	47.7	240.5	0.55	3.62	10.7	5.3
29H-3, 140-150	309.29	20.48	7.57	3.50	25.1	11.8	47.5	195.2	0.46	3.84	10.7	13.2
30H-3, 140-150	319.86	20.79	7.39	3.71	23.5	11.0	47.5	237.7	0.59	5.37	10.6	5.3
31H-3, 140-150	331.43	21.12	7.37	3.54	23.4	11.3	48.0	231.8	0.30	3.51	10.6	4.5
32H-3, 140-150	342.26	21.44	7.53	3.54	23.0	11.3	47.7	235.0	0.30	4.39	10.7	4.3
33H-3, 140-150	353.54	21.77	7.60	3.54	23.3	10.4	44.8	229.1	0.27	3.47	10.4	4.7
34H-3, 140-150	364.32	22.09	7.56	3.61	24.2	11.0	46.7	234.4	0.37	3.63	10.5	7.5
39X-3, 140-150	417.10	23.63	7.42	3.07	25.9	11.1	50.8	185.6	0.34	1.11	10.7	8.6
40X-3, 140-150	426.60	23.90	7.40	2.78	25.7	9.5	43.8	161.1	0.49	BDL	9.9	9.7
41X-3, 140-150	436.10	24.18	7.73	3.21	24.4	10.7	50.2	161.2	BDL	0.19	10.7	12.3
42X-3, 140-150	445.60	24.46	7.46	2.83	25.4	12.1	50.9	145.0	0.16	0.21	10.6	15.0
43X-3, 140-150	455.20	24.74	7.50	2.73	24.0	9.5	45.1	114.7	0.21	0.19	10.3	19.4
44X-3, 140-150	464.80	25.02	7.43	2.54	24.1	10.0	48.0	101.3	0.11	0.29	10.5	32.4

Table S1. Continued

U1335B												
Sample	Depth (mcd)	Age (Ma)	pH	Alkalinity (mM)	SO_4^{2-} (mM)	Ca^{2+} (mM)	Mg^{2+} (mM)	Sr^{2+} (µM)	Mn^{2+} (µM)	Fe^{2+} (µM)	K^+ (mM)	Li^+ (µM)
36H-3, 140-150	382.65	22.62	7.59	4.32	24.9	10.9	47.9	208.3	BDL	2.88	10.6	4.7
37H-2, 140-150	392.95	22.92	7.60	3.57	23.6	11.5	50.0	212.4	BDL	3.22	10.6	6.1
39H-3, 140-150	411.45	23.46	7.51	3.52	23.8	11.1	50.3	196.0	BDL	3.17	10.6	7.3

BDL: below detection limit (0.1 µM for Mn^{2+}; 0.2 µM for Fe^{2+}; 0.2 µM for Sr^{2+})

U1336B												
Sample	Depth (rcmd)	Age (Ma)	pH	Alkalinity (mM)	SO_4^{2-} (mM)	Ca^{2+} (mM)	Mg^{2+} (mM)	Sr^{2+} (µM)	Mn^{2+} (µM)	Fe^{2+} (µM)	K^+ (mM)	Li^+ (µM)
2H-2, 145-150	5.28	12.34	7.71	2.39	26.2	10.1	50.0	83.7	BDL	BDL	n.d.	23.9
2H-5, 145-150	9.78	12.73	7.96	2.71	25.9	10.6	49.0	93.8	BDL	BDL	n.d.	23.2
3H-2, 145-150	16.81	13.35	7.73	2.66	26.9	11.6	49.9	109.5	BDL	BDL	n.d.	23.2
3H-5, 145-150	21.31	13.75	7.75	2.69	26.0	11.7	48.1	115.6	BDL	BDL	11.4	22.9
4H-2, 145-150	28.01	14.33	7.78	2.72	25.4	12.7	46.7	121.9	0.18	BDL	10.7	21.5
4H-5, 145-150	32.51	14.73	7.74	2.84	26.8	13.7	48.1	134.6	1.11	BDL	11.9	22.3
5H-2, 145-150	38.91	15.29	7.76	2.79	25.1	13.8	45.9	142.9	2.91	BDL	10.3	21.3
5H-5, 145-150	43.41	15.69	7.69	2.82	25.7	14.4	46.7	145.8	4.66	BDL	10.8	20.2
6H-2, 145-150	50.36	16.30	7.62	2.75	24.9	14.5	44.9	154.5	5.53	BDL	10.4	19.8
6H-5, 145-150	54.86	16.69	7.61	2.60	27.3	15.8	47.6	157.6	5.38	BDL	11.2	19.4
7H-3, 145-150	62.56	17.37	7.70	2.70	25.5	15.8	45.6	165.3	6.23	BDL	10.5	18.9
8H-3, 140-150	71.96	18.19	7.76	2.63	24.6	16.0	43.5	176.9	6.29	BDL	9.9	17.5
9H-3, 140-150	81.59	19.04	7.45	2.63	24.7	16.9	43.7	186.1	5.82	BDL	9.8	17.0
10H-3, 140-150	92.47	19.64	7.59	2.67	26.0	18.5	45.1	201.0	4.37	BDL	10.1	16.5
11H-3, 140-150	102.47	20.23	7.61	2.73	24.0	18.3	41.8	211.4	3.17	BDL	9.3	16.5
12H-3, 140-150	113.79	20.90	7.59	2.30	25.0	19.4	43.3	220.5	2.74	4.36	10.0	15.5
13H-3, 140-150	125.04	21.56	7.78	2.66	24.0	19.5	41.1	231.1	2.34	8.60	9.4	14.3
14H-3, 140-150	137.26	22.05	7.45	2.29	24.1	20.1	40.8	236.5	2.12	9.92	9.3	14.1
15H-3, 140-150	147.57	22.39	7.44	1.73	23.9	26.4	32.5	342.2	1.61	18.43	8.6	8.9
18H-3, 140-150	167.67	23.06	7.08	1.34	23.1	28.4	29.8	390.2	1.75	14.88	8.2	7.9
19H-3, 140-150	177.17	23.77	7.52	1.24	22.7	28.7	29.2	404.2	1.77	11.74	8.2	8.1

Table S1. Continued

U1336B												
Sample	Depth (rcmd)	Age (Ma)	pH	Alkalinity (mM)	SO_4^{2-} (mM)	Ca^{2+} (mM)	Mg^{2+} (mM)	Sr^{2+} (µM)	Mn^{2+} (µM)	Fe^{2+} (µM)	K^+ (mM)	Li^+ (µM)
20H-3, 140-150	186.67	24.36	7.24	1.01	22.2	28.9	28.4	417.8	1.76	17.08	7.9	8.8

n.d.: not determined; BDL: below detection limit (0.1 µM for Mn^{2+}; 0.6 µM for Fe^{2+}; 0.8 µM for Sr^{2+})

U1337A												
Sample	Depth (rcmd)	Age (Ma)	pH	Alkalinity (mM)	SO_4^{2-} (mM)	Ca^{2+} (mM)	Mg^{2+} (mM)	Sr^{2+} (µM)	Mn^{2+} (µM)	Fe^{2+} (µM)	K^+ (mM)	Li^+ (µM)
2H-2, 145-150	3.14	0.55	7.70	2.82	27.6	10.8	52.5	82.7	114.62	BDL	11.2	27.7
2H-5, 145-150	7.64	0.81	7.64	2.75	28.8	10.3	53.0	79.1	140.28	BDL	10.9	24.7
3H-2, 145-150	13.84	1.17	7.63	2.73	28.8	10.8	52.5	83.4	133.36	1.86	11.2	24.2
3H-5, 145-150	18.34	1.44	7.62	2.72	27.4	11.3	54.1	81.7	122.74	BDL	11.4	23.5
4H-2, 145-150	23.48	1.74	7.69	2.85	29.1	10.8	53.9	83.0	106.29	0.76	11.4	23.4
4H-5, 145-150	27.98	2.01	7.66	2.71	28.7	11.0	53.6	83.7	105.24	BDL	11.4	24.0
5H-2, 145-150	35.65	2.46	7.65	3.76	28.7	10.8	52.5	86.9	106.24	7.28	11.3	23.2
5H-5, 145-150	40.15	2.72	7.65	2.67	28.6	11.1	53.5	85.4	104.09	0.67	11.3	23.2
6H-2, 145-150	46.28	3.08	7.65	2.75	28.7	11.2	53.9	85.3	101.66	BDL	11.4	22.7
6H-5, 145-150	50.78	3.35	7.70	2.71	29.3	10.9	52.5	85.0	96.01	BDL	11.4	22.5
7H-3, 145-150	59.73	3.87	7.68	2.90	28.6	11.3	53.8	87.5	101.65	1.56	11.4	22.9
8H-3, 145-150	70.01	4.39	7.59	2.66	28.4	10.9	52.4	87.1	95.79	BDL	11.2	22.1
9H-3, 145-150	80.76	4.82	7.69	3.01	28.6	11.7	52.5	90.1	96.83	1.28	11.2	21.9
10H-3, 145-150	90.75	5.22	7.58	2.79	27.2	10.7	52.2	87.2	92.72	0.55	10.8	21.0
11H-3, 145-150	101.30	5.64	7.63	2.80	28.3	10.8	52.4	87.9	78.97	1.46	11.0	20.0
12H-3, 145-150	111.54	6.05	7.65	2.87	28.7	11.4	54.0	90.6	69.57	0.86	11.3	20.3
13H-3, 145-150	121.98	6.47	7.57	2.85	27.9	11.5	54.3	89.2	61.12	0.48	11.4	19.6
14H-3, 150-155	133.57	6.93	7.60	2.90	27.6	11.0	52.5	89.9	48.55	BDL	10.8	19.0
15H-3, 145-150	144.78	7.38	7.59	3.08	27.6	11.2	53.2	91.1	38.02	0.96	10.8	18.7
16H-3, 145-150	154.89	7.78	7.57	3.05	27.5	11.4	52.5	93.4	36.74	0.52	10.9	18.2
17H-3, 145-150	165.86	8.22	7.58	3.52	27.1	10.7	52.2	93.1	40.38	BDL	10.4	18.4
18H-3, 147-152	177.26	8.68	7.62	3.07	28.2	12.0	52.5	96.5	42.41	2.78	11.1	17.5
19H-3, 145-150	187.59	9.09	7.62	3.19	27.4	11.5	52.5	98.8	45.17	0.40	10.8	17.5
20H-3, 145-150	197.83	9.50	7.64	3.18	26.9	11.8	53.8	103.0	44.38	0.23	10.9	17.1

Table S1. Continued

U1337A												
Sample	Depth (rcmd)	Age (Ma)	pH	Alkalinity (mM)	SO_4^{2-} (mM)	Ca^{2+} (mM)	Mg^{2+} (mM)	Sr^{2+} (µM)	Mn^{2+} (µM)	Fe^{2+} (µM)	K^+ (mM)	Li^+ (µM)
21H-3, 145-150	207.79	9.90	7.61	3.37	27.7	11.9	53.7	103.7	45.16	BDL	10.7	17.2
23X-3, 145-150	227.63	10.69	7.58	3.21	27.5	11.7	53.4	102.8	33.71	0.77	10.7	17.2
24X-2, 145-150	236.50	11.05	7.58	3.53	27.4	11.1	48.8	108.6	24.93	0.80	9.7	17.3
25X-3, 145-150	248.72	11.54	7.63	3.37	27.8	11.3	52.4	102.1	14.65	1.34	10.4	16.7
26X-3, 145-150	258.03	11.91	7.61	3.26	27.6	11.8	53.8	103.8	8.19	1.15	10.8	16.9
28X-2, 140-150	274.25	12.56	7.49	3.90	25.8	12.1	50.5	183.0	0.77	2.80	10.1	6.3
29X-2, 140-150	291.33	13.24	7.52	3.36	26.5	12.2	50.6	175.7	1.31	1.32	10.5	9.0
30X-4, 140-150	305.16	13.79	7.65	3.55	27.1	12.3	50.5	184.3	0.82	3.96	10.2	8.5
31X-3, 140-150	313.84	14.14	7.55	3.80	26.2	12.5	52.3	178.4	0.58	6.15	10.6	7.0
32X-3, 140-150	323.04	14.51	7.57	2.81	26.6	11.9	49.9	176.1	0.70	2.70	9.9	7.6
33X-3, 140-150	331.75	14.86	7.50	3.77	26.6	12.2	50.5	180.4	0.64	5.36	10.2	6.4
34X-3, 140-150	342.60	14.92	7.53	3.65	26.2	12.9	50.5	170.2	1.85	1.70	10.3	6.9
35X-3, 140-150	351.97	15.42	7.52	3.61	26.7	12.7	52.1	176.1	0.87	3.39	10.3	7.9
36X-3, 140-150	362.19	15.95	7.57	3.80	26.6	12.6	50.3	171.8	1.80	0.10	10.2	7.0
37X-3, 140-150	373.23	16.54	7.58	3.51	27.4	12.7	50.6	189.0	3.05	1.43	10.2	8.7
38X-2, 140-150	382.67	17.03	7.55	3.67	26.9	12.5	50.5	175.5	2.45	BDL	10.0	8.3
39X-3, 140-150	394.18	17.64	7.57	3.49	26.8	12.4	50.6	171.9	2.15	3.17	10.0	8.8
40X-3, 140-150	406.36	18.28	7.56	3.55	26.6	12.1	50.5	157.0	1.69	2.62	9.7	9.7
41X-3, 140-150	416.94	18.84	7.68	2.49	26.6	11.4	50.6	137.7	1.32	0.91	10.4	11.5
42X-3, 140-150	428.92	19.47	n.d.	n.d.	26.5	11.7	51.5	137.4	2.06	1.56	10.1	10.6
43X-3, 140-150	438.34	19.96	7.68	2.98	27.7	12.1	53.8	140.8	1.02	0.22	10.7	13.5
44X-3, 140-150	447.64	20.45	7.59	2.86	26.9	11.1	50.9	127.1	BDL	BDL	10.1	14.2
45X-3, 140-150	458.75	21.04	7.61	3.19	27.1	11.4	52.3	116.4	BDL	BDL	10.1	15.8
46X-3, 140-150	474.72	21.88	7.60	3.27	27.0	11.4	52.9	111.0	BDL	BDL	10.1	16.5
47X-3, 140-150	486.42	22.49	7.60	3.02	26.8	11.2	53.4	102.5	BDL	BDL	10.2	20.8

n.d.: not determined; BDL: below detection limit (0.09 µM for Mn^{2+}; 0.03 µM for Fe^{2+}; 1.0 µM for Sr^{2+})

Table S1. Continued

U1338A												
Sample	Depth (rcmd)	Age (Ma)	pH	Alkalinity (mM)	SO_4^{2-} (mM)	Ca^{2+} (mM)	Mg^{2+} (mM)	Sr^{2+} (µM)	Mn^{2+} (µM)	Fe^{2+} (µM)	K^{+} (mM)	Li^{+} (µM)
1H-1, 145-150	1.49	0.40	7.67	2.81	28.5	11.0	53.5	85.5	74.73	BDL	11.1	25.6
2H-2, 145-150	7.13	0.78	7.57	2.88	28.0	10.7	53.3	103.9	138.53	BDL	11.1	23.6
2H-5, 145-150	11.63	1.08	7.57	3.04	26.6	10.9	53.9	120.1	148.56	BDL	10.9	22.0
3H-2, 145-150	17.38	1.47	7.60	3.23	28.2	10.9	53.4	138.7	136.02	BDL	11.1	20.5
3H-5, 145-150	21.88	1.77	7.50	3.15	25.8	10.9	54.7	142.3	125.78	0.70	11.3	19.0
4H-2, 145-150	28.27	2.20	7.53	3.33	27.2	11.2	54.9	166.2	120.93	1.71	11.8	18.5
4H-5, 145-150	32.77	2.50	7.52	3.38	26.0	11.1	52.9	171.1	102.71	2.12	11.1	17.8
5H-2, 145-150	39.55	2.95	7.59	3.25	25.8	10.5	52.8	193.6	76.31	6.54	11.3	17.3
5H-5, 145-150	44.05	3.26	7.56	3.32	26.6	10.8	54.4	202.5	72.34	6.71	11.6	16.7
6H-2, 145-150	49.21	3.60	7.60	3.38	27.3	10.9	55.5	222.7	63.98	5.07	12.0	16.4
6H-5, 145-150	53.71	3.90	7.56	3.58	26.6	11.1	54.1	233.7	56.91	BDL	11.6	15.8
7H-3, 145-150	60.86	4.38	7.59	3.45	26.5	11.0	54.8	243.6	39.95	2.29	11.8	14.8
8H-3, 145-150	72.23	5.14	7.49	3.63	24.3	10.4	53.3	253.2	20.32	BDL	11.1	13.1
9H-3, 145-150	83.10	5.87	7.53	4.09	28.6	10.7	52.7	285.0	11.33	BDL	10.3	11.9
10H-3, 145-150	93.38	5.63	7.58	3.86	25.8	10.8	53.1	307.5	6.81	BDL	10.7	10.5
11H-3, 145-150	103.93	5.88	7.54	3.74	23.5	10.5	50.7	333.8	4.91	BDL	10.9	10.4
12H-3, 145-150	114.90	6.22	7.55	3.84	24.5	10.0	52.8	311.4	2.67	BDL	10.6	8.4
13H-3, 145-150	125.92	6.56	7.48	3.91	24.9	10.3	51.5	340.5	2.96	BDL	10.5	8.0
14H-3, 145-150	135.93	6.87	7.53	4.06	24.5	10.9	53.1	359.1	2.25	BDL	10.8	7.0
15H-3, 145-150	146.50	7.20	7.51	4.10	23.5	10.5	51.0	356.4	1.78	BDL	10.3	6.4
16H-3, 145-150	157.06	7.53	7.45	4.21	22.5	10.7	50.8	366.2	2.41	BDL	10.7	5.6
17H-3, 145-150	168.18	7.88	7.52	4.08	24.9	10.7	50.6	365.4	4.21	0.67	10.6	5.2
18H-3, 145-150	179.03	8.22	7.53	3.62	24.8	11.2	53.1	380.0	5.86	1.01	11.3	5.1
19H-3, 145-150	189.30	8.54	7.52	3.95	24.6	10.7	52.4	382.8	5.33	BDL	11.3	4.6
20H-3, 145-150	199.44	8.85	7.50	3.85	25.0	11.3	53.7	397.7	7.77	1.10	12.0	4.7
21H-3, 145-150	210.14	9.18	7.52	3.94	25.1	11.3	50.7	389.5	9.76	0.43	11.6	4.2
22H-3, 145-150	221.05	9.52	7.61	3.90	25.7	11.8	53.4	401.1	13.35	4.26	11.9	4.3
23H-3, 145-150	231.84	9.86	7.56	4.09	24.4	11.8	53.4	390.2	12.56	3.73	11.7	3.6

TableS1. Continued

U1338A												
Sample	Depth (rcmd)	Age (Ma)	pH	Alkalinity (mM)	SO_4^{2-} (mM)	Ca^{2+} (mM)	Mg^{2+} (mM)	Sr^{2+} (µM)	Mn^{2+} (µM)	Fe^{2+} (µM)	K^+ (mM)	Li^+ (µM)
24H-3, 145-150	242.98	10.21	7.49	3.96	24.1	11.3	52.8	374.2	13.41	12.36	11.0	3.8
25H-3, 146-151	253.46	10.53	7.49	3.63	25.2	11.1	53.1	347.1	10.20	3.36	11.2	3.2
26H-3, 145-150	263.43	10.84	7.53	3.64	25.0	11.3	53.2	374.6	9.18	BDL	11.5	3.5
27X-3, 140-150	272.73	11.13	7.58	4.10	24.6	11.5	53.1	325.0	5.85	2.32	11.1	3.0
29X-3, 140-150	293.31	11.78	7.62	3.80	25.5	11.6	53.2	316.0	2.78	0.90	11.0	4.2
32X-3, 140-150	325.57	12.78	7.43	4.05	24.7	12.2	53.2	192.6	1.91	5.98	10.5	3.4
33X-3, 140-150	336.42	13.12	7.50	3.35	27.3	12.0	53.2	186.1	2.14	6.25	10.6	5.5
34X-3, 140-150	347.53	13.46	7.44	3.93	25.5	11.8	53.1	174.0	2.53	1.77	10.3	4.0
38X-3, 140-150	380.93	14.50	7.64	3.19	26.6	11.4	53.2	147.6	1.64	0.92	10.6	8.8
39X-3, 140-150	390.81	14.81	7.59	3.22	25.3	11.1	52.1	137.9	1.85	BDL	10.5	9.2
41X-3, 140-150	425.92	15.91	7.58	3.22	25.4	11.6	55.8	122.5	1.19	BDL	10.6	12.8
42X-3, 140-150	435.12	16.19	7.54	3.87	27.1	12.1	55.6	107.8	0.37	BDL	10.4	15.7
44X-3, 140-150	451.56	16.70	7.63	2.91	25.5	11.2	54.8	88.9	0.53	BDL	10.1	24.9
U1338B												
32H-3, 145-150	316.47	12.50	7.50	4.13	28.2	12.6	50.9	204.4	1.47	BDL	10.6	3.3
36H-3, 140-150	359.44	13.84	7.49	4.02	25.2	n.d.	n.d.	183.3	2.25	1.72	n.d.	4.4

n.d.: not determined; BDL: below detection limit (0.02 µM for Fe^{2+})

Table S1. Continued. Pore water data from squeezed whole-round samples from ODP Site 1218A, compiled from Lyle et al. (2002).

1218A										
Sample	Depth (mcd)	pH	Alkalinity (mM)	SO_4^{2-} (mM)	Ca^{2+} (mM)	Mg^{2+} (mM)	Sr^{2+} (µM)	Mn^{2+} (µM)	K^{+} (mM)	Li^{+} (µM)
1H-4, 145-150	9.03	7.27	2.80	30.1	10.7	53.8	88.0	31.0	12.4	27.0
2H-3, 145-150	16.42	7.20	3.18	31.8	11.4	53.7	90.0	38.0	12.7	26.0
3H-3, 145-150	26.91	7.20	3.30	31.1	10.8	52.7	88.0	21.0	12.4	26.0
4H-3, 145-150	37.39	7.27	3.63	28.4	11.7	53.2	93.0	6.8	12.1	25.0
5H-3, 145-150	47.87	7.27	3.54	28.4	11.5	52.8	95.0	1.3	12.0	26.0
6H-3, 145-150	58.36	7.26	3.62	28.9	11.6	53.2	98.0	0.9	11.5	25.0
10H-3, 145-150	100.29	7.15	3.48	27.4	12.4	52.7	108.0	3.2	11.5	24.0
13H-3, 145-150	131.74	7.10	3.89	27.7	11.9	52.8	108.0	7.7	11.2	23.0
15H-3, 145-150	152.71	7.13	3.75	26.3	13.8	50.2	111.0	5.3	11.4	24.0
18H-3, 145-150	184.16	7.14	3.85	27.5	14.1	49.9	117.0	3.3	11.1	24.0
22X-3, 145-150	223.56	7.17	3.80	26.5	14.7	49.5	119.0	3.3	11.0	24.0
25X-3, 145-150	255.34	7.16	3.65	29.3	15.0	49.3	119.0	1.7	10.7	24.0
28X-3, 145-150	287.12	7.23	3.41	28.2	16.0	50.2	116.0	2.0	10.5	25.0
30X-2, 145-150	304.45	7.32	2.26	27.1	13.9	49.2	92.0	1.7	9.8	33.0

Table S1. Continued. Pore water data from squeezed whole-round samples from ODP Sites 804 and 807, compiled from Kroenke et al. (1991).

804B										
Sample	Depth (mbsf)	pH	Alkalinity (mM)	SO_4^{2-} (mM)	Ca^{2+} (mM)	Mg^{2+} (mM)	Sr^{2+} (µM)	Mn^{2+} (µM)	K^+ (mM)	Li^+ (µM)
1H-2, 145-150	2.95	7.5	3.53	27.7	10.7	51.4	108	21	10.5	25.9
2H-4, 145-150	10.65	7.4	4.55	27.4	11.2	51.7	158	12	10.6	21.8
3H-4, 145-150	20.15	7.4	3.77	28.0	11.6	51.6	201	4	11.2	20.9
4H-4, 145-150	29.65	7.8	3.53	27.7	11.9	50.8	242	BDL	11.2	20.9
5H-4, 145-150	39.15	7.6	3.54	27.2	12.2	50.2	272	BDL	11.1	20.4
6H-4, 145-150	48.65	7.6	3.64	26.4	12.5	49.8	300	BDL	10.9	19.5
9H-4, 145-150	77.15	7.8	3.77	26.5	13.5	48.8	392	BDL	10.6	17.2
12H-4, 145-150	105.65	7.6	3.75	25.7	14.7	47.5	460	BDL	11.9	15.9
15H-4, 145-150	134.15	7.6	3.56	25.1	15.8	46.1	514	BDL	10.8	15.0
804C										
18X-2, 145-150	161.25	7.6	3.39	25.7	16.2	45.8	521	BDL	9.91	15.9
21X-1, 145-150	188.85	n.d.	n.d.	25.3	17.7	43.8	577	n.d.	9.89	15.9
24X-1, 140-150	217.90	7.9	3.76	24.9	18.5	43.6	573	7	9.40	18.7
27X-2, 0-10	246.90	7.8	4.28	26.6	19.9	42.1	608	3	9.63	18.3
30X-3, 140-150	278.80	7.6	3.74	24.8	21.3	42.1	608	BDL	9.72	18.3
33X-3, 140-150	307.49	7.6	3.64	25.4	22.4	41.8	621	n.d.	8.70	18.3

n.d.: not determined; BDL: below detection limit

807A										
Sample	Depth (mbsf)	pH	Alkalinity (mM)	SO_4^{2-} (mM)	Ca^{2+} (mM)	Mg^{2+} (mM)	Sr^{2+} (µM)	Mn^{2+} (µM)	K^+ (mM)	Li^+ (µM)
1H-3, 145-150	4.45	7.5	3.51	27.4	10.6	52.3	130	13	10.8	24.2
2H-4, 145-150	13.35	7.5	3.64	27.4	10.9	52.3	208	4	11.4	21.0
3H-4, 145-150	22.85	7.5	4.17	27.5	11.3	51.8	284	BDL	11.2	20.1
4H-4, 145-150	32.35	7.6	4.04	26.7	11.3	51.4	356	BDL	11.4	19.6
5H-4, 145-150	41.85	7.6	4.16	26.4	11.4	50.9	425	BDL	11.4	18.2
6H-4, 145-150	51.35	7.6	4.29	26.1	11.7	50.6	476	BDL	11.3	17.3
9H-4, 145-150	79.85	7.6	4.69	26.0	12.2	48.6	619	BDL	11.4	15.5
12H-4, 145-150	108.35	7.2	5.08	25.0	12.7	47.6	753	BDL	11.0	13.2

Table S1. Continued

807A										
Sample	Depth (mbsf)	pH	Alkalinity (mM)	SO_4^{2-} (mM)	Ca^{2+} (mM)	Mg^{2+} (mM)	Sr^{2+} (µM)	Mn^{2+} (µM)	K^+ (mM)	Li^+ (µM)
15H-5, 145-150	137.10	7.2	5.36	23.6	13.3	46.9	840	BDL	10.7	12.3
18H-4, 145-150	165.35	7.6	5.63	22.9	13.9	45.7	904	BDL	10.9	11.4
21H-4, 145-150	193.85	7.6	5.78	22.6	14.6	44.4	927	BDL	10.9	11.4
24H-4, 145-150	222.35	7.6	5.97	22.2	15.0	43.6	905	BDL	10.7	11.3
27H-4, 145-150	250.85	7.8	5.92	22.5	15.5	43.2	896	BDL	10.9	11.3
30X-4, 140-150	279.70	7.1	5.8	22.0	15.8	42.2	896	BDL	10.8	12.2
33X-3, 140-150	306.70	7.1	6.23	21.8	16.4	41.8	907	BDL	10.7	13.6
36X-3, 140-150	335.30	7.1	6.32	21.6	16.8	41.6	899	BDL	10.5	14.9
39X-2, 140-150	362.80	7.6	5.73	21.4	17.2	41.1	907	BDL	10.5	15.8
42X-4, 140-150	395.10	7.6	5.26	21.4	17.6	40.3	896	BDL	10.4	18.3
45X-5, 140-150	425.70	7.1	5.24	21.9	18.0	40.3	876	BDL	10.4	19.4
48X-3, 140-150	451.50	7.6	n.d.	21.5	18.4	40.0	900	BDL	10.3	19.9
51X-3, 140-150	480.50	7.6	5.01	21.8	19.0	39.4	896	BDL	10.3	17.6
54X-4, 0-10	509.60	7.5	5.05	21.4	19.0	39.6	878	BDL	10.2	16.2
57X-4, 140-150	539.60	7.7	4.25	21.6	19.3	40.0	860	BDL	10.1	15.3
60X-4, 140-150	568.50	7.1	5.30	21.8	19.5	39.2	874	BDL	9.96	14.0
63X-4, 0-10	596.10	7.2	5.01	21.1	19.7	39.0	836	BDL	9.95	15.3
66X-2, 140-150	623.50	7.6	4.85	21.4	19.6	39.5	800	BDL	9.82	15.3
70X-4, 140-150	665.10	7.6	4.36	21.0	19.9	39.3	817	BDL	9.70	13.5
72X-2, 140-150	681.10	7.6	3.94	21.0	20.2	38.8	862	BDL	9.85	12.1
75X-4, 140-150	713.10	n.d.	n.d.	21.2	20.5	38.5	853	BDL	9.81	11.7
78X-2, 0-10	737.70	n.d.	n.d.	21.2	20.8	38.2	866	n.d.	9.62	12.1
82X-3, 140-150	778.90	7.6	4	21.5	21.2	38.9	865	BDL	9.35	11.7

n.d.: not determined; BDL: below detection limit

Table S2. Element/Ca ratios and porosity of analysed bulk carbonate leachates.

U1334A									
Sample	Depth (rmcd)	Age (Ma)	Mg/Ca (mmol/mol)	Sr/Ca (mmol/mol)	Mn/Ca (mmol/mol)	Ba/Ca (mmol/mol)	Fe/Ca (µmol/mol)	Porosity (%)	$CaCO_3$ (wt %)
3H-2, 145-150	22.62	13.10	30.19	2.671	0.317	5.230	36.68	86.77	27.6
7H-3, 140-150	67.52	20.79	3.029	1.846	0.159	0.847	35.18	63.22	76.7
11H-3, 140-150	111.02	23.21	1.988	2.117	1.158	1.956	22.82	62.80	79.3
14H-3, 140-150	143.53	25.02	1.957	1.989	2.117	1.275	29.52	66.50	82.2
17H-3, 140-150	178.32	26.96	2.561	2.111	1.203	1.098	n.d.	67.05	90.5
20H-3, 140-150	224.06	29.50	2.254	1.933	0.604	1.089	38.08	47.43	85.9
22H-3, 140-150	245.06	30.67	1.791	1.957	1.368	1.030	21.95	53.65	88.2
26X-3, 140-150	287.64	32.88	2.712	1.884	0.774	1.544	26.79	65.05	79.6
30X-3, 140-150	330.64	37.04	8.022	1.849	0.014	2.295	38.09	70.86	71.7

U1335A									
Sample	Depth (mcd)	Age (Ma)	Mg/Ca (mmol/mol)	Sr/Ca (mmol/mol)	Mn/Ca (mmol/mol)	Ba/Ca (mmol/mol)	Fe/Ca (µmol/mol)	Porosity (%)	$CaCO_3$ (wt %)
1H-2, 145-150	3.09	1.23	4.149	1.813	0.392	2.209	10.33	82.39	58.8
1H-4, 145-150	6.09	1.64	6.186	1.849	0.470	2.445	14.57	82.19	69.9
2H-2, 145-150	12.86	2.58	4.543	1.616	0.377	2.732	11.09	81.43	62.0
3H-2, 145-150	22.66	3.94	10.90	1.936	0.477	5.026	14.17	87.70	41.2
3H-5, 145-150	27.16	4.56	8.662	1.913	1.266	2.928	15.56	83.91	42.3
4H-2, 145-150	33.89	5.50	12.58	2.338	0.946	6.899	17.35	76.67	22.5
5H-2, 145-150	45.52	7.11	2.689	1.792	3.063	0.598	17.85	73.94	87.8
6H-5, 145-150	60.34	9.17	2.675	1.754	3.058	0.953	15.98	73.58	83.8
8H-3, 140-150	79.49	11.21	1.713	2.159	0.956	0.623	14.08	67.26	89.4
9H-3, 145-150	88.67	11.65	2.362	2.152	0.561	1.380	14.38	68.72	86.2
10H-3, 145-150	100.40	12.21	1.877	1.856	0.486	0.731	9.61	67.76	91.2
13H-3, 140-150	131.04	13.68	3.033	1.792	0.967	1.069	15.08	68.72	86.9
14H-3, 140-150	142.60	14.24	2.567	1.927	0.947	1.202	13.19	68.32	84.1
22H-3, 140-150	229.28	18.40	2.810	1.938	1.526	1.190	n.d.	67.46	79.5
27H-3, 140-150	287.74	19.85	2.905	1.883	0.692	1.033	26.80	61.23	90.2
30H-3, 140-150	319.86	20.79	2.690	1.746	0.491	0.826	21.72	59.21	93.3
39X-3, 140-150	417.10	23.63	2.343	1.955	0.355	1.180	14.79	58.40	89.7
43X-3, 140-150	455.20	24.74	2.781	1.838	1.110	0.981	14.92	58.00	89.9
44X-3, 140-150	464.80	25.02	3.345	1.949	0.316	1.174	14.36	59.87	84.2
U1335B									
37H-2, 140-150	392.95	22.92	2.497	1.911	0.518	1.016	n.d.	60.68	n.d.

Table S2. Continued

U1336B									
Sample	Depth (rmcd)	Age (Ma)	Mg/Ca (mmol/mol)	Sr/Ca (mmol/mol)	Mn/Ca (mmol/mol)	Ba/Ca (mmol/mol)	Fe/Ca (µmol/mol)	Porosity (%)	$CaCO_3$ (wt %)
2H-2, 145-150	5.28	12.34	2.959	1.561	0.661	0.640	32.13	62.09	94.4
2H-5, 145-150	9.78	12.73	2.693	1.723	0.779	0.797	13.72	65.14	74.6
3H-2, 145-150	16.81	13.35	2.677	1.831	1.275	1.602	20.76	67.80	91.1
3H-5, 145-150	21.31	13.75	3.039	1.883	1.220	1.836	24.94	69.24	86.0
4H-2, 145-150	28.01	14.33	2.782	1.775	0.686	1.448	31.93	69.99	89.5
4H-5, 145-150	32.51	14.73	4.261	1.779	0.790	1.618	39.99	70.52	90.7
5H-2, 145-150	38.91	15.29	3.427	1.297	0.890	0.932	36.24	72.31	84.6
5H-5, 145-150	43.41	15.69	3.210	1.435	0.861	0.901	34.39	71.40	79.8
6H-2, 145-150	50.36	16.30	3.162	1.473	1.007	1.158	18.05	68.01	88.6
6H-5, 145-150	54.86	16.69	5.392	2.187	0.619	2.316	n.d.	74.72	80.6
7H-3, 145-150	62.56	17.37	3.076	1.826	0.462	2.017	35.56	72.07	85.4
8H-3, 140-150	71.96	18.19	2.594	1.593	0.529	1.845	23.85	67.14	77.7
9H-3, 140-150	81.59	19.04	2.751	1.420	1.012	1.024	22.33	62.65	86.7
10H-3, 140-150	92.47	19.64	2.388	1.376	1.210	0.847	21.17	61.05	90.5
11H-3, 140-150	102.47	20.23	2.546	1.822	1.028	1.490	37.35	64.11	91.9
12H-3, 140-150	113.79	20.90	1.860	1.508	1.094	1.100	26.72	61.45	88.0
13H-3, 140-150	125.04	21.56	1.691	1.394	1.105	0.895	35.67	59.43	94.0
14H-3, 140-150	137.26	22.05	1.925	1.345	1.169	0.715	43.42	55.75	87.1
15H-3, 140-150	147.57	22.39	1.553	1.341	1.235	1.018	34.07	60.21	92.9
18H-3, 140-150	167.67	23.06	1.472	1.301	0.975	1.423	24.69	57.91	90.4
19H-3, 140-150	177.17	23.77	1.514	1.225	1.091	1.534	24.22	60.37	84.9
20H-3, 140-150	186.67	24.36	1.351	1.562	0.881	1.519	24.04	58.45	89.5

U1337A									
Sample	Depth (rmcd)	Age (Ma)	Mg/Ca (mmol/mol)	Sr/Ca (mmol/mol)	Mn/Ca (mmol/mol)	Ba/Ca (mmol/mol)	Fe/Ca (µmol/mol)	Porosity (%)	$CaCO_3$ (wt %)
2H-5, 145-150	7.64	0.81	15.68	1.996	2.029	5.836	9.95	84.58	26.6
3H-5, 145-150	18.34	1.44	4.519	1.882	2.245	2.229	14.76	84.97	47.9
5H-2, 145-150	35.65	2.46	10.00	1.741	4.103	3.486	13.41	84.15	54.9
8H-3, 145-150	70.01	4.39	12.30	1.824	10.81	4.344	16.40	85.77	30.4
10H-3, 145-150	90.75	5.22	7.457	2.155	11.07	2.324	22.38	77.41	67.9
11H-3, 145-150	101.3	5.64	15.15	2.303	9.322	5.531	18.19	78.44	51.5
15H-3, 145-150	144.78	7.38	3.062	2.218	5.100	2.016	12.79	80.29	62.5
20H-3, 145-150	197.83	9.50	11.69	2.822	14.11	4.825	19.92	80.82	36.2

Table S2. Continued

U1337A									
Sample	Depth (rmcd)	Age (Ma)	Mg/Ca (mmol/mol)	Sr/Ca (mmol/mol)	Mn/Ca (mmol/mol)	Ba/Ca (mmol/mol)	Fe/Ca (µmol/mol)	Porosity (%)	$CaCO_3$ (wt %)
24X-2, 145-150	236.5	11.05	1.291	2.519	2.296	0.800	18.68	75.72	n.d.
26X-3, 145-150	258.03	11.91	2.522	2.134	1.536	1.382	13.58	67.91	70.1
28X-2, 140-150	274.25	12.56	2.260	1.921	1.458	0.780	13.54	65.89	86.6
30X-4, 140-150	305.16	13.79	2.796	2.179	1.295	1.163	15.18	69.81	83.6
36X-3, 140-150	362.19	15.95	3.219	1.886	2.209	1.227	18.38	67.68	85.2
44X-3, 140-150	447.64	20.45	2.559	2.067	1.122	1.174	16.75	59.22	90.1
46X-3, 140-150	474.72	21.88	3.123	1.642	0.729	1.120	14.42	57.19	93.5

U1338A									
Sample	Depth (rmcd)	Age (Ma)	Mg/Ca (mmol/mol)	Sr/Ca (mmol/mol)	Mn/Ca (mmol/mol)	Ba/Ca (mmol/mol)	Fe/Ca (µmol/mol)	Porosity (%)	$CaCO_3$ (wt %)
1H-1, 145-150	1.49	0.40	4.078	1.751	0.933	1.902	17.30	85.50	59.8
4H-2, 145-150	28.27	2.20	4.242	2.223	2.901	1.549	13.69	80.72	58.4
6H-2, 145-150	49.21	3.60	11.69	2.098	3.219	2.340	15.21	84.37	34.1
8H-3, 145-150	72.23	5.14	0.997	2.335	3.968	0.678	11.28	63.67	74.5
10H-3, 145-150	93.38	5.63	2.047	2.275	2.638	0.815	16.34	73.73	77.8
12H-3, 145-150	114.9	6.22	2.527	2.068	2.275	0.573	18.53	67.22	77.5
14H-3, 145-150	135.93	6.87	1.620	2.192	1.591	0.964	11.82	75.82	57.4
16H-3, 145-150	157.06	7.53	1.957	2.150	1.843	0.655	15.21	66.68	70.4
18H-3, 145-150	179.03	8.22	2.690	2.114	2.752	1.275	11.23	72.50	59.0
20H-3, 145-150	199.44	8.85	5.336	2.347	2.391	2.218	14.07	78.07	66.3
22H-3, 145-150	221.05	9.52	32.18	2.959	2.313	4.997	28.42	76.76	48.8
24H-3, 145-150	242.98	10.21	3.561	2.664	3.542	1.981	15.47	75.77	52.2
26H-3, 145-150	263.43	10.84	1.392	2.425	3.462	1.591	11.63	68.38	63.0
44X-3, 140-150	451.56	16.70	3.994	1.662	1.156	1.380	11.77	n.d.	84.6
U1338B									
36H-3, 140-150	359.44	13.84	1.830	2.259	2.646	0.815	13.77	65.20	77.9
STDEV (2σ)			**0.2355**	**0.0417**	**0.1452**	**0.0417**	**2.232**		

n.d.: not determined

Table S3. $^{87}Sr/^{86}Sr$ ratios of analysed pore waters and bulk carbonate leachates.

U1334A			Pore water	Bulk carbonate
Sample	Depth (rmcd)	Age (Ma)	$^{87}Sr/^{86}Sr$	$^{87}Sr/^{86}Sr$
1H-4, 145-150	5.95	9.36	0.709145	n.d.
3H-2, 145-150	22.62	13.10	0.709066	0.708846
7H-3, 140-150	67.52	20.79	0.708927	0.708361
11H-3, 140-150	111.02	23.21	0.708838	0.708232
14H-3, 140-150	143.53	25.02	n.d.	0.708111
17H-3, 140-150	178.32	26.96	0.708699	0.708051
20H-3, 140-150	224.06	29.50	n.d.	0.707972
22H-3, 140-150	245.06	30.67	0.708719	0.707957
26X-3, 140-150	287.64	32.88	n.d.	0.707847
30X-3, 140-150	330.64	37.04	0.709048	0.708084

U1335A			Pore water	Bulk carbonate
Sample	Depth (rmcd)	Age (Ma)	$^{87}Sr/^{86}Sr$	$^{87}Sr/^{86}Sr$
1H-2, 145-150	3.09	1.23	n.d.	0.709149
1H-4, 145-150	6.09	1.64	0.709144	0.709133
2H-2, 145-150	12.86	2.58	n.d.	0.709097
3H-2, 145-150	22.66	3.94	n.d.	0.709030
3H-5, 145-150	27.16	4.56	0.709051	0.709040
4H-2, 145-150	33.89	5.50	n.d.	0.708991
5H-2, 145-150	45.52	7.11	n.d.	0.709046
6H-5, 145-150	60.34	9.17	0.708967	0.709069
8H-3, 140-150	79.49	11.21	0.708937	0.708954
10H-3, 145-150	100.40	12.21	n.d.	0.708833
13H-3, 140-150	131.04	13.68	n.d.	0.708997
14H-3, 140-150	142.60	14.24	0.708856	0.708958
22H-3, 140-150	229.28	18.40	0.708767	0.708535
27H-3, 140-150	287.74	19.85	0.708701	0.708550
30H-3, 140-150	319.86	20.79	0.708701	0.708457
39X-3, 140-150	417.10	23.63	0.708688	0.708394
43X-3, 140-150	455.20	24.74	0.708790	0.708227
44X-3, 140-150	464.80	25.02	0.708883	0.708253
U1335B				
37H-2, 140-150	392.95	22.92	0.708670	0.708400

U1336B			Pore water	Bulk carbonate
Sample	Depth (rmcd)	Age (Ma)	$^{87}Sr/^{86}Sr$	$^{87}Sr/^{86}Sr$
2H-2, 145-150	5.28	12.34	n.d.	0.708835
2H-5, 145-150	9.78	12.73	0.708957	0.708832
3H-2, 145-150	16.81	13.35	n.d.	0.708829
3H-5, 145-150	21.31	13.75	n.d.	0.708824
4H-2, 145-150	28.01	14.33	n.d.	0.708798

Table S3. Continued

U1336B			Pore water	Bulk carbonate
Sample	Depth (rmcd)	Age (Ma)	$^{87}Sr/^{86}Sr$	$^{87}Sr/^{86}Sr$
4H-5, 145-150	32.51	14.73	0.708678	0.708785
5H-2, 145-150	38.91	15.29	n.d.	0.708756
5H-5, 145-150	43.41	15.69	n.d.	0.708728
6H-2, 145-150	50.36	16.30	0.708551	0.708722
6H-5, 145-150	54.86	16.69	0.708536	0.708684
7H-3, 145-150	62.56	17.37	n.d.	0.708628
8H-3, 140-150	71.96	18.19	0.708468	0.708531
9H-3, 140-150	81.59	19.04	n.d.	0.708494
10H-3, 140-150	92.47	19.64	0.708387	0.708452
11H-3, 140-150	102.47	20.23	n.d.	0.708357
12H-3, 140-150	113.79	20.90	0.708319	0.708315
13H-3, 140-150	125.04	21.56	0.708308	0.708303
14H-3, 140-150	137.26	22.05	n.d.	0.708286
15H-3, 140-150	147.57	22.39	0.708146	0.708262
18H-3, 140-150	167.67	23.06	n.d.	0.708193
19H-3, 140-150	177.17	23.77	n.d.	0.708171
20H-3, 140-150	186.67	24.36	0.708099	0.708134

U1337A			Pore water	Bulk carbonate
Sample	Depth (rmcd)	Age (Ma)	$^{87}Sr/^{86}Sr$	$^{87}Sr/^{86}Sr$
2H-5, 145-150	7.64	0.81	0.709164	0.709166
3H-5, 145-150	18.34	1.44	n.d.	0.709115
5H-2, 145-150	35.65	2.46	n.d.	0.709111
8H-3, 145-150	70.01	4.39	n.d.	0.709044
10H-3, 145-150	90.75	5.22	0.709113	0.709033
11H-3, 145-150	101.3	5.64	n.d.	0.709007
15H-3, 145-150	144.78	7.38	n.d.	0.708934
20H-3, 145-150	197.83	9.50	0.709072	0.708902
24X-2, 145-150	236.5	11.05	0.709040	0.708868
26X-3, 145-150	258.03	11.91	0.709039	0.708838
28X-2,140-150	274.25	12.56	0.708844	0.708839
30X-4, 140-150	305.16	13.79	0.708811	0.708837
36X-3, 140-150	362.19	15.95	n.d.	0.708718
37X-3, 140-150	373.23	16.54	0.708832	n.d.
44X-3, 140-150	447.64	20.45	0.708848	0.708403
46X-3, 140-150	474.72	21.88	0.708908	0.708371

U1338A			Pore water	Bulk carbonate
Sample	Depth (rmcd)	Age (Ma)	$^{87}Sr/^{86}Sr$	$^{87}Sr/^{86}Sr$
1H-1, 145-150	1.49	0.403570	0.709158	0.709165
4H-2, 145-150	28.27	2.198365	0.709059	0.709082

Table S3. Continued

U1338A			Pore water	Bulk carbonate
Sample	Depth (rmcd)	Age (Ma)	$^{87}Sr/^{86}Sr$	$^{87}Sr/^{86}Sr$
6H-2, 145-150	49.21	3.601764	0.709032	0.709043
8H-3, 145-150	72.23	5.144565	0.708998	0.709048
10H-3, 145-150	93.38	5.627076	0.708979	0.709010
12H-3, 145-150	114.9	6.217975	0.708975	0.708976
14H-3, 145-150	135.93	6.873060	0.708957	0.708959
16H-3, 145-150	157.06	7.531259	0.708954	0.708937
18H-3, 145-150	179.03	8.215625	0.708936	0.708953
20H-3, 145-150	199.44	8.851396	0.708958	0.708934
22H-3, 145-150	221.05	9.524548	0.708950	0.708915
24H-3, 145-150	242.98	10.207667	0.708941	0.708899
26H-3, 145-150	263.43	10.844685	0.708908	0.708888
44X-3, 140-150	451.56	16.70	0.709092	0.708645
U1338B				
36H-3, 140-150	359.44	13.84	0.708956	0.708829

			$^{87}Sr/^{86}Sr$	
IAPSO seawater			0.709171 ± 0.000023	

n.d.: not determined

Table S4. Model variables and output from the 1-D sediment diagenesis model for Sites U1336 and U1338. See text for further details.

	Site U1336	Site U1338
Recrystallisation:		
λ (Myr^{-1})	0.00725	0.00250
β (Myr^{-1})	0.045	0.060
γ (m)	30	80
Boundary conditions:		
$Sr^{2+}_{sed\text{-}init}$ (molal)	0.016	0.021
$Sr^{2+}_{seawater}$ (µM)	92	92
Partition coefficients		
$K_{Sr/Ca}$	0.015	0.015
% Recrystallised	37	21

Table S5. Coefficients for the rate of recrystallisation as a function of depth.

Recrystallisation constants	IODP Site U1336B	IODP Site U1338A	ODP Site 807A	DSDP Site 590B
λ (Myr^{-1})	0.00725	0.00250	0.00100	0.01100
β (Myr^{-1})	0.045	0.060	0.090	0.140
γ (m)	30	80	140	50

Recrystallisation constants for ODP Site 807A are from Higgins and Schrag (2012) and for DSDP Site 590B from Richter and DePaolo (1987).

Table S6. Data for sample U1336B 20H3 used for mass balance calculation.

Pore water	Sr concentration (µM)	417.8
	Sr content (ppm)[a]	36.61
	$\delta^{88/86}$Sr (‰)	0.700
Bulk carbonate	Sr content (ppm)[b]	1223
	Ca content (ppm)	358000
	Sr/Ca ratio (mmol/mol)	1.562

[a] The Sr content (ppm) of the pore water was calculated from the Sr concentration reported from Pälike et al. (2010).

[b] The Sr content (ppm) of the bulk carbonate was calculated from the Sr/Ca ratio and the Ca content from this sample. The Ca content was estimated from the $CaCO_3$ content given by Pälike et al. (2010).

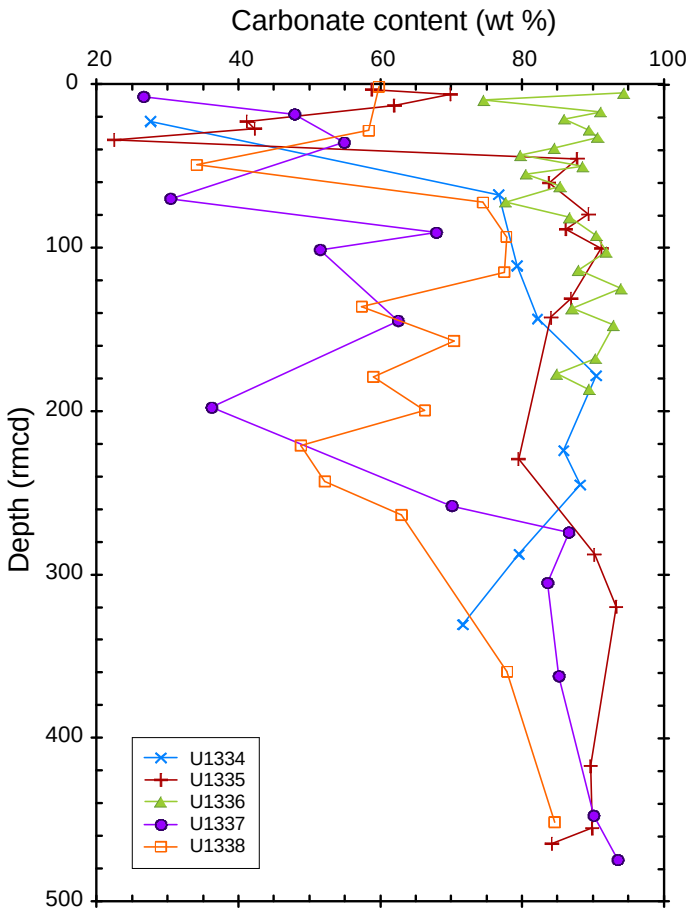

Figure S1. $CaCO_3$ content of the bulk carbonates shown in Figure 5 from the PEAT sites plotted against revised metres composite depth (rmcd) (Pälike et al., 2010; Westerhold et al., 2012; Wilkens et al., 2013).

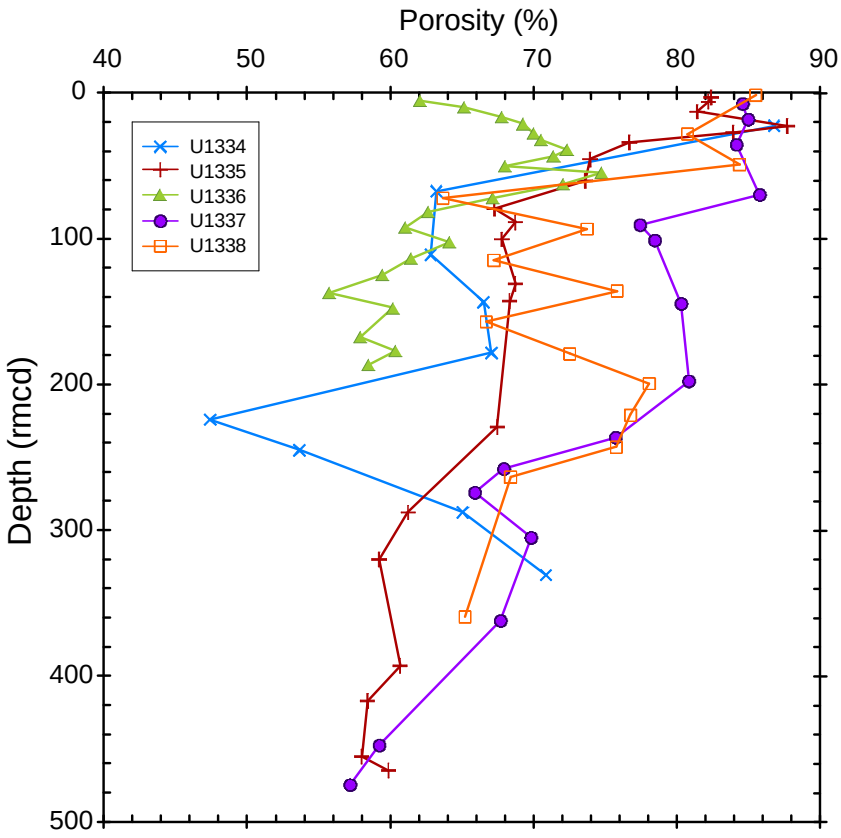

Figure S2. Porosity data from the PEAT sites plotted against revised metres composite depth (rmcd) (Pälike et al., 2010; Westerhold et al., 2012; Wilkens et al., 2013).

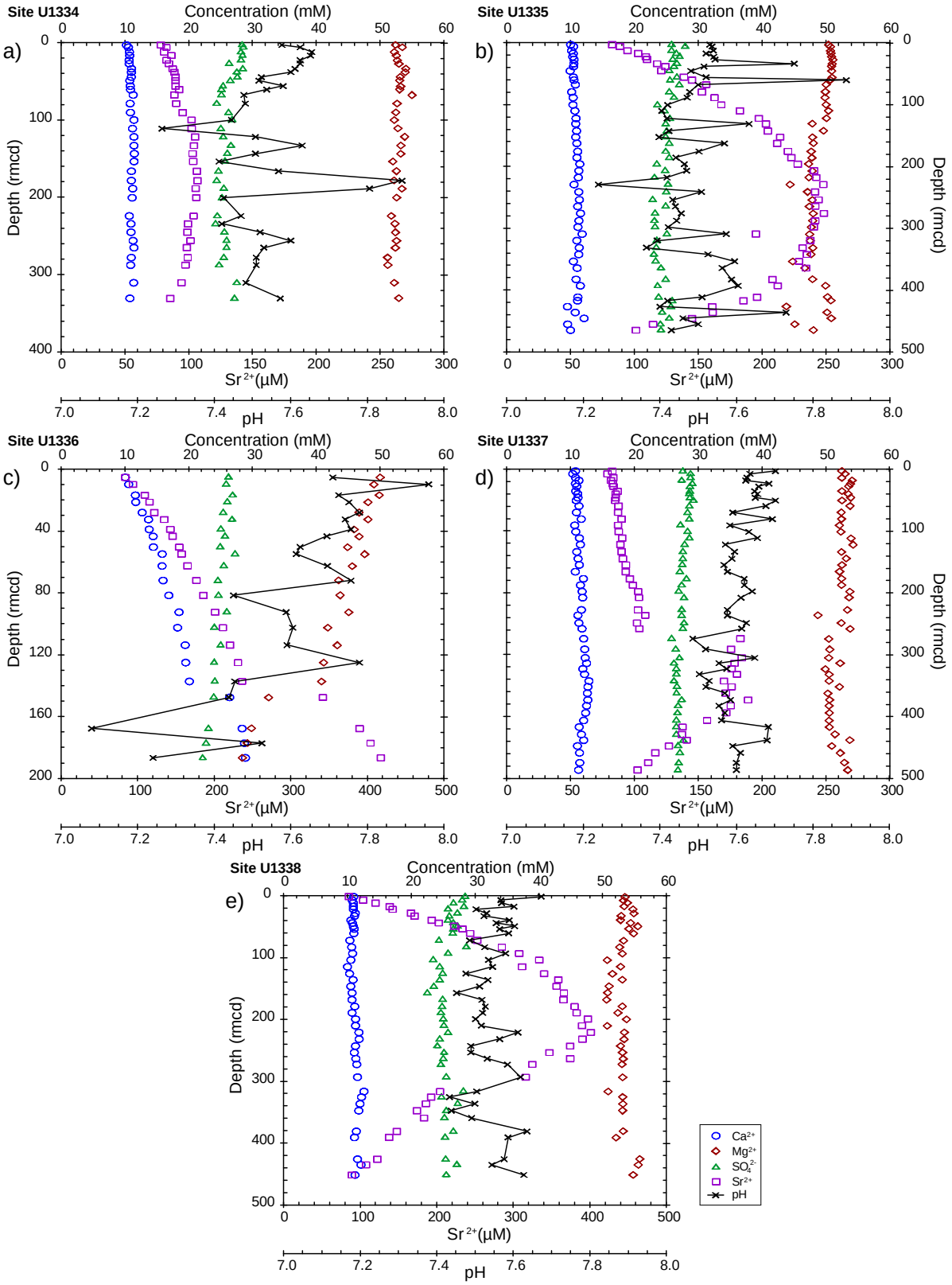

Figure S3. Pore water Ca^{2+} (open blue circles), Mg^{2+} (open red diamonds), Sr^{2+} (open purple squares), SO_4^{2-} (open green triangles) and pH (black crosses) of the PEAT sites investigated plotted against depth given in rmcd. Data are from Pälike et al. (2010). Revised composite depths are from Westerhold et al. (2012) and Wilkens et al. (2013). Please note the different scales for depth and Sr^{2+}.

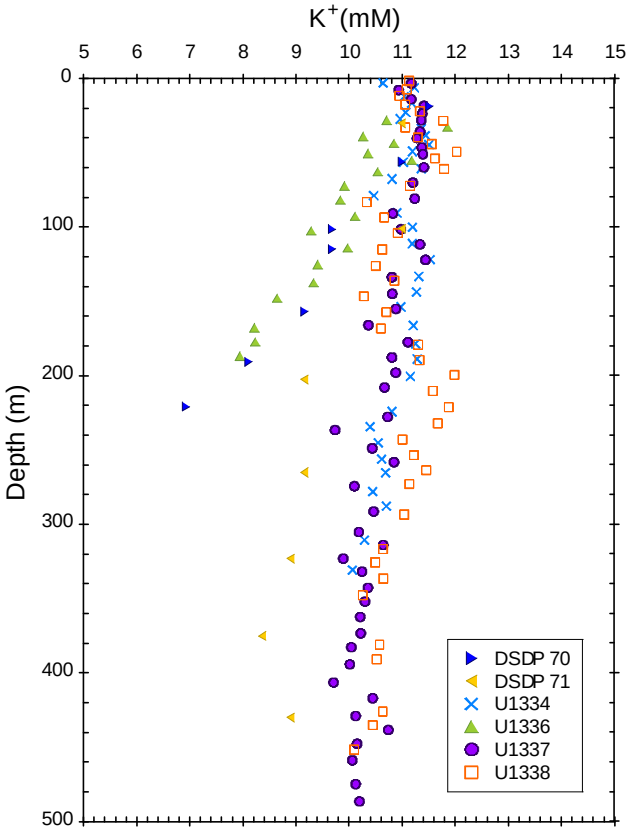

Figure S4. Pore water K^+ profiles plotted against depth illustrating reaction with the basement. Data for DSDP Sites 70 (blue triangles) and 71 (yellow triangles) are from Tracey et al. (1971) and data for the PEAT Sites U1334 (blue crosses), U1336 (green triangles), U1337 (purple circles) and U1338 (orange open squares) are from Pälike et al. (2010). Depths for PEAT sites are given in rmcd from Westerhold et al. (2012) and Wilkens et al. (2013). Depth scale for DSDP Sites 70 and 71 is mbsf.

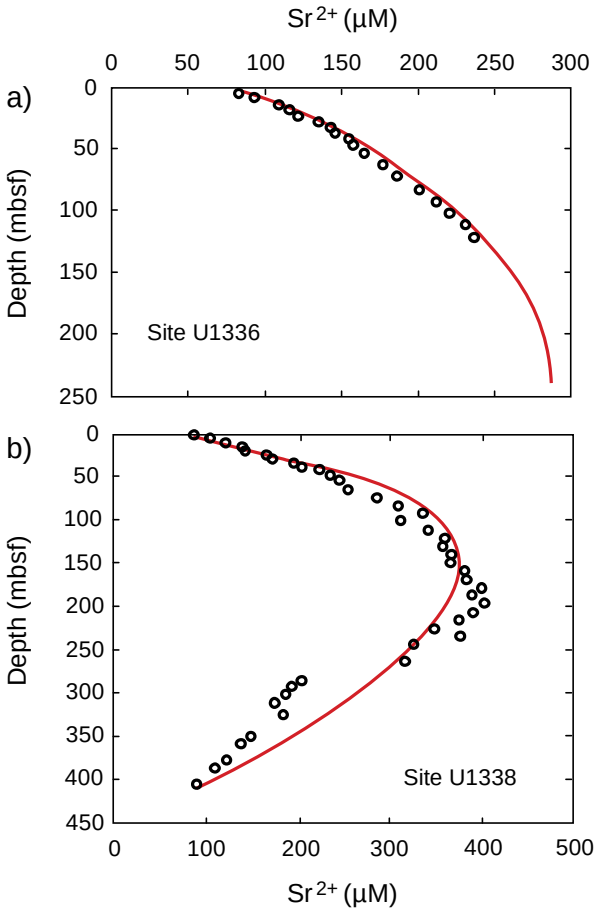

Figure S5. Results for 1-D sediment diagenesis model for Sites U1336 a) and U1338 b). The red line denotes the model output. For details see Table S4 and supplement.

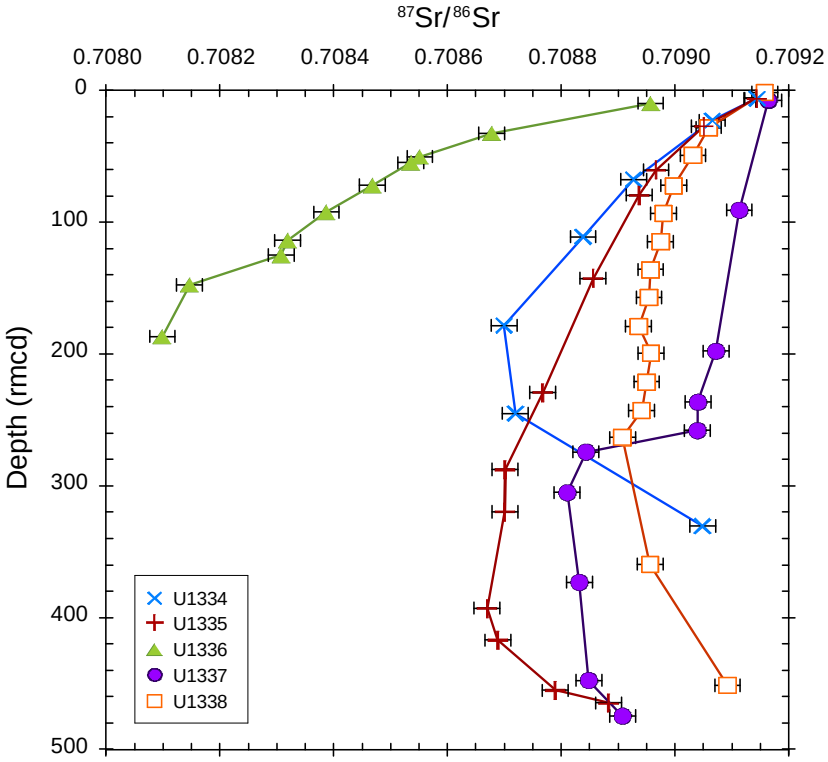

Figure S6. $^{87}Sr/^{86}Sr$ of pore waters of the PEAT sites plotted against revised metres composite depth. Revised composite depths are from Westerhold et al. (2012) and Wilkens et al. (2013). Error bars for the PEAT sites denote the 2σ uncertainties of repeated measurements of IAPSO seawater.

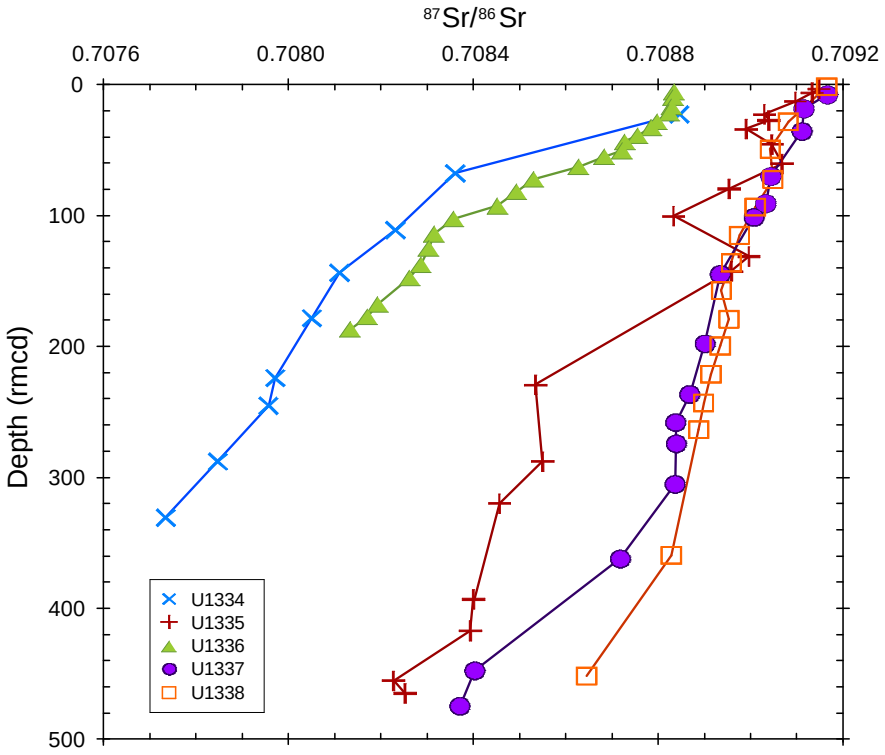

Figure S7. $^{87}Sr/^{86}Sr$ of bulk carbonate leachates of the PEAT sites plotted versus revised metres composite depth. Revised composite depths are from Westerhold et al. (2012) and Wilkens et al. (2013). Error bars for all sites are as big as the symbol size and denote the 2σ uncertainties of repeated measurements of IAPSO seawater.

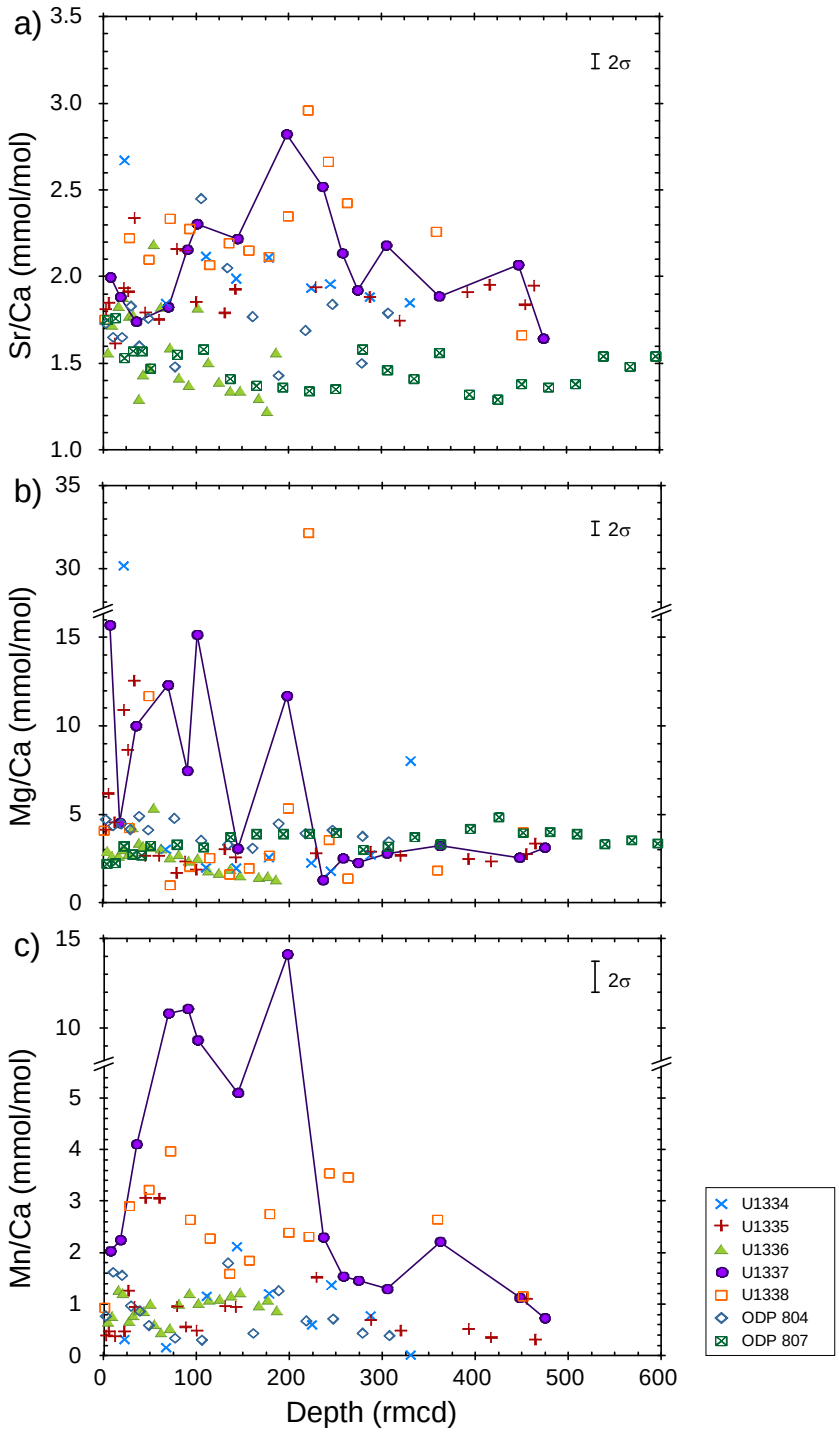

Figure S8. Element/Ca ratios of bulk carbonate leachates shown against revised metres composite depth with a) Sr/Ca ratios, b) Mg/Ca ratios, and c) Mn/Ca ratios. Revised composite depths are from Westerhold et al. (2012) and Wilkens et al. (2013). Values from ODP Sites 804 and 807, in metres below seafloor (mbsf), are from Delaney and Linn (1993). Error bars represent the 2σ uncertainty estimates of repeated measurements of one sample.

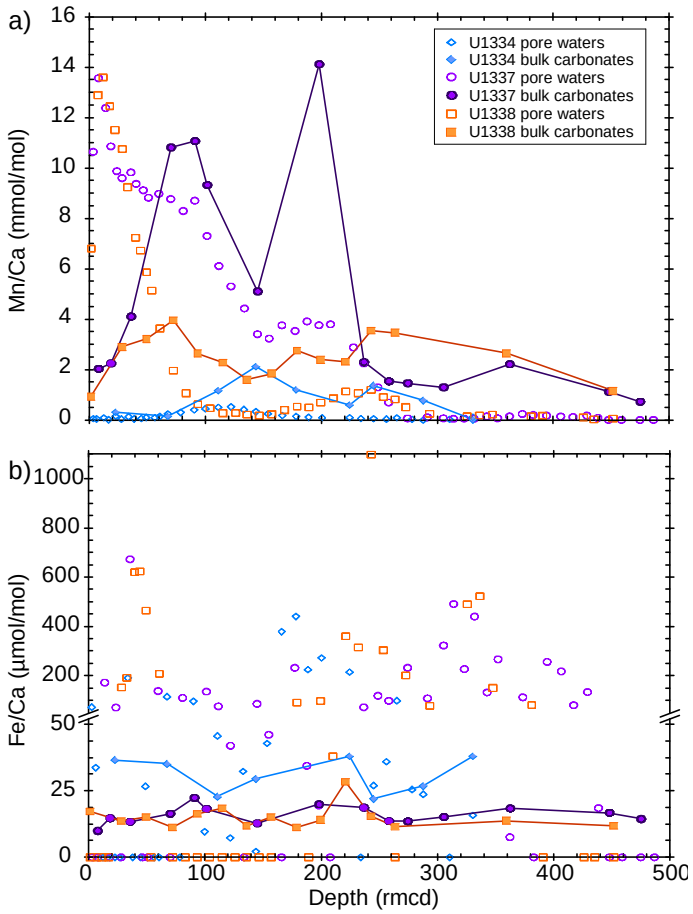

Figure S9. Mn/Ca a) and Fe/Ca b) ratios of bulk carbonate leachates and pore waters of Sites U1334 (blue diamonds), U1337 (purple circles) and U1338 (orange squares) plotted against depth in revised metres composite depth. Revised composite depths are from Westerhold et al. (2012) and Wilkens et al. (2013). Closed symbols represent bulk carbonate leachates and open symbols are pore water samples. Data for pore waters are from Pälike et al. (2010).

Supplementary text

1-D model of sediment diagenesis at Sites U1336 and U1338

Sediment diagenesis is simulated using a 1-D reactive transport model which incorporates the Sr content of the pore water and sediment. The numerical model used to simulate the sediment-pore water system is described in detail elsewhere (Higgins and Schrag, 2012) but is briefly reviewed here. The model is based on a 1-D diffusion-advection-reaction equation (Richter and DePaolo, 1987):

$$\phi(z) \cdot \frac{\partial({}^{n}_{f}X)}{\partial t} = \frac{\partial}{\partial z}\left(\phi(z) \cdot D_{{}^{n}X} \cdot \frac{\partial({}^{n}_{f}X)}{\partial t}\right) - \frac{\partial}{\partial z}\left(\phi(z) \cdot w(z) \cdot {}^{n}_{f}X(z)\right) - \phi(z) \cdot F_{{}^{n}_{f}X(z)} \qquad \text{(S1)}$$

where ${}^{n}_{f}X$ is the concentration of isotope n of element X in mol kg^{-1} pore water, z is depth below the sediment-water interface, $D_{{}^{n}X}$ is the depth-dependent bulk sediment diffusion coefficient (m^2 yr^{-1}) for element X, ϕ is the depth-dependent but time-invariant porosity, ω is an advective velocity (m yr^{-1}), and $F_{{}^{n}X(z)}$ is the recrystallisation reaction for element X (mol X kg sed^{-1} yr^{-1}). We define $F_{{}^{n}_{f}X(z)}$ following (Richter and DePaolo, 1987):

$$F_{{}^{n}_{f}X(z)} = R(z) \cdot M(z) \cdot ({}^{n}_{s}X - K_X \cdot {}^{n}_{f}X) \qquad \text{(S2)}$$

where $R(z)$, is the depth and age dependent rate constant for recrystallisation (yr^{-1}), $M(z)$ is the local solid to pore water mass ratio, ${}^{n}_{s}X$ is the concentration of isotope n of element X in mol kg^{-1} sediment, ${}^{n}_{f}X$ is the concentration of isotope n of element X in mol kg^{-1} pore water, $\alpha_{X-calcite}$ is the isotopic fractionation factor for element X relative to the low mass (e.g. ^{24}Mg, ^{40}Ca), and K_X is the distribution coefficient for element X between pore water and solid. K_X is related to the distribution coefficient for the element X to Ca ratio ($K_{X/Ca}$) by:

$$K_X = (Ca_s/Ca_f) \cdot K_{X/Ca} \qquad \text{where} \qquad K_{X/Ca} = {(X/Ca)_s}\Big/{(X/Ca)_f}\,. \qquad \text{(S3)}$$

To calculate pore water Ca^{2+} profiles, we assume mass balance for calcite recrystallisation such that $M_{Ca} + M_{Sr} = 1$, where M is the mol fraction of that element in the newly recrystallised calcite. In addition, we assume that recrystallisation results

are associated with no net calcite precipitation or dissolution. We assume that the chemistry of the recrystallising biogenic carbonate is identical to the bulk sediment. $R(z)$ is parameterised following (Richter and DePaolo, 1987):

$$R(z) = \lambda + \beta \cdot e^{-\gamma/z} \quad \text{(S4)}$$

where $\lambda, \beta,$ and γ are coefficients for the rate of recrystallisation as a function of depth. The coefficient λ is the background recrystallisation rate at depth, $\lambda + \beta$ is the initial recrystallisation rate and γ is the rate at which the recrystallisation rate changes with depth.

We model the deposition of a sediment column and the chemical cycling of its pore water using boxes of unconsolidated sediment, deposited at rates determined by the age and thickness of the sediment column, and compacted according to the observed porosity/depth relation. The modelled sediment column at Site U1336 is made up of 40 boxes, it is 7.4 metres thick (initially), and has been deposited over 32 Myrs. At Site U1338, the sediment column consists of 44 boxes, it is 13.0 metres thick (initially), and has been deposited over 18 Myrs. Initial conditions for the pore water are acquired from the concentration and isotopic composition of seawater at the time of sediment deposition. Boundary conditions for the model are the concentration of Sr in seawater through time (upper boundary) and either a fixed-concentration (seawater Sr^{2+} concentration for lower boundary at U1338) or zero-flux (lower boundary at U1336). We include fluid flow originating from compaction. The principle variables of the model are the rate of sediment recrystallisation ($R(z)$), the distribution coefficient for Mg and Sr between pore water and calcite ($K_{Sr/Ca}$); and the lower boundary condition. Our approach is to find the set of values for these variables which satisfies the observations from the pore water and sediment. Model variables associated with these results are listed in Table S4.

Chapter 2

Minimal influence of recrystallisation on middle Miocene benthic foraminiferal stable isotope stratigraphy in the eastern equatorial Pacific

Janett Voigt[a,*], Ed C. Hathorne[a], Ann Holbourn[b], and Martin Frank[a]

[a]GEOMAR Helmholtz Centre for Ocean Research Kiel, Wischhofstr. 1-3, 24148 Kiel, Germany

[b]Institute of Geosciences, Christian-Albrecht-University, Ludewig-Meyn-Str. 10, 24118 Kiel, Germany

*Corresponding author, e-mail address: jvoigt@geomar.de

In review in: Paleoceanography, reference no. 2015PA002822

Abstract

Stable carbon and oxygen isotopes ($\delta^{13}C$ and $\delta^{18}O$) of foraminiferal tests are amongst the most important tools in palaeoceanography, but the extent to which recrystallisation of the tests can alter the isotopic composition of the shells is not well known. Here we compare middle Miocene (16-13 Ma) benthic foraminiferal stable isotope records from eastern equatorial Pacific sites recovered during the Integrated Ocean Drilling Program (IODP) Expedition 320/321 to investigate the effect of recrystallisation. To test an extreme case, we analysed stable isotope compositions of benthic foraminifera from Site U1336, for which the geochemistry of bulk carbonates and associated pore waters demonstrated extensive recrystallisation resulting from an enhanced thermal gradient. Despite this diagenetic overprinting, the amplitudes and absolute values of the stable isotopes are in good agreement with high resolution records from better preserved Sites U1337 and U1338 nearby. For example, the carbon isotope events of the Monterey Excursion are recorded without any significant alteration and the stable isotope data show clear orbital cyclicities corresponding to both long (400 kyr) and short (100 kyr) eccentricity. Our results suggest most recrystallisation is restricted to the carbonate matrix and the benthic

foraminifera retain their original $\delta^{13}C$ and $\delta^{18}O$. Thus, benthic foraminifera can be reliably used for isotope analysis, stratigraphy and palaeoceanographic studies of carbonate-rich sediments in which the bulk carbonates experienced extensive recrystallisation, which demonstrates the recrystallisation occurred rapidly after deposition from pore waters with an isotope composition similar to the bottom waters.

1. Introduction

The calcite tests of foraminifera preserved in marine sediments are widely used to reconstruct a range of marine environmental parameters including past seawater temperature, salinity, and global ice volume (e.g., Lear et al., 2000; Zachos et al., 2001a, 2008). However, ancient foraminiferal tests are often altered after deposition by recrystallisation during which the original biogenic calcite is replaced by secondary (inorganic) calcite. Significant changes in stable isotope ($\delta^{13}C$ and $\delta^{18}O$) and Mg/Ca ratios of recrystallised planktonic foraminifera have been reported, which can bias palaeo-temperatures and interpretations of palaeo-climatic variability (Pearson et al., 2001; Sexton et al., 2006). Pearson et al. (2001) found that diagenetic effects on planktonic $\delta^{18}O$ could explain the “cool tropic paradox” of the Paleocene and Eocene given that altered planktonic foraminifera tend to have higher $\delta^{18}O$ values indicating cooler temperatures. These authors also found that well preserved foraminifera from clay-rich sediments appear “glassy” under the light microscope, when wet. In contrast, less well preserved tests are opaque (“frosty”) under the light microscope (Sexton et al., 2006; Pearson and Burgess, 2008). Scanning Electron Microscope (SEM) imaging revealed that the wall structure of well preserved foraminiferal tests consists of different layers with fine, distinct calcite crystals, whereas the layers in less well preserved foraminifera have become more uniform and the original calcite crystals have been replaced by micron sized secondary calcite crystals (Sexton et al., 2006; Hodell et al., 2007; Pearson and Burgess, 2008; Sexton and Wilson, 2009). The “glassy” tests in clay-rich sediments are considered to retain the most reliable geochemical signatures because of the excellent preservation (e.g., Pearson et al., 2001, 2007; Stewart et al., 2004; Sexton et al., 2006; Bown et al., 2008; Pearson and Burgess, 2008), whereas most carbonate-rich, pelagic ooze sediments are prone to

recrystallisation. However, a recent study indicated that the stable isotope compositions of benthic foraminifera from Oligocene age oozes from the eastern equatorial Pacific show negligible intersite offsets, although the investigated sites had different recrystallisation histories and the preservation states of foraminiferal tests differed markedly (Edgar et al., 2013). Two high resolution Miocene benthic foraminiferal stable isotope records from IODP Sites U1337 and U1338 also show good agreement (Tian et al., 2013; Holbourn et al., 2014), suggesting negligible variation between those sites. Other studies focusing on the eastern equatorial Pacific also indicated that benthic foraminifera (Drury et al., 2014) and mid-Miocene planktonic foraminifera are well preserved (Fox and Wade, 2013).

To test the reliability of past benthic stable isotope records, we examined the pronounced Miocene variations recorded in eastern equatorial Pacific sediments subjected to variable carbonate preservation. The cores of IODP Expedition 320/321 recovered one of the most complete Miocene sections allowing detailed studies at the Pacific palaeo-equator. The Mi-1 glaciation at 22.8 Ma marks a prominent but transient, cold event most likely triggered by orbital parameters (Zachos et al., 2001b; Pälike et al., 2006). This event represents an important step in the global climate system towards the transition from the warm greenhouse climate of the Paleogene to the Neogene icehouse climate (e.g., Zachos et al., 2001b). The Cenozoic long-term cooling trend was subsequently interrupted by an extended warm interval from ~17 to 14.7 Ma termed the Middle Miocene Climate Optimum (e.g., Flower and Kennett, 1993; Holbourn et al., 2005, 2007). This interval is characterized by 100 kyr eccentricity variability and shows low mean $\delta^{18}O$ values but a high variability in both, $\delta^{13}C$ and $\delta^{18}O$ (Holbourn et al., 2007, 2014). Characteristic for the middle Miocene are the distinct maxima in $\delta^{13}C$ of the “Monterey Carbon Isotopic Excursion” (e.g., Vincent and Berger, 1985; Holbourn et al., 2007), which were associated with 400 kyr long eccentricity cycles (e.g., Woodruff and Savin, 1991; Shevenell et al., 2004; Holbourn et al., 2005, 2007, 2014). During the Monterey Excursion $\delta^{13}C$ and $\delta^{18}O$ co-varied indicating a close coupling of the global carbon cycle and climate system (e.g., Vincent and Berger, 1985; Woodruff and Savin, 1991; Flower and Kennett, 1993). Periodic increases in organic carbon burial probably caused the $\delta^{13}C$ maxima and thereby reduced atmospheric CO_2, resulting in global cooling (Vincent and Berger,

1985; Woodruff and Savin, 1991; Flower and Kennett, 1993, 1994). This cooling trend culminated in a major cooling event, associated with massive ice-sheet expansion on Antarctica at ~13.9 Ma (e.g., Flower and Kennett, 1994; Holbourn et al., 2005, 2007). However, to date only a few high-resolution foraminiferal stable isotope records cover this important interval (Shevenell et al., 2004, 2008; Holbourn et al., 2005, 2007, 2014; Tian et al., 2013, 2014).

One overall aim of the IODP Expedition 320/321 was to validate and extend the astronomical calibration of the Geological Timescale for the Cenozoic by using bio-, chemo- and magnetostratigraphy at the equator (Pälike et al., 2010). For Site U1336, a well resolved magnetic dataset was established, in particular for the early to middle Miocene (Ohneiser et al., 2013). It is therefore useful to transfer the palaeo-magnetic results of Site U1336 to Sites U1337 and U1338, where the polarity chronology for this time interval is less well resolved (Pälike et al., 2010) to improve the global Geological Timescale.

Here we present benthic foraminiferal stable isotope data from IODP Site U1336, which were generated as part of a broader study of carbonate diagenesis. To compare specific time intervals between the different sites of the Pacific Equatorial Age Transect, it was necessary to establish a benthic foraminiferal stable isotope record for Site U1336 to precisely constrain intervals within the middle Miocene, already defined for Sites U1337 and U1338 (Tian et al., 2013; Holbourn et al., 2014). The U1336 middle Miocene benthic stable isotope record is compared with high resolution records from nearby Sites U1337 (Tian et al., 2013) and U1338 (Holbourn et al., 2014) to evaluate possible offsets caused by recrystallisation of the foraminiferal tests. In contrast to the other sites, Site U1336 has extensively altered bulk carbonates in sections older than 20.2 Ma, as a consequence of an inferred large thermal gradient primarily driving carbonate recrystallisation (Voigt et al., 2015). Sr is released to the pore waters during the recrystallisation of biogenic carbonates and is thus an important proxy to identify recrystallised sediments (e.g., Baker et al., 1982; Elderfield and Gieskes, 1982; Stout, 1985; Gieskes et al., 1986; Richter, 1993). Persistent recrystallisation at Site U1336 is evident from pore waters with $^{87}Sr/^{86}Sr$ ratios lower than contemporaneous seawater in sediments older than 14.7 Ma (Figure S1) likely resulting from upward diffusion of Sr released from older biogenic

carbonates recrystallised deeper in the sediment section (Voigt et al., 2015). Furthermore, pore water Sr^{2+} concentrations of Site U1336 increase with depth with a steep gradient as a result of excess Sr^{2+} released to the pore waters during recrystallisation. Diagenetic alteration is generally accompanied by lower Sr/Ca ratios of bulk carbonates because less Sr is incorporated into secondary calcite (e.g., Baker et al., 1982; Delaney, 1989). Site U1336 generally shows lower bulk carbonate Sr/Ca ratios compared to the other PEAT sites, which confirms significant recrystallisation even in the section < 20 Ma (Voigt et al., 2015). Here we show that even in carbonate sediments with clear geochemical signs of ongoing recrystallisation the stable isotope composition of benthic foraminifera is not altered.

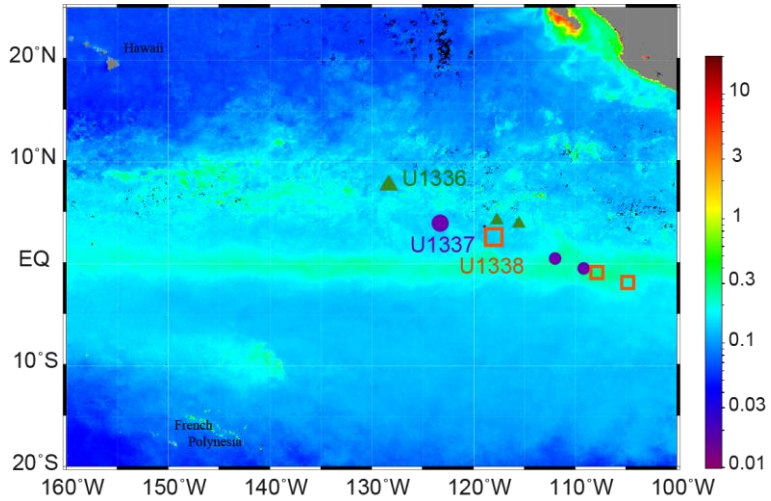

Figure 1. Equatorial Pacific map showing the averaged chlorophyll a data of June 2012-2014 (Ocean Color, NASA) as well as the present geographical and backtracked location of the PEAT sites included in this study (Pälike et al., 2010). The present location of each site is represented by larger symbols. The backtracked positions were estimated from Pälike et al. (2010); the sites originated from the East Pacific Rise and moved in a north-west direction since.

2. Materials and Methods

2.1 Site Description

All three sites of this study were recovered during the IODP Pacific Equatorial Age Transect Expedition 320/321 (Figure 1) and detailed lithological descriptions are provided in Pälike et al. (2010). All depths are given in revised metres composite depth (rmcd) (Wilkens et al., 2013). Site U1336 covers the early Oligocene to middle Miocene carbonate sedimentation until the site subsided below the carbonate compensation depth at around 12 Ma (Pälike et al., 2010, 2012) resulting in clay

accumulation thereafter. The site is located in the eastern equatorial Pacific (7°42.067'N, 128°15.253'W) close to the Clipperton Fracture Zone (~30 km) in a water depth of 4286 m (Pälike et al., 2010). This depth was shallower during middle Miocene at 3800-3900 m (Pälike et al., 2012). The recovered sediment succession consists of a carbonate-rich nannofossil ooze (on average 87.3 % $CaCO_3$) (Pälike et al., 2010).

Site U1337 (3°50.007'N, 123°12.356'W) recovered sediments from the Oligocene/Miocene boundary to Holocene age. Site U1337 is located 700 km southeast of Site U1336 in a water depth of 4461 m and a reconstructed middle Miocene water depth of 3800-4050 m (Pälike et al., 2012). Site U1338 (2°30.469'N, 117°58.178'W) is comprised of sediments of Miocene to Holocene age and is located 1300 km southeast of Site U1336 in a water depth of 4200 m (Pälike et al., 2010) corresponding to a middle Miocene water depth of 3200-3600 m (Pälike et al., 2012). As the Pacific plate moved away from the East Pacific Rise, the sites left the equatorial zone of high productivity between 2° north and south of the equator during different time intervals. The sediment successions of Sites U1337 and U1338 also consist of carbonate-rich nannofossil and microfossil oozes containing on average 61.7 % and 71.2 % $CaCO_3$, respectively (Pälike et al., 2010).

2.2 Sample preparation for $\delta^{13}C$ and $\delta^{18}O$ measurements

Samples from Site U1336 were taken from 12.04-48.19 rmcd at 6 to 15 cm intervals (corresponding to a 5.1 to 17.8 kyr resolution), but the sampling was increased to 2 to 4 cm in the section between 40.94 and 41.76 rmcd (~1.7-3.4 kyr resolution) corresponding to 15.45-15.38 Ma. Samples of 20 cm^3 sediment volume were freeze-dried, then washed over a 63 µm sieve and the residue was dried at 40°C and sieved into different size fractions. Specimens of the two epifaunal benthic foraminiferal species *Cibicidoides wuellerstorfi* and *Cibicidoides mundulus* were picked from the > 250 µm fraction for stable carbon and oxygen isotope analyses. Analyses of mixtures of the two species were performed for about half of the samples; mono-specific tests were measured for the remaining samples. In the interval between 43.20 and 48.19 rmcd, only *C. mundulus* was analysed given that *C. wuellerstorfi* was not present in this section. For 20 samples, these species were also picked from

the 150-250 µm fraction. For 26 samples, where foraminifera were scarce, only 1 or 2 individuals were analysed. Between three and six individual tests per sample were cracked into large fragments, cleaned in ethanol in an ultrasonic bath, and dried at room temperature following the method described in Holbourn et al. (2005).

2.3 $\delta^{13}C$ and $\delta^{18}O$ analyses

Isotope measurements were performed on a Thermo MAT 253 mass spectrometer at GEOMAR equipped with a Carbo-Kiel device Type IV. Samples were reacted with 99 % H_3PO_4 at 74°C. The $\delta^{13}C$ and $\delta^{18}O$ data are given relative to the Vienna Pee Dee Belemnite (VPDB) and are referenced to the National Institute of Standards and Technology (NIST) carbonate isotope standard NBS 19. The 1σ external reproducibility of the in-house carbonate standard (Solnhofen limestone) was ± 0.06 ‰ and ± 0.09 ‰ for $\delta^{13}C$ and $\delta^{18}O$, respectively (n = 124). Replicate measurements performed for 17 % of the samples gave a mean reproducibility of ± 0.09 ‰ and ± 0.12 ‰ and for $\delta^{13}C$ and $\delta^{18}O$, respectively. A t-test was performed on mono-specific results of 7 % of the samples and indicated no significant offset of the $\delta^{13}C$ and $\delta^{18}O$ signatures between the two species and the data of both species show a 1:1 relationship (Figure S2).

2.4 Orbital tuning of colour reflectance b*

To create an alternative age model to the stratigraphy of core U1336, based on the initial shipboard age model (Pälike et al., 2010) and a revised palaeo-magnetic age model (Ohneiser et al., 2013), the high resolution colour reflectance b* record of Site U1336 (2-5 cm) (Wilkens et al., 2013) was tuned to the eccentricity of Laskar et al. (2004) (Figure 2a) using AnalySeries Version 2.0 (Paillard et al., 1996). The temporal resolution of the U1336 isotope data is too low for independent tuning to an orbital solution, but the ship board measured reflectance parameter b* (blue-yellow), representing changes in lithology, can thus be used to analyse their cyclicity (Blum, 1997). Colour reflectance b* maxima, reflecting dark sediment layers corresponding to elevated proportions of radiolarians (Pälike et al., 2010), were tuned to maxima (100 kyr) in eccentricity (Laskar et al., 2004). Age/depth tie points are presented in Table S1. However, the tuning of colour reflectance b* appears less reliable for the intervals 15.75-15.25 Ma and 13.70-13.50 Ma, where the 100 kyr filtered record does

not match the amplitudes of the target solution (Laskar et al., 2004) (Figure 2b). For the interval from 14.6 to 14.1 Ma, where both filtered records do not show clear 100 kyr cyclicity, obliquity cycles prevail as clearly evident in the filtered colour reflectance b* record (Figure S3).

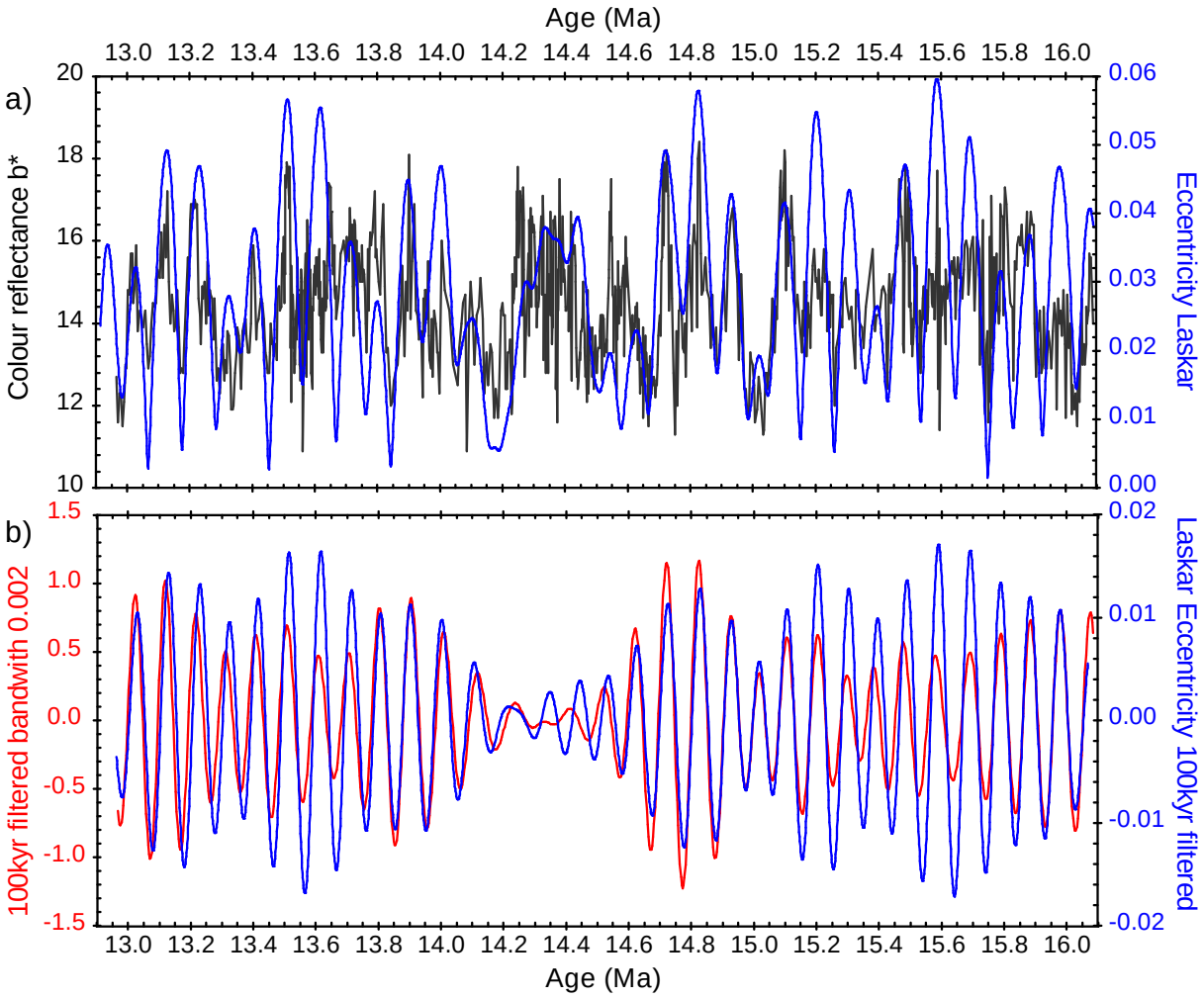

Figure 2. a) Tuning of colour reflectance b* of Site U1336 (dark grey) to the orbital eccentricity solution of Laskar et al. (2004) (blue) from 16.1 to 12.9 Ma. b) Comparison of the tuned 100 kyr filtered record of colour reflectance b* (red) to the 100 kyr filtered eccentricity of Laskar et al. (2004) (blue).

3. Results

3.1 Benthic foraminiferal $\delta^{18}O$ and $\delta^{13}C$ of Site U1336

The investigated interval of Site U1336 covers the time period from 16 to 12.9 Ma and the $\delta^{18}O$ and $\delta^{13}C$ data set has a time resolution between 5.1 and 17.8 kyr except for a short interval (15.45-15.38 Ma) with higher time resolution (1.7-3.4 kyr),

comprising a section of darker coloured sediment with a higher proportion of radiolarians (Pälike et al., 2010).

The $\delta^{18}O$ and $\delta^{13}C$ data show synchronous changes from 16 to about 14.22 Ma. $\delta^{13}C$ oscillated between 1.3 and 2.0 ‰ at amplitudes between 0.3 and 0.6 ‰, except for an abrupt decrease to 0.77 ‰ centred at 15.57 Ma (Figure 3a). At the same time, the $\delta^{18}O$ values fluctuated around a mean of 1.54 ‰ at amplitudes between 0.4 and 0.6 ‰. There was a comparably abrupt negative shift reaching 0.74 ‰ at 15.57 Ma (Figure 3b). After 14.22 Ma, $\delta^{18}O$ displays a trend to heavier values with the most rapid increase at ~13.9-13.8 Ma, and then varied around a mean $\delta^{18}O$ of 2.11 ‰ between 13.84 and 13 Ma. Near 13.7 Ma the $\delta^{18}O$ record diverged from that of $\delta^{13}C$ in that the $\delta^{13}C$ values decreased continuously from ~13.72 to 13 Ma, whereas the $\delta^{18}O$ signatures essentially stayed constant (Figures 3a and 3b).

The stable isotope data of Site U1336 show low frequency variations that follow the long eccentricity cycles (400 kyr). Comparison of 400 kyr filtered $\delta^{18}O$ record with long eccentricity cycles from Laskar et al. (2004) documents a good match from ~14.7-13.0 Ma (Figure 3d). Prior to 14.7 Ma, the isotope record of Site U1336 does not match the target solution of Laskar et al. (2004) and lag behind by ~60 kyr.

4. Discussion

4.1 Carbon isotope events of the Monterey Excursion

Although the stable isotope record of Site U1336 exhibits a relatively low temporal resolution (1.7-17.8 kyr), the $\delta^{18}O$ and $\delta^{13}C$ data show a very good agreement with high resolution records of Sites U1337 (3-4 kyr) (Tian et al., 2013) and U1338 (1-3 kyr) (Holbourn et al., 2014) (Figure 4). In particular, the carbon isotope events of the Monterey Excursion (Woodruff and Savin, 1991; Holbourn et al., 2005) can clearly be identified including the 400 kyr CM events (CM 3b, CM 4a, CM 4b, CM 5a, CM 5b and CM 6) according to the subdivision of Holbourn et al. (2007).

The highest $\delta^{13}C$ values of the Monterey Excursion (16.8-14.7 Ma) occurred during the carbon isotope events CM 3b and CM 4a (Holbourn et al., 2007, 2014). The

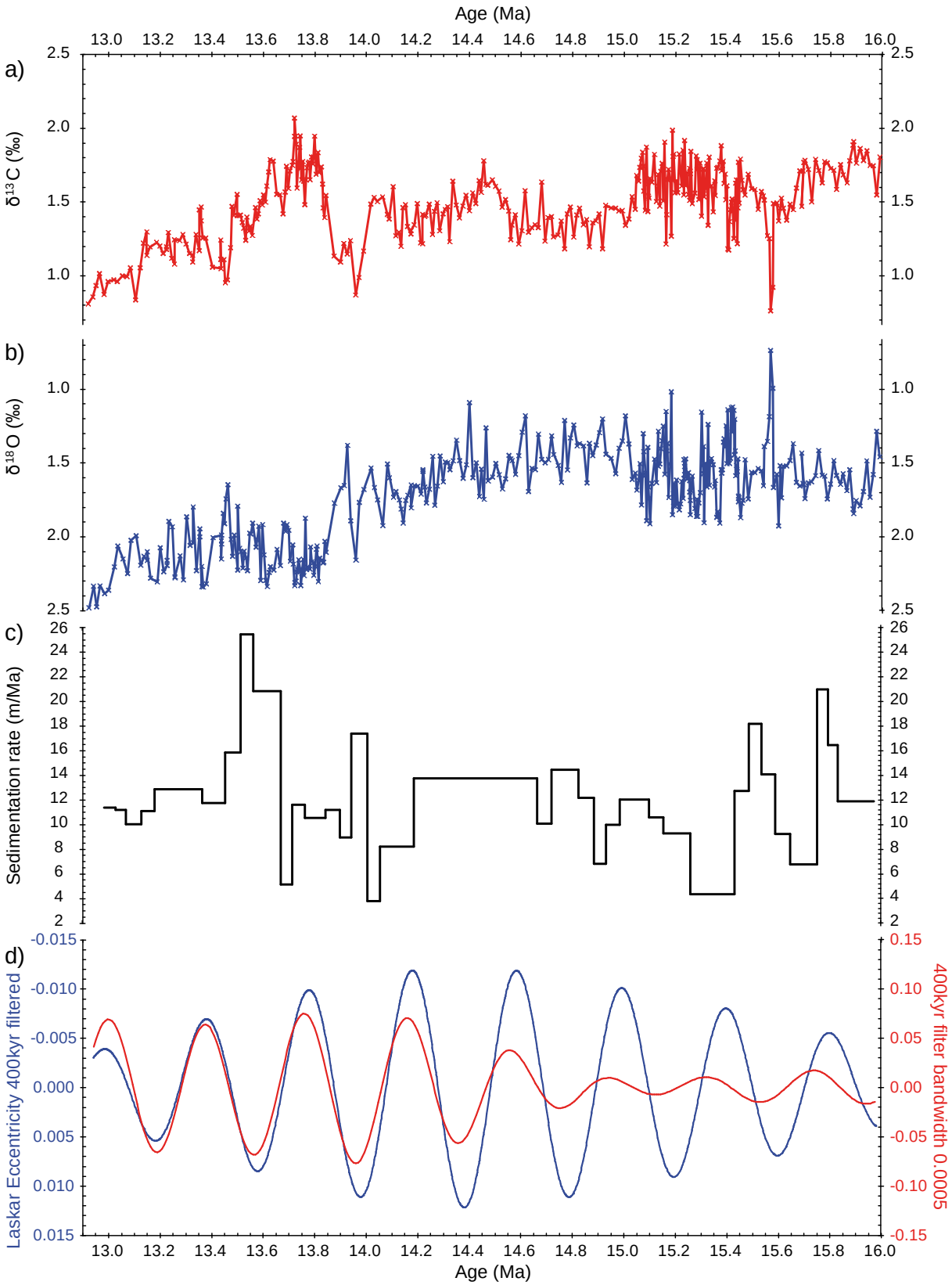

Figure 3. Comparison of Site U1336 a) benthic $\delta^{13}C$, b) benthic $\delta^{18}O$, c) calculated sedimentation rates and d) 400 kyr filtered eccentricity of Laskar et al. (2004) (blue) together with the benthic $\delta^{18}O$ record filtered for 400 kyr cycles (red) from 16 to 12.9 Ma.

maximum $\delta^{13}C$ values during CM 3b are 1.80 ‰ and 2.00 ‰ for Sites U1337 (Tian et al., 2013) and U1338 (Holbourn et al., 2014), respectively. The record of U1337, however, most likely does not show the maximum carbon isotope values because the record only extends back to 15.89 Ma (Tian et al., 2013) and the highest values of Site U1338 were recorded between 16.0 and 15.9 Ma (Holbourn et al., 2014). The maximum $\delta^{13}C$ value of Site U1336 of 1.91 ‰ compares very well to that of the other two sites. The onset of the carbon isotope excursion CM 4a is marked by a peak warmth episode centred at 15.6 Ma, which can be clearly identified in all three records (Figure 4). This abrupt warming was associated with a sharp decline in $\delta^{13}C$ and the amplitudes of the $\delta^{18}O$ and $\delta^{13}C$ values were essentially identical. The $\delta^{18}O$ values decrease to 0.74 ‰, 0.63 ‰ and 0.67 ‰, and the $\delta^{13}C$ values decline to 0.77 ‰, 0.82 ‰ and 0.76 ‰ at Sites U1336, U1337 (Tian et al., 2013) and U1338 (Holbourn et al., 2014), respectively (Figure 4). This peak warmth period is also identified at the subtropical ODP Sites 1146 (South China Sea) and 1237 (Nazca Ridge, off Peru) reaching lowest values at Site 1146 ($\delta^{18}O$ = 0.33 ‰, $\delta^{13}C$ = 0.21 ‰) (Holbourn et al., 2005, 2007). This pronounced decrease in $\delta^{18}O$ and $\delta^{13}C$ is accompanied by a minimum in carbonate content and may have been linked to a pulse of intense warming on Antarctica (Warny et al., 2009; Holbourn et al., 2014). The maximum $\delta^{13}C$ value of 1.99 ‰ of the CM 4a is slightly higher for Site U1336; but the other sites show comparable values with 1.74 ‰ and 1.72 ‰ at U1337 (Tian et al., 2013) and U1338 (Holbourn et al., 2014), respectively.

The intense increase in $\delta^{18}O$ of Site U1336 between 13.93-13.72 Ma marks the onset of the global Miocene cooling and has been attributed to Antarctic ice-sheet expansion and deep-water cooling (e.g., Shackleton and Kennett, 1975; Miller et al., 1991; Woodruff and Savin, 1991; Holbourn et al., 2005, 2007). The drastic 0.95 ‰ change in $\delta^{18}O$ at Site U1336 is in agreement with the measured increases at Sites U1337 (1.04 ‰) (Tian et al., 2013) and U1338 (1.32 ‰) (Holbourn et al., 2014). This change in $\delta^{18}O$ is associated with the onset of event CM 6 (e.g., Holbourn et al., 2005, 2007, 2014) during which the corresponding shift in $\delta^{13}C$ is 0.92 ‰ at Site U1336 and is comparable to 0.88 ‰ and 0.90 ‰ at Sites U1337 (Tian et al., 2013) and U1338 (Holbourn et al., 2014), respectively.

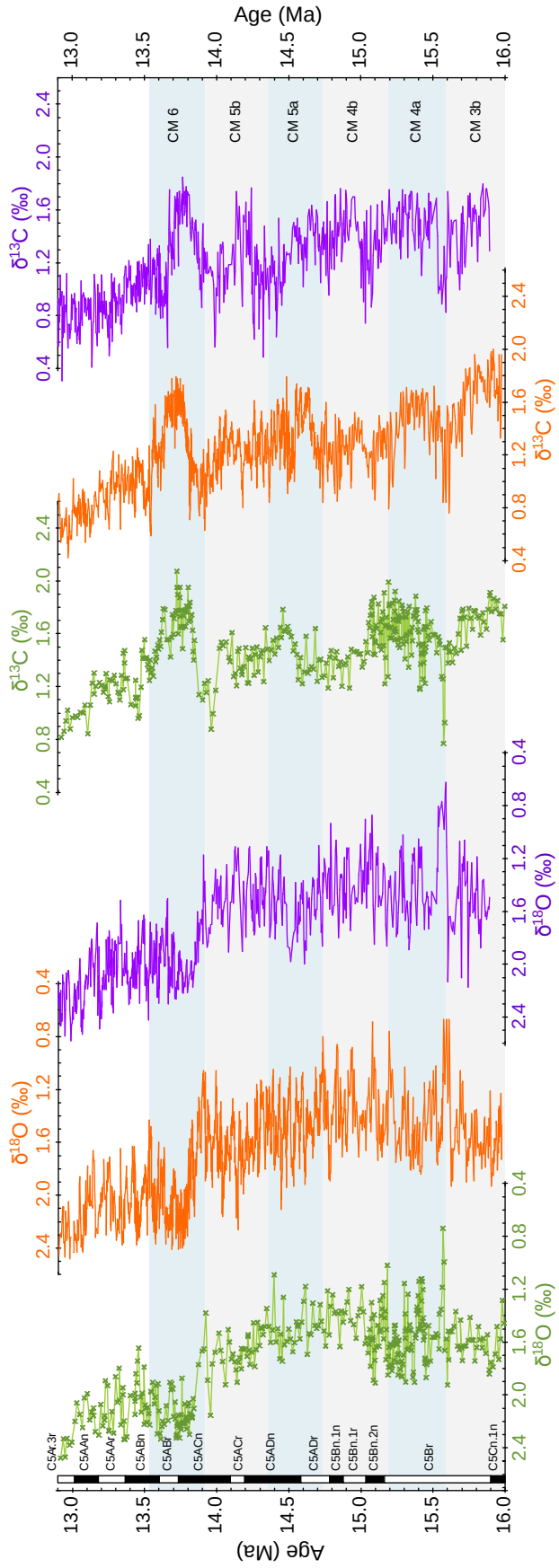

Figure 4. Comparison of benthic stable isotope time series of Site U1336 (green) with U1337 in purple (Tian et al., 2013) and U1338 in orange (Holbourn et al., 2014). It is important to note that each stable isotope record is based on a different tuning approach. Coloured bands illustrate the carbon isotope events of the Monterey Excursion (subdivisions by Holbourn et al., 2007). The polarity stratigraphy of Site U1336 (Pälike et al., 2010; Ohneiser et al., 2013) is provided for comparison with the other records.

The co-varying benthic $\delta^{18}O$ and $\delta^{13}C$ data of Sites U1336, U1337 and U1338 (Figure 4) indicate that global ice volume and deep water temperature changes largely coincided with changes in the global carbon cycle (e.g., Vincent and Berger, 1985; Flower and Kennett, 1993, 1994; Pälike et al., 2006; Kirtland Turner, 2014). These changes in benthic $\delta^{18}O$ and $\delta^{13}C$ data occurred on an orbital timescale during the middle Miocene and were possibly linked via a carbon cycle feedback loop involving climate, weathering, carbonate preservation and atmospheric CO_2 (e.g., Vincent and Berger, 1985; Flower and Kennett, 1994; Zachos et al., 2008, 2010; Ma et al., 2011; Kirtland Turner, 2014).

Although the $\delta^{18}O$ signatures of Site U1336 are comparable to that of Site U1338 (and Site U1337) throughout the entire investigated interval, discrepancies exist between the $\delta^{13}C$ records. The $\delta^{13}C$ record seems to have been more variable within event CM 4 with partially higher values (by up to 0.4 ‰) between 15.23 and 15.00 Ma (Figure 4). The $\delta^{13}C$ record of Site U1336 also shows increased values compared to Site U1338 between 13.36 and 13.00 Ma with offsets varying between 0.2 and 0.4 ‰. There is no significant difference in $\delta^{13}C$ values between Sites U1336 and U1337 during the time interval between 15.23 and 15.00 Ma, but the $\delta^{13}C$ values of Site U1336 are higher (by up to 0.4 ‰) between ~14.51 and 14.24 Ma and between 13.36 and 13.12 Ma (by 0.2 ‰) (Figure 4). These observed deviations in $\delta^{13}C$ values may have been caused by small changes in productivity due to different palaeo-latitudes, but may also result from different tuning approaches and/ or different resolution of the isotope records. The $\delta^{13}C$ values of Sites U1337 and U1338 do not differ markedly, except for the time intervals between 14.96-14.85 Ma and 14.24-14.13 Ma (Figure 4). Both sites were still in the equatorial zone of high productivity during the entire investigated time interval (Figure 1) (Pälike et al., 2010), which possibly resulted in fewer differences between the $\delta^{13}C$ data due to similar productivity in the upper ocean. In contrast, Site U1336 travelled out of the high productivity zone at ~23 Ma (see also Figure 1) (Pälike et al., 2010), resulting in decreased productivity in comparison to the other sites. In general, the benthic $\delta^{13}C$ signal is influenced by local primary productivity and deep water circulation (e.g., Belanger et al., 1981). Due to the proximity of the sites, the latter can be assumed to be identical at the sites, thus differences in primary productivity might lead to the

observed changes in benthic $\delta^{13}C$ values. Organic material, formed in the surface layer, is depleted in ^{13}C and when it sinks to the deep ocean, it is remineralised lowering the $\delta^{13}C$ of the inorganic carbon pool of the deep ocean. Therefore, less ^{13}C-depleted carbon might be incorporated into benthic foraminiferal tests resulting in elevated benthic $\delta^{13}C$ values. Further, the onset of event CM 6 occurred 40-70 kyr earlier at Site U1337 (13.99 Ma) and at Site U1336 (13.96 Ma) than at Site U1338 (13.92 Ma), which most likely results from the different tuning approaches applied.

4.2 Orbital cyclicity

Clear cyclicity is seen in various properties at Site U1336 such as sediment colour, Gamma Ray Attenuation (GRA) bulk density and stable isotopes. Both long and short eccentricity cycles can be identified in the stable isotopes (Figures 3d and 5). Although the stable isotope record of Site U1336 does not match the 400 kyr cycles of Laskar et al. (2004) well for the entire record (Figure 3d), it is evident that the stable isotope data reflect long eccentricity cycles since the carbon isotope events of the Monterey Excursion can clearly be distinguished and those events are known to be related to 400 kyr cyclicity (e.g., Woodruff and Savin, 1991; Shevenell et al., 2004; Holbourn et al., 2005, 2007, 2014). In the interval from ~16.0 to 14.6 Ma, when there is no apparent match of filtered $\delta^{18}O$ data to the 400 kyr cycles, short eccentricity cycles (100 kyr) are visible (Figure 5) corresponding to the pronounced 100 kyr cycles at Site U1338 (Holbourn et al., 2014). Although the 100 kyr cycles are not very well defined, due to the sampling resolution, they match the filtered eccentricity (Laskar et al., 2004) between 15.45 and 14.65 Ma (Figure 5b). Prior to that interval, the $\delta^{18}O$ record lags behind by ~30-50 kyr and is almost exactly out of phase (Figure 5b). This offset is most likely caused by the tuning method applied. The high resolution record of magnetic susceptibility (2-3 kyr) (Wilkens et al., 2013), matches well with the 400 kyr cycles between ~14.5 and 13.4 Ma and the 100 kyr cycles at 16.0-15.5 Ma, ~14.1-13.8 Ma and ~13.5-13.0 Ma (Figure S4). The high resolution record of GRA bulk density (2-3 kyr) (Wilkens et al., 2013) matches the long eccentricity cycles between ~14.4 and 13.6 Ma and the record agrees with the short eccentricity cycles at 16.0-15.2 Ma, at 14.90-14.65 Ma and at ~13.5-13.0 Ma (Figure S5).

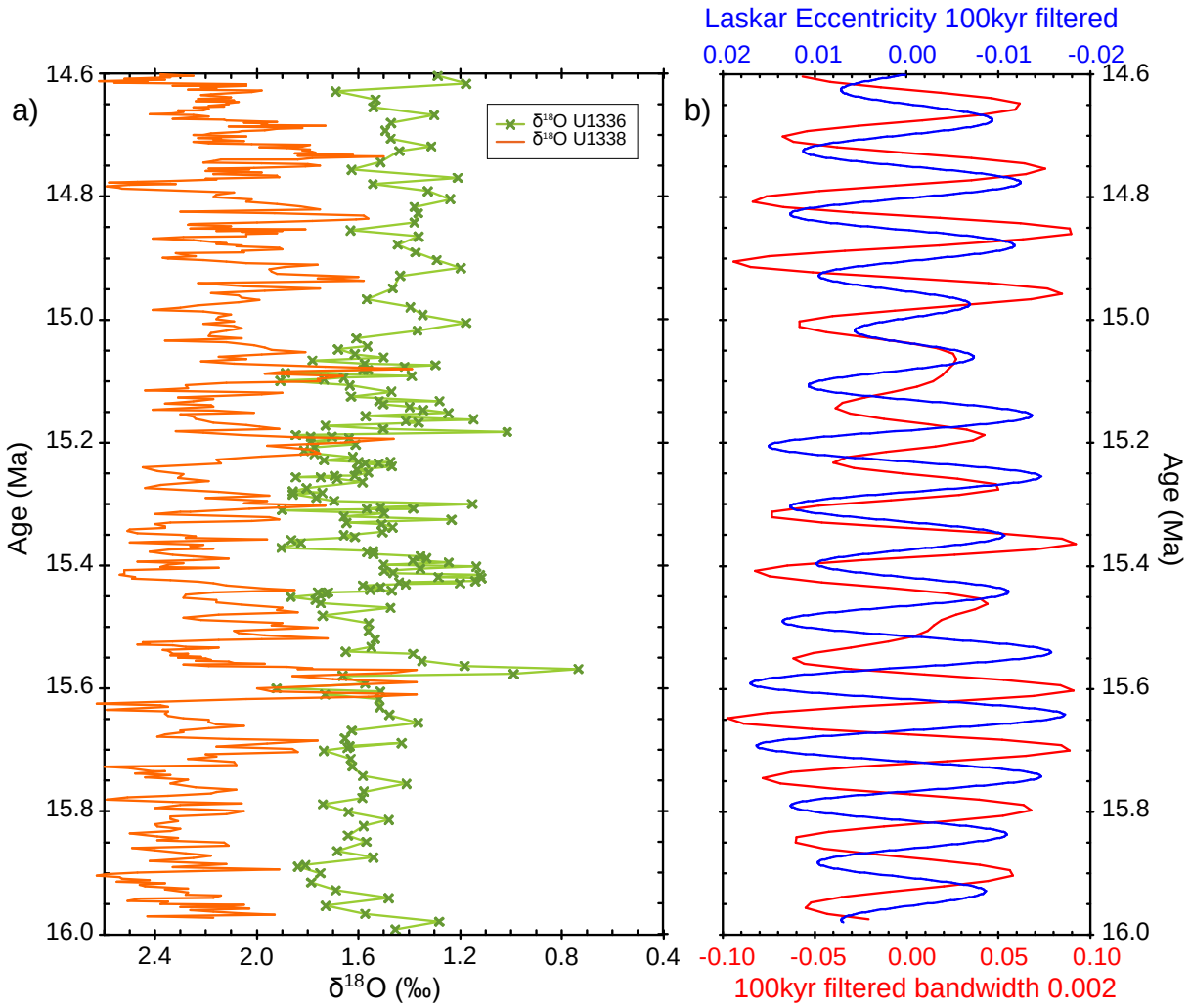

Figure 5. a) $\delta^{18}O$ data of Site U1336 (green) shown for 16.0-14.6 Ma, including the time interval with highest resolution (1.7-3.4 kyr time resolution), plotted against age. The record is compared with that of Site U1338 (orange) (Holbourn et al., 2014). The $\delta^{18}O$ data of U1336 clearly indicate short eccentricity cycles (100 kyr) in accord with the record of Site U1338. The record of U1338 has been shifted by + 0.7 ‰ to facilitate comparison. b) The 100 kyr filtered $\delta^{18}O$ record of Site U1336 (red) is compared to the 100 kyr filtered eccentricity of Laskar et al. (2004) (blue).

Magnetic susceptibility as a proxy for changes in sediment composition can be linked to climate-controlled depositional or diagenetic processes. In the record of Site U1336, the magnetic susceptibility is positively correlated with the darker coloured sediment bands and inversely correlated with GRA bulk density (Figure 6), an indicator for changes in lithology and porosity. These darker coloured sediments contain more radiolarians and clay (Pälike et al., 2010), which have a lower GRA bulk density and higher magnetic susceptibility values than calcite (Mayer, 1979). Low $\delta^{18}O$ values are associated with the darker bands, especially between 46.8-31.8 rmcd (15.88-14.60 Ma) (Figure 6), which are therefore related to short

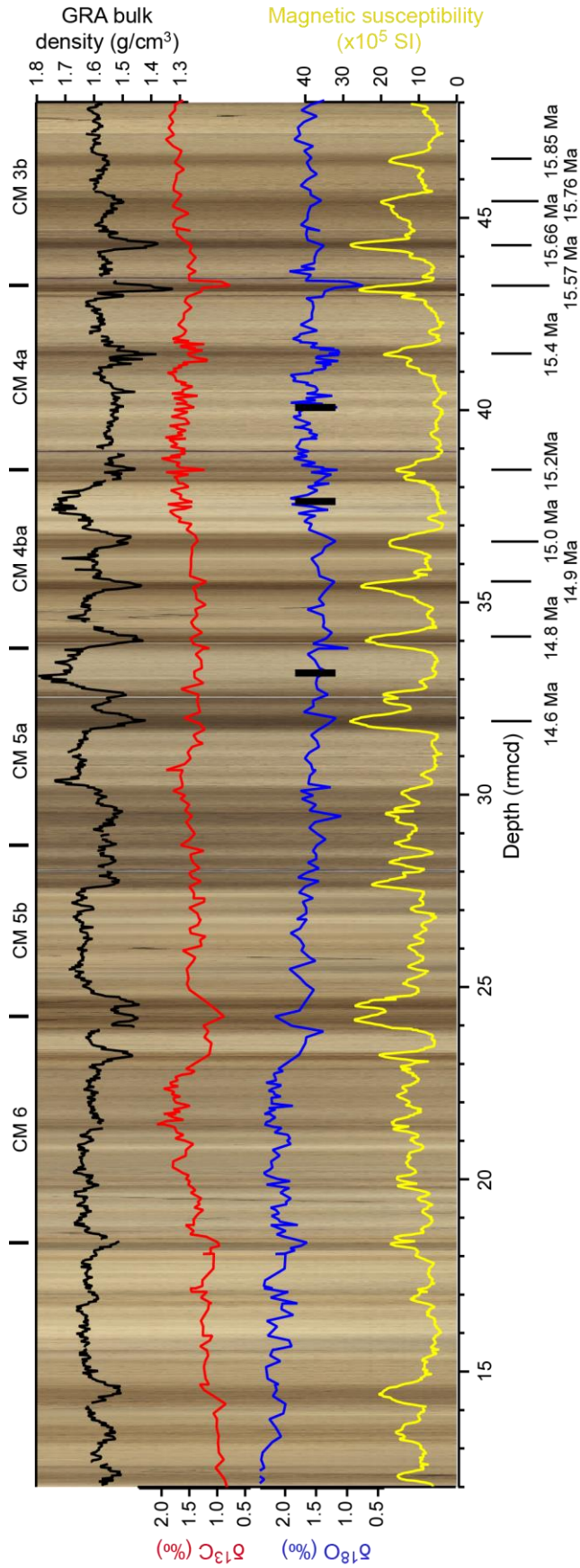

Figure 6. $\delta^{18}O$ and $\delta^{13}C$ record of U1336 and lithology proxies plotted on top of the core splice image from 48-12 rmcd (16-13 Ma). Data for GRA bulk density, magnetic susceptibility and the splice image are adopted from Wilkens et al. (2013). Revised depth scale is from Wilkens et al. (2013). GRA bulk density data (black) and magnetic susceptibility (yellow) are inversely related and are associated with darker coloured bands of the sediment. $\delta^{18}O$ (blue) also seems to be correlated with the sediment colour, which is not clearly shown for $\delta^{13}C$ (red). In the interval from 46.8-31.8 rmcd short eccentricity cycles (100 kyr) can be observed illustrated by the darker coloured sediment bands. The ages of each isotope excursion (low $\delta^{18}O$), coinciding with these bands, are shown below. Carbon isotope events of the Monterey Excursion are given above the splice image and indicate the depth range of each event. Black bars mark the depth, where missing 100 kyr cycles would be located.

warm periods. These darker bands most likely resulted from carbonate dissolution events during warm periods leaving mainly the siliceous fraction in the sediments of these bands (Figure 7a). These warm events, marked by low $\delta^{18}O$ and $\delta^{13}C$ values, are also identified at Site U1338 and are associated with low carbonate content due to carbonate dissolution as well (Figure 7b) (Holbourn et al., 2014). At Site U1338 these periods are paced by 100 kyr eccentricity cycles (Holbourn et al., 2014), which seems to be the case at Site U1336 as well given that the darker bands occurred approximately every 100 kyr from 15.4 to 14.6 Ma (Figure 6). Three 100 kyr cycles are, however, missing within this interval, at 15.3 Ma (~40.0 rmcd), at ~15.1 Ma (~37.4 rmcd) and at ~14.7 Ma (~33.2 rmcd), where the colour does not change (Figure 6). Neither the stable isotopes nor the other sediment properties indicate a 100 kyr cycle around 15.5 Ma (Figure 6). Low values of U1336 GRA bulk density correlates with the darker sediment bands, paced by ~100 kyr, thus there is a positive correlation between GRA bulk density and orbital cycles (Figure 6) (see also Hodell et al., 2001; Gorgas and Wilkens, 2002). In addition, GRA bulk density and the carbonate content are closely positively correlated at Sites U1336 and U1338 (Figure 7) (Lyle et al., 2012; Shackford et al., 2014) confirming low carbonate accumulation rates due to carbonate dissolution in the darker sediment bands (Figure 6).

Five densely spaced dark sediment bands, which appear like one wide band, are observed between ~30.2 and 27.5 rmcd (14.46-14.23 Ma) (Figure 6). These bands may be related to obliquity cycles, identified at Site U1338 between 14.6 and 14.2 Ma (Holbourn et al., 2014), and magnetic susceptibility at Site U1336 matches the obliquity well between ~14.60 and 14.24 Ma (Figure S4) confirming that relationship. GRA bulk density matches the obliquity band around 14.65-14.25 Ma (Figure S5). In contrast to these parameters, obliquity cycles in colour reflectance b* can only be identified between ~14.63 and 14.40 Ma (Figure S3), but cannot be resolved in the stable isotopes at Site U1336 due to the coarse resolution during that interval. The deposition of another series of dark bands at ~24.7-23.8 rmcd (14.00-13.92 Ma) preceded the onset of and continued into carbon isotope event CM 6 marking a period of two sharp decreases in the carbonate content (Figure 7) (Pälike et al., 2010). These peaks with low carbonate content were also recorded at Site U1338 at

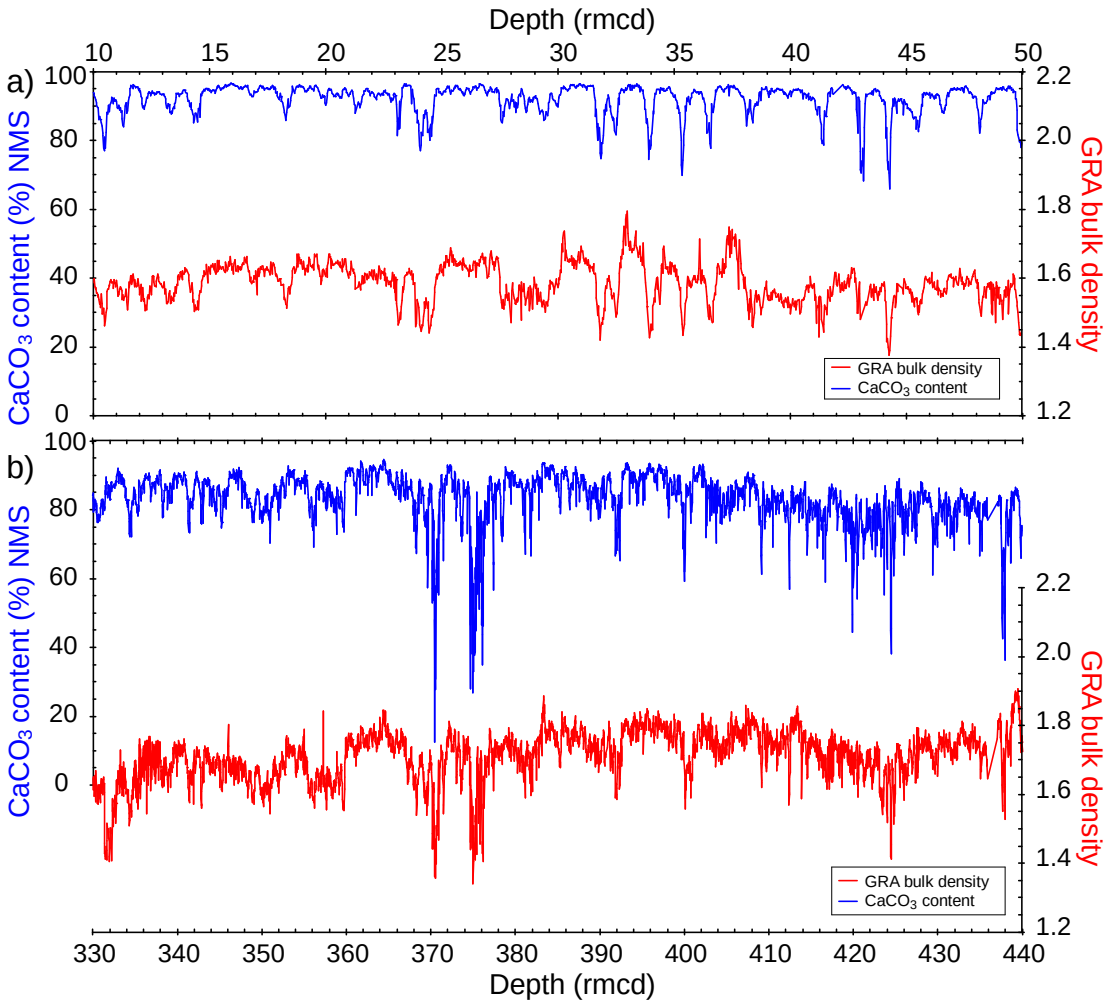

Figure 7. Correlation between GRA bulk densities and carbonate content. The GRA bulk density (red) and the $CaCO_3$ content (blue) are positively correlated and are shown for a) Sites U1336 and b) U1338 illustrating the depth range of the investigated interval (~16-13 Ma). Data for the GRA bulk densities are from Wilkens et al. (2013), the $CaCO_3$ content data of Site U1336 are from Shackford et al. (2014) and the carbonate content data of Site U1338 are from Lyle et al. (2012).

14.04-13.96 Ma and at ~13.84-13.76 Ma and have been attributed to intense opal accumulation occurring just before and during the major $\delta^{18}O$ increase at 13.90-13.75 Ma (Holbourn et al., 2014). This increased rate of opal accumulation represented two high productivity events and was attributed to intensified equatorial upwelling leading to enhanced diatom production (Holbourn et al., 2014). High sedimentation rates during these intervals (Figure 3c; Figure 2 in Holbourn et al., 2014) indicate fast burial and thus low carbonate dissolution (Holbourn et al., 2014), although the carbonate content shows a pronounced decrease (Figure 7), which might indicate dilution of carbonates by intense opal production. GRA bulk density and magnetic susceptibility at Site U1336 also reveal the contemporaneous

occurrence of silica spikes, suggesting that these two productivity events affected the entire eastern equatorial Pacific.

4.3 Effect of tuning approaches on calculated sedimentation rates

As the resolution of the $\delta^{18}O$ and $\delta^{13}C$ record is too low for independent orbital tuning, the high resolution data of the colour reflectance b* of Site U1336 (Wilkens et al., 2013) were used to obtain an orbital tuned age model (Figure 2). The derived ages result in a very good agreement of the $\delta^{18}O$ and $\delta^{13}C$ record to the other sites, although there are some uncertainties. This independent tuning of Site U1336 using colour reflectance b* allows to investigate the robustness of this tuning to the U1336 age model based on magnetostratigraphy (Ohneiser et al., 2013) (Table S2). By comparing both age models, it is possible to evaluate if the excellent palaeo-magnetic dataset of Site U1336 can be exported and used to improve the stratigraphy at Sites U1337 and U1338, where no or less reliable magnetic data exist (Pälike et al., 2010). Such a comparison can be done using the calculated sedimentation rates.

The calculated sedimentation rates at Site U1336 follow the general trend of estimates derived from magnetostratigraphy and magnetic palaeo-intensity (Ohneiser et al., 2013) from 15.2 to 13.0 Ma but show more variability and detail (Figure S6). The age models differ markedly during the carbon isotope events CM 3b, 4a and 6 with an increase in the sedimentation rates to more than 18 m/Ma. A short-lived peak is observed between 15.84 and 15.76 Ma, which may have been related to an increase in opal accumulation and thus high productivity seen at Site U1338 (Holbourn et al., 2014; Figure 2 therein). Between 15.76-15.64 Ma low sedimentation rates (Figures 3c and S6) may be ascribed to a pronounced decrease in carbonate content (Figure 7a). After the peak warmth event at 15.57 Ma, which also corresponded to a short period of low carbonate content (Figure 7) caused by dissolution (Holbourn et al., 2014), the sedimentation rates rapidly recovered and peaked at 18 m/Ma between 15.54 and 15.49 Ma indicating enhanced productivity and organic carbon burial (Holbourn et al., 2014). This peak was followed by a sharp decline in sedimentation rates down to 4 m/Ma resulting in an offset of 12 m/Ma between the sedimentation rate estimates based on palaeo-magnetic data (Ohneiser

et al., 2013) and orbital tuning of the colour reflectance b* (Figure S6). In the record of Site U1338, the sedimentation rates also decreased following the carbonate recovery after the peak warmth event (Holbourn et al., 2014) suggesting similar processes were involved. The interval preceding carbon isotope event CM 6 (14.04-13.94 Ma) exhibited a short decrease followed by an increase in the sedimentation rates (Figures 3c and S6). The short-lived event of low sedimentation rates may have represented a short warm period indicated by lower $\delta^{18}O$ and $\delta^{13}C$. The high sedimentation rates between 13.99 and 13.94 Ma possibly reflect increased opal accumulation (Holbourn et al., 2014) (see also Section 4.2). The sedimentation rates during CM 6 from 13.88 to 13.70 Ma were moderate with about 11 m/Ma, but they increased markedly after the event (13.65-13.44 Ma), which reflects higher productivity and an improvement in carbonate preservation in the colder climate (Holbourn et al., 2005, 2014; Pälike et al., 2012). Although a pronounced increase in the rates is observed in the sedimentation estimates derived from palaeo-magnetic data (Ohneiser et al., 2013) for this interval, the intense increase in the sedimentation rates marks another large offset between both models (Figure S6). It is, therefore, most likely that the different age models with distinct time resolution result in different sedimentation rates.

4.4 Robustness of benthic foraminiferal stable isotopes as palaeoceanographic proxies

Despite the bulk carbonates of Site U1336 being extensively recrystallised (Voigt et al., 2015), the benthic stable isotope record shares the same structure of amplitudes and timing as the records of the better preserved sites nearby (Figures 4 and 7). More importantly, even the finer details of the benthic foraminiferal stable isotope record of Site U1336 agree well with the better preserved high resolution records of Sites U1337 (Tian et al., 2013), U1338 (Holbourn et al., 2014) (Figures 4 and 7) and the high resolution record (~4-9 kyr) of the subtropical ODP Site 1237 (Holbourn et al., 2005, 2007). However, the $^{87}Sr/^{86}Sr$ ratio of bulk sediments at Site U1336 suggests that a late phase of recrystallisation occurred at depths below 100 rmcd (> 20 Ma) (Voigt et al., 2015). Between 14.7-12.5 Ma, the U1336 bulk carbonate Sr/Ca ratios are ~1.80 mmol/mol, but decrease to an average of 1.37 mmol/mol between 16 and 15.3 Ma (Figure 8) (Voigt et al., 2015). This low value is comparable

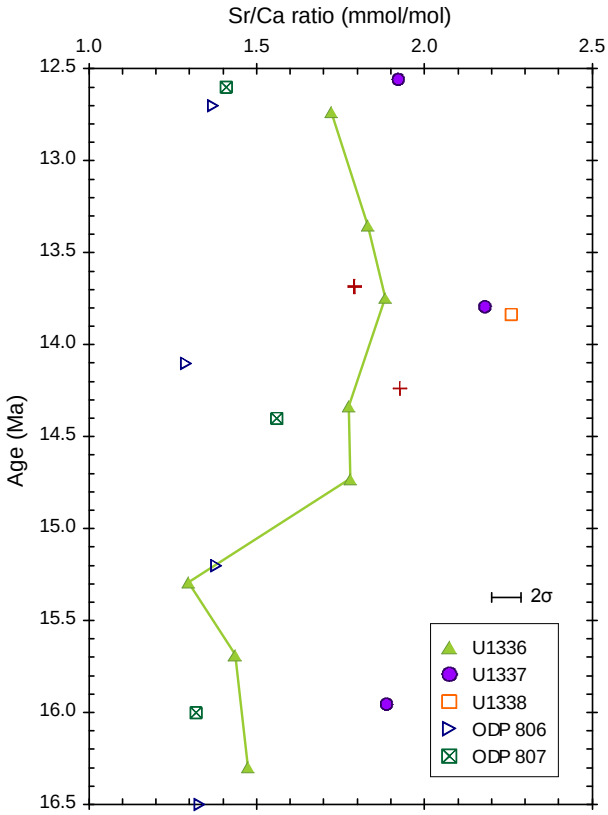

Figure 8. Sr/Ca ratios of bulk carbonate leachates plotted against age (modified after Voigt et al., 2015). Values from ODP Sites 806 and 807 are from Delaney and Linn (1993). Error bars represent the 2σ uncertainty estimates and were estimated from repeated measurements of the same samples.

to the more recrystallised ODP Sites 806 and 807 with average bulk carbonate Sr/Ca ratios of 1.46 and 1.41 mmol/mol, respectively (Figure 8) (Delaney and Lynn, 1993). This suggests that the bulk carbonates of U1336 between 16 to 15.3 Ma are altered (Figures 8 and S1) (Voigt et al., 2015), but we nevertheless find no significant difference in the benthic foraminiferal stable isotope record for this period (Figure 4). Between 15.23 and 15 Ma, a small deviation in the U1336 $\delta^{13}C$ values from the U1338 $\delta^{13}C$ record is observed with a maximum offset of 0.44 ‰ (Figure 4). This difference in $\delta^{13}C$ values between both sites is most likely caused by changes in surface productivity (see Section 4.1). However, the $\delta^{13}C$ records of Sites U1337 and U1336 match well between 15.23-15 Ma, although Site U1337 was, like Site U1338, within the high productivity zone of the equator suggesting similar productivity for both sites, whereas Site U1336 had long travelled out of the high productivity zone. This offset in $\delta^{13}C$ values could, however, also result from carbonate dissolution and subsequent recrystallisation because recrystallised tests tend to have elevated $\delta^{13}C$ values (e.g., Pearson et al., 2001; Sexton et al., 2006). This, in turn, would imply that

Site U1337 is also recrystallised during that time interval, although this has not been reported. Therefore, slight offsets caused by different productivity are the best explanation for the small deviation in $\delta^{13}C$ between Sites U1336 and U1338 between 15.23 and 15 Ma.

Based on data from Oligocene sections from the eastern equatorial Pacific, Edgar et al. (2013) suggested that recrystallisation occurred relatively quickly (< 10 Ma) after burial at shallow depths to maintain the original geochemical signal. This is confirmed in the upper sections of Site U1336, where the radiogenic Sr isotope ($^{87}Sr/^{86}Sr$) data suggest fast recrystallisation of bulk carbonates (within ~1.5 Ma) after burial, but below 100 rmcd the radiogenic Sr isotopes indicate a late phase of recrystallisation (Figure S1) (Voigt et al., 2015). In order to preserve the original $\delta^{18}O$ and $\delta^{13}C$ signal, the benthic tests possibly remained in approximately the same water mass during recrystallisation, thus recording similar temperature and isotopic composition of bottom seawater and pore waters (Schrag et al., 1995; Schrag, 1999; Pearson et al., 2001; Edgar et al., 2013). This implies that the tests recrystallised relatively rapidly (within a few Myrs) in shallow sediment depths, where there was still diffusional exchange between bottom seawater and pore waters (e.g., Schrag et al., 1995; Sexton and Wilson, 2009; Edgar et al., 2013). Although it is still debated whether biogenic and inorganic carbonates precipitate in isotopic equilibrium with seawater, pore waters, in which recrystallisation occurs, possibly reflect $\delta^{18}O$ and $\delta^{13}C$ equilibrium conditions since pore water processes are thought to be very slow and thus are close to isotopic equilibrium (e.g., McCrea, 1950; O'Neil et al., 1969; Kim and O'Neil, 1997; Zeebe, 1999; Zeebe et al., 1999; Dietzel et al., 2009). This is supported by Ca isotopes, which suggest conditions close to equilibrium (e.g., Fantle and DePaolo, 2007; DePaolo 2011; Böhm et al., 2012). In Table 1, the composition of secondary inorganic calcite that would precipitate from Site U1336 pore waters has been estimated. Using these values, the amount of inorganic calcite that would be needed to detect a change in the benthic foraminiferal isotope composition has been calculated (see Section 2.3). The recrystallised $\delta^{18}O$ composition was estimated following two scenarios: 1) early recrystallisation in shallow depths near bottom waters, and 2) a late phase of recrystallisation, as observed at Site U1336 (Voigt et al., 2015), using pore water $\delta^{18}O$ data from nearby sites (Lawrence et al., 1975). For

Table 1. Calculated composition of inorganic calcite and percentage of recrystallisation required to alter benthic foraminiferal stable isotope values detectably (above 2σ measurement uncertainty).

	Time slice (Ma)	Bottom seawater T (°C)[a]	$\delta^{18}O$ seawater (‰ PDB)[b]	$\delta^{18}O$ fractionation factor[c]	$\delta^{18}O$ inorganic calcite (‰)[d]	$\delta^{18}O$ primary calcite (‰)[e]	Percentage recrystallised $\delta^{18}O$ (%) to shift by 0.24 ‰[f]	$\delta^{18}O$ recrystallised (‰)[f]	Average $\delta^{18}O$ (‰) of Site U1336
Early recrys-tallisa-tion	13.5-13.2	5	-0.22	1.0329	-0.20	1.99	11	1.75	2.06
	13.9-13.8	5.9	-0.27	1.0327	-0.25	1.91	11	1.67	2.12
	13.9-13.8	6.1	-0.76	1.0327	-0.75	1.91	9	1.67	2.12
	16.0-15.2	6.2	-0.71	1.0326	-0.70	1.51	11	1.27	1.56
	Time slice (Ma)	Estimated T (°C)[g]	measured $\delta^{18}O$ pore water (‰ PDB)[h]	$\delta^{18}O$ fractionation factor[c]	$\delta^{18}O$ inorganic calcite (‰)[d]	$\delta^{18}O$ primary calcite (‰)[e]	Percentage recrystallised $\delta^{18}O$ (%) to shift by 0.24 ‰[f]	$\delta^{18}O$ recrystallised (‰)[f]	Average $\delta^{18}O$ (‰) of Site U1336
Late phase of recrys-tallisa-tion	13.5-13.2	7.6	-1.19	1.0323	-1.20	1.99	8	1.75	2.06
	13.9-13.8	11.2	-1.97	1.0315	-2.00	1.91	6	1.68	2.12
	16.0-15.2	13.7	-1.78	1.0309	-1.80	1.51	7	1.27	1.56
	16.0-15.2	7.6	-0.51	1.0323	-0.50	1.51	12	1.27	1.56

Table 1. continued

	Time slice (Ma)	Bottom water T (°C)[a]			$\delta^{13}C$ inorganic calcite (‰)[i]	$\delta^{13}C$ primary calcite (‰)[e]	Percentage recrystallised $\delta^{13}C$ (%) to shift by 0.18 ‰[f]	$\delta^{13}C$ recrystallised (‰)[f]	Average $\delta^{13}C$ (‰) of Site U1336
Late phase of recrys-tallisa-tion	13.5-13.2	5			-	0.97	-	-	1.22
	13.9-13.8	5.9			2.07	1.25	22	1.43	1.66
	13.9-13.8	6.1			2.07	1.25	22	1.43	1.66
	16.0-15.2	6.2			2.19	1.54	27	1.72	1.61

[a] Bottom water temperatures were estimated from Lear et al. (2000).

[b] $\delta^{18}O$ of seawater, calculated from benthic foraminiferal Mg temperatures and $\delta^{18}O$ data, were estimated from Lear et al. (2000).

[c] Fractionation factors for the temperatures given were calculated using the equation from Kim and O'Neil (1997).

[d] $\delta^{18}O$ of inorganic calcite was calculated using the equation: $\delta^{18}O_{calcite}$ = fractionation factor α ($\delta^{18}O_{seawater}$ + 1)-1, and the $\delta^{18}O$ of seawater or pore water and fractionation factors in columns 4 and 5.

[e] The stable isotope values are averages for each time slice using the record from Holbourn et al. (2014) assuming good preservation.

[f] Percentages and composition of recrystallised stable isotopes were calculated by: $\delta i_{recrystallised} = (\delta i_{inorganic\ calcite} * x)+(\delta i_{primary\ calcite} * 1-x)$ where x is the fraction of inorganic calcite precipitated during recrystallisation.

[g] Estimated temperatures for the depths of the pore water samples from DSDP Sites 71 and 72 from Lawrence et al. (1975) (column 4) using the geothermal gradient of those sites (Von Herzen et al., 1971).

[h] Measured $\delta^{18}O$ values of pore waters from DSDP Sites 71 and 72, data are from Lawrence et al. (1975).

[i] Bulk carbonate $\delta^{13}C$ (‰) is used as $\delta^{13}C$ of inorganic calcite. Data are from Pälike et al. (2006) from the Mi1 glaciation (~23 Ma) assuming similar values during the major cooling step at 13.9-13.8 Ma; data used for the time slice 16.0-15.2 Ma are averages from 22.5-22.0 Ma with comparable $\delta^{13}C$ values to the Miocene climate optimum. These values of $\delta^{13}C$ = ~2 ‰ are in good agreement with $\delta^{13}C$ model and experimental studies (e.g., Mook, 1986; Zeebe et al., 1999; Walter et al., 2007).

simplicity, it is assumed that the secondary calcite is formed in isotopic equilibrium. The average benthic stable isotope signature of Site U1338 (Holbourn et al., 2014) during each time slice was adopted to represent primary biogenic calcite. The percentages of recrystallised calcite needed to change the benthic $\delta^{18}O$ values significantly are between 6 and 12 % (Table 1). However, the average U1336 $\delta^{18}O$ values are higher than the estimated recrystallised $\delta^{18}O$ composition suggesting that $\delta^{18}O$ is well preserved at Site U1336 for all time slices as recrystallisation would lead to lower $\delta^{18}O$ values (Table 1). The average $\delta^{13}C$ values of Site U1336 are higher than those of U1338 (primary calcite) and therefore suggest detectable recrystallisation of 50 % and 11 % for the time intervals 13.93-13.72 Ma and 16.0-15.2 Ma, respectively (Table 1). However, the $\delta^{18}O$ values indicate very good preservation of the U1336 tests and $\delta^{18}O$ is more sensitive to recrystallisation than $\delta^{13}C$ (e.g., Pearson et al., 2001; Sexton et al., 2006). Therefore, this discrepancy between the $\delta^{13}C$ values of Sites U1336 and U1338 might be explained by their geographic location and thus different surface productivity during the time intervals (see Section 4.1) instead of recrystallisation. Nevertheless, it is surprising that the amount of recrystallisation required to shift the $\delta^{18}O$ detectably is the highest at the time interval 16.0-15.2 Ma (Table 1, row 10). This might suggest low contribution of inorganic calcite during this time interval, although the Sr proxies of the sediment and pore waters (Sr/Ca and $^{87}Sr/^{86}Sr$ ratios) show increased recrystallisation in sediments older than 14.7 Ma (Figure 8) (Voigt et al., 2015). Further, SEM images of the benthic foraminiferal tests of Site U1336 suggest some degree of recrystallisation through all time intervals, which is not supported by the stable isotope data (Table 1). These results suggest that the benthic foraminiferal tests preserve the original geochemical signature during the investigated time intervals (16-13 Ma). Therefore, only minor, if any, recrystallisation occurred early after burial (within a few Myrs) at shallow sediment depths. However, it cannot be ruled out that benthic foraminiferal stable isotope compositions of Site U1336 are more severely affected by recrystallisation in the deeper sediment section (> 100 m, corresponding to > 20 Ma).

Edgar et al. (2013) further suggested that burial depth and sedimentation rates do not influence the recrystallisation of benthic foraminifera. The difference in burial depth between the shallowest (U1336, 174 m) and the deepest buried site (U1337,

450 m) is larger than at the sites investigated by Edgar et al. (2013). Sites U1337 and U1338 experienced higher sedimentation rates than U1336 (Pälike et al., 2010), but $\delta^{18}O$ data of all three sites are nevertheless in good agreement (Figure 4). Although the time slice studied is comparable (~3 Myrs), the resolution of the records compared here is higher with 9 kyr on average for Site U1336 compared to 20 kyr (Edgar et al., 2013). This higher resolution of the data allows a more detailed comparison of the stable isotopes between the sites and shows a good agreement throughout the entire studied time interval. Although the sites investigated by Edgar et al. (2013) comprise older sediments (Eocene-Oligocene) and are thus comparable to Site U1336, the bulk carbonate radiogenic Sr isotopes of Site U1334, one of the sites studied by the authors, do not suggest a later stage of recrystallisation like observed at Site U1336 (Voigt et al., 2015).

Another parameter that would change the foraminiferal $\delta^{18}O$ signature of newly formed recrystallised calcite is the geothermal gradient. The oxygen isotope fractionation is temperature dependent, resulting in lower $\delta^{18}O$ values at higher temperatures with a decrease in the fractionation factor by 0.00023 per Kelvin (Kim and O'Neil, 1997; Watkins et al., 2013). The geothermal gradients of Sites U1337 and U1338 are similar showing values of 32.4°C/km and 34.4°C/km, respectively (Pälike et al., 2010). Unfortunately, no *in-situ* temperatures were measured at Site U1336, but a comparison of pore water Mg/Ca gradients with other sites in the region suggests a much steeper thermal gradient for Site U1336 (~79°C/km) (Voigt et al., 2015), which is considered to be the primary driver of carbonate recrystallisation at this site (Voigt et al., 2015). Nevertheless, the U1336 $\delta^{18}O$ data show no significant offset from the U1337 and U1338 records (Table 1; Figure 4). Furthermore, the temperature range for the investigated depth interval at Site U1336 is 2.4-5.3°C using the geothermal gradient and the bottom temperature of 1.46°C in the study area (Pälike et al., 2010), whereas the sediment temperatures of the depth range corresponding to the time interval 16-13 Ma are twice as high at Sites U1337 and U1338 (Pälike et al., 2010). Therefore and with regard to the good agreement of the stable isotope compositions between the three sites, any influence of the geothermal gradient on $\delta^{18}O$ and $\delta^{13}C$ signatures was obviously too small to cause any significant changes in the isotopic compositions of the benthic foraminiferal tests.

Moreover, benthic foraminifera also have less porous and thicker calcified tests than planktonic foraminifera, which may impede the replacement of the original biogenic calcite with secondary calcite. Therefore, the findings of this study may not hold true for planktonic foraminifera.

4.5 Integrating magnetostratigraphy and isotope stratigraphy

Unfortunately, the palaeo-magnetic signal of Sites U1337 and U1338 has been compromised during the mid-Miocene by reductive diagenesis, possibly by the dissolution of magnetite (Pälike et al., 2010). Our new benthic stable isotope data allows the well resolved palaeo-magnetic stratigraphy of Site U1336 to be transferred to Sites U1337 and U1338 (Figure 4). To assess the reliability of this, we compare the independent orbital tuning of Site U1336 (colour reflectance b*) with the age model based on palaeo-magnetic data (see Section 4.3). The orbital tuning of colour reflectance b* can be directly related to the benthic foraminiferal stable isotopes since the changes in the isotope record are reflected in the lithology of the succession (see Section 4.2). The calculated sedimentation rates of Site U1336 derived by magnetostratigraphy and magnetic palaeo-intensity ("Chron" age model hereafter) (Ohneiser et al., 2013) with the sedimentation rates based on the colour reflectance b* (orbital age model) shows good agreement, but exhibits more variability and detail (Figure S6) (see Section 4.3). The Chron age model for this period relies on relatively few reversals and thus cannot exhibit the detail of orbitally tuned, high resolution records, such as the foraminiferal stable isotope records of Sites U1337, U1338 or the colour reflectance of Site U1336. This may explain the discrepancies between the Chron and orbital age models ranging from 18-171 kyr (Table S2). A recent study showed that the $CaCO_3$ content data of Site U1336 were offset by ~100 kyr at ~17 Ma when the data were adjusted to the Chron age model (Ohneiser et al., 2013) (Keegan Wilson, 2014; see Figure 13 therein). Only two magnetic data points exist between 15.89 and 15.16 Ma, suggesting constant sedimentation rates within this time interval, which clearly does not agree with the detailed sedimentation rates derived from the orbital age model resulting in large offsets within this interval (Table S2) (see Section 4.3). The largest differences between the age models occur within Chrons C5Bn.2n-C5ADn (15.16-14.19 Ma) (Figure S6), where the magnetostratigraphy is less well constrained due to different possible calibrations

(Ohneiser et al., 2013). The time interval thereafter (14.19-13.02 Ma) shows lower offsets with an average of 67 kyr, suggesting a better correlation between the age models except for the short intervals at 13.99-13.94 Ma and 13.65-13.50 Ma, where the sedimentation rates markedly differ (Table S2) (see Section 4.3). These differences between the models most likely result from the amount and choice of tie points, but also suggest that high resolution stable isotopes and colour reflectance records are more sensitive to regional and global events. However, the overall good agreement of the stable isotope records and considering these caveats the mid-Miocene magnetostratigraphy of Site U1336 can be transferred to Sites U1337 and U1338 using our new data.

5. Conclusions

Although the bulk sediments of Site U1336 show increased and persistent recrystallisation in sediments older than 14.7 Ma (Figure 8), the benthic foraminiferal stable isotope record is in good agreement with high resolution records in well preserved cores from Sites U1337 (Tian et al., 2013) and U1338 (Holbourn et al., 2014). Carbon isotope events of the Monterey Excursion can be clearly identified within the investigated interval (16-13 Ma). The absolute values and amplitudes of $\delta^{18}O$ and $\delta^{13}C$ signatures compare well with those from the neighbouring Sites U1337 (Tian et al., 2013) and U1338 (Holbourn et al., 2014) (Figure 4). Despite the relatively coarse time resolution (5.1-17.8 kyr), long eccentricity cycles (400 kyr) are clearly evident, and within the interval of 15.45-14.65 Ma even the short eccentricity cycles (100 kyr) can be distinguished (Figures 3d and 5b). The good agreement of the stable isotope records of Site U1336 with high resolution records of better preserved successions and the orbital cyclicity signals indicate that benthic foraminifera preserved much of the original geochemical signal despite recrystallisation of the bulk sediment. This can be explained by fast recrystallisation (within a few Myrs) after burial at shallow depths. Thus, the tests remained in approximately the same water mass with similar temperature and isotopic composition of bottom seawater and pore waters, resulting in negligible offsets from primary $\delta^{18}O$ and $\delta^{13}C$ values. Moreover, the benthic foraminiferal tests experienced no significant recrystallisation in the deeper sediment sections as is indicated for the

bulk carbonates of that site. Therefore, the benthic foraminifera at such locations can reliably be used for isotope analyses, establishment of stratigraphies, and for palaeoceanographic reconstructions. Further, the strong resemblance of our stable isotope data of Site U1336 to the records of Sites U1337 and U1338 in combination with shipboard scanning results (colour reflectance b*) allows a transfer of the very well resolved palaeo-magnetic results (Ohneiser et al., 2013) to Sites U1337 and U1338.

Acknowledgements

This work was funded by the German Science Foundation, DFG, HA 5751/1-1 and HA 5751/2-1 (PEAT). We thank Isabel Rohr and Julia Langer for preparing the samples and help picking the benthic foraminifera. We further thank Lulzim Haxhiaj, Kirstin Werner, Christelle Not, Andrea Bodenbinder and Fynn Wulf for measuring the stable isotopes. Roy Wilkens kindly provided the U1336 splice image and the data for GRA bulk density and magnetic susceptibility. We also thank Jacek Raddatz, Daniel Gebrigeorgis Yirgaw and Dirk Nürnberg for help with AnalySeries. Steffanie Kraft is acknowledged for helpful discussions at an early stage of the manuscript.

References

Baker P. A., Gieskes J. M., and Elderfield H. (1982) Diagenesis of carbonates in deep-sea sediments – evidence from Sr/Ca ratios and interstitial dissolved Sr^{2+} data. *J. Sediment. Petrol.* **52**, 71-82.

Belanger P. E., Curry W. B., and Matthews R. K. (1981) Core-top evaluation of benthic foraminiferal isotopic ratios for paleo-oceanographic interpretations. *Paleogeogr. Paleoclimatol. Paleoecol.* **33**, 205-220.

Blum P. (1997) Reflectance, Spectrophotometry and Colorimetry. In: *Physical properties handbook: a guide to the shipboard measurement of physical properties of deep-sea cores*, ODP Tech. Note 26.

Böhm F., Eisenhauer A., Tang J., Dietzel M., Krabbenhöft A., Kisakürek B., and Horn C. (2012) Strontium isotope fractionation of planktic foraminifera and inorganic calcite. *Geochim. Cosmochim. Acta* **93**, 300-314.

Bown P. R., Dunkley Jones T., Lees J. A., et al. (2008) A Paleogene calcareous microfossil Konservat-Lagerstätte from the Kilwa Group of coastal Tanzania. *Geol. Soc. Am. Bull.* **120**, 3-12.

Delaney M. L. (1989) Temporal changes in interstitial water chemistry and calcite recrystallization in marine sediments. *Earth Planet. Sci. Lett.* **95**, 23-37.

Delaney M. L. and Linn L. J. (1993) Interstitial water and bulk calcite chemistry, Leg 130, and calcite recrystallization. In: *Proc. ODP. Sci. Res* 130 (eds. W. H. Berger, L. W. Kroenke, T. R. Janecek, et al.). Ocean Drilling Program, pp. 561-572.

DePaolo D. J. (2011) Surface kinetic model for isotopic and trace element fractionation during precipitation of calcite from aqueous solutions. *Geochim. Cosmochim. Acta* **75**, 1039-1056.

Dietzel M., Tang J., Leis A., and Köhler S. J. (2009) Oxygen isotopic fractionation during inorganic calcite precipitation – Effects of temperature, precipitation rate and pH. *Chem. Geol.* **268**, 107-115.

Drury A. J., Lee G. P., Pennock G. M., and John C. M. (2014) Data report: Late Miocene to early Pliocene coccolithophore and foraminiferal preservation at Site U1338 from scanning electron microscopy. In: *Proc. IODP,* 320/321: Tokyo (eds. H. Pälike, et al.). (Integrated Ocean Drilling Program Management International, Inc.). doi:10.2204/iodp.proc.320321.218.2014.

Edgar K. M., Pälike H., and Wilson P. A. (2013) Testing the impact of diagenesis on the $\delta^{18}O$ and $\delta^{13}C$ of benthic foraminiferal calcite from a sediment burial depth transect in the equatorial Pacific. *Paleoceanography* **28**, 468-480.

Elderfield H. and Gieskes J. M. (1982) Sr isotopes in interstitial waters of marine sediments from Deep Sea Drilling Project cores. *Nature* **300**, 493-497.

Fantle M. S. and DePaolo D. J. (2007) Ca isotopes in carbonate sediment and pore fluid from ODP Site 807A: The Ca^{2+}(aq)-calcite equilibrium fractionation factor and calcite recrystallization rates in Pleistocene sediments. *Geochim. Cosmochim. Acta* **71**, 2524-2546.

Feldmann G. C. (2014) Monthly chlorophyll concentration map, June 2012-2014, Map V20121532014181.L3m, NASA Ocean Color Web.

Flower B. P. and Kennett J. P. (1993) The middle Miocene ocean/climate transition: High-resolution oxygen and carbon isotopic records from DSDP Site 588A, southwest Pacific. *Paleoceanography* **8**, 811-843.

Flower B. P. and Kennett J. P. (1994) The middle Miocene climatic transition: East Antarctic ice sheet development, deep ocean circulation and global carbon cycling. *Paleogeogr. Paleoclimatol. Paleoecol.* **108**, 537-555.

Fox L. R. and Wade B. S. (2013) Systematic taxonomy of early-middle Miocene planktonic foraminifera from the equatorial Pacific Ocean: Integrated Ocean Drilling Program, Site U1338. *J. Foramin. Res.* **43**, 374-405.

Gieskes J. M., Elderfield H., and Palmer M. R. (1986) Strontium and its isotopic composition in interstitial waters of marine carbonate sediments. *Earth Planet. Sci. Lett.* **77**, 229-235.

Gorgas T. J. and Wilkens R. H. (2002) Sedimentation rates off SW Africa since the late Miocene deciphered from spectral analyses of borehole and GRA bulk density profiles: ODP Sites 1081-1084. *Mar. Geol.* **180**, 29-47.

Hodell D. A., Curtis J. H., Sierro F. J., and Raymo M. E. (2001) Correlation of late Miocene to early Pliocene sequences between the Mediterranean and North Atlantic. *Paleoceanography* **16**, 164-178.

Hodell D. A., Kamenov G. D., Hathorne E. C., Zachos J. C., Röhl U., and Westerhold T. (2007) Variations in the strontium isotope composition of seawater during the Paleocene and early Eocene from ODP Leg 208 (Walvis Ridge). *Geochem. Geophys. Geosyst.* **8**, Q09001, doi:10.1029/2007GC001607.

Holbourn A., Kuhnt W., Schulz M., and Erlenkeuser H. (2005) Impacts of orbital forcing and atmospheric carbon dioxide on Miocene ice-sheet expansion. *Nature* **438**, 483-487.

Holbourn A., Kuhnt W., Schulz M., Flores J.-A., and Andersen N. (2007) Orbitally-paced climate evolution during the middle Miocene "Monterey" carbon-isotope excursion. *Earth Planet. Sci. Lett.* **261**, 534-550.

Holbourn A., Kuhnt W., Lyle M., Schneider L., Romero O., and Andersen N. (2014) Middle Miocene climate cooling linked to intensification of eastern equatorial Pacific upwelling. *Geology* **42**, 19-22.

Keegan Wilson J. (2014) Early Miocene carbonate dissolution in the eastern equatorial Pacific. Ph. D. thesis, Texas A&M University.

Kim S. T. and O'Neil J. R. (1997) Equilibrium and nonequilibrium oxygen isotope effects in synthetic carbonates. *Geochim. Cosmochim. Acta* **61**, 3461-3475.

Kirtland Turner S. (2014) Pliocene switch in orbital-scale carbon cycle/climate dynamics. *Paleoceanography* **29**, 1256-1266.

Laskar J., Robutel P., Joutel F., Gastineau M., Correia A., and Levrard B. (2004) A long term numerical solution for the insolation quantities of the Earth. *Astron. Astrophys.* **428**, 261-285.

Lawrence J. R., Gieskes J. M., and Broecker W. S. (1975) Oxygen isotope and cation composition of DSDP pore waters and the alteration of Layer II basalts. *Earth Planet. Sci. Lett.* **27**, 1-10.

Lear C. H., Elderfield H., and Wilson P. A. (2000) Cenozoic Deep-Sea Temperatures and Global Ice Volumes from Mg/Ca in Benthic Foraminiferal Calcite. *Science* **287**, 269-272.

Lyle M., Olivarez Lyle A., Gorgas T., Holbourn A., Westerhold T., Hathorne E., Kimoto K., and Yamamoto S. (2012) Data report: Raw and normalized elemental data along the Site U1338 splice from X-ray fluorescence scanning. In: *Proc. IODP,* 320/321: Tokyo (eds. H. Pälike, et al.). (Integrated Ocean Drilling Program Management International, Inc.). doi:10.2204/iodp.proc.320321.203.2012.

Ma W. T., Tian J., Li Q. Y., and Wang P. X. (2011) Simulation of long eccentricity (400-kyr) cycle in ocean carbon reservoir during Miocene climate optimum: Weathering and nutrient response to orbital change. *Geophys. Res. Lett.* 38, L10701, doi:10.1029/2011GL047680.

Mayer L. A. (1979) Deep-sea carbonates: acoustic, physical, and stratigraphic properties. *J. Sediment. Petrol.* **49**, 819-836.

McArthur J. M., Howarth R. J., and Baily T. R. (2001) Strontium isotope stratigraphy: LOWESS version 3: best fit to the marine Sr-isotope curve for 0-509 Ma and accompanying look-up table for deriving numerical age. *J. Geol.* **109**, 155-170.

McCrea J. M. (1950) On the isotopic chemistry of carbonates and a paleotemperature scale. *J. Chem. Phys.* **18**, 849-857.

Miller K. G., Wright J. D., and Fairbanks R. G. (1991) Unlocking the ice house: Oligocene-Miocene oxygen isotopes, eustasy, and margin erosion. *J. Geophys. Res.* **96**, 6829-6848.

Mook W. G. (1986) ^{13}C in atmospheric CO_2. *Neth. J. Sea Res.* **20**, 211-223.

Ohneiser C., Acton G., Channell J. E. T., Wilson G. S., Yamamoto Y., and Yamazaki T. (2013) A middle Miocene relative paleointensity record from the Equatorial Pacific. *Earth Planet. Sci. Lett.* **374**, 227-238.

O'Neil J. R., Clayton R. N., and Mayeda T. K. (1969) Oxygen isotope fractionation in divalent metal carbonates. *J. Chem. Phys.* **51**, 5547-5558.

Paillard D., Labeyrie L., and Yiou P. (1996) Macintosh Program Performs Time-Series Analysis. *Eos, Trans*. *Am. Geophys. Union* **77**, 379.

Pälike H., Norris R. D., Herrle J. O., Wilson P. A., Coxall H. K., Lear C. H., Shackleton N. J., Tripati A. K., and Wade B. S. (2006) The Heartbeat of the Oligocene Climate System. *Science* **314**, 1894-1898.

Pälike H., Lyle M., Nishi H., Raffi I., Gamage K., Klaus A., and the Expedition 320/321 Scientists (2010) *Proc. IODP*, 320/321: Tokyo (Integrated Ocean Drilling Program Management International, Inc.).

Pälike H., Lyle M. W., Nishi H., et al. (2012) A Cenozoic record of the equatorial Pacific carbonate compensation depth. *Nature* **488**, 609-614.

Pearson P. N. and Burgess C. E. (2008) Foraminifer test preservation and diagenesis: comparison of high latitude Eocene sites. *Geol. Soc. London, Spec. Pub.* **303**, 59-72.

Pearson P. N., Ditchfield P. W., Singano J., Harcourt-Brown K. G., Nicholas C. J., Olsson R. K., Shackleton N. J., and Hall M. A. (2001) Warm tropical sea surface temperatures in the Late Cretaceous and Eocene epochs. *Nature* **413**, 481-487.

Pearson P. N., van Dongen B. E., Nicholas C. J., Pancost R. D., Schouten S., Singano J. M., and Wade B. S. (2007) Stable warm tropical climate through the Eocene epoch. *Geology* **35**, 211-214.

Richter F. M. (1993) Fluid flow in deep-sea carbonate: estimates based on porewater Sr. *Earth Planet. Sci. Lett.* **119**, 133-141.

Schrag D. P. (1999) Effects of diagenesis on the isotopic record of late Paleogene tropical sea surface temperatures. *Chem. Geol.* **161**, 215-224.

Schrag D. P., DePaolo D. J., and Richter F. M. (1995) Reconstructing past sea-surface temperatures - Correcting for diagenesis of bulk marine carbonate. *Geochim. Cosmochim. Acta* **59**, 2265-2278.

Sexton P. F. and P. A. Wilson (2009) Preservation of benthic foraminifera and reliability of deep-sea temperature records: Importance of sedimentation rates, lithology, and the need to examine test wall structure. *Paleoceanography* **24**, PA2208, doi:10.1029/2008PA001650.

Sexton P. F., Wilson P. A., and Pearson P. N. (2006) Microstructural and geochemical perspectives on planktic foraminiferal preservation: "Glassy" versus "Frosty". *Geochem. Geophys. Geosyst.* **7**, 1-29.

Shackford J. K., Lyle M., Wilkens R., and Tian J. (2014) Data report: raw and normalized elemental data along the Site U1335, U1336, and U1337 splices from X-ray fluorescence scanning. In: *Proc. IODP,* 320/321: Tokyo (eds. H. Pälike, et al.). (Integrated Ocean Drilling Program Management International, Inc.). doi:10.2204/iodp.proc.320321.216.2014.

Shackleton N. J. and Kennett J. P. (1975) Paleotemperature history of the Cenozoic and the initiation of Antarctic glaciation: Oxygen and carbon analyses in DSDP Sites 277, 279, and 281. In: *Init. Repts. DSDP* 29 (eds. J. P. Kennett, et al.). Deep Sea Drilling Project,

pp. 743-755, doi:10.2973/dsdp.proc.29.117.1975.

Shevenell A. E., Kennett J. P., and Lea D. W. (2004) Middle Miocene Southern Ocean Cooling and Antarctic Cryosphere Expansion. *Science* **305**, 1766-1770.

Shevenell A. E., Kennett J. P., and Lea D. W. (2008) Middle Miocene ice sheet dynamics, deep-sea temperatures, and carbon cycling: A Southern Ocean perspective. *Geochem. Geophys. Geosyst.* **9**, Q02006, doi:10.1029/2007GC001736.

Stewart D. R. M., Pearson P. N., Ditchfield P. W., and Singano J. M. (2004) Miocene tropical Indian Ocean temperatures: evidence from three exceptionally preserved foraminiferal assemblages from Tanzania. *J. Afr. Earth Sci.* **40**, 173-190.

Stout P. M. (1985) Interstitial water chemistry and diagenesis of biogenic sediments from the eastern equatorial Pacific, Deep Sea Drilling Project Leg 85. In: *Init. Repts. DSDP* 85 (eds. L. Mayer, E. Theyer, et al.). Deep Sea Drilling Project, pp. 805-820.

Tian J., Yang M., Lyle M. W., Wilkens R., and Shackford J. K. (2013) Obliquity and long eccentricity pacing of the Middle Miocene climate transition. *Geochem. Geophys. Geosyst.* **14**, 1740-1755.

Tian J., Ma W., Lyle M. W., and Shackford J. K. (2014) Synchronous mid-Miocene upper and deep oceanic $\delta^{13}C$ changes in the east equatorial Pacific linked to ocean cooling and ice sheet expansion. *Earth Planet. Sci. Lett.* **406**, 72-80.

Vincent E. and Berger W. H. (1985) Carbon dioxide and polar cooling in the Miocene: The Monterey hypothesis. In*: The Carbon Cycle and Atmospheric CO_2: Natural Variations Archean to Present* (eds. E. T. Sundquist and W. S. Broecker). Amer. Geophys. Union Geophys. Monogr. 32, pp. 455-468.

Voigt J., Hathorne E. C., Frank M., Vollstaedt H. and Eisenhauer A. (2015) Variability of carbonate diagenesis in equatorial Pacific sediments deduced from radiogenic and stable Sr isotopes. *Geochim. Cosmochim. Acta* **148**, 360-377.

Von Herzen R. P., Fiske R. J., and Sutton G. H. (1971) Geothermal measurements on Leg 8. In: *Init. Repts. DSDP* 8 (eds. J. I. Tracey, G. H. Sutton, W. D. Nesteroff, et al.). Deep Sea Drilling Project, pp. 837-849.

Walter L. M., Ku T. C. W., Muehlenbachs K., Patterson W. P., and Bonnell L. (2007) Controls on the $\delta^{13}C$ of dissolved inorganic carbon in marine pore waters: An integrated case study of isotope exchange during syndepositional recrystallization of biogenic carbonate sediments (South Florida Platform, USA). *Deep-Sea Res. II* **54**, 1163-1200.

Warny S., Askin A. R., Hannah M. J., Mohr B. A. R., Raine J. I., Harwood D. N., Florindo F., and the SMS Science Team (2009) Palynomorphs from a sediment core reveal a sudden remarkably warm Antarctica during the middle Miocene. *Geology* **37**, 955-958.

Watkins J. M., Nielsen L. C., Ryerson F. J., and DePaolo D. J. (2013) The influence of kinetics on the oxygen isotope composition of calcium carbonate. *Earth Planet. Sci. Lett.* **375**, 349-360.

Wilkens R. H., Dickens G. R., Tian J., Backman J., and the Expedition 320/321 Scientists (2013) Revised composite depth scales for Sites U1336, U1337, and U1338. In: *Proc. IODP,* 320/321: Tokyo (eds. H. Pälike, et al.). (Integrated Ocean Drilling Program Management International, Inc.). doi:10.2204/iodp.proc.320321.209.2013.

Woodruff F. and Savin S. (1991) Mid-Miocene isotope stratigraphy in the deep sea: High resolution correlations, paleoclimatic cycles, and sediment preservation. *Paleoceanography* **6**, 755-806.

Zachos J., Pagani M., Sloan L., Thomas E., and Billups K. (2001a) Trends, Rhythms, and Aberrations in Global Climate 65 Ma to Present. *Science* **292**, 686-693.

Zachos J. C., Shackleton N. J., Revenaugh J. S., Palike H., and Flower B. P. (2001b) Climate Response to Orbital Forcing Across the Oligocene-Miocene Boundary. *Science* **292**, 274-278.

Zachos J. C., Dickens G. R., and Zeebe R. E. (2008) An early Cenozoic perspective on greenhouse warming and carbon-cycle dynamics. *Nature* **451**, 279-283.

Zachos J. C., McCarren H., Murphy B., Röhl U., and Westerhold T. (2010) Tempo and scale of late Paleocene and early Eocene carbon isotope cycles: Implications for the origin of hyperthermals. *Earth Planet. Sci. Lett.* **299**, 242-249.

Zeebe R. E. (1999) An explanation of the effect of seawater carbonate concentration on foraminiferal oxygen isotopes. *Geochim. Cosmochim. Acta* **63**, 2001-2007.

Zeebe R. E., Bijima J., and Wolf-Gladrow D. A. (1999) A diffusion-reaction model of carbon isotope fractionation in foraminifera. *Mar. Chem.* **64**, 199-227.

Supplementary Material

Table S1. Age tie points between colour reflectance b* values given in revised depths (Wilkens et al., 2013) and the orbital solution for eccentricity from Laskar et al. (2004) used for the tuning of Site U1336.

Depth (rmcd)	Age (Ma)	Sedimentation rates (m/Ma)
11.83	12.984	11.4
12.32	13.027	11.2
12.78	13.068	10.0
13.38	13.128	11.1
13.94	13.178	12.9
16.33	13.364	11.7
17.38	13.453	15.9
18.32	13.513	25.5
19.57	13.562	20.8
21.79	13.669	5.2
22.03	13.715	11.6
22.60	13.764	10.5
23.43	13.843	11.2
24.06	13.899	9.0
24.46	13.943	17.4
25.53	14.005	3.8
25.72	14.055	8.2
26.79	14.186	13.7
33.39	14.666	10.1
33.93	14.720	14.5
35.46	14.826	12.2
36.19	14.885	6.8
36.51	14.932	10.0
37.05	14.986	12.0
38.42	15.100	10.6
38.99	15.154	9.3
39.97	15.260	4.4
40.72	15.431	12.8
41.45	15.488	18.2
42.33	15.536	14.1
43.08	15.589	9.3
43.62	15.648	6.8
44.32	15.752	21.0
45.19	15.793	16.4
45.84	15.833	11.9
48.25	16.034	13.6
48.83	16.077	13.6

Table S2. Comparison of Site U1336 age models derived from magnetostratigraphy and colour reflectance b* for the polarity chron reversals between 16 and 13 Ma.

Depth (rmcd)[a]	Polarity chron	Age chrons (Ma)[a]	Age colour reflectance b* (Ma)	Offset (kyr)
12.37	C5Ar.3r/C5AAn	13.015	12.970	45
13.87	C5AAn/C5AAr	13.183	13.096	87
15.74	C5AAr/C5ABn	13.369	13.253	116
19.34	C5ABn/C5ABr	13.605	13.556	49
21.24	C5ABr/C5ACn	13.734	13.716	18
24.68	C5ACn/C5ACr	14.095	14.005	90
25.32	C5ACr/C5ADn	14.194	14.059	135
30.03	C5ADn/C5ADr	14.581	14.455	126
32.26	C5ADr/C5Bn.1n	14.784	14.642	142
33.09	C5Bn.1n/C5Bn.1r	14.877	14.712	165
34.87	C5Bn.1r/C5Bn.2n	15.032	14.862	170
36.38	C5Bn.2n/C5Br	15.160	14.989	171
48.42	C5Br/C5Cn.1n	15.898	16.001	-103

[a] Depths and ages for the polarity chrons are from Ohneiser et al. (2013).

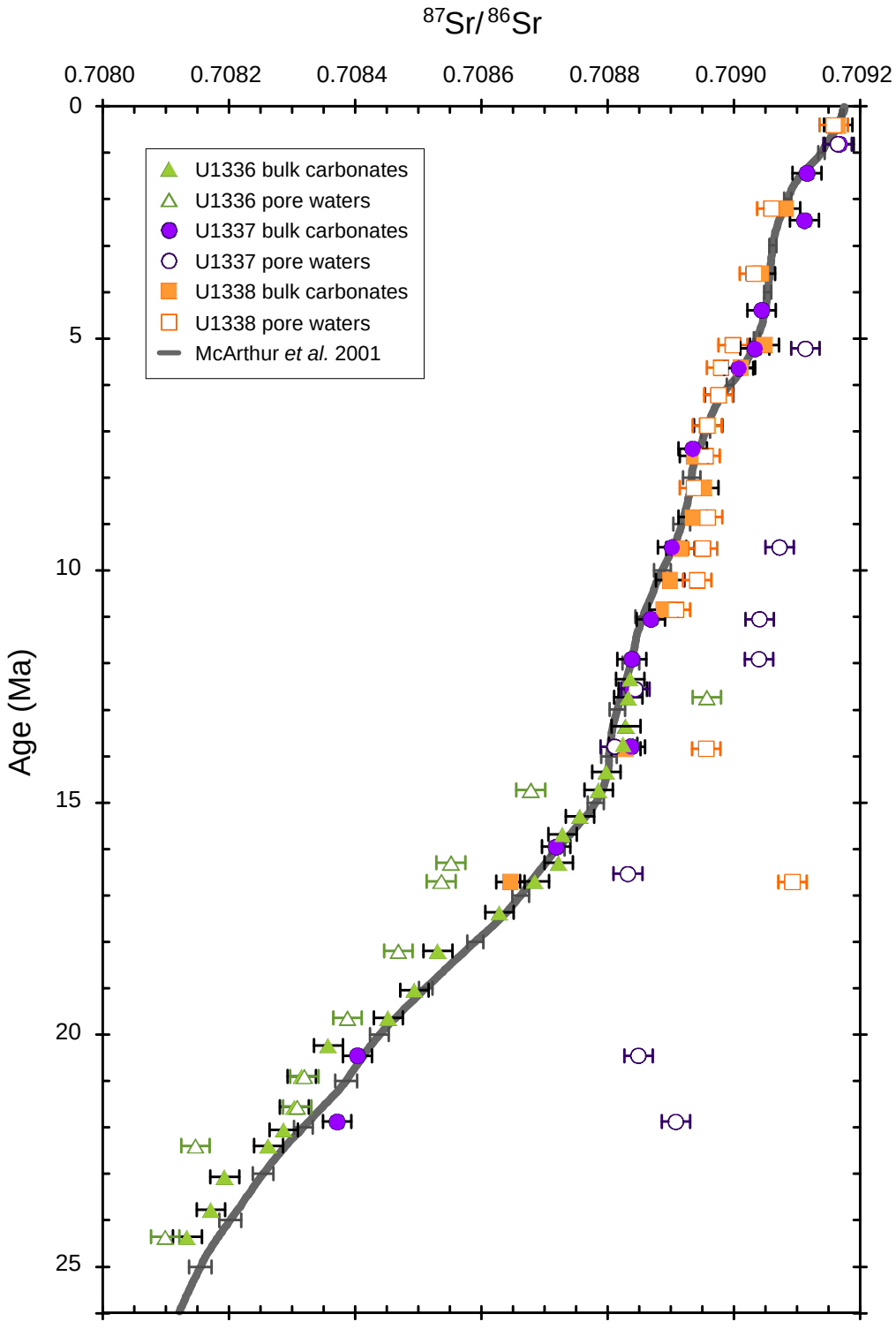

Figure S1. $^{87}Sr/^{86}Sr$ of bulk carbonate leachates shown versus age (modified after Voigt et al., 2015). The $^{87}Sr/^{86}Sr$ of contemporaneous seawater is illustrated by the grey line (McArthur et al., 2001, LOWESS fit, version 3) and represents the contemporary seawater composition based on a compilation of 13 published sources for shown numerical ages. Error bars of the seawater Sr isotope curve represent the 2σ uncertainties of the data compiled by McArthur et al. (2001). Error bars denote the 2σ uncertainties of repeated measurements of IAPSO seawater.

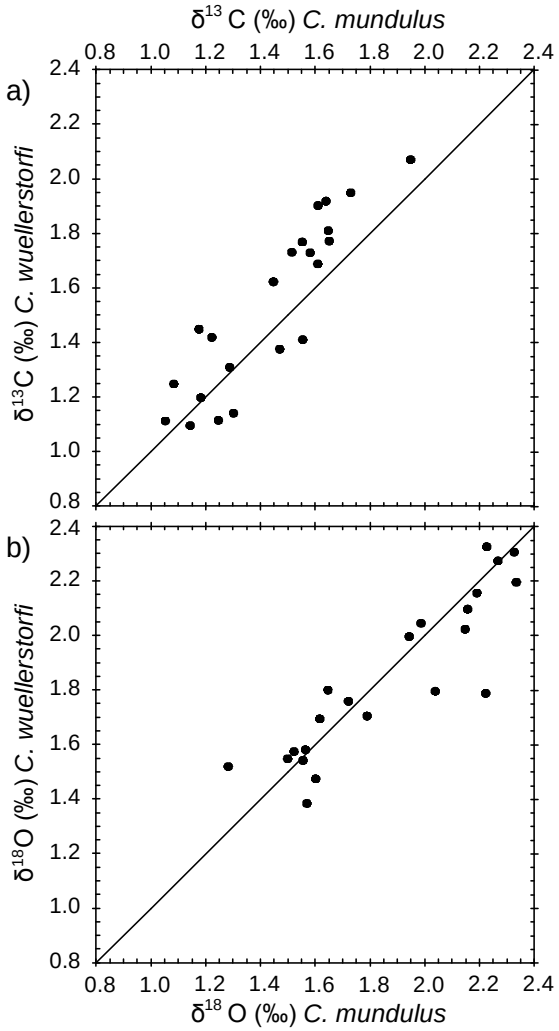

Figure S2. Crossplot of the benthic foraminiferal species used for a) stable carbon and b) oxygen analyses (*C. wuellerstorfi* and *C. mundulus*). The line shows a 1:1 relationship with zero offset between the species.

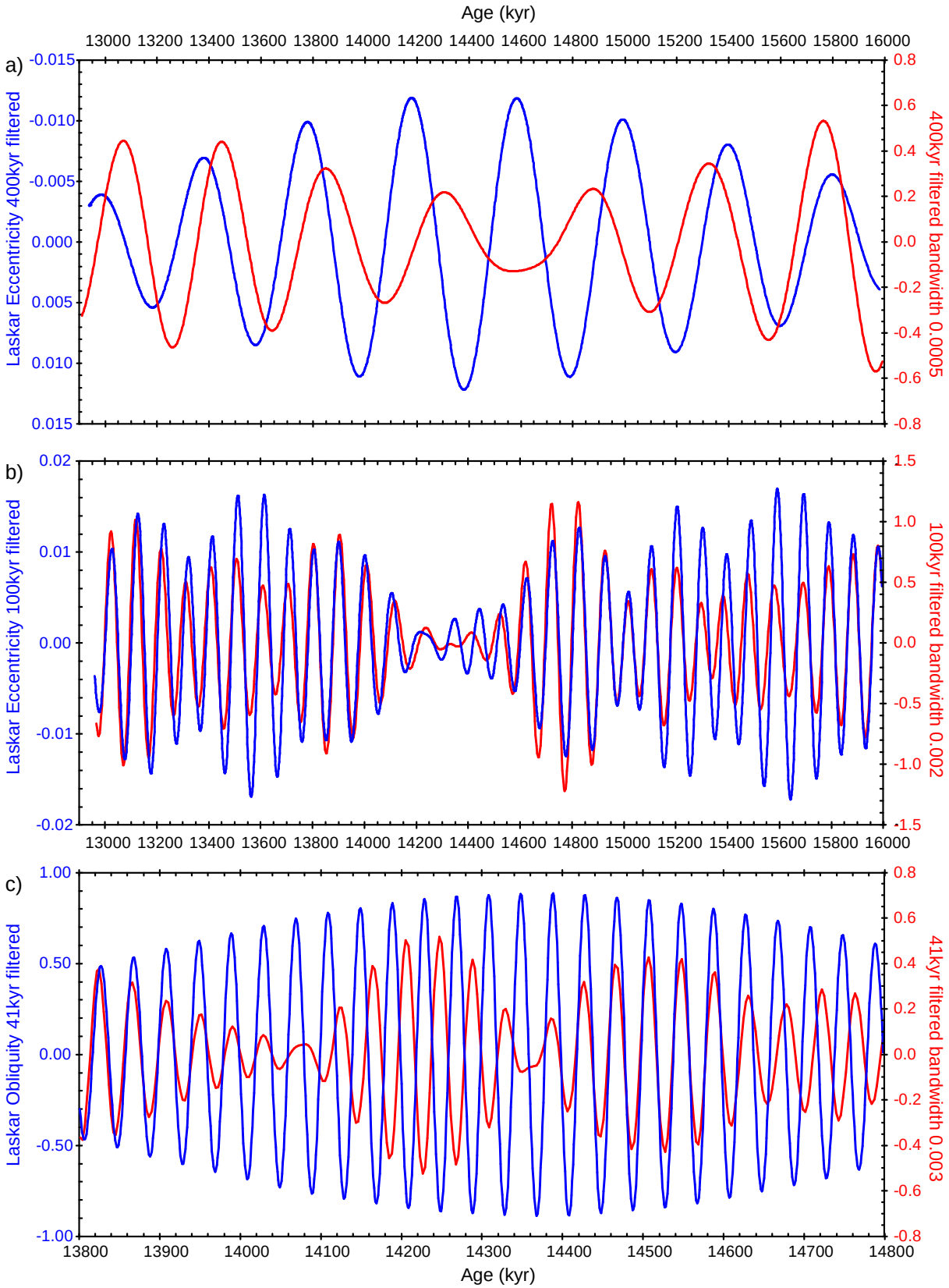

Figure S3. Comparison of the filtered high resolution data of colour reflectance b* with the filtered orbital solution of Laskar et al. (2004) (blue). a) The colour reflectance b* is shown as black line and display the records filtered for 400 kyr, b) 100 kyr and c) 41 kyr. The data are from Wilkens et al. (2013).

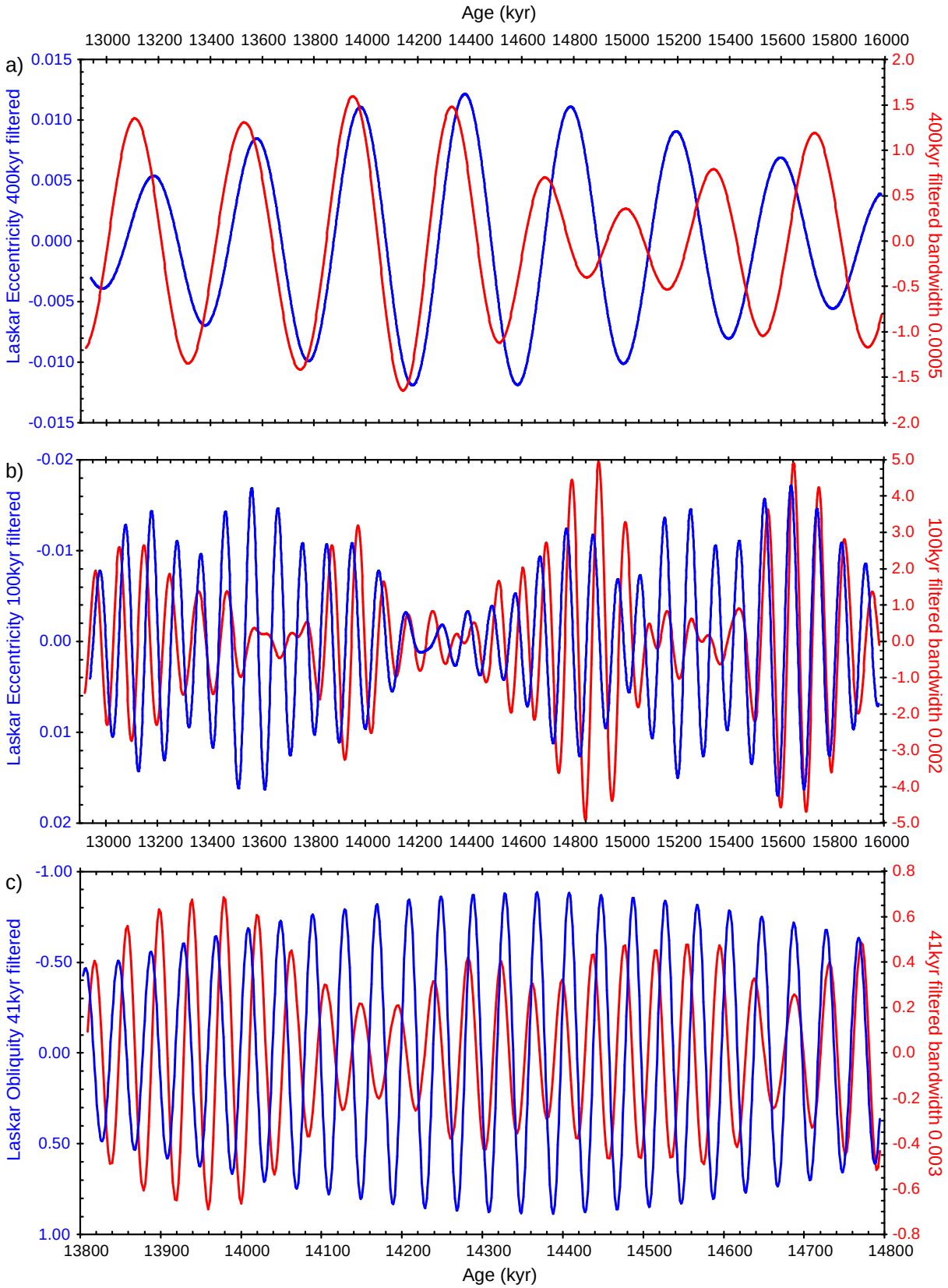

Figure S4. Comparison of the filtered high resolution data of magnetic susceptibility with the filtered orbital solution of Laskar et al. (2004) (blue). a) The magnetic susceptibility is shown as black line and display the records filtered for 400 kyr, b) 100 kyr and c) 41 kyr (lower panel). The data are from Wilkens et al. (2013).

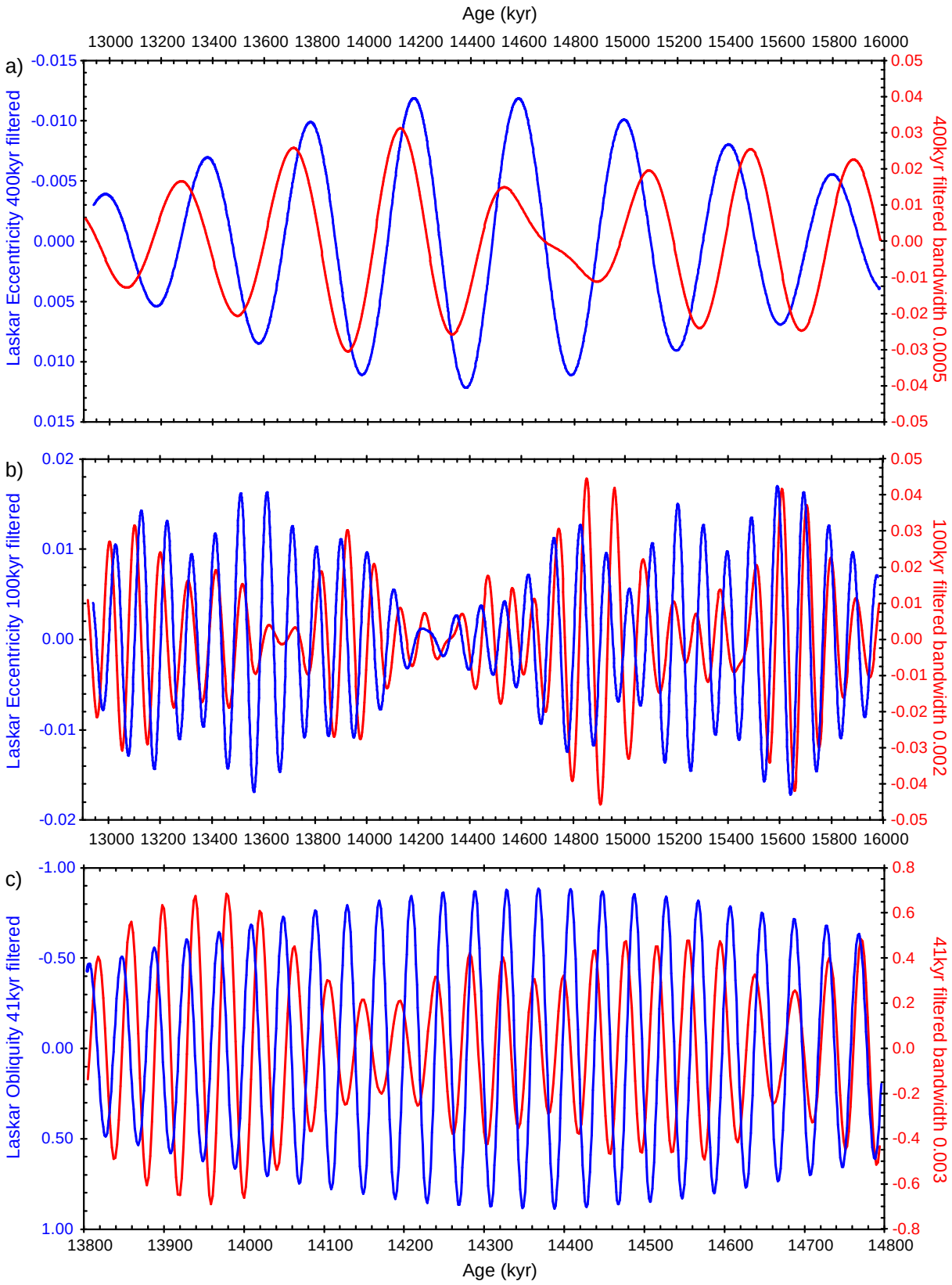

Figure S5. Comparison of the filtered high resolution data of GRA bulk density with the filtered orbital solution of Laskar et al. (2004) (blue). a) The GRA bulk density is shown as black line and display the records filtered for 400 kyr, b) 100 kyr and c) 41 kyr (lower panel). The data are from Wilkens et al. (2013).

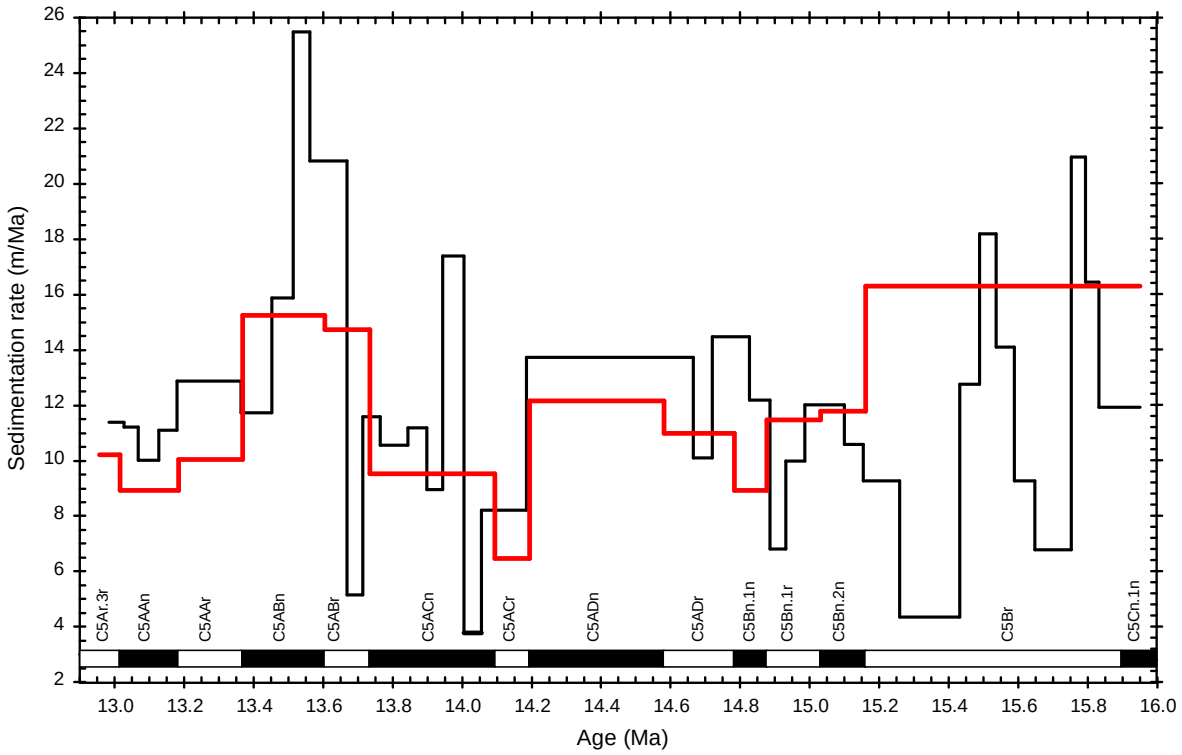

Figure S6. Comparison of the calculated sedimentation rates of Site U1336 based on the age model of colour reflectance b* (black) and the age model derived from palaeo-magnetic data in red (Ohneiser et al., 2013). The polarity stratigraphy of Site U1336 (Pälike et al., 2010; Ohneiser et al., 2013) is given for comparison.

Chapter 3

Variable preservation of geochemical proxy signatures in recrystallised planktonic foraminifera

Janett Voigt[a,*], Ed C. Hathorne[a], Martin Frank[a] and Jan Fietzke[a]

[a]GEOMAR Helmholtz Centre for Ocean Research Kiel, Wischhofstr. 1-3, 24148 Kiel, Germany

*Corresponding author, e-mail address: jvoigt@geomar.de

A version of this chapter is going to be submitted

Abstract

The calcite tests of foraminifera used for reconstructing oceanic and climatic conditions in the past can be altered after deposition by recrystallisation processes replacing the original biogenic calcite with secondary calcite. The exact consequences of recrystallisation for the elemental composition of foraminifera are still not well known. It is clear, however, that detailed knowledge on the degree of preservation of foraminifera is vital to obtain reliable geochemical proxy data. Here we present laser ablation ICP-MS derived element/Ca ratio depth profiles through test walls of the planktonic foraminiferal species *Dentoglobigerina venezuelana* for specific time intervals from eastern equatorial Pacific sediments recovered during the Integrated Ocean Drilling Program (IODP) Expedition 320/321. One of the goals of this study was to investigate the effects of carbonate recrystallisation. Ancient tests from sediment sections between 7 and 27 Ma exhibit intratest Mg/Ca and Mn/Ca heterogeneity comparable to modern foraminifera, whereas Sr/Ca ratios do generally not show such variations across the test walls. However, for the majority of the tests from the older time intervals at 22.8 and 27 Ma, Sr/Ca ratios decrease by more than 0.2 mmol/mol from the outer towards the inner test wall, clearly indicating recrystallisation. Site U1336 shows the highest percentages of recrystallised tests, which is also evident in SEM images. Moreover, several Sr parameter (Sr^{2+}, Sr/Ca,

$^{87}Sr/^{86}Sr$) indicate that bulk carbonates of this site are extensively altered caused by an inferred strong geothermal gradient at this site. SEM images indicate increasing alteration of the tests with age but also suggest different degrees of recrystallisation of individual tests within the same sediment samples. Decreasing Sr/Ca and increasing Mn/Ca ratios towards the inner calcite suggest that the submicron sized crystals of the inner layers are more susceptible to recrystallisation, most likely due to their higher surface area. Although a high percentage of the tests of the older time intervals is recrystallised, the Mg/Ca heterogeneity is still preserved and average values do not significantly differ from Mg/Ca values of modern foraminifera. This implies that these tests still retained most of their original Mg/Ca signal and can reliably be used for temperature reconstructions.

1. Introduction

The elemental and isotopic composition of calcite tests of foraminifera extracted from marine sediments record various environmental parameters, which are widely used to reconstruct oceanic and climatic conditions in the past, such as seawater temperature, salinity and global ice volume (e.g., Lear et al., 2000; Zachos et al., 2001, 2008). However, ancient foraminiferal tests are altered by recrystallisation after deposition resulting in significant changes of stable isotope composition and element/Ca ratios, which bias the reconstructions of palaeo-temperatures and the climate of the past (e.g., Pearson et al., 2001; Sexton et al., 2006). Therefore, it is important to quantify the impacts of recrystallisation on proxy data obtained from foraminiferal tests in order to extract reliable palaeo-environmental information from tests with variable preservation.

In recent years, micro-analytical methods such as laser ablation inductively coupled plasma mass spectrometry (LA-ICP-MS), electron microprobe mapping (EMP) and nanoscale secondary ion mass spectrometry (NanoSIMS) have significantly improved our understanding of biomineralisation and trace metal distribution in foraminiferal test walls revealing how foraminifera record environmental parameters (e.g., Eggins et al., 2003, 2004; Hathorne et al., 2003; Kunioka et al., 2006; Vetter et al., 2013a; Spero et al., 2015). LA depth profiling and EMP analyses showed that

trace elements are heterogeneously distributed within the tests (Eggins et al., 2003; Hathorne et al., 2003, 2009; Kunioka et al., 2006; Sadekov et al., 2010; Creech et al., 2010; Bolton and Marr, 2013; Vetter et al., 2013b) implying that ontogenetic variability (Bolton et al., 2011; van Raden et al., 2011; Jonkers et al., 2012) and seasonal or even diurnal signals (Eggins et al., 2004; Sadekov et al., 2008; Vetter et al., 2013a; Spero et al., 2015) are incorporated into the tests that can be identified by the high spatial resolution these techniques offers. Both methods have the advantage that sample preparation is straightforward and extensive cleaning of the tests prior to analysis is not necessary (Eggins et al., 2003). At the same time the efficiency of different cleaning protocols for conventional analyses can be assessed using LA-ICP-MS (e.g., Hathorne et al., 2003; Pena et al., 2005, 2008; Marr et al., 2013; Vetter et al., 2013b). These techniques are powerful tools to identify diagenetic or contaminant phases associated with foraminiferal tests, which bias many palaeo-climatic records (Brown and Elderfield, 1996; Pena et al., 2005; Regenberg et al., 2007; Creech et al., 2010; Sadekov et al., 2010; Bolton et al., 2011). Post-analytical data processing allows the extraction of pristine calcite domains providing reliable data (Reichart et al., 2003; Creech et al., 2010; Kozdon et al., 2013). Since LA-ICP-MS is microdestructive (Hathorne et al., 2003; Pena et al., 2008; Creech et al., 2010; Bolton et al., 2011), multiple analyses are possible to further quantify the preservation state or to accurately determine the isotopic compositions of the foraminiferal tests.

Mg/Ca ratios of foraminiferal tests are widely used to reconstruct past seawater temperatures (e.g., Nürnberg et al., 1996; Lea et al., 1999; Dekens et al., 2002; Anand et al., 2003). Several studies indicate that Mg/Ca ratios measured by LA-ICP-MS also allow reliable and accurate reconstruction of palaeo-temperatures (Eggins et al., 2003; Sadekov et al., 2008, 2010; Hathorne et al., 2009; Creech et al., 2010). Mg/Ca ratios can also be used for the assessment of diagenetic overgrowth, but this turned out not to be straightforward since some studies found decreasing Mg/Ca (Brown and Elderfield, 1996; Lea et al., 2000; Rosenthal et al., 2000) and others increasing Mg/Ca ratios (Sexton et al., 2006; Creech et al., 2010; Kozdon et al., 2013) as a consequence of recrystallisation. Therefore, it is important to better understand how exactly recrystallisation impacts the elemental composition of foraminiferal tests. Sr/Ca ratios have long been used to identify and assess

diagenetic alteration (e.g., Matter et al., 1975; Baker et al., 1982; Elderfield et al., 1982; Brown and Elderfield, 1996) given that lower amounts of Sr are incorporated into secondary calcite (e.g., Baker et al., 1982; Delaney, 1989). Thus, secondary calcite contributions result in decreased Sr/Ca ratios of recrystallised tests. Sr/Ca and Mg/Ca ratios vary species-specifically due to distinct calcification processes and calcification rates (e.g., Elderfield et al., 1982; Stoll et al., 1999; Kisakürek et al., 2008). Recent planktonic foraminifera exhibit values of 1-2 mmol/mol and 1-10 mmol/mol, respectively (e.g., Rosenthal et al., 1997; Russell et al., 2004). Mn/Ca ratios also provide valuable information about the amount of diagenetic overgrowths. Elevated values have been reported for recrystallised tests because Mn-Fe oxyhydroxide or authigenic manganese carbonate coatings are formed (Boyle, 1983; Franklin and Morse, 1983; Pena et al., 2005). Recent non-contaminated foraminifera exhibit Mn/Ca ratios of 0.01–0.2 mmol/mol (Rosenthal et al., 1999; Harding et al., 2006).

Here we present element/Ca ratios of foraminiferal tests, measured by LA-ICP-MS and EMP, from selected time intervals of sediments from the IODP Expedition 320/321 Pacific Equatorial Age Transect (PEAT) in the eastern equatorial Pacific (Figure 1). These foraminiferal tests are characterised by varying preservation states and the impact of recrystallisation was investigated. The sediments of the studied PEAT sites are of similar age and initial composition but have been subjected to different diagenetic histories due to variable subsidence, sedimentation rates and geothermal gradients. This natural diagenesis laboratory is ideal for studying recrystallisation and the preservation of geochemical proxies in foraminifera.

Table 1. Details of the investigated PEAT Sites (for further information see Pälike et al., 2010).

Site	Geographic location	Water depth (m)	Age of underlying crust (Ma)
U1334	7°59.998'N, 131°58.408'W	4799	~38
U1335	5°18.735'N, 126°17.002'W	4328	~26
U1336	7°42.067'N, 128°15.253'W	4286	~32
U1337	3°50.007'N, 123°12.356'W	4461	~24
U1338	2°30.469'N, 117°58.178'W	4200	~18

2. Materials and Methods

2.1 Site description and sampling strategy

The sediment cores U1334 to U1338 investigated here were recovered during IODP Expedition 320/321 (Figure 1). Site locations and basic coring data are summarised in Table 1 (Pälike et al., 2010). The sequences, spanning the period from the late Eocene to the present, represent a continuous Cenozoic record of equatorial Pacific sedimentation. The cores were recovered along an age transect, in which different sites were located within the high productivity zone of the equator at different time intervals as the Pacific plate moved away from East Pacific Rise (Pälike et al., 2010). All PEAT sites consist of nanno- and microfossil ooze and are relatively carbonate-rich ranging from 40.1 to 97.8 % $CaCO_3$. Opal-rich layers corresponding to low carbonate content are found at Sites U1335, U1337 and U1338, and reach < 1 % $CaCO_3$ in some layers of Site U1337. The amounts of clay are minor and are more pronounced at the top of the sediment sequences, especially at Sites U1334 and U1336, where a clay layer has accumulated since the sites subsided below the carbonate compensation depth (CCD) near 12 Ma (Pälike et al., 2010; Pälike et al., 2012). All other sites are at present still above the CCD (Pälike et al., 2010; Pälike et al., 2012), which is the depth below which the rate of calcite supply equals the

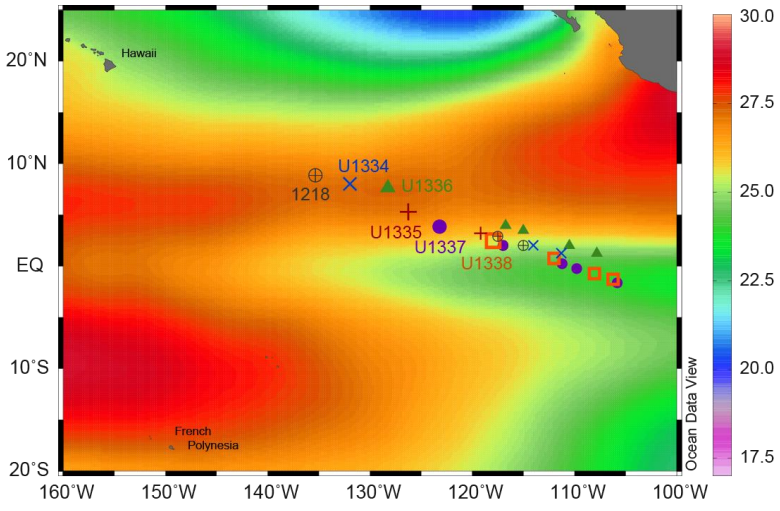

Figure 1. Map of modern sea surface temperature distribution (World Ocean Atlas 2009; Locarnini et al., 2010) indicating the present geographical and backtracked locations of the PEAT sites (Pälike et al., 2010) and ODP Site 1218 (Lyle et al., 2002) investigated in this study. The present day location of each site is represented by larger symbols. The backtracked positions are estimated from Pälike et al. (2010). The coring sites were initially located close to the East Pacific Rise and have moved in a north-west direction since.

dissolution rate resulting in absent calcite accumulation. Further details about the sedimentology of the PEAT sites can be found in Pälike et al. (2010).

ODP Site 1218 is discussed for comparison and is also located in the eastern equatorial Pacific (8°53.378'N, 135°22.000'W) about 380 km northwest of Site U1334 in a water depth of 4828 m (Lyle et al., 2002). Site 1218 shows a 52 m thick layer of radiolarian clay overlying 211 m of nannofossil ooze and chalk (Lyle et al., 2002). This clay layer, similar to Site U1334, reflects the subsidence of this site below the CCD near 12 Ma (Lyle et al., 2002; Pälike et al., 2012). Detailed information on Site 1218 can be found in Lyle et al. (2002).

Five intervals have been chosen for this study based on their palaeoceanographic and climatic significance, as well as their distinct ages as these are short and significant events. These intervals span a timeframe from ~7 to 27 Ma and are detailed below. 1) Near 7 Ma, a pronounced diatom mat was recovered at Site U1337 and corresponding diatom-rich layers were found at Sites U1335 and U1338 (Pälike et al., 2010). These layers show low carbonate contents (Pälike et al., 2010; Lyle et al., 2012; Keegan Wilson, 2014) and low abundances of planktonic foraminifera (Pälike et al., 2010), especially at Site U1337, suggesting intense carbonate dissolution. Within these opal-rich layers, foraminifera are partly badly preserved (Drury et al., 2014). Samples for this interval at Sites U1335, U1337 and U1338 were chosen according to the PEAT age model and lithology (Pälike et al., 2010). 2) The middle Miocene cooling is a key interval in the transition from the warm greenhouse climate of the Paleogene to the icehouse climate of the late Cenozoic (e.g., Zachos et al., 2001). This global cooling trend culminated at 13.9 Ma with a 1 ‰ increase in benthic foraminiferal $\delta^{18}O$ indicating massive ice sheet expansion on Antarctica (e.g., Flower and Kennett, 1994; Shevenell et al., 2004; Holbourn et al., 2005, 2007). The increase in $\delta^{18}O$ was associated with the carbon isotope event CM 6 of the Monterey Excursion (e.g., Holbourn et al., 2005, 2007, 2014) reflecting a close coupling of carbon cycle feedbacks and global climate during the Cenozoic (e.g., Shevenell et al., 2004; Pälike et al., 2012). This interval at Sites U1336, U1337 and U1338 is precisely defined using high resolution benthic foraminiferal $\delta^{18}O$ and $\delta^{13}C$ isotope records (Tian et al., 2013; Holbourn et al., 2014; Voigt et al., 2015a). 3) The warm periods of the Miocene climate optimum interrupted the general cooling trend towards

the icehouse climate of the present (e.g., Zachos et al., 2001; Holbourn et al., 2007, 2014). The peak warmth at 15.6 Ma associated with a sharp decline in $\delta^{13}C$ and $\delta^{18}O$ was the most striking feature of the Miocene climate optimum (Holbourn et al., 2007, 2014; Tian et al., 2013; Voigt et al., 2015a). This isotopic signature was accompanied by a minimum in carbonate content (Lyle et al., 2012; Holbourn et al., 2014; Voigt et al., 2015a) and a shoaling of the lysocline. This time interval at Sites U1336, U1337 and U1338 is also precisely defined by the high resolution benthic foraminiferal $\delta^{18}O$ and $\delta^{13}C$ isotope records (Tian et al., 2013; Holbourn et al., 2014; Voigt et al., 2015a). 4) The Mi-1 glaciation at 22.8 Ma is a pronounced transient glaciation, which is thought to have been orbitally triggered (Zachos et al., 2001; Pälike et al., 2006). During the Mi-1 glaciation the CCD deepened by about 50 m (Pälike et al., 2012) indicating an enhanced carbonate preservation. This interval is precisely defined at ODP Site 1218 (B. Wade, personal communication, 2012) and has been transferred to Site U1334 by correlation of several sediment proxy data between the sites (Westerhold et al., 2012). The sites were aligned using high resolution data of magnetic susceptibility, Gamma ray attenuation bulk density, virtual geomagnetic pole and X-ray fluorescence core scanning data (Westerhold et al., 2012). At Site U1336 this interval is defined by magneto- and biostratigraphy (Pälike et al., 2010). 5) During Oligocene cycle 67 a transient glacial event occurred near 27 Ma that shows the highest benthic foraminiferal $\delta^{18}O$ values of the entire Oligocene at Site 1218 (Wade and Pälike, 2004; Pälike et al., 2006). This event was also associated with a maximum in carbonate content (Pälike et al., 2006) indicating enhanced carbonate preservation similar to the Mi-1 glaciation. This time interval is precisely defined by high resolution benthic foraminiferal $\delta^{18}O$ at Site 1218 (Wade and Pälike, 2004, 2005) and this depth has been adopted for Site U1334 by correlation of various sediment proxies of Site U1334 to Site 1218, similar to the method applied for the time interval 22.8 Ma (Westerhold et al., 2012). At Site U1336 this interval is defined by magneto- and biostratigraphy (Pälike et al., 2010).

2.2 Sample preparation

Samples of 10 cm^3 sediment volume were freeze-dried, then washed over a 63 µm sieve and the residue sieved into different size fractions after drying at 40°C. Specimens of different planktonic species were picked from the size fraction

> 250 µm. Each individual shell was placed in a separate acid-cleaned safe-lock vial and was then cleaned in few drops of deionised 18.2 MΩ water. Subsequently it was ultrasonicated for 20 s and the supernatant was pipetted off. This step was repeated three times. Then few drops of ultrapure ethanol were added, ultrasonicated for 20 s and the supernatant was again discarded. The sample was then rinsed in 0.5 ml deionised 18.2 MΩ water, ultrasonicated for 30 s and the supernatant was pipetted off. The cleaned foraminifera were dried at room temperature in a clean picking cell. For laser ablation analysis, the cleaned foraminifera were placed on a carbon adhesive pad on a glass slide.

Prior to Scanning Electron Microscope (SEM) imaging, the shells were broken into large fragments to analyse wall cross sections and were gold coated. For subsequent electron microprobe analyses, the samples were embedded in Araldite epoxy resin (Araldite 2020, Huntsman Advanced Materials) in vacuum (CitoVac, Struers) to form a 25 mm diameter round block. This block was ground to the level of best exposure of wall cross sections of the tests and polished to produce a smooth surface by means of a polishing device (TegraPol 21, Struers) and polishing solutions (DiaPro, Struers). The block was then coated with carbon for the EMP analyses.

Modern foraminifera (*Globigerinoides quadrilobatus*, *Orbulina universa* and *Neogloboquadrina dutertrei*) from a box core sample (M35010-2, Caribbean Sea, 2696 m) were analysed for comparison with the ancient tests (Figure 2). For the time interval at 7 Ma, only *O. universa* was used for laser ablation analyses as this species was present at all sites investigated for this time interval. *Dentoglobigerina venezuelana* was one of the dominant species found at the other time intervals and was therefore mainly used for laser ablation analyses. For comparison, specimens of surface dwelling species like *Globigerinoides ruber*, *Gs. quadrilobatus*, *Globigerinoides triloba* and *O. universa,* as well as upper thermocline dweller *Dentoglobigerina altispira* (e.g., Pearson and Shackleton, 1995) were analysed as well. Individuals of *D. venezuelana* are divided into morphotypes 1 and 2 according to Stewart et al. (2012) but were merged into one morphotype (Type 2) in this study. This type has an irregular (kummerform), flattened final chamber and a rectangular or low arched aperture. Type 3 was used as described by Stewart and co-workers and has a large, embracing final chamber and an asymmetric rectangular aperture. The

described morphotypes of *D. venezuelana* do not show any geochemical variations and can therefore be analysed together (Stewart et al., 2012). This extinct species is thought to have been a deeper water dweller calcifying in the lower thermocline of the equatorial Pacific for the time span investigated in this study (Wade and Pälike, 2004; Wade et al., 2007).

2.3 Laser ablation ICP-MS analyses and data processing

Laser ablation analyses were conducted at GEOMAR using a New Wave 193 nm excimer laser system, equipped with a large format cell, coupled to a quadrupol ICP-MS (Agilent 7500cs). Instrumental operating conditions are summarised in Table S1. Depth profiles of intratest variation of the chemical composition through the foraminiferal tests were obtained by ablating through the test wall, and stopping the laser when the test was penetrated. First, a gas blank was measured with the laser beam blocked by a shutter during that time. Then the shutter was removed and the sample was ablated. Raw counts were processed offline. The gas blank was subtracted and element/Ca ratios were calculated by reference to the glass standards 610 and 612, distributed by the National Institute of Standards and Technology (NIST), and normalised to reported values of those standards (Jochum et al., 2011). A 2σ outlier rejection was performed and the profiles were smoothed for illustrations using a three point running mean. External reproducibility of this technique for spot to spot analysis was 1.18 ± 0.10 mmol/mol (STDEV: 8.0 %, 1σ) for Mg/Ca and 1.61 ± 0.04 mmol/mol (STDEV: 2.5 %, 1σ) for Sr/Ca ratios, determined by repeated measurements of the giant clam reference material JCt-1 (n = 55). These average values agree with recently reported values (Mg/Ca: 1.29 ± 0.09 mmol/mol, Sr/Ca: 1.68 ± 0.06 mmol/mol; Hathorne et al., 2013). Mn concentrations of the JCt-1 were below the detection limit (< 3.4 ppm). For depth profiling the standard deviation of the JCt-1 was 0.13 mmol/mol (STDEV: 10.7 %, 1σ) for Mg/Ca and 0.13 mmol/mol (STDEV: 7.9 %, 1σ) for Sr/Ca ratios, as well determined by repeated measurements of the giant clam reference material JCt-1 (n = 55).

2.4 Electron Microprobe mapping

Analyses were performed using a JEOL JXA 8200 electron microprobe. Operating conditions are summarised in Table S2. Element distribution patterns for Mg, Ca, Sr

and Mn were measured using a free-shape map of exposed wall cross sections. Foraminifera samples (*D. venezuelana*) were calibrated to an OKA calcite grain used as a standard. Repeated measurements of this standard (n = 4) yielded a Mg/Ca of 5.55 ± 0.14 mmol/mol (2σ), Sr/Ca of 26.40 ± 0.37 mmol/mol (2σ) and Mn/Ca of 4.12 ± 0.13 mmol/mol (2σ). Mg/Ca, Sr/Ca and Mn/Ca values of different OKA calcite grains are summarised in Table S3. Element/Ca ratios of foraminiferal wall cross sections were calculated from the raw counts of each element using Matlab (MathWorks Inc.). Raw ratios were corrected for machine bias using the reported and measured element/Ca ratio of the standard. The composition of individual OKA grains is homogeneous within the 2σ uncertainties (Table S3). The averages of the OKA element/Ca ratios measured in August 2005 and in September 2010 were used for calibration as the two grains and the one used in this study are from the same batch and thus the values are comparable.

3. Results

3.1 LA-ICP-MS analyses

Modern foraminiferal Mg/Ca and Mn/Ca profiles through the test walls reveal intratest heterogeneity with increasing values from the outer calcite towards the inner calcite, whereas modern Sr/Ca ratios are essentially homogenous throughout the test (Figure 2). The ancient tests also exhibit such heterogeneity through the test for Mg/Ca and Mn/Ca profiles (Figure 3). The Mg/Ca ratios of ancient *O. universa* increase from 1.45 mmol/mol in the outer calcite to 2.19 mmol/mol in the inner calcite. These values are much lower than the modern ones (Figures 2 and 3). Mn/Ca ratios of ancient *O. universa* range from 0.09-0.63 mmol/mol from the outer to the inner calcite (Figure 3a). Sr/Ca ratios of this species are also essentially homogeneous and range from 0.95-1.24 mmol/mol. (Figure 3a). Mg/Ca ratios across the tests of *D. venezuelana* range from 0.90 mmol/mol in the outer calcite to 4.33 mmol/mol in the inner calcite, which represents increases by factors of 2-5 (Figures 3b-e). Mn/Ca ratios of *D. venezuelana* show increases from 0.04 to up to 4.56 mmol/mol from the outer towards the inner calcite with highest values reached at Sites U1337 and U1338 at 13.9 Ma, at Site U1338 at 15.6 Ma, as well as at Sites

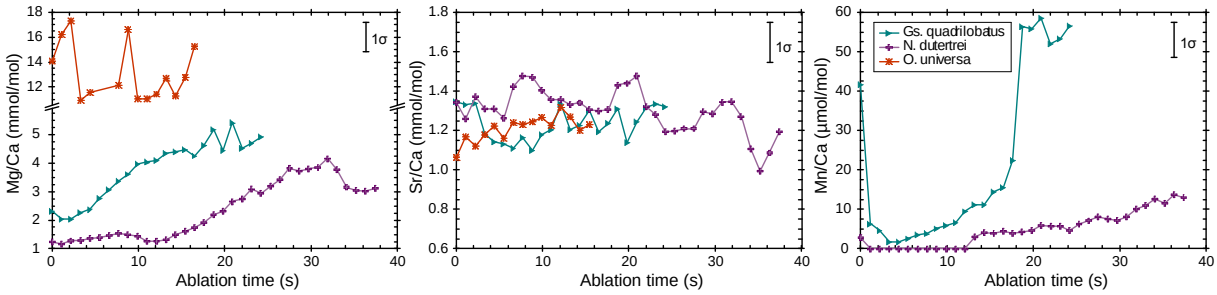

Figure 2. LA-ICP-MS depth profiles from the outer towards the inner calcite showing element/Ca ratios of modern foraminifera plotted against ablation time. Samples of surface dwelling species *Gs. quadrilobatus* (turquois triangles) and *O. universa* (orange stars) and thermocline dweller *N. dutertrei* (purple crosses) were analysed. The depth profile through the *O. universa* shells indicates two high Mg/Ca bands that are common for that species. Error bars represent the 1σ uncertainties of the element/Ca ratios for depth profiles obtained from repeated measurements of the JCt-1 calcite standard.

U1334 and 1218 at 27 Ma. The Mn/Ca ratios increase by a factor of 3-16 towards the inner calcite. The Sr/Ca values of *D. venezuelana* range from 1.01-1.46 mmol/mol (Figures 3b-e).

An outer layer enriched in trace metals (except Sr) is observed for most measured profiles (Figures 2 and 3), which was fully ablated after 10-12 s, corresponding to ~1-2 µm (Figures 2 and 3), but for few profiles this phase is extended to up to 25 s (~5 µm) (Figure 3e).

3.2 Electron Microprobe measurements

Element/Ca ratio maps of the wall cross sections of the sample tests measured by EMP confirm increasing values from the outer towards the inner calcite for Mg/Ca and Mn/Ca (Figures 4a and c). The Mg/Ca ratios range from about 1.0 mmol/mol to about 4.4 mmol/mol, and the Mn/Ca ratios have a range from 0.3 mmol/mol to about 4.0 mmol/mol. The average values of Mg/Ca (2.89 mmol/mol) and Mn/Ca (1.28 mmol/mol), are within the range of those measured by LA-ICP-MS. Sr/Ca ratios are again more uniform across the test walls at values ranging from 0.8-1.9 mmol/mol and show an average of 1.54 mmol/mol.

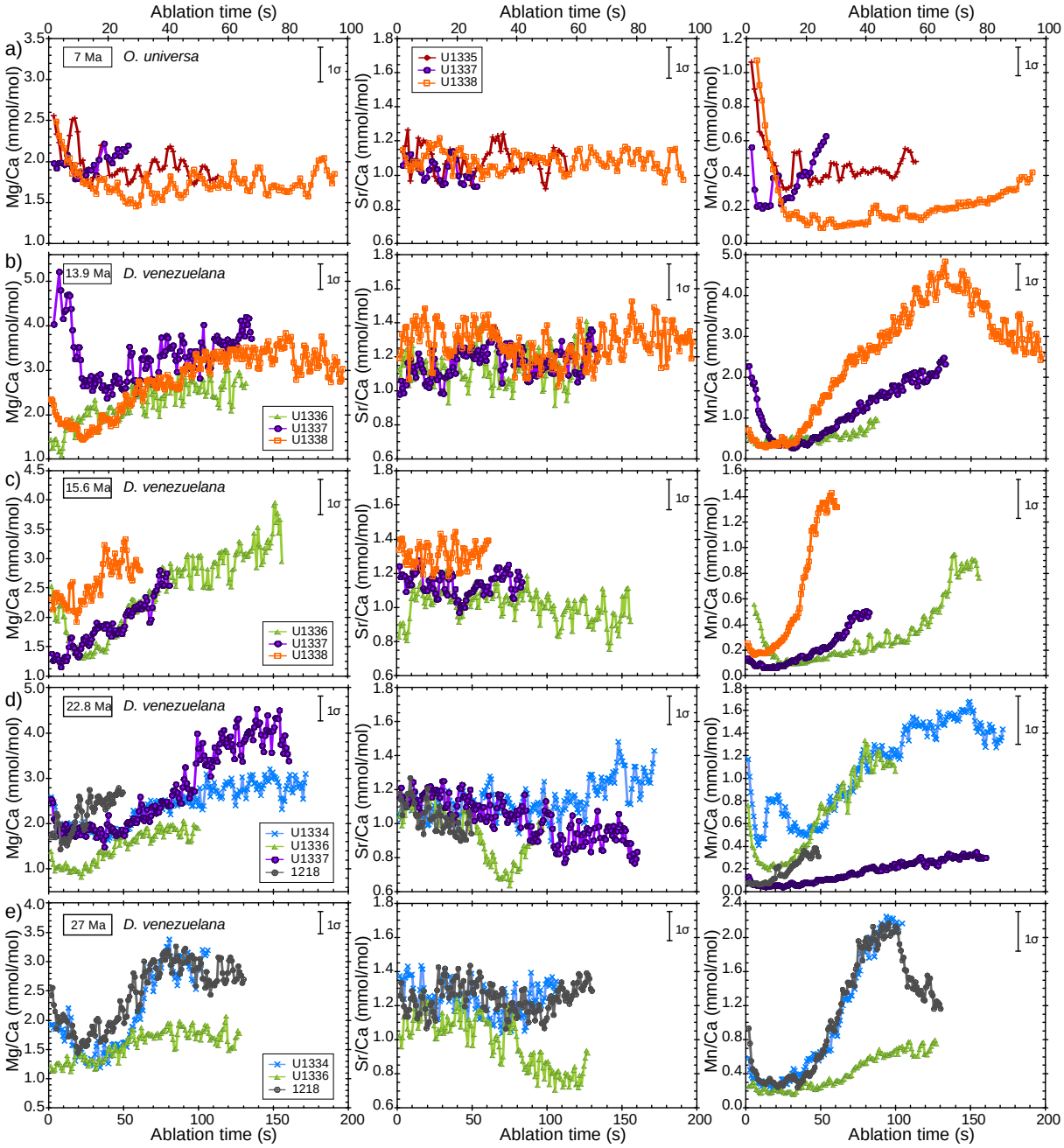

Figure 3. LA-ICP-MS depth profiles of ancient foraminiferal tests plotted against ablation time (1 s approximately corresponds to a layer thickness of 150 nm). Element/Ca ratios are illustrated for PEAT Sites U1334 (blue crosses), U1335 (red crosses), U1336 (green triangles), U1337 (purple circles) and U1338 (orange open squares) and ODP Site 1218 (grey crossed circles) at the different time intervals. Element/Ca ratios at 7 Ma show tests of *O. universa* a), whereas all other time intervals illustrate depth profiles of *D. venezuelana* b-e). Tests were ablated from the outer towards the inner calcite. Error bars denote the 1σ uncertainties element/Ca ratios for depth profiles obtained from repeated measurements of the JCt-1. Please note the different scale on the y-axes and the shorter ablation time at a).

3.3 SEM imaging

All ancient test wall cross sections show evidence of recrystallisation to varying extents in the SEM images (Figures 5 and 6). Wall cross sections of *O. universa* from the 7 Ma section show signs of dissolution (Figures 6a-c). Coccoliths and fragments of diatoms were found in some pores of these tests, as well as inside of the tests indicating that the cleaning with deionised 18.2 MΩ water and ethanol was not completely efficient.

Wall cross sections of *D. venezuelana* of all sites for the time intervals at 13.9 and 15.6 Ma show different calcite layers with submicron crystals at the inner and elongated larger crystals at the outer calcite (Figure 5). The inner wall surface is smooth and some tests are filled with few coccoliths, but the pores are preserved (Figure 5). At 22.8 Ma, tests from Site U1334 are relatively well preserved including the different layers, whereas for some specimens of Site U1336 those layers cannot be distinguished anymore and the tests are partially filled, mainly with coccoliths (Figure 6e). In the tests of Sites U1337 and 1218 at 22.8 Ma the different calcite layers are visible (Figure 6f), but some tests have coccoliths in the inside and some individuals of Site 1218 show partially dissolved pores on the inner wall surface. At 27 Ma, the calcite layers of tests from Site U1334 are mostly present (Figure 6g), but some tests are filled with coccoliths and bigger crystals (≥ 1 µm) found at the inner wall surface started to fill pores. The different layers can still be distinguished in tests of ODP Site 1218 at 27 Ma (Figure 6i), the inner wall surface is mostly smooth and the pores are preserved, but tests show some coccoliths and few bigger crystals at the inner wall surface. Tests from Site U1336 at 27 Ma are least preserved and appear cemented: The different calcite layers cannot be distinguished anymore for most tests, the pores are often completely infilled and large secondary crystals are found at the inner wall surfaces filling the pores (white arrows in Figure 6h).

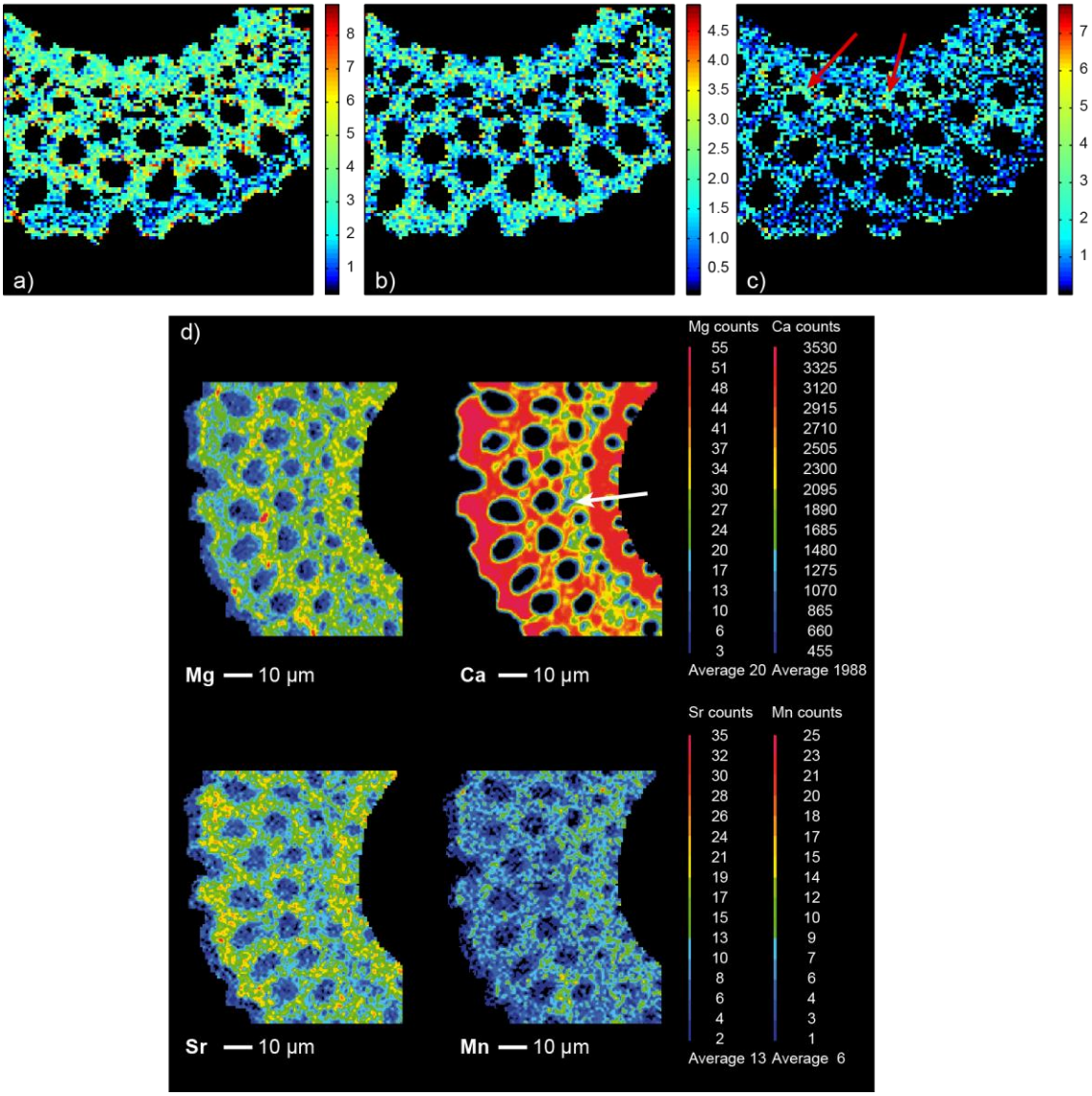

Figure 4. Electron microprobe maps of ancient *D. venezuelana* tests of Site U1336 from 13.9 Ma. Maps show Mg/Ca a), Sr/Ca b) and Mn/Ca c) distribution as well as intensity maps of those elements across the test wall cross section. Colour bars on the right represent the element/Ca ratios in mmol/mol a-c) and element counts d). The inner part of the test wall is shown on the top of panels a-c) and on the right in d). Mn/Ca are elevated near the original location of the Primary Organic Membrane (POM) c), indicated by red arrows, where Ca counts and thus Ca concentrations exhibit the lowest values d) (white arrow).

4. Discussion

4.1 Heterogeneity across the test walls

4.1.1 LA-ICP-MS analyses

Most laser ablation profiles show the presence of an outer layer, termed surface veneer, which is enriched in trace elements (Figures 2 and 3) (see also Eggins et al.,

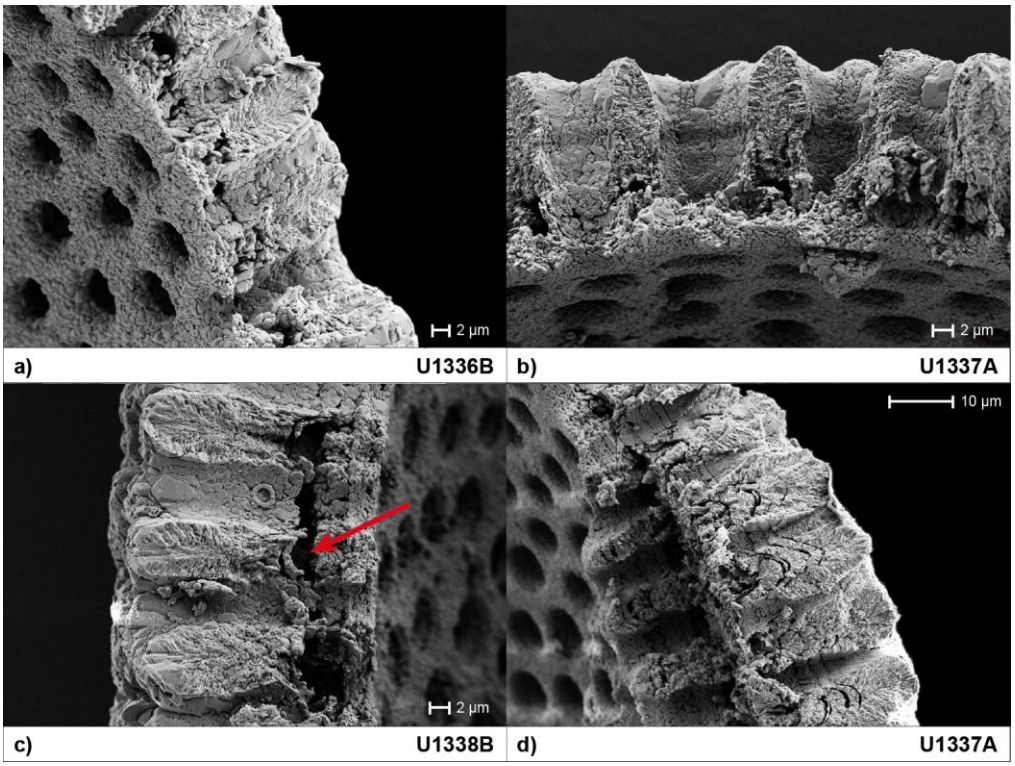

Figure 5. SEM images of wall cross sections of *D. venezuelana* from a section at 15.6 Ma. Different calcite layers can be distinguished, in which thin layers with submicron sized crystallites denote the inner calcite and large elongated crystals form the outer calcite (crust). Spaces between the calcite layers indicate dissolution of the original location of the POM layer (red arrow) suggesting early states of recrystallisation. Parts of the inner calcite of the test of U1337 d) has been chipped off probably during cracking into large fragments, but the test illustrates several successive calcite layers of the outer calcite, which were subjected to dissolution.

2003; Hathorne et al., 2009; Creech et al., 2010; van Raden et al., 2011; Vetter et al., 2013b). Generally, this outer layer is relatively thin (~1-2 µm) and quickly ablated. However, few profiles, especially of the older time intervals, have a thicker outer layer characterised by high Mg/Ca and Mn/Ca ratios (Figure 3e). This thicker outer layer may be a combination of the surface veneer and a diagenetic coating indicating recrystallisation of this test. However, an extended layer with high Mg/Ca (~21 s until ablated, corresponding to ~4 µm) is observed at a *D. venezuelana* test wall of Site U1338 at 13.9 Ma (not shown here), which does not indicate intense recrystallisation based on Sr/Ca ratios and thus the thicker outer layer may not represent a coating. Vetter et al. (2013b) claimed that the high ratios measured at the beginning of the ablation profiles may be an artefact of the ablation technique since reductively cleaned foraminiferal tests also showed these high element/Ca ratios. Assuming the elevated element/Ca values were an ablation artefact, all element profiles would be

affected similarly including measurements of the standards, which was not observed, and the Sr/Ca ratios also do not show such a layer (Figures 2 and 3). Therefore, the high element/Ca ratios of the outer layer observed here cannot be explained by such an artefact, although the used tests were not cleaned reductively. Further, it was suggested that the outer veneer is of biogenic origin as it is also present in foraminifera from plankton tows (Eggins et al., 2003; Bolton et al., 2011). Thus, the difference in thickness of the outer layer observed most likely represents natural variability between individual tests.

Mg/Ca and Mn/Ca ratios are heterogeneous through the test and increase from the outer towards the inner calcite, which is comparable to the trends in modern foraminifera (Figures 2 and 3) (see also Eggins et al., 2003; Hathorne et al., 2009; van Raden et al., 2011; Bolton and Marr, 2013). The lower Mg/Ca and Mn/Ca ratios at the outer calcite of *D. venezuelana* most likely represent the gametogenic calcite crust (e.g., Bé, 1980; Hathorne et al., 2009; van Raden et al., 2011; Bolton and Marr, 2013), which has larger and more elongated crystals than the inner calcite with submicron crystals (Figure 5). Thus, the crystal structure seems to be an important factor controlling the incorporation of trace metals (e.g., Erez et al., 2003) but also the temperature and depth of the formation of this layer play a role (e.g., Eggins et al., 2003; Erez et al., 2003; Bolton et al., 2011; Jonkers et al., 2012). The Mg/Ca profiles through ancient *O. universa* exhibit only a slight increase towards the inner calcite and no high Mg/Ca bands were resolved (Figure 3a), although such bands are typical for this species (Figure 2) (e.g., Eggins et al., 2004; Vetter et al., 2013b; Spero et al., 2015). Mn/Ca values of *O. universa* also increase towards the inner calcite, but the maximum values are almost one magnitude lower than the values of *D. venezuelana* (Figure 3).

In spite of the fact that the Mg/Ca ratios are heterogeneous, the range of the average *D. venezuelana* Mg/Ca (1.45-2.92 mmol/mol) and also *D. venezuelana* Sr/Ca (1.01-1.32 mmol/mol) ratios through the entire test are within the range of modern planktonic foraminifera (e.g., Rosenthal et al., 1997; Russell et al., 2004). The average Mg/Ca ratios are relatively low because of the deeper habitat of *D. venezuelana* (Wade and Pälike, 2004; Wade et al., 2007; Stewart et al., 2012). However, the range of average *D. venezuelana* Mn/Ca ratios (0.06- 2.54 mmol/mol,

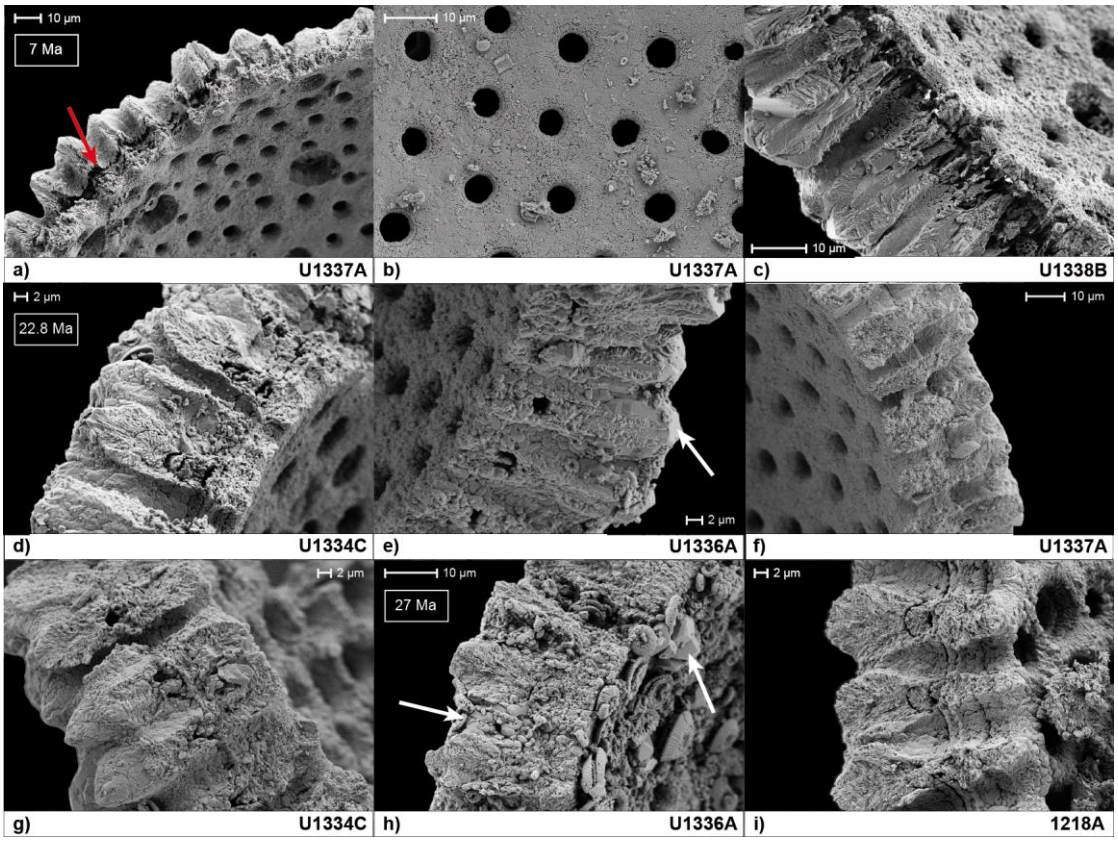

Figure 6. SEM images of test wall cross sections of *O. universa* from 7 Ma a-c) and *D. venezuelana* from 22.8 Ma d-f) and 27 Ma g-i). Tests of *O. universa* show intense dissolution around the former POM layer and the tests are partially filled with fragments of other foraminiferal tests, diatoms and coccoliths b). The inner surface surrounding the pores also shows signs of dissolution b). Tests of *D. venezuelana* from 22.8 Ma show signs of recrystallisation given that overgrowth of coarser crystals is observed on some inter-pore ridges e), indicated by the arrow, and the different calcite layers have become more uniform f). At 27 Ma, tests of ODP Site 1218 are better preserved i) than tests of Site U1334 g), but tests of Site U1336 are cemented illustrated by completely filled pores and larger crystals (≥ 1 µm) of inorganic calcite found at the inner calcite e) (arrows).

mean: 0.65 mmol/mol) and also the maximum values of laser ablation profiles are higher than reported for non-contaminated foraminifera (Rosenthal et al., 1999; Harding et al., 2006). These higher ratios could indicate recrystallisation and thus will be discussed in detail in Section 4.2.1.

Although most of the average element/Ca ratios and the profiles through the tests of *D. venezuelana* are within the range of values observed for other foraminifera, the element/Ca ratios between specimens of the same sample are highly variable. The analysis of 87 tests of *D. venezuelana* exhibits no significant difference in the profiles between sites and time intervals concerning Mg/Ca and Mn/Ca (Figure 3). Furthermore, different chambers of one individual *D. venezuelana* test show no

significant differences in element/Ca ratios (Figure S1). The different morphotypes of *D. venezuelana* also exhibit similar element/Ca ratios through the tests (Figure S2) indicating that the morphotypes do not need to be separated for geochemical analyses as already proposed by Stewart et al. (2012).

Despite the more homogeneous Sr/Ca ratios for most of the profiles, some tests of *D. venezuelana*, mainly from the older time intervals, exhibit significant variations through the test wall (Figure 7a). Histograms of these profiles were tested for bimodal distribution using the Matlab function Akaike Information Criterion (Akaike, 1974) (Figures 7b-g). A bimodal distribution of Sr/Ca ratios would suggest distinct layers with different Sr/Ca values and the low values might reflect areas of increased dissolution and recrystallisation. Only 2 tests (Figures 7c and g) show an indication of a bimodal distribution, but the probability is low and thus this pattern of variation is best explained by intratest variability. However, Figure 7 illustrates that individual tests show differences in skewness: Figures 7b and e show a right-skewed distribution, whereas Figure 7c has a left-skewed distribution and Figure 7f has nearly zero skewness, so it is almost symmetrical. The histograms of Figures 7c and g have significant frequencies for values < 1 mmol/mol, which suggests that these tests have been more intensely recrystallised than the others. Histograms of homogenous Sr/Ca profiles indicate a symmetrical (Gaussian) distribution representing unaltered profiles. However, a right-skewed distribution might also suggest good preservation as these profiles have significant frequencies of higher Sr/Ca values (> 1.3 mmol/mol), but this needs to be tested.

4.1.2 Electron Microprobe measurements

The electron microprobe analyses confirm the results obtained by LA-ICP-MS. Mg/Ca and Mn/Ca ratios of *D. venezuelana* increase from the outer towards the inner calcite (Figures 4a-c). The measured values are in the same range as the LA-ICP-MS derived data. A Student's t-test was performed, which shows that the Mg/Ca and Mn/Ca ratios of the outer calcite are on average 1.89 and 0.99 mmol/mol and the inner calcite values are 3.24 and 1.46 mmol/mol, respectively, which confirms that the Mg/Ca and Mn/Ca values of the outer and inner calcite differ significantly. Elevated Mg/Ca and Mn/Ca values, although observed only at some tests, are found

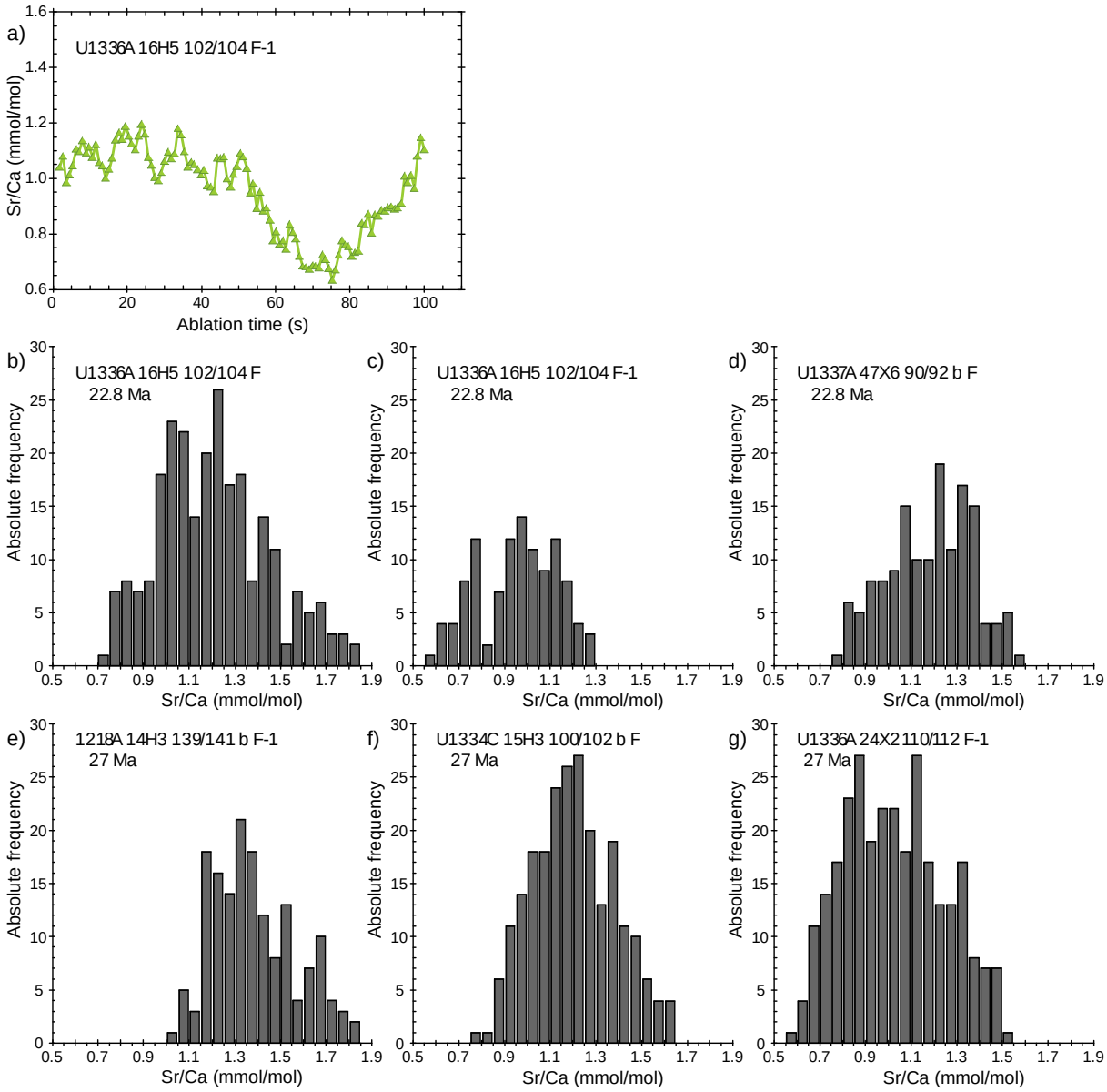

Figure 7. Histograms of Sr/Ca ratios of tests displaying significant Sr/Ca variations through the test wall a). Mainly tests from the older time intervals, 22.8 Ma b-d) and 27 Ma e-g), exhibited such patterns. These profiles were tested for possible bimodal distribution using the Matlab function Akaike Information Criterion (Akaike, 1974), which did not clearly indicate bimodal distribution for any of the tests analysed. Bimodal distribution suggests different calcite layers with distinct Sr/Ca ratios possibly indicating dissolution and recrystallisation.

near the original location of the Primary Organic Membrane (POM), where Ca counts and thus Ca concentrations exhibit the lowest values (arrows in Figures 4c and d), which has also been described in earlier studies (e.g., Eggins et al., 2004; Kunioka et al., 2006). High element/Ca ratios found at the inner or outer surface or around pores are possibly caused by edge effects (Hathorne et al., 2009).

The microprobe measurements also confirm that the Sr/Ca ratios of *D. venezuelana* are homogeneous throughout the test wall (Figure 4b). The Student's t-test reveals that the Sr/Ca ratios do not differ between the outer and the inner calcite showing average values of 1.61 and 1.57 mmol/mol, respectively. The average microprobe Sr/Ca ratios are higher than the values measured by LA-ICP-MS by ~14 %, but they are still within the 2σ uncertainties (see Section 2.3).

4.2 Recrystallisation

4.2.1 LA-ICP-MS analyses

4.2.1.1 Decreasing Sr/Ca profiles

Although there is no significant difference between the sites and time intervals, half of all measured Sr/Ca profiles decrease by more than 0.2 mmol/mol towards the inner calcite with the highest percentages reached for the older time intervals at 22.8 and 27 Ma, which indicates recrystallisation (Table 2). In 58.3 % of Site U1336 profiles and in 22.0 % of all other sites (including ODP Site 1218) Sr/Ca ratios decrease. Taking only depth profiles of *D. venezuelana* into account, 63.8 % of U1336 Sr/Ca profiles decline and 30.6 % of Sr/Ca profiles of the other sites are affected. The Sr/Ca values drop to values as low as 0.46 mmol/mol (Site U1336, 22.8 Ma, profile not shown here). Considering all sites and time intervals, Site U1336 reaches the highest percentages of decreasing Sr/Ca profiles of *D. venezuelana* (Figure 8). In addition, the time interval at 15.6 Ma of Site U1336 is considerably affected by recrystallisation (Table 2, Figure 8b), which is supported by lower bulk carbonate Sr/Ca ratios in the sections older than 14.8 Ma (Voigt et al., 2015a). Site U1336 shows intense recrystallisation of bulk carbonates in sediments older than 20 Ma enhanced by a high geothermal gradient since this site is located close to a fracture zone (Voigt et al., 2015b), which most likely explains the high percentage of decreasing Sr/Ca profiles at this site. For the time intervals at 13.9 and 15.6 Ma, the tests of the measured surface dwelling species also show a considerable amount of decreasing Sr/Ca profiles compared to the thermocline dwellers (including *D. venezuelana*) (Table 2). This suggests that surface dwellers are more prone to recrystallisation than deeper dwelling species, which includes the samples of Site U1336.

Table 2. Number of LA profiles through test walls showing decreasing Sr/Ca ratios and total number of measured profiles per site and time interval

Time interval	Species	U1334		U1336		U1337		U1338		1218	
		decreasing	total	decreasing	total	decreasing	total	decreasing	total	decreasing	total
7 Ma	*O. universa*	-	-	-	-	0	3	0	4	-	-
13.9 Ma	*D. venezuelana* surface dweller	-	-	0	14	2	6	2	10	-	-
				3	22	1	3	5	15		
	thermocline dweller			2	6	2	2	0	3		
15.6 Ma	*D. venezuelana* surface dweller	-	-	8	13	2	8	2	5	-	-
				20	23	0	3	1	5		
	thermocline dweller			4	6	0	2	0	2		
22.8 Ma	*D. venezuelana*	3	10	18	18	15	20	-	-	2	4
27 Ma	*D. venezuelana*	10	13	11	13	-	-	-	-	7	13

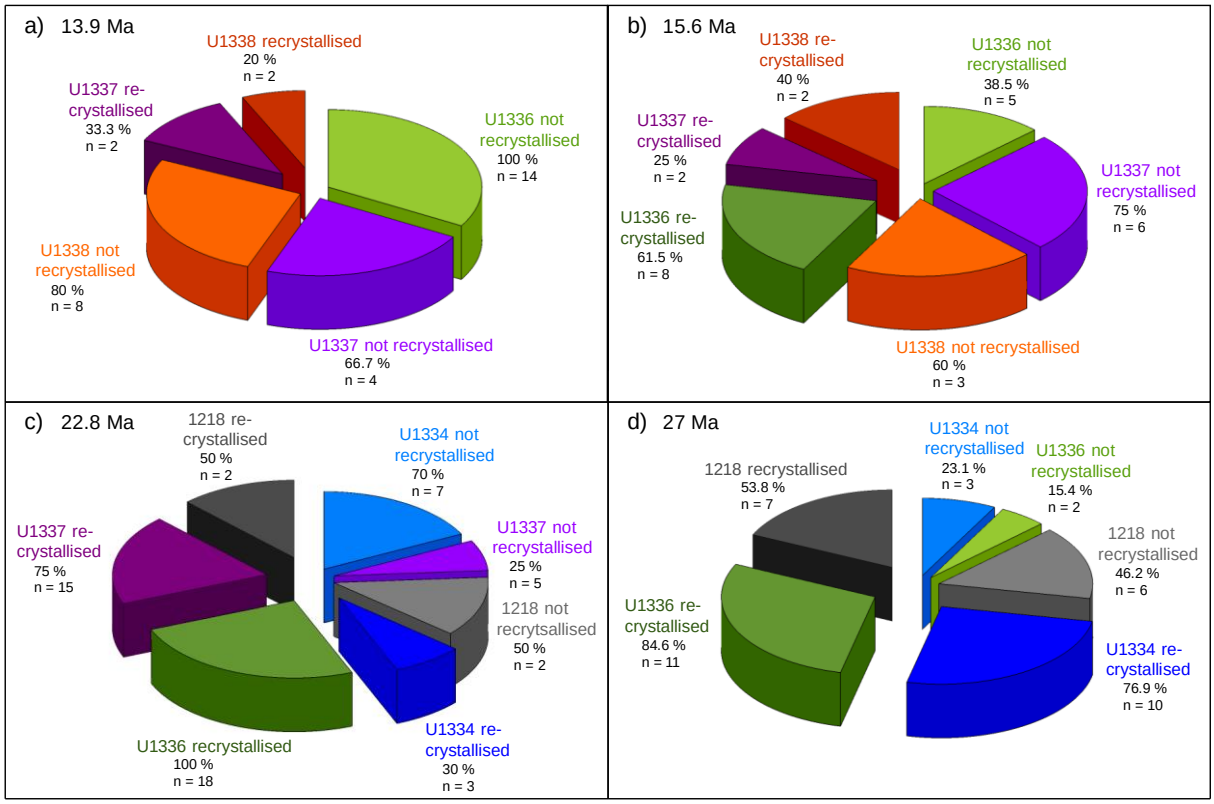

Figure 8. Pie charts illustrating the percentage of homogeneous and decreasing Sr/Ca profiles of *D. venezuelana* per site and time interval. Slices representing the proportion of decreasing Sr/Ca ratios are shown in darker colour.

Despite that many Sr/Ca profiles significantly decrease, the averages of the entire test walls will mostly not indicate recrystallisation given that the averages between 0.94 and 1.1 mmol/mol are close to 1.0 mmol/mol, which is still within the range of unaltered foraminifera (e.g., Rosenthal et al., 1997; Russell et al., 2004). Therefore, wet chemical analyses of the whole tests of several individuals will often not suggest recrystallisation since only single individuals in one sample may be affected (Table 2, Figure 9). Figure 9b clearly illustrates this for *D. venezuelana* tests of the older time intervals, in which the highest percentages of decreasing Sr/Ca profiles are observed (Table 2). For example, the average values of Site U1337 samples do not show low values indicating recrystallisation (Figure 9b), although 75 % of all Sr/Ca profiles decrease (Figure 8c). Similarly, the averages of 27 Myrs old samples of Site U1334 exhibit relatively high Sr/Ca values compared to Site U1336 (Figure 9b), but 77 % of U1334 tests show decreasing Sr/Ca profiles. The averages of Site U1336, however, are significantly lower than at the other sites (Figure 9b), which is also reflected by the maximum percentages of decreasing Sr/Ca profiles. A Student's t-test, which

compares all Sr/Ca average values of single chambers of each site with the other sites also indicates that Site U1336 is significantly different from the other sites for the older time intervals (Table 3) demonstrating that Site U1336 is indeed strongly affected by recrystallisation. Although the older time intervals show the highest percentage of decreasing Sr/Ca ratios, there is no significant trend for one specific time interval (Table 2, Figure 9a). This Sr/Ca heterogeneity suggests recrystallisation occurred in a more open system for some individual tests and that the degree of recrystallisation can vary between tests from the same sediments samples and for all time intervals.

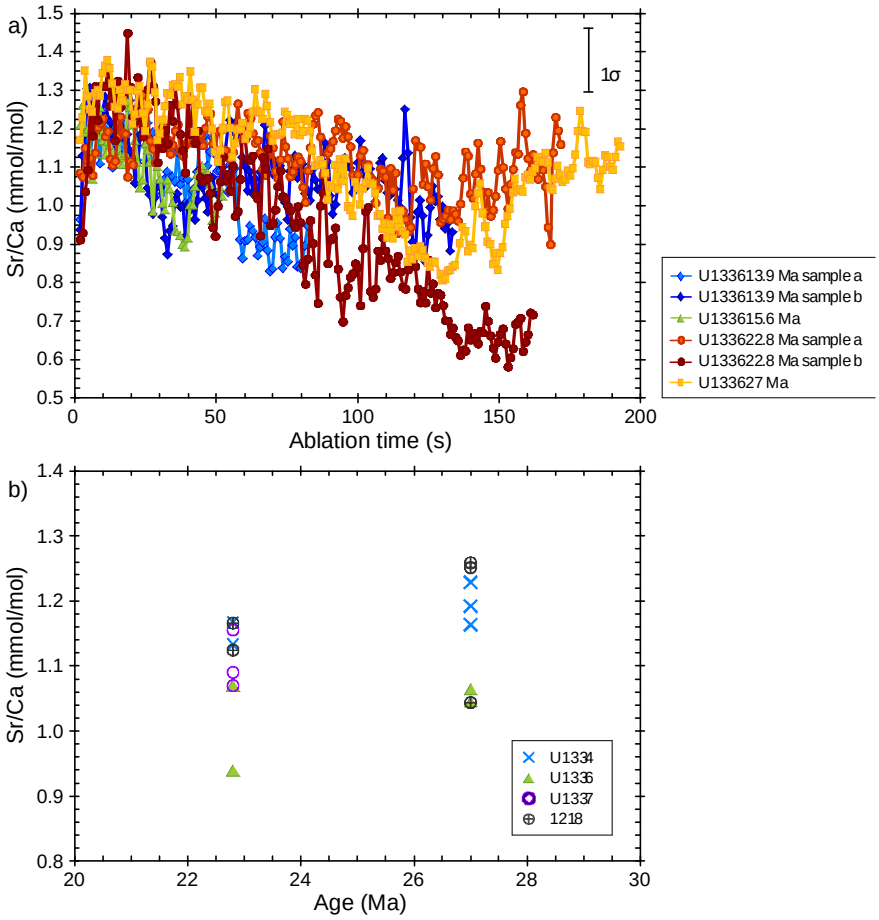

Figure 9. Sr/Ca profiles of individual *D. venezuelana* tests of Site U1336 for the different time intervals plotted versus ablation time a). Similar colours represent the same time interval. The Sr/Ca profiles indicate that individual tests are differently preserved through all time intervals. Tests were ablated from the outer towards the inner calcite. Error bar represents the 1σ uncertainty for depth profiles of repeated measurements of the JCt-1. Average Sr/Ca ratios per sample (two tests each) are compared for the different sites for the time intervals at 22.8 and 27 Ma b) illustrating the variability of samples of the same time interval and "normal" Sr/Ca averages, although the Sr/Ca ratios decrease through the test wall a).

4.2.1.2 Influence of recrystallisation on Mg/Ca profiles

The tests of ancient *O. universa* specimens exhibit markedly decreased Mg/Ca ratios accompanied by significantly low averages of the test profiles (1.46-2.43 mmol/mol) compared to modern tests (~12.8 mmol/mol) (Figures 2 and 3a). This decrease in Mg/Ca most likely results from dissolution and recrystallisation of the tests in deeper water. That means the inner parts of the tests with originally high Mg/Ca probably dissolved preferentially (e.g., Brown and Elderfield, 1996), which might be caused by the high surface area of the small crystallites of the inner calcite (see Section 4.3), possibly accompanied by less Mg^{2+} incorporation during recrystallisation because of the low deep water temperatures. Laboratory dissolution experiments indicate that partly dissolved specimens of *O. universa* still retain the high Mg/Ca bands (Sadekov et al., 2010). This, however, is not confirmed by our data. In contrast to the stations from Sadekov et al. (2010), the sites investigated for the time interval at 7 Ma were below the lysocline at that time (Pälike et al., 2010, 2012), which possibly explains the absence of the high Mg/Ca bands in our data due to increased dissolution (see also Figures 6a-c). The lysocline is the depth interval, where carbonate dissolution becomes first noticeable. Furthermore, Mn/Ca ratios in modern *O. universa* tests were mostly below detection limit (< 3.4 ppm Mn) but increased in ancient tests also indicating recrystallisation of those tests. However, Sr/Ca ratios of these tests do not decrease towards the inner calcite (Figure 3a), which may suggest that recrystallisation occurred extremely rapidly so that most of the original Sr/Ca signal was incorporated again during recrystallisation.

Individual tests of *D. venezuelana* that show signs of recrystallisation by decreasing Sr/Ca ratios have been suspected to have either elevated (Sexton et al., 2006; Kozdon et al., 2013) or lowered Mg/Ca ratios (Brown and Elderfield, 1996; Lea et al., 2000; Rosenthal et al., 2000) as recrystallisation in deeper colder water masses decreases the Mg/Ca and the incorporation of inorganic calcite with high Mg content increases the Mg/Ca of recrystallised tests. However, there is no clear trend in the Mg/Ca ratios between sites and time intervals in our data, except that Site U1336 has generally lower average Mg/Ca (Figure 10). Nevertheless, the Mg/Ca profiles of all sites and time intervals are still similar to modern or better preserved tests (Figures 2 and 3). A Student's t-test revealed that averaged test Mg/Ca ratios of *D. venezuelana*

Table 3. Student's t-test results of average Sr/Ca values of test chambers for the time intervals at 22.8 and 27 Ma. Sr/Ca values are compared between the sites and given in mmol/mol.

t-test: Two-sample assuming unequal variances

22.8 Ma	*U1336*	*U1334*	*U1336*	*1218*	*U1336*	*U1337*
Mean	0.976	1.150	0.976	1.145	0.976	1.104
Variance	0.023	0.005	0.023	0.009	0.023	0.007
Observations	15	10	15	6	15	16
Hypothesized mean difference	0		0		0	
degrees of freedom	21		15		22	
t Statistic	-3.84		-3.06		-2.89	
P(T<=t) one-tail	0.0005		0.0040		0.0042	
t critical one-tail	1.72		1.75		1.72	
P(T<=t) two-tail	0.0010		0.0080		0.0085	
t critical two-tail	2.08		2.13		2.07	
27 Ma	*U1336*	*U1334*	*U1336*	*1218*		
Mean	1.054	1.210	1.054	1.176		
Variance	0.005	0.003	0.005	0.030		
Observations	11	13	11	13		
Hypothesized mean difference	0		0			
degrees of freedom	19		16			
t Statistic	-5.96		-2.33			
P(T<=t) one-tail	<0.0001		0.0166			
t critical one-tail	1.73		1.75			
P(T<=t) two-tail	<0.0001		0.0331			
t critical two-tail	2.09		2.12			

The t statistic is in all cases lower than the negative t critical two-tail, which means that the null hypothesis, that the Sr/Ca values are not different, is rejected.

do not differ significantly between recrystallised and better preserved tests for all sites, analysed over all time intervals, except for Site U1336; which gives systematically lower values (Figure 10). However, when the averaged U1336 Mg/Ca ratios of the time intervals at 13.9 and 15.6 Ma are grouped, there is no significant difference between the Mg/Ca ratios of recrystallised and better preserved tests. The same is valid when the averaged U1336 Mg/Ca ratios of the time intervals at 22.8 and 27 Ma are grouped. Thus, the data suggest that the Mg/Ca ratios of the older time intervals of Site U1336 are significantly different compared to the values of the middle Miocene time intervals. When the test Mg/Ca ratios were averaged for the

grouped time intervals, the Mg/Ca ratios differ by 14.4 % corresponding to a temperature change of ~1.6°C (assuming 1°C change per 9 % change in Mg/Ca; Lea et al., 2000). This difference in average U1336 Mg/Ca values for the different time intervals indicates that the tests of the older time intervals are more recrystallised than those of the younger time intervals, which is supported by other proxies, such as $^{87}Sr/^{86}Sr$ and Sr/Ca ratios of bulk carbonates (Voigt et al., 2015b). However, the t-test results clearly indicate that this difference in Mg/Ca is not observed at the other sites, even for the older time intervals. Therefore considering the other sites, even recrystallised tests could be used for Mg/Ca thermometry, but those data should be handled with care to ensure reliable datasets.

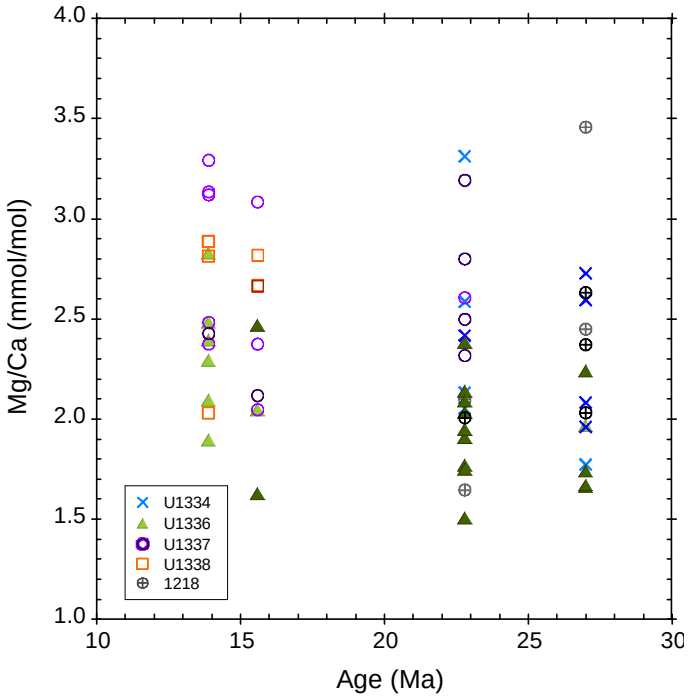

Figure 10. Variability of average test Mg/Ca ratios of *D. venezuelana* for the different sites and time intervals. Tests displaying decreasing Sr/Ca profiles are shown in darker colour.

4.2.1.3 Diagenetic alteration of Mn/Ca profiles

In contrast to the Mg/Ca, the Mn/Ca ratios of *D. venezuelana* seem to change in relation to declining Sr/Ca values. The maximum Mn/Ca ratios (of the inner calcite) decreases from the final (F) to the antepenultimate (F-2) chamber for the majority of tests of the older time intervals in which the Sr/Ca ratios decrease. In most cases, all chambers of a test are affected by a decrease in Sr/Ca, although only the chambers F to F-2 were analysed. This decrease in maximum Mn/Ca values towards the earlier

chambers is only significant for the older time intervals, but it is not when all time intervals are considered. The lower Mn/Ca ratios of the earlier chambers may suggest that they are better preserved than the final chamber, but the reason for that is not clear. However, the fact that this pattern is not significant when all time intervals are considered suggests that the decreasing Mn/Ca values might be overestimated for the older time intervals because of the higher percentage of decreasing Sr/Ca ratios (Figures 8c and d).

High Mn/Ca ratios of the inner calcite are observed at Sites U1337 (at 13.9 Ma), U1338 (at 13.9 and 15.6 Ma), U1334 and 1218 (at 27 Ma). The foraminiferal tests of Sites U1337 and U1338 may have incorporated Mn^{2+} from the pore waters during recrystallisation as the partition coefficient of Mn^{2+} is high (~15) (Pingitore, 1978) and thus could partially explain the elevated Mn/Ca values in foraminifera and bulk carbonates. Generally, a partition coefficient > 1 means that this trace element is incorporated very effectively into the secondary calcite (e.g., Pingitore, 1978; Rimstidt et al., 1998). This partition coefficient was used to calculate the Mn/Ca composition of secondary calcite that would form from the pore waters (Table 4) (Pälike et al., 2010). Results reveal high Mn/Ca values (up to 200 mmol/mol) in the upper sediment sections of Sites U1337 and U1338, but Mn/Ca decreases towards the bottom of the sediment cores. This might explain the higher bulk carbonate Mn/Ca ratios of these two sites throughout the entire sediment column compared to the other sites and in particular the elevated Mn/Ca ratios (up to 14 mmol/mol) in the upper sediment sections corresponding to ~10 Myrs (Voigt et al., 2015b, see Table S2 therein). Since recrystallisation at these sites occurred relatively rapid after deposition (within a few Myrs) (Voigt et al., 2015b), the bulk carbonates and possibly the foraminiferal tests incorporated Mn^{2+} to a greater extent as pore water Mn^{2+} concentration in the upper sediment layer is high (up to 149 µmol/l) (Pälike et al., 2010) resulting in an enormous supply of Mn^{2+} during recrystallisation. Such high pore water Mn^{2+} concentrations were most likely caused because both sites were at the high productivity zone of the equator during the time intervals at 13.9 and 15.6 Ma (see also Figure 1) (Pälike et al., 2010). High productivity leads to reducing subsurface sediments due to the degradation of organic matter which, in turn, causes the release of Mn^{2+} into the pore waters (Klinkhammer, 1980a; Klinkhammer and Bender, 1980;

Table 4. Mn/Ca values for selected time intervals for pore waters, foraminifera and calculated secondary calcite.

Time interval	Mn/Ca values[a]	U1334	U1336	U1337	U1338	1218
13.9 Ma	pore water[b]	-	0.01	0.07	0.19	-
	maximal values of foraminiferal inner calcite[c]		1.18	2.47	4.56	
	calculated secondary calcite[d]		0.13	1.01	2.87	
15.6 Ma	pore water[b]	-	0.32	0.07	0.10	-
	maximal values of foraminiferal inner calcite[c]		0.95	0.51	1.43	
	calculated secondary calcite[d]		4.85	1.03	1.54	
22.8 Ma	pore water[b]	0.45	0.06	0.01	-	0.26
	maximal values of foraminiferal inner calcite[c]	1.68	1.33	0.34		0.38
	calculated secondary calcite[d]	6.75	0.92	0.13		3.87
27 Ma	pore water[b]	0.14	-	-	-	0.38
	maximal values of foraminiferal inner calcite[c]	1.85	0.80			2.16
	calculated secondary calcite[d]	2.07	-			5.76

[a] All values are given in mmol/mol.

[b] Data for the pore water concentrations of the PEAT sites are from Pälike et al. (2010) and from ODP Site 1218 are from Lyle et al. (2002).

[c] The maximal foraminiferal Mn/Ca value is given for each site and time interval for the shown foraminifera profiles in Figures 3b-e.

[d] The Mn/Ca value of secondary calcite were estimated by $Mn/Ca_{calcite} = k_{Mn}\, Mn/Ca_{pore\ water}$ using the partition coefficient k = 15 (Pingitore, 1978) and the pore water data.

Landing and Bruland, 1987; Pena et al., 2005; Wei et al., 2009) originating from sinking particles that had adsorbed Mn while sinking through the water column (Martin and Knauer, 1983, 1984; Boyle, 1983; Franklin and Morse, 1983; Martin et al., 1985; Pingitore et al., 1988). The Mn/Ca values of the foraminifera and secondary calcite agree well at Site U1338 at 15.6 Ma suggesting that recrystallisation of the foraminiferal tests caused the observed Mn/Ca ratio. However, the high partition coefficient of Mn^{2+} alone cannot explain the measured Mn/Ca values of the foraminiferal tests as the calculated Mn/Ca values of secondary calcite are lower at Sites U1337 and U1338 at 13.9 Ma compared to the maximal values in the foraminifera (Table 4). Further, the recrystallised Mn/Ca ratios at Site U1337 are similar for the time intervals at 13.9 and 15.6 Ma, but this is not reflected in the foraminiferal ratios (Table 4, Figures 3b and c). It is possible that the high Mn^{2+} partition coefficient favours the precipitation of manganese carbonates during continued recrystallisation (Boyle, 1983; Franklin and Morse, 1983; Pingitore et al.,

1988; Pena et al., 2005) and thus removed Mn^{2+} from deeper pore waters without altering the foraminiferal tests or the Mn^{2+} pore water concentration decreased by diffusion over time resulting in lower Mn/Ca ratios of possible secondary calcite formed compared to the foraminiferal values. Pena et al. (2008) found similarly high and more elevated Mn/Ca ratios accompanied by high Mg/Ca ratios of *N. dutertrei*, also a deeper dweller. They concluded that these high element/Ca ratios resulted from Mn-rich contaminant phases (kutnahorite), which formed a thin layer on the inner calcite. In their study, the high Mn/Ca values were directly associated with high Mg/Ca ratios, which means that the high values occurred at the same depth of the test, and the higher the Mn/Ca the higher were the Mg/Ca ratios. The elevated Mn/Ca ratios, found in this study, do not show such a clear relationship (Figure 3). High Mg/Ca ratios are observed for Site U1337 at 22.8 Ma, for example, but the Mn/Ca ratios are noticeably low compared to the other sites for the same time interval (Figure 3d). In addition, the laser ablation data clearly show that these higher Mn values are associated with Ca and Sr, so the Mn is incorporated into the calcite lattice and indicates most likely broad layers of high Mn/Ca within the calcite instead layers of kutnahorite. There is also no clear relationship between the presence of high Mn/Ca values of the inner calcite and recrystallisation as neither the SEM images (Figure 5) nor Sr/Ca ratios (Figures 3b and c) indicate intense recrystallisation for the tests of Sites U1337 and U1338 at 13.9 and 15.6 Ma. A Student's t-test also showed that the averaged Mn/Ca of a recrystallised chamber is not significantly different from the average Mn/Ca of better preserved chambers for all sites and time intervals, except for Site U1336 at 27 Ma; but this exception most likely results from the low amount of better preserved chambers. Furthermore, the high bulk carbonate Mn/Ca ratios of Sites U1337 and U1338 are not associated with increased Fe/Ca ratios, which would indicate the presence of Mn-Fe-oxides. Thus, the Mn was most likely precipitated as part of authigenic carbonates and incorporated into recrystallised calcites (Voigt et al., 2015b). Unfortunately, Fe/Ca ratios were not measured in foraminifera samples to exclude the presence of Mn-Fe-oxides, but the association of Mn with Ca and Sr strongly points to the Mn being precipitated as a carbonate phase. It is also possible that the foraminifera of Sites U1337 and U1338 have incorporated a relatively high amount of Mn during their life cycle since the sites were still close to the East Pacific Rise, where high seawater Mn^{2+} concentrations

were found due to hydrothermal activity (Elderfield, 1976; Klinkhammer, 1980b; Klinkhammer and Bender, 1980; Pena et al., 2005), lateral transport from hydrothermal vents (Elderfield, 1976; Martin and Knauer, 1984; Martin et al., 1985) and aeolian input of particulate Mn (Klinkhammer and Bender, 1980; Martin and Knauer, 1984; Landing and Bruland, 1987). However, the values measured in the water column were too low and cannot account for the high Mn values found in the foraminiferal tests so that this possibility is unlikely. Therefore, the high Mn/Ca ratios of Sites U1337 and U1338 are most likely caused by the incorporation of Mn^{2+} within the sediment column during recrystallisation, but the tests are only altered to a minor extent so that the Sr/Ca signal has not changed noticeably.

The elevated Mn/Ca ratios of the inner calcite at Sites U1334 and 1218 at 27 Ma might also indicate recrystallisation, although the bulk carbonates of Site U1334 do not indicate significantly increased values (Voigt et al., 2015b). Nevertheless, the Mn/Ca values of the calculated secondary calcite imply that recrystallisation can possibly account for the elevated Mn/Ca ratios measured in the foraminifera (Table 4). Although the Sites U1334 and 1218 were located at the high productivity zone of the equator at 27 Ma (see also Figure 1) (Pälike et al., 2010), a recrystallisation process similar to Sites U1337 and U1338 seems unlikely because the pore water Mn^{2+} concentration and thus the secondary calcite Mn/Ca ratios of the upper sediment sections are too low to fully account for the incorporation of Mn^{2+} into the inner calcite of the foraminiferal tests. However, it is possible that the tests recrystallised later in deeper sediments. The Mn/Ca values of secondary calcite at Site U1334 suggest higher Mn/Ca of recrystallised foraminiferal tests at 22.8 Ma compared to 27 Ma (Table 4). The foraminiferal tests, however, show the opposite, which suggests that other factors influence the Mn^{2+} incorporation into the tests as well or this might be related to the lower proportion of recrystallised tests at 22.8 Ma (Table 2; Figures 8c and d). However, this concept, that the increased Mn^{2+} incorporation during recrystallisation due to the high partition coefficient alone can account for the observed Mn/Ca values, contradicts with the results obtained for Site U1336 as the highest secondary calcite Mn/Ca values occurred at the time interval at 15.6 Ma, where the foraminifera exhibit the lowest Mn/Ca ratios (Table 4). Moreover, the foraminiferal Mn/Ca ratios of Site U1336 at 27 Ma are low (< 1 mmol/mol) in

comparison to Sites U1334 and 1218 (Figure 3e), although U1336 is located in the proximity to those sites, which would suggest similar conditions in the sediment column. Site U1336 is intensively recrystallised especially in sediments older than 20 Ma (Voigt et al., 2015b), therefore even higher Mn/Ca values than those of Sites U1334 and 1218 would be expected. The U1336 bulk carbonate Mn/Ca ratios increase slightly in sediments older than 18.2 Ma but are comparable to those of Site U1334 (Voigt et al., 2015b), which is not reflected in the foraminiferal data. It has been suggested that Mn is leached from the sediments at sites with a high geothermal gradient (Elderfield, 1976), which is the case at Site U1336 (Voigt et al., 2015b). However, the *in-situ* temperature in the sediments of U1336 (although not measured) is most likely not as high as at hydrothermal vents and thus Mn^{2+} might not be removed by processes associated with hydrothermal activity. Several lines of evidence indicate strong reactivity in the U1336 sediments older than 20 Ma (Voigt et al., 2015b), which could involve a process that removes Mn^{2+} from the sediments and pore waters so that less Mn^{2+} is available during the recrystallisation of bulk carbonates and foraminiferal tests. Interestingly, the SEM images of Sites U1334 and 1218 indicate better preservation than for Site U1336 (Figures 6g-i) (see Section 4.2.2), although the Mn/Ca ratios are high, similar to the situation at Sites U1337 and U1338. However, the Sr/Ca ratios decrease for the majority of tests from Sites U1334 and 1218 at 27 Ma (Table 2) indicating more pronounced recrystallisation at these sites compared to Sites U1337 and U1338. On the other hand, Site U1336 has the lowest Mn/Ca ratios at 27 Ma, but other proxies, such as Sr/Ca ratios, and the SEM images (see Section 4.2.2) point out that this site is most recrystallised, which is also confirmed by analyses of the bulk carbonates and pore waters (Voigt et al., 2015b).

Nevertheless, the high Mn/Ca ratios of foraminiferal tests suggest the preferential incorporation of Mn^{2+} into the inner calcite during recrystallisation forming a Mn-rich carbonate phase independent of the degree of alteration of the tests.

4.2.2 SEM imaging

Tests of *O. universa* can exhibit multiple layers of alternating higher and lower Mg/Ca ratios (e.g., Eggins et al., 2004; Vetter et al., 2013b; Spero et al., 2015). Parts of the

test with higher Mg/Ca ratio have been suggested to be more prone to dissolution, especially below the lysocline (Sadekov et al., 2010). Johnstone et al. (2010) suggested that preferential dissolution of high Mg/Ca, associated with the small crystallites of the inner calcite leaves spaces between the calcite layers, which are visible in SEM images. Figures 6a and c clearly show such empty spaces (red arrow) and Figure 6a suggests that dissolution occurred because the smaller crystallites are more susceptible due to their high (reactive) surface area. Moreover, parts of the inner wall surfaces appear dissolved, in particular around the pores and coccoliths, fragments of diatoms and other detritus were found on the inner surface (Figure 6b) suggesting increased alteration of the tests (e.g., Tribble and Wilkens, 1999; Pearson and Burgess, 2008; Johnstone et al., 2010).

Wall cross sections of *D. venezuelana* of all sites for the time intervals at 13.9 and 15.6 Ma show signs of dissolution leaving spaces between the calcite layers (red arrow in Figure 5c). The different calcite layers in poorly preserved foraminifera, of the older time intervals, have become more uniform and the original calcite crystals have been replaced by ≥ 1µm sized secondary (inorganic) calcite crystals (white arrow in Figure 6h), which clearly indicates recrystallisation (Sexton et al., 2006; Hodell et al., 2007; Regenberg et al., 2007; Pearson and Burgess, 2008; Sexton and Wilson, 2009). Furthermore, the inter-pore ridges show overgrowths of larger, coarser crystals, mostly in tests of the older time intervals (white arrow in Figure 6e) but also some of the tests of the 15.6 Ma period are affected, which also indicates that the tests are less well preserved (e.g., Sexton et al., 2006). The tests of Sites U1334 and 1218 of the older time intervals are better preserved than tests from Site U1336, which are obviously cemented. The different calcite layers of U1336 tests cannot be distinguished for most tests, the pores are often completely filled with coccoliths and large secondary crystals are found on the inner wall surface (white arrows in Figure 6h), which mostly completely fill the pores. Although the 27 Myrs old foraminiferal tests of Site U1336 appear cemented and the geochemical data indicate that these tests are intensively recrystallised, they still have retained the shape of foraminifera reflecting the long time scale over which recrystallisation takes place. This means that initial recrystallisation probably occurred relatively rapidly (within a few Myrs) (Voigt et al., 2015b), whereby crystals form that are geochemically

indistinguishable from the original biogenic ones because most of the trace elements are incorporated again into the secondary calcite, which also explains why the Mg/Ca heterogeneity across the test walls is preserved. However, the recrystallisation process continues progressively in the sediment column resulting in the growth of large, coarse, inorganic calcite crystals replacing the original structure by filling pores as well as producing overgrowth on the inter-pore ridges and the inner surfaces (Figures 6e and h) (Sexton et al., 2006; Regenberg et al., 2007; Pearson and Burgess, 2008).

Wall cross sections of tests with decreasing Sr/Ca ratios (Figures 5a-c) can be similar in their morphology to tests with homogeneous Sr/Ca ratios (Figure 5d) and thus different preservation states during initial recrystallisation are not distinct in SEM images. In general, the SEM images of the ancient tests show that the preservation decreases with increasing age, although tests of the Sites 1218 and U1334 are better preserved than those of Site U1336 (Figures 6d, g, i). However, the SEM images also suggest different preservation states for individuals of the same sediment sample in agreement with the LA data (see Section 4.2.1).

4.3 Implications

The combination of LA-derived trace metal analysis (Mg/Ca, Mn/Ca) and SEM imaging indicate intense dissolution of ancient *O. universa* tests, although the Sr/Ca ratios do not decrease in those tests (Figures 3a and 6a-c). A recent study showed that the high Mg/Ca bands within this species are preserved (above the lysocline) (Sadekov et al., 2010), but the absence of such bands in the ancient tests (Figure 3a) raises the question if *O. universa* initially possessed high Mg/Ca bands during the Miocene at all or if these bands were dissolved preferentially when the site subsided below the lysocline, which happened for all sites investigated here. The time interval that these tests represent (7 Ma) is characterised by diatom-rich layers at Sites U1335, U1337 and U1338 accompanied by low carbonate contents and low foraminifera abundances (Pälike et al., 2010). The degradation of organic matter leads to a low pH and thus aggressive pore waters dissolving the carbonates, which is evident in the low carbonate content of these sites at ~7 Ma (Lyle et al., 2012; Shackford et al., 2014). Consequently, intense carbonate dissolution led to poorly

preserved foraminifera within the opal-rich layers (Drury et al., 2014), which is evident from the SEM images (Figures 6a-c).

Lower Sr/Ca ratios and increased Mn/Ca ratios in the inner calcite of tests of the older time intervals suggest that the inner calcite is more susceptible to recrystallisation because of its porosity and shell texture (see also Brown and Elderfield, 1996; Pena et al., 2005, 2008; Regenberg et al., 2007; Johnstone et al., 2010; Kozdon et al., 2013; Vetter et al., 2013b). Reactive or aggressive pore waters and sediment particles most likely enter through the pores or aperture of the tests into the inner space and it was suggested that the recrystallisation process starts there as the inner void of a test might operate as an even more reductive microenvironment (Pearson and Burgess, 2008; Pena et al., 2008). Foraminiferal tests stay intact to depths of hundreds of metres and are mostly not filled with coccoliths and detritus increasing the total porosity of the sediment (Figure 11) (Tribble and Wilkens, 1999). Thus, pore waters, sediment grains and fragments of biogenic tests could gradually fill the inner space of the foraminifera creating such microenvironments within semi-enclosed systems, in which recrystallisation takes place. This might explain the different preservation state of specimens of the same sample. Considering the test structure, the submicron sized crystals of the primary (inner) calcite seem to be more affected by recrystallisation possibly because of their higher surface area (e.g., 1983; Boyle, 1983; Pearson and Burgess, 2008), whereas the large elongated crystals of the (gametogenic) outer crust appears to be more resistant to recrystallisation (Johnstone et al., 2010, 2011).

Although a high proportion of the older tests analysed are recrystallised, the profiles of the Mg/Ca ratios still show the same trend as modern foraminifera (Figures 2 and 3) and also the average Mg/Ca values of test walls are comparable to a modern thermocline dweller, *N. dutertrei* (Figure 2). A direct comparison of average test Mg/Ca ratios of *D. venezuelana* from 22.8 Ma reveal that the Mg/Ca values are similar to samples from the equatorial Atlantic from the same time (Stewart et al., 2012) resulting in essentially the same temperatures for the equatorial Atlantic ODP Site 925 (Stewart et al., 2012), Sites U1334 and U1337, when the equation from Stewart et al. (2012), corrected for seawater Mg/Ca at the Oligocene/Miocene boundary is used. The Mg/Ca values (and thus the temperature estimates) of Sites

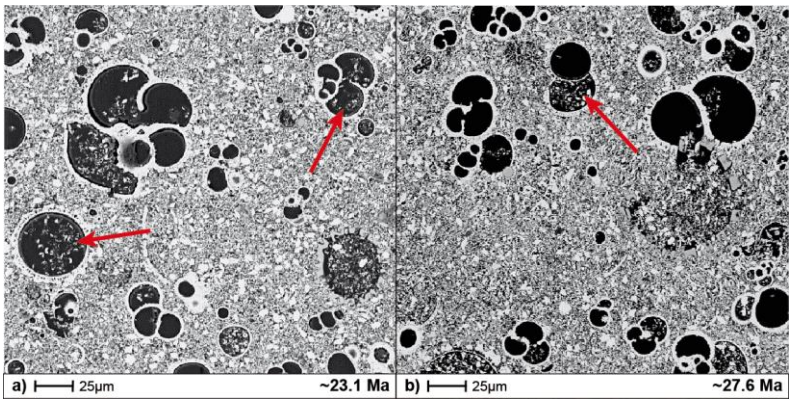

Figure 11. Backscattered electron microscopy images of bulk sediment samples from the western equatorial Pacific Site 807A (by courtesy of R. Wilkens, University of Hawaii at Manoa, USA), embedded in epoxy resin. The images show a high proportion of macro-porosity (Tribble and Wilkens, 1999), which is the open pore space of the deposited foraminifera. This open pore space might operate as microenvironment when the test gets filled with detritus and fragments (arrows).

U1336 and 1218 are significantly lower (1.95 and 1.92 mmol/mol, respectively) than Site 925 (2.57 mol/mol) (Stewart et al., 2012) and Site U1337 (2.68 mmol/mol), which exhibit the highest Mg/Ca values of this time interval, although a high percentage of the tests is recrystallised (Table 2, Figure 8c). Site 925 contains higher proportions of clay minerals and has an average carbonate content of 64 % (Curry et al., 1995), which is comparable to Site U1337 (62 %) (Pälike et al., 2010). Miocene tests of *D. venezuelana* from Site 925 also show similar signs of recrystallisation (Stewart et al., 2012) indicating that the preservation state might be similar to the tests investigated here. Nonetheless, the fact that the average Mg/Ca values of all sites and time intervals are not significantly different to modern Mg/Ca ratios of *N. dutertrei* may suggest that Mg/Ca is not as susceptible to diagenetic alteration as some previous studies indicate (e.g., Brown and Elderfield, 1996; Lea et al., 2000; Dekens et al., 2002). Furthermore, a temperature estimate of the surface dwelling species *Gs. quadrilobatus*, from Site U1336 grouped for time the intervals at 13.9 and 15.6 Ma, exhibit 27°C using the equation for Pacific *Gs. sacculifer* from Dekens et al. (2002). This value agrees well with seawater surface temperature estimates for the tropical eastern Pacific (~27°C) at ~13 Ma (LaRiviere et al., 2012). Although the majority of the *Gs. quadrilobatus* tests show recrystallisation by decreasing Sr/Ca ratios, this good agreement of estimated surface temperatures indicates that the Mg/Ca values are relatively robust towards recrystallisation. In addition, Kozdon et al. (2013) suggested that recrystallised Mg/Ca only slightly differs from the original biogenic

signal because the major part of Mg and Ca dissolved from the tests is incorporated again into the secondary calcite. Therefore, the recrystallised Mg/Ca at least partially reflects the original Mg/Ca of the foraminiferal test. It is also possible that the high Mg/Ca of the inner calcite is dissolved and recrystallises in the sediment lowering the average Mg/Ca ratio of the tests because of the low temperature at depth (e.g., Brown and Elderfield, 1996; Lea et al., 2000; Rosenthal et al., 2000). Additionally, minor amounts of inorganic calcite with high Mg/Ca (Mucci, 1987; Oomori et al., 1987; Erez, 2003) could be incorporated as well, which might result in average test Mg/Ca ratios similar to the original signal when both processes (the decrease in Mg/Ca due to lower temperature and the precipitation of inorganic calcite) are combined. That means that possibly both processes may nearly cancel each other out. But the degree of change in recrystallised Mg/Ca is possibly dependent on the species when surface and thermocline dwellers are compared due to their different original ("starting") Mg/Ca ratio. To test this assumption, a Student's t-test was performed comparing the average Mg/Ca ratios of surface (*Gs. ruber*, *Gs. triloba* and *Gs. quadrilobatus*) and thermocline dwellers (*D. venezuelana* and *D. altispira*) of Sites U1336 and U1338 for the time intervals at 13.9 and 15.6 Ma. The results indicate that average Mg/Ca values of better preserved tests of Site U1336 are significantly different for surface and thermocline dwellers. The same is valid when all tests are considered despite their preservation state, but no significant difference between surface and thermocline species can be found when only recrystallised tests are compared. In contrast to Site U1336, the average Mg/Ca ratios of surface and thermocline dwellers from Site U1338 are not significantly different independent of their preservation state. These contrasting results may be explained by the geographical position of the sites during the time intervals. Site U1338 was still located within the upwelling area near the equator (Figure 1) (Pälike et al., 2010), which means lower surface temperatures and a shallower thermocline resulting in similar Mg/Ca values for both depth habitats. On the other hand, Site U1336 had already travelled out of the upwelling region (Figure 1), which implies a greater temperature difference between surface and thermocline dwellers. In the better preserved tests of Site U1336 this relationship is evident in the Mg/Ca ratios indicating a 3.1°C temperature difference, assuming a 9 % change in the Mg/Ca ratio is associated with 1°C difference (Lea et al., 2000). The fact that the recrystallised

tests do not exhibit this Mg/Ca difference anymore indicate that recrystallisation lowers the Mg/Ca values of the surface species resulting in comparable Mg/Ca ratios to thermocline dwellers. This points to recrystallisation of the tests at colder temperatures at depth and partial incorporation of inorganic calcite. Therefore, the Mg/Ca ratios of surface dwellers become indistinguishable from those of the thermocline dwellers since the recrystallisation process affects all tests in a similar way. However, the hypothesis that most of the original Mg/Ca signal is re-incorporated into the secondary calcite seems likely since surface dwelling species from Sites U1336, U1337 and U1338 for the time intervals at 13.9 and 15.6 Ma still retain Mg/Ca values comparable to modern values despite different preservation states (Table 5), which also indicates that the temperature estimate of U1336 *Gs. quadrilobatus* may provide reasonable values for those time intervals. Therefore, Mg/Ca ratios can most liklely be reliably used for palaeo-temperature reconstructions even when the tests are recrystallised to a degree similar to our study, especially by using unaltered parts of the test determined by the laser ablation profile (Creech et al., 2010; Kozdon et al., 2013). This, however, indicates that Mg/Ca ratios (at least concerning surface dwellers) cannot be used as reliable indicator of recrystallisation as already suggested by Kozdon et al. (2013).

Mn/Ca, similar to the Mg/Ca ratios, do not reliably indicate the degree of recrystallisation as the Mn/Ca ratios of *D. venezuelana* from Sites U1337 and U1338 at 13.9 Ma are similar to those at Sites U1334 and 1218 at 27 Ma despite the fact that the older tests have independently been shown to be more strongly recrystallised (Figures 5, 6 and 10). The presence of Mn-rich phases suggests some alteration of the tests in the sediment column. In general, Mn^{2+} values vary with sediment depth and redox processes. Further, the difference between Mn concentrations prevailing in seawater during biomineralisation and pore waters after deposition is very high (up to 148 µmol/l; data from Klinkhammer, 1980b; Pälike et al., 2010) and thus large changes in Mn/Ca in foraminiferal tests can evolve in the sediment column after deposition.

In contrast to Mg/Ca and Mn/Ca, the Sr/Ca ratios decrease to a higher extent with progressive recrystallisation. Although the variability between specimens of the same

sediment sample is relatively high (Figure 9), the percentage of decreasing Sr/Ca ratios through the test wall increases with increasing degree of recrystallisation (Table 2). Thus, Sr/Ca ratios of single shells are ideal indicators of recrystallisation and can even hint at the state of preservation.

Table 5. Student's t-test results of foraminiferal test average Mg/Ca values of surface dwelling species (at 13.9 and 15.6 Ma) compared to modern surface dwellers. Mg/Ca values are given in mmol/mol.

t-test: Two-sample assuming unequal variances

surface dwellers	*U1336*	*modern*	*U1337*	*modern*	*U1338*	*modern*
Mean	3.59	4.18	3.15	4.18	3.58	4.18
Variance	0.319	0.364	0.279	0.364	1.274	0.364
Observations	16	4	2	4	13	4
Hypothesized mean difference	0		0		0	
degrees of freedom	4		2		10	
t Statistic	-1.75		-2.14		-1.37	
P(T<=t) one-tail	0.077		0.083		0.101	
t critical one-tail	2.13		2.92		1.82	
P(T<=t) two-tail	0.154		0.166		0.201	
t critical two-tail	2.78		4.30		2.23	
surface dwellers	*better preserved*[a]	*modern*	*all*[b]	*modern*		
Mean	3.56	4.18	3.56	4.18		
Variance	0.793	0.364	0.690	0.364		
Observations	14	4	31	4		
Hypothesized mean difference	0		0			
degrees of freedom	7		5			
t Statistic	-1.61		-1.83			
P(T<=t) one-tail	0.076		0.063			
t critical one-tail	1.89		2.02			
P(T<=t) two-tail	0.151		0.126			
t critical two-tail	2.36		2.57			

The t statistic is in all cases neither lower than the negative t critical two-tail nor higher than the t critical two-tail therefore the null hypothesis, saying that the Mg/Ca ratios do not differ, is not rejected.

[a] Only average test Mg/Ca values of surface dwellers of Sites U1336-U1338 were used, where the profile do not exhibit decreasing Sr/Ca ratios.

[b] All average test Mg/Ca values of surface dwellers of Sites U1336-U1338were used despite the preservation state.

5. Conclusion

Laser ablation profiles and electron microprobe analysis show that foraminiferal Mg/Ca and Mn/Ca ratios of *D. venezuelana*, recovered from sediments targeting the time intervals 7 and 27 Ma, increase from the outer towards the inner calcite and are comparable to modern tests. This trend is observed for all tests analysed and thus there is no significant difference between the sites and time intervals investigated in this study. The Sr/Ca ratios are essentially homogeneous throughout the tests. However, the element/Ca ratios are highly variable between individual specimens of the same sample.

Sr/Ca ratios decrease by more than 0.2 mmol/mol towards the inner calcite with the highest percentages found for the older time intervals at 22.8 and 27 Ma clearly indicating recrystallisation. Site U1336 is most affected by recrystallisation, which is also evident in SEM images. This site is thought to have experienced extensive diagenetic alteration of bulk carbonates caused by a strong geothermal gradient, which is confirmed by the planktonic foraminiferal data. Elevated Mn/Ca ratios of some sites and time intervals indicate the preferential incorporation of Mn^{2+} to the inner calcite, which possibly results from aggressive or reducing sediment conditions below the equatorial high productivity zone or from the proximity to the East Pacific Rise with hydrothermal Mn^{2+} input. The decrease in Sr/Ca and the increase in Mn/Ca ratios towards the inner calcite suggest that the inner calcite is more susceptible to recrystallisation as the submicron sized crystals of this inner layer exhibit larger surface areas and therefore dissolve first.

SEM images show increasing alteration with progressive age, but the images also suggest different preservation states for individual tests of the same sediment sample. This means that the degree of recrystallisation can vary between individual specimens.

Our results clearly show that LA-ICP-MS profiles through single foraminiferal tests can readily identify recrystallisation, but even recrystallised tests can, for example, be used for Mg/Ca-derived palaeo-temperature estimates. This is a great advantage to wet chemistry analyses using normally several individuals, where it is difficult to assess recrystallisation when diagenetic alteration is not intense. Since laser ablation

is microdestructive, the foraminiferal test can be used for further analyses, such as SEM, secondary ion mass spectrometry and electron microprobe mapping, which then allow quantifying the preservation state in more detail.

Acknowledgement

This study was funded by the German Science Foundation, DFG, HA 5751/1-1 and HA 5751/2-1 (PEAT). We thank Ann Holbourn for providing foraminifera samples from Sites U1337 and U1338 for the time intervals at 13.9 and 15.6 Ma and Isabel Rohr for preparing the samples. SEM images were taken at the MARUM, Bremen and we thank Petra Witte for her help with the SEM imaging. Jeroen Groeneveld is acknowledged for helpful interpretation of the SEM images. Nico Glock is also thanked for his help with embedding the samples in epoxy. We further thank Mario Thöner for assistance and technical support during the electron microprobe measurements. Daniel Gebrigeorgis Yirgaw is acknowledged for assistance with Matlab.

References

Akaike H. (1974) A new look at the statistical model identification. *IEEE T. Automat. Contr.* **19**, 716-723.

Anand P., Elderfield H., and Conte M. H. (2003) Calibration of Mg/Ca thermometry in planktonic foraminifera from a sediment trap time series. *Paleoceanography* **18**, 1050-1065.

Baker P. A., Gieskes J. M., and Elderfield H. (1982) Diagenesis of carbonates in deep-sea sediments-evidence from Sr/Ca ratios and interstitial dissolved Sr^{2+} data. *J. Sediment. Petrol.* **52**, 71-82.

Bé A. W. H. (1980) Gametogenic calcification in a spinose planktonic foraminifer, *Globigerinoides sacculifer* (Brady). *Mar. Micropaleontol.* **5**, 283-310.

Bolton A., Baker J. A., Dunbar G. B., L. Carter L., Smith E. G. C., and Neil H. L. (2011) Environmental versus biological controls on Mg/Ca variability in *Globigerinoides ruber* (white) from core top and plankton tow samples in the southwest Pacific Ocean. *Paleoceanography* **26**, PA2219, doi:10.1029/2010PA001924.

Bolton A. and Marr J. P. (2013) Trace element variability in crust-bearing and non crustbearing *N. incompta*, P-D intergrade and *G. inflata* from the Southwest Pacific Ocean: potential paleoceanographic implications. *Mar. Micropaleontol.* **100**, 21-33.

Boyle E. A. (1983) Manganese carbonate overgrowths on foraminifera tests. *Geochim. Cosmochim. Acta* **47**, 1815-1819.

Brown S. J. and Elderfield H. (1996) Variation in Mg/Ca and Sr/Ca ratios of planktonic foraminifera caused by postdepositional dissolution: Evidence of shallow Mg-dependent dissolution. *Paleoceanography* **11**, 543-551.

Creech J. B., Baker J. A., Hollis C. J., Morgans H. E. G., and Smith E. G. C. (2010) Eocene sea temperatures for the mid-latitude southwest Pacific from Mg/Ca ratios in planktonic and benthic foraminifera. *Earth Planet. Sci. Lett.* **299**, 483-495.

Curry W. B., Shackleton N. J., Richter C., et al. (1995) Site 925. In: *Proc. ODP. Init. Repts.* 154 (eds. W. B. Curry, N. J. Shackleton, C. Richter, et al.). Ocean Drilling Program, pp. 55-152, doi:10.2973/odp.proc.ir.154.104.1995.

Dekens P. S., Lea D. W., Pak D. K., and Spero H. J. (2002) Core top calibration of Mg/Ca in tropical foraminifera: Refining paleotemperature estimation. *Geochem. Geophys. Geosyst.* **3**, 1022, doi:10.1029/2001GC000200.

Delaney M. L. (1989) Temporal changes in interstitial water chemistry and calcite recrystallization in marine sediments. *Earth Planet. Sci. Lett.* **95**, 23-37.

Drury A. J., Lee G. P., Pennock G. M., and John C. M. (2014) Data report: Late Miocene to early Pliocene coccolithophore and foraminiferal preservation at Site U1338 from scanning electron microscopy. In: *Proc. IODP,* 320/321: Tokyo (eds. H. Pälike, et al.).

(Integrated Ocean Drilling Program Management International, Inc.). doi:10.2204/iodp.proc.320321.218.2014.

Eggins S., De Deckker P., and Marshall J. (2003) Mg/Ca variation in planktonic foraminifera tests: implications for reconstructing palaeo-seawater temperature and habitat migration. *Earth Planet. Sci. Lett.* **212**, 291-306.

Eggins S., Sadekov A., and De Deckker P. (2004) Modulation and daily banding of Mg/Ca in *Orbulina universa* tests by symbiont photosynthesis and respiration: A complication for seawater thermometry?. *Earth Planet. Sci. Lett.* **225**, 411-419.

Elderfield H. (1976) Manganese fluxes to the oceans. *Mar. Chem.* **4**, 103-132.

Elderfield H., Gieskes J. M., Baker P. A., Oldfield R. K., Hawkesworth C. J., and Miller R. (1982) $^{87}Sr/^{86}Sr$ and $^{18}O/^{16}O$ ratios, interstitial water chemistry and diagenesis in deep-sea carbonate sediments of the Ontong Java Plateau. *Geochim. Cosmochim. Acta* **46**, 2259-2268.

Erez J. (2003) The source of ions for biomineralization in foraminifera and their implications for paleoceanographic proxies. *Rev. Mineral. Geochem.* **54**, 115-149.

Flower B. P. and Kennett J. P. (1994) The middle Miocene climatic transition: East Antarctic ice sheet development, deep ocean circulation and global carbon cycling. *Palaeogeogr. Palaeoclimatol. Palaeoecol.* **108**, 537-555.

Franklin M. L. and Morse J. W. (1983) The interaction of manganese(II) with the surface of calcite in dilute solutions and seawater. *Mar. Chem.* **12**, 241-254.

Gabitov R. I., Gagnon A. C., Guan Y., Eiler J. M., and Adkins J. F. (2013) Accurate Mg/Ca, Sr/Ca, and Ba/Ca ratio measurements in carbonates by SIMS and NanoSIMS and an assessment of heterogeneity in common calcium carbonate standards. *Chem. Geol.* **356**, 94-108.

Gaetani G. A. and Cohen A. L. (2006) Element partitioning during precipitation of aragonite from seawater: A framework for understanding paleoproxies. *Geochim. Cosmochim. Acta* **70**, 4617-4634.

Harding D. J., Arden J. W., and Rickaby R. E. M. (2006) A method for precise analysis of trace element/calcium ratios in carbonate samples using quadrupole inductively coupled plasma mass spectrometry. *Geochem. Geophys. Geosyst.* **7**, Q06003, doi:10.1029/2005GC001093.

Hathorne E. C., Alard O., James R. H., and Rogers N. W. (2003) Determination of intratest variability of trace elements in foraminifera by laser ablation inductively coupled plasma-mass spectrometry. *Geochem. Geophys. Geosyst.* **4**, 8408, doi:10.1029/2003GC000539.

Hathorne E. C., James R. H., Savage P., and Alard O. (2008) Physical and chemical characteristics of particles produced by laser ablation of biogenic calcium carbonate. *J. Anal. At. Spectrom.* **23**, 240-243.

Hathorne E. C., James R. H., and Lampitt R. S. (2009) Environmental versus biomineralization controls on the intratest variation in the trace element composition of the planktonic foraminifera *G. inflata* and *G. scitula*. *Paleoceanography* **24**, PA4204, doi:10.1029/2009PA001742.

Hathorne E. C., Gagnon A., Felis T., et al. (2013) Interlaboratory study for coral Sr/Ca and other element/Ca ratio measurements. *Geochem. Geophys. Geosyst.* **14**, 3730-3750.

Hodell D. A., Kamenov G. D., Hathorne E. C., Zachos J. C., Röhl U., and Westerhold T. (2007) Variations in the strontium isotope composition of seawater during the Paleocene and early Eocene from ODP Leg 208 (Walvis Ridge). *Geochem. Geophys. Geosyst.* **8**, Q09001, doi:10.1029/2007GC001607.

Holbourn A., Kuhnt W., Schulz M., and Erlenkeuser H. (2005) Impacts of orbital forcing and atmospheric carbon dioxide on Miocene ice-sheet expansion. *Nature* **438**, 483-487.

Holbourn A., Kuhnt W., Schulz M., Flores J.-A., and Andersen N. (2007) Orbitally-paced climate evolution during the middle Miocene "Monterey" carbon-isotope excursion. *Earth Planet. Sci. Lett.* **261**, 534-550.

Holbourn A., Kuhnt W., Lyle M., Schneider L., Romero O., and Andersen N. (2014) Middle Miocene climate cooling linked to intensification of eastern equatorial Pacific upwelling. *Geology* **42**, 19-22.

Jochum K. P., Weis U., Stoll B., Kuzmin D., Yang Q., Raczek I., Jacob D. E., Stracke A., Birbaum K., Frick D. A., Günther D., and Enzweiler J. (2011) Determination of reference values for NIST SRM 610-617 glasses following ISO guidelines. *Geostand. Geoanalytical Res.* **35**, 397-429.

Johnstone H. J. H., Schulz M., Barker S., and Elderfield H. (2010) Inside story: An X-ray computed tomography method for assessing dissolution in the tests of planktonic foraminifera. *Mar. Micropaleontol.* **77**, 58-70.

Johnstone H. J. H., Yu J., Elderfield H., and Schulz M. (2011) Improving temperature estimates derived from Mg/Ca of planktonic foraminifera using X-ray computed tomography-based dissolution index, XDX. *Paleoceanography* **26**, PA1215, doi:10.1029/2009PA001902.

Jonkers L., de Nooijer L. J., Reichart G.-J., Zahn R., and Brummer G.-J. A. (2012) Encrustation and trace element composition of *Neogloboquadrina dutertrei* assessed from single chamber analyses – implications for paleotemperature estimates. *Biogeosciences* **9**, 4851-4860.

Keegan Wilson J. (2014) Early Miocene carbonate dissolution in the eastern equatorial Pacific. Ph. D. thesis, Texas A&M University.

Kisakürek B., Eisenhauer A., Böhm F., Garbe-Schönberg D., and Erez J. (2008) Controls on shell Mg/Ca and Sr/Ca in cultured planktonic foraminifera. *Earth Planet. Sci. Lett.* **273**, 260-269.

Klinkhammer G. P. (1980a) Early diagenesis in sediment from the eastern equatorial Pacific, II. Pore water metal results. *Earth Planet. Sci. Lett.* **49**, 81-101.

Klinkhammer G. P. (1980b) Observations of the distribution of manganese over the East Pacific Rise. *Chem. Geol.* **29**, 211-226.

Klinkhammer G. P. and Bender M. L. (1980) The distribution of manganese in the Pacific Ocean. *Earth Planet. Sci. Lett.* **46**, 361-384.

Kozdon R., Kelly D. C., Kitajima K., Strickland A., Fournelle J. H., and Valley J. W. (2013) In situ $\delta^{18}O$ and Mg/Ca analyses of diagenetic and planktic foraminiferal calcite preserved in a deep-sea record of the Paleocene-Eocene thermal maximum. *Paleoceanography* **28**, 517-528.

Kunioka D., Shirai K., Takahata N., Sano Y., Toyofuku T., and Ujiie Y. (2006) Microdistribution of Mg/Ca, Sr/Ca, and Ba/Ca ratios in *Pulleniatina obliquiloculata* test by using a NanoSIMS: Implication for the vital effect mechanism. *Geochem. Geophys. Geosyst.* **7**, Q12P20, doi:10.1029/2006GC001280.

Landing W. M. and Bruland K. W. (1987) The contrasting biogeochemistry of iron and manganese in the Pacific Ocean. *Geochim. Cosmochim. Acta* **51**, 29-43.

LaRiviere J. P., Ravelo A. C., Crimmins A., Dekens P. S., Ford H. L., Lyle M., and Wara M. W. (2012) Late Miocene decoupling of oceanic warmth and atmospheric carbon dioxide forcing. *Nature* **486**, 97-100.

Lea D. W., Mashiotta T. A., and Spero H. J. (1999) Controls on magnesium and strontium uptake in planktonic foraminifera determined by live culturing. *Geochim. Cosmochim. Acta* **63**, 2369-2379.

Lea D. W., Pak D. K., and Spero H. J. (2000) Climate Impact of Late Quaternary Equatorial Pacific Sea Surface Temperature Variations. *Science* **289**, 1719-1724.

Locarnini R. A., Mishonov A. V., Antonov J. I., Boyer T. P., Garcia H. E., Baranova O. K., Zweng M. M., and Johnson D. R. (2010) World Ocean Atlas 2009, Volume 1: Temperature. In: *NOAA Atlas NESDIS 68* (eds. S. Levitus). U.S. Government Printing Office, Washington, D.C., pp. 184.

Lear C. H., Elderfield H., and Wilson P. A. (2000) Cenozoic Deep-Sea Temperatures and Global Ice Volumes from Mg/Ca in Benthic Foraminiferal Calcite. *Science* **287**, 269-272.

Lyle M., Wilson P. A., Janecek T. R., et al. (2002) Site 1218. In: *Proc. ODP. Init. Repts.* 199 (eds. P. A. Wilson, M. Lyle, and J. V. Firth). Ocean Drilling Program.

Lyle M., Olivarez Lyle A., Gorgas T., Holbourn A., Westerhold T., Hathorne E., Kimoto K., and Yamamoto S. (2012) Data report: Raw and normalized elemental data along the Site U1338 splice from X-ray fluorescence scanning. In: *Proc. IODP*, 320/321: Tokyo (eds. H. Pälike, et al.). (Integrated Ocean Drilling Program Management International, Inc.). doi:10.2204/iodp.proc.320321.203.2012.

Marr J. P., Bostock H. C., Carter L., Bolton A., and Smith E. (2013) Differential effects of cleaning procedures on the trace element chemistry of planktonic foraminifera. *Chem. Geol.* **351**, 310-323.

Martin J. H. and Knauer G. A. (1983) VERTEX: Manganese transport with $CaCO_3$. *Deep-Sea Res.* **30**, 411-425.

Martin J. H. and Knauer G. A. (1984) VERTEX: Manganese transport through oxygen minima. *Earth Planet. Sci. Lett.* **67**, 35-47.

Martin J. H., Knauer G. A., and Broenkow W. (1985) VERTEX: The lateral transport of manganese in the northeast Pacific. *Deep-Sea Res.* **32**, 1405-1427.

Matter A., Douglas R. G., and Perch-Nielsen K. (1975) Fossil preservation, geochemistry, and diagenesis of pelagic carbonates from Shatsky Rise, Northwest Pacific. In: *Init. Repts*. *DSDP* 32 (eds. R. L. Larson, R. Moberly, et al.). Deep Sea Drilling Project, pp. 891-921.

Mucci A. (1987) Influence of temperature on the composition of magnesian calcite overgrowth precipitated from seawater. *Geochim. Cosmochim. Acta* **51**, 1977-1984.

Nürnberg D., Bijma J., and Hemleben C. (1996) Assessing the reliability of magnesium in foraminiferal calcite as a proxy for water mass temperature. *Geochim. Cosmochim. Acta* **60**, 803-814.

Oomori T., Kaneshima H., Maezato Y., and Kitano Y. (1987) Distribution coefficient of Mg^{2+} ions between calcite and solution at 10-50°C. *Mar. Chem.* **20**, 327-336.

Pälike H., Norris R. D., Herrle J. O., Wilson P. A., Coxall H. K., Lear C. H., Shackleton N. J., Tripati A. K., and Wade B. S. (2006) The Heartbeat of the Oligocene Climate System. *Science* **314**, 1894-1898.

Pälike H., Lyle M., Nishi H., Raffi I., Gamage K., Klaus A., and the Expedition 320/321 Scientists (2010) *Proc. IODP*, 320/321: Tokyo (Integrated Ocean Drilling Program Management International, Inc.).

Pälike H., Lyle M. W., Nishi H., et al. (2012) A Cenozoic record of the equatorial Pacific carbonate compensation depth. *Nature* **488**, 609-614.

Pearson P. N. and Burgess C. E. (2008) Foraminifer test preservation and diagenesis: comparison of high latitude Eocene sites. *Geol. Soc. London, Spec. Pub.* **303**, 59-72.

Pearson P. N. and Shackleton N. J. (1995) Neogene multispecies planktonic foraminifer stable isotope record, Site 871, Limalok Guyot. In: *Proc. ODP. Sci. Res.* 144 (eds. J. A. Haggerty, I. Primoli Silva, F. Rack, and M K. McNutt). Ocean Drilling Program, pp. 401-410.

Pearson P. N., Ditchfield P. W., Singano J., Harcourt-Brown K. G., Nicholas C. J., Olsson R. K., Shackleton N. J., and Hall M. A. (2001) Warm tropical sea surface temperatures in the Late Cretaceous and Eocene epochs. *Nature* **413**, 481-487.

Pena L. D., Calvo E., Cacho I., Eggins S., and Pelejero C. (2005) Identification and removal of Mn-Mg-rich contaminant phases on foraminiferal tests: Implications for Mg/Ca past

temperature reconstructions. *Geochem. Geophys. Geosyst.* **6**, Q09P02, doi:10.1029/2005GC000930.

Pena L. D., Cacho I., Calvo E., Pelejero C., Eggins S., and Sadekov A. (2008) Characterization of contaminant phases in foraminifera carbonates by electron microprobe mapping. *Geochem. Geophys. Geosyst.* **9**, Q07012, doi:10.1029/2008GC002018.

Pingitore N. E. (1978) The behaviour of Zn^{2+} and Mn^{2+} during carbonate diagenesis: theory and applications. *J. Sediment. Petrol.* **48**, 799-814.

Pingitore N. E., Eastman M. P., Sandidge M., Oden K., and Freiha B. (1988) The coprecipitation of manganese(II) with calcite: an experimental study. *Mar. Chem.* **25**, 107-120.

Regenberg M., Nürnberg D, Schönfeld J, and Reichart G.-J. (2007) Early diagenetic overprint in Caribbean sediment cores and its effect on the geochemical composition of planktonic foraminifera. *Biogeosciences* **4**, 957-973.

Reichart G.-J., Jorissen F., Anschutz P., and Mason P. R. D. (2003) Single foraminiferal test chemistry records the marine environment. *Geology* **31**, 355-358.

Rimstidt J. D., Balog A., and Webb J. (1998) Distribution of trace elements between carbonate minerals and aqueous solutions. *Geochim. Cosmochim. Acta* **62**, 1851-1863.

Rosenthal Y., Boyle E. A., and Slowey N. (1997) Temperature control on the incorporation of magnesium, strontium, fluorine, and cadmium into benthic foraminiferal shells from Little Bahama Bank: Prospects for thermocline paleoceanography. *Geochim. Cosmochim. Acta* **61**, 3633-3643.

Rosenthal Y., Field M. P., and Sherrell R. M. (1999) Precise determination of element/calcium ratios in calcareous samples using sector field inductively coupled plasma mass spectrometry. *Anal. Chem.* **71**, 3248-3253.

Rosenthal Y., Lohmann G. P., Lohmann K. C., and Sherrell R. M. (2000) Incorporation and preservation of Mg in *Globigerinoides sacculifer*: Implications for reconstructing the temperature and $\delta^{18}O$ of seawater. *Paleoceanography* **15**, 135-145.

Russell A. D., Hönisch B., Spero H. J., and Lea D. W. (2004) Effects of seawater carbonate ion concentration and temperature on shell U, Mg, and Sr in cultured planktonic foraminifera. *Geochim. Cosmochim. Acta* **68**, 4347-4361.

Sadekov A., Eggins S. M., De Deckker P., and Kroon D. (2008) Uncertainties in seawater thermometry deriving from intratest and intertest Mg/Ca variability in *Globigerinoides ruber*. *Paleoceanography* **23**, PA1215, doi:10.1029/2007PA001452.

Sadekov A. Y., Eggins S. M., Klinkhammer G. P., and Rosenthal Y. (2010) Effects of seafloor and laboratory dissolution on the Mg/Ca composition of *Globigerinoides sacculifer* and *Orbulina universa* tests – a laser ablation ICPMS microanalysis perspective. *Earth Planet. Sci. Lett.* **292**, 312-324.

Schlitzer R. (2012) Ocean Data View. available online at http://odv.awi.de.

Sexton P. F. and P. A. Wilson (2009) Preservation of benthic foraminifera and reliability of deep-sea temperature records: Importance of sedimentation rates, lithology, and the need to examine test wall structure. *Paleoceanography* **24**, PA2208, doi:10.1029/2008PA001650.

Sexton P. F., Wilson P. A., and Pearson P. N. (2006) Microstructural and geochemical perspectives on planktic foraminiferal preservation: "Glassy" versus "Frosty". *Geochem. Geophys. Geosyst.* **7**, 1-29.

Shackford J. K., Lyle M., Wilkens R., and Tian J. (2014) Data report: raw and normalized elemental data along the Site U1335, U1336, and U1337 splices from X-ray fluorescence scanning. In: *Proc. IODP,* 320/321: Tokyo (eds. H. Pälike, et al.). (Integrated Ocean Drilling Program Management International, Inc.). doi:10.2204/iodp.proc.320321.216.2014.

Shevenell A. E., Kennett J. P., and Lea D. W. (2004) Middle Miocene Southern Ocean Cooling and Antarctic Cryosphere Expansion. *Science* **305**, 1766-1770.

Spero H. J., Eggins S. M., Russell A. D., Vetter L., Kilburn M. R., and Hönisch B. (2015) Timing and mechanism for intratest Mg/Ca variability in a living planktic foraminifer. *Earth Planet. Sci. Lett.* **409**, 32-42.

Stewart J. A, Wilson P. A., Edgar K. M., Anand P., and James R. H. (2012) Geochemical assessment of the palaeoecology, ontogeny, morphotypic variability and palaeoceanographic utility of "*Dentoglobigerina*" *venezuelana*. *Mar. Micropaleontol.* **84-85**, 74-86.

Stoll H. M., Schrag D. P., and Clemens S. C. (1999) Are seawater Sr/Ca variations preserved in quaternary foraminifera?. *Geochim. Cosmochim. Acta* **63**, 3535-3547.

Tian J., Yang M., Lyle M. W., Wilkens R., and Shackford J. K. (2013) Obliquity and long eccentricity pacing of the Middle Miocene climate transition. *Geochem. Geophys. Geosyst.* **14**, 1740-1755.

Tribble J. S. and Wilkens R. H. (1999) Mineralogy and microfabric of sediment from the western Mediterranean Sea. In: *Proc. ODP. Sci. Res.* 161 (eds. R. Zahn, M. C.Comas, and A. Klaus). Ocean Drilling Program, pp. 99-110.

van Raden U. J., Groeneveld J., Raitzch M., and Kucera M. (2011) Mg/Ca in the planktonic foraminifera *Globorotalia inflata* and *Globigerinoides bulloides* from Western Mediterranean plankton tow and core top samples. *Mar. Micropaleontol.* **78**, 101-112.

Vetter L., Kozdon R., Mora C. I., Eggins S. M., Valley J. W., Hönisch B., and Spero H. J. (2013a) Micron-scale intrashell oxygen isotope variation in cultured planktic foraminifers. *Geochim. Cosmochim. Acta* **107**, 267-278.

Vetter L., Spero H. J., Russell A. D., and Fehrenbacher J. S. (2013b) LA-ICP-MS depth profiling perspective on cleaning protocols for elemental analyses in planktic foraminifers. *Geochem. Geophys. Geosyst.* **14**, 2916-2931.

Voigt J., Hathorne E. C., Holbourn A., and Frank M., Minimal influence of recrystallization on middle Miocene benthic foraminiferal stable isotope stratigraphy in the eastern equatorial Pacific. *Paleoceanography* (2015a) *in review.*

Voigt J., Hathorne E.C., Frank M., Vollstaedt H., and Eisenhauer A. (2015b) Variability of carbonate diagenesis in equatorial Pacific sediments deduced from radiogenic and stable Sr isotopes. *Geochim. Cosmochim. Acta* **148**, 360-377.

Wade B. S. and Pälike H. (2004) Oligocene climate dynamics. *Paleoceanography* **19**, PA4019, doi:10.1029/2004PA001042.

Wade B. S. and Pälike H. (2005) Data report: Oligocene paleoceanography of the equatorial Pacific Ocean: Planktonic and benthic foraminifer stable isotope results from Site 1218. In: *Proc. ODP. Sci. Res.* 199 (eds. P. A. Wilson, M. Lyle, and J. V. Firth). Ocean Drilling Program, pp. 1-12.

Wade B. S., Berggren W. A., and Olsson R. K. (2007) The biostratigraphy and paleobiology of Oligocene planktonic foraminifera from the equatorial Pacific Ocean (ODP Site 1218). *Mar. Micropaleontol.* **62**, 167-179.

Wei G.-J., Zou L., Deng W.-F., Li X.-H., Liu Y., and Chen J.-F. (2009) Mn/Ca ratio in planktonic foraminifer from ODP Site 1144, the northern South China Sea: A possible paleoclimate indicator. *Geochem. J.* **43**, 235-246.

Westerhold T., Röhl U., Wilkens R., et al. (2012) Revised composite depth scales and integration of IODP Sites U1331-U1334 and ODP Sites 1218-1220. In: *Proc. IODP,* 320/321: Tokyo (eds. H. Pälike, et al.). (Integrated Ocean Drilling Program Management International, Inc.). doi:10.2204/iodp.proc.320321.201.2012.

Zachos J., Pagani M., Sloan L., Thomas E., and Billups K. (2001) Trends, Rhythms, and Aberrations in Global Climate 65 Ma to Present. *Science* **292**, 686-693.

Zachos J. C., Dickens G. R., and Zeebe R. E. (2008) An early Cenozoic perspective on greenhouse warming and carbon-cycle dynamics. *Nature* **451**, 279-283.

Supplementary Material

Table S1. LA-ICP-MS operating conditions

	Conditions used
Laser ablation system	UP 193fx excimer laser (New Wave Research^{TM}) equipped with large format cell
Spot size	75 µm
Repetition rate	4-6 Hz
Energy density (Fluence)	~2-3 J/cm² for standards, ~0.8-1.2 J/cm² for samples and JCt-1
Carrier gas flow (He)	0.75 l/min
Effective ablation duration	60 or 120 s for standards and JCt-1, 140 s for samples
ICP-MS	Agilent 7500cx
RF power	<1 W
Forward power	1500 W
Carrier gas flow (Ar)	~1 l/min
Dwell time	50 ms
Isotopes monitored	^{7}Li, ^{11}B, ^{23}Na, ^{24}Mg, ^{26}Mg, ^{27}Al, ^{39}K, ^{43}Ca, ^{44}Ca, ^{55}Mn, ^{66}Zn, ^{88}Sr, ^{111}Cd, ^{137}Ba, ^{139}La, ^{232}Th, ^{238}U

Table S2. Operating conditions for Electron Microprobe Mapping

	Conditions used	
Beam current	30 nA	
Accelerating voltage	15 kV	
Pixel size	1 µm	
Accumulations	3	
Dwell time	100 ms	
Elements monitored with corresponding crystal used	Mg Ca Sr Mn Fe	TAPH PETJ TAPJ LIFH LIFH

Table S3. Element/Ca ratios of different grains of OKA calcite standard

Sample	Mg/Ca (mmol/mol)	Sr/Ca (mmol/mol)	Mn/Ca (mmol/mol)	Reference
OKA I	4.86	19.00		Gabitov et al. 2013
OKA II	4.59	19.39		Gabitov et al. 2013
OKA III	4.89	18.82		Gabitov et al. 2013
OKA IV	4.70	18.99		Gabitov et al. 2013
average OKA	**4.76**	**19.05**		Gabitov et al. 2013
OKA	4.47	19.30		Gaetani and Cohen 2006
OKA I	4.56	18.20	4.63	Hathorne et al. 2008
OKA II	4.49	18.29	4.67	Hathorne et al. 2008
OKA I	4.87	18.43	4.67	Hathorne and Glock, measured 2010
OKA II	4.38	18.77	4.85	Hathorne and Glock, measured 2010
average OKA	**4.58**	**18.42**	**4.70**	

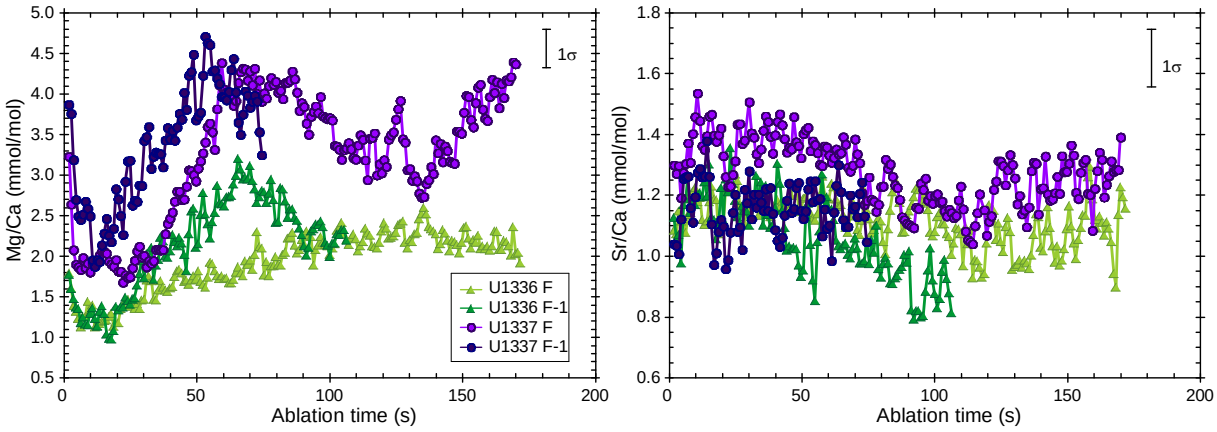

Figure S1. LA-ICP-MS depth profiles through different chambers of the same individual test of *D. venezuelana*. Depth profiles through the final (F) and penultimate (F-1) chamber reveal no significant difference in Mg/Ca and Sr/Ca ratios. Sites U1336 (green triangles) and U1337 (purple circles) are shown as representatives for all other sites. Tests were ablated from the outer to the inner calcite. Error bars denote the element/Ca 1σ uncertainties for depth profiles of repeated measurements of the JCt-1.

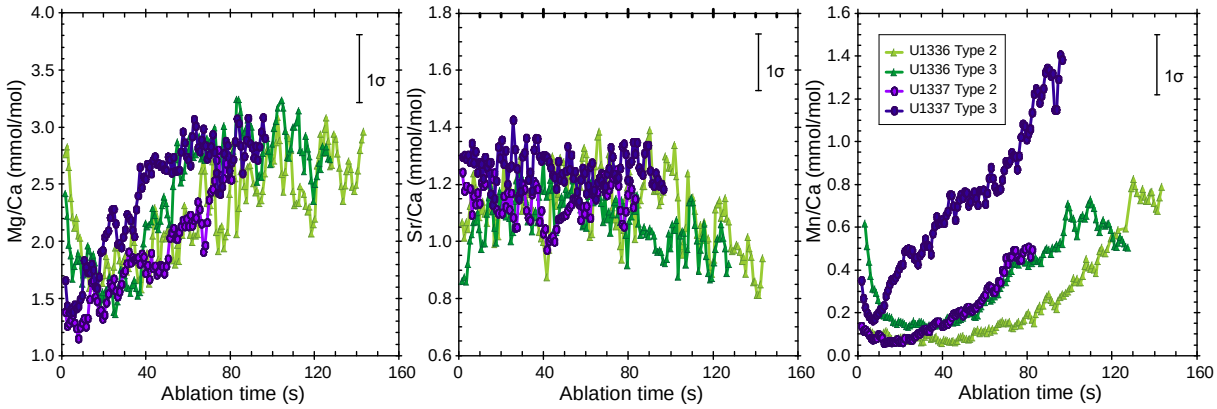

Figure S2. Element/Ca profiles through the tests of the morphotypes T2 and T3 of *D. venezuelana*. The depth profiles of Sites U1336 (green triangles) and U1337 (purple circles) represent all other sites investigated as the element/Ca ratios of the morphotypes do not differ significantly. Tests were ablated from the outer to the inner calcite. The error bars represent the 1σ uncertainties of element/Ca ratios for depth profiles obtained from repeated measurements of the JCt-1.

III. Conclusions and outlook

III.1 Conclusions

This thesis comprises a multi-component study of recrystallisation in bulk carbonates, pore waters and foraminiferal tests obtained from specific time intervals of sediment cores from the IODP Expedition 320/321 Pacific Equatorial Age Transect (PEAT). The analysis of bulk carbonates and associated pore waters revealed that recrystallisation mostly occurred relatively rapidly (within 1.5 million years after deposition) as the $^{87}Sr/^{86}Sr$ ratios of bulk carbonate leachates are indistinguishable (within 2σ uncertainties) from contemporaneous seawater (McArthur et al., 2001). In sediments older than 20.2 Ma, radiogenic $^{87}Sr/^{86}Sr$ ratios of Site U1336 bulk carbonate leachates and associated pore waters show lower values than contemporaneous seawater suggesting a late phase of recrystallisation. The lower ratios observed at this site indicate that Sr dissolved from older carbonates was incorporated during recrystallisation. Further, the Sr/Ca ratios of the bulk carbonates of Site U1336 are generally lower compared to the other PEAT sites and decrease with depth supporting more extensive recrystallisation at this site. Stable Sr isotope analyses of bulk carbonate leachates and associated pore waters indicate a fractionation during recrystallisation. The $\delta^{88/86}Sr$ values of Site U1336 pore waters increase with depth suggesting an isotope fractionation process during recrystallisation, during which the secondary calcite preferentially incorporates the lighter Sr isotopes (^{86}Sr), which in turn leads to an enrichment of ^{88}Sr in the pore waters. In summary, these parameters indicate extensive alteration of the bulk carbonates of Site U1336. Strong gradients in pore water Mg^{2+} and Ca^{2+} concentrations of Site U1336 suggest a high geothermal gradient, which seems to be the primary driver of the intense recrystallisation observed at this site.

The geochemical signature of foraminiferal tests was analysed at high resolution to investigate the preservation of proxies and their reliability. For comparison of specific time intervals between the different PEAT sites, it was necessary to establish a benthic foraminiferal stable isotope record for Site U1336 to precisely constrain intervals within the middle Miocene (16-13 Ma). This record shows good agreement with high resolution records from neighbouring Sites U1337 (Tian et al., 2013) and U1338 (Holbourn et al., 2014). The carbon isotope events of the Monterey Excursion

can clearly be identified and the absolute values and amplitudes of the stable isotopes are in accord with those from the other two sites less affected by recrystallisation. Despite the relatively coarse time resolution (5.1-17.8 kyr) of our record, long (400 kyr) and short (100 kyr) eccentricity cycles can clearly be distinguished. Although Site U1336 bulk sediments exhibit intense and persistent recrystallisation in sediments older than 14.7 Ma, the stable isotope records of Site U1336 agree well with the high resolution records of better preserved sites and the clear orbital cyclicity signals indicate that the benthic foraminifera retained most of their original geochemical signal.

Laser ablation profiles through the test walls of the planktonic foraminifera species *Dentoglobigerina venezuelana* from specific time intervals were measured and exhibit intratest heterogeneity for Mg/Ca and Mn/Ca ratios, whereas Sr/Ca is generally homogenous. These element/Ca patterns are comparable to modern foraminifera. However, Sr/Ca ratios decrease by more than 0.2 mmol/mol towards the inner calcite indicating recrystallisation. The highest percentages of recrystallised tests are observed for the older time intervals at 22.8 and 27 Ma. Tests of Site U1336 turn out to be most affected by recrystallisation, which confirms the extensive diagenetic alteration of bulk carbonates experienced at this site. Decreasing Sr/Ca and increasing Mn/Ca ratios towards the inner calcite suggest that the inner calcite is more susceptible to recrystallisation possibly caused by its crystal structure. Furthermore, SEM images illustrate increasing alteration with age of the samples. SEM images and laser ablation data also suggest different preservation states for individual tests of the same sediment sample implying that recrystallisation can vary from specimen to specimen. The laser ablation depth profiles through the tests clearly indicate that this technique can readily identify recrystallisation.

In summary, the analysis of bulk carbonates and associated pore waters of Site U1336 indicate extensive and persistent recrystallisation in sediments older than 14.7 Ma, most likely caused by the high geothermal gradient at this site. This is reflected by the decrease of Sr/Ca ratios of planktonic foraminifera and SEM images support increasing alteration with age. However, benthic foraminifera seem to be better preserved given that the benthic stable isotope record of this site is in very good agreement with records from better preserved sites, although benthic tests from the most intensely altered section (> 20 Ma) have not been measured. This indicates

that recrystallisation occurred rapidly after burial at shallow depths and that the benthic tests remained in approximately the same water mass with similar temperature and isotopic composition of bottom seawater and pore waters. This resulted in negligible offsets from primary $\delta^{18}O$ and $\delta^{13}C$ values, whereas the planktonic tests experienced recrystallisation at greater depth and thus different environmental conditions compared to their depth of calcification. Furthermore, planktonic foraminifera are more prone to recrystallisation and dissolution because their tests are thinner and more fragile than those of the benthic foraminifera as documented by numerous studies. Our data confirm that benthic foraminifera of the diagenetically altered PEAT sediments can be reliably used for palaeoceanographic reconstructions.

III.2 Outlook

This study clearly indicates that recrystallisation is a complex process and more work needs to be done to better understand the factors controlling the variability of recrystallisation. The evaluation of the effects of recrystallisation on carbonate sediments has to be determined for each studied site as the sediment conditions and the diagenetic histories are different due to variable subsidence, sedimentation rates, lithology, carbonate saturation state of the bottom water and geothermal gradients. Besides, there are a few open questions: Can pore water stable Sr $\delta^{88/86}Sr$ data be used as a reliable indicator of carbonate sediment recrystallisation or is Site U1336 due to its sediment conditions a special case? Why are some individual foraminiferal tests of the same species better preserved than others from the same sediment sample? Are laser ablation ICP-MS depth profiles of benthic foraminiferal tests similar to planktonic ones? And do laser ablation ICP-MS-derived element/Ca ratios of benthic foraminiferal tests also indicate the preservation state and can thus be used as a tool to identify recrystallisation? These and more questions arose from this study and will have to be addressed in future studies to improve our current knowledge of recrystallisation and to further test the reliability of geochemical proxies in foraminiferal tests.

Danksagung

Zunächst möchte ich der Deutschen Forschungsgemeinschaft (HA 5751/1-1, HA 5751/2-1) für die finanzielle Unterstützung danken, ohne die diese Studie nicht möglich gewesen wäre.

An erster Stelle möchte ich mich ganz herzlich bei meinem Betreuer Dr. Ed Hathorne bedanken, der mir die Welt der Isotopenchemie eröffnet hat. Ich möchte Dir für Deine Betreuung, die vielen wertvollen Diskussionen und Problemlösungen und natürlich auch für Deine Geduld danken. Deine Tür stand stets offen bei Fragen und Problemen. Du hast mir Mut und Kraft gegeben und an mich geglaubt, wenn es mal nicht so gut lief. Ohne Deine Unterstützung hätte ich das nicht geschafft.

Ich danke Prof. Dr. Martin Frank für die tolle Unterstützung, die Korrekturen und Ratschläge. Vielen Dank dafür, dass Du immer ein offenes Ohr hattest und mir Mut gemacht hast. Danke auch für die schönen Betriebsausflüge.

Ganz herzlichen Dank an Jutta, dafür dass Du immer das passende Werkzeug, Gefäß oder sonstiges parat hast. Für jedes technische und organisatorische Problem hattest Du stets eine einfache wie geniale Lösung. Vielen Dank auch für die vielen lustigen und ermutigenden Gespräche.

Ein großes Dankeschön geht an meine Hiwis Isabel und Julia für Eure unermüdliche Hilfe beim Waschen der Proben, Fraktionieren und Picken der Foraminiferen. Ohne Euch wäre diese Arbeit so nicht möglich gewesen.

Desweiteren möchte ich mich bei Nadine für das Ausleihen diverser Pickutensilien danken. Ich danke Hauke und Ana Kolevica für die Hilfe bei der Probenvorbereitung und der Messung der stabilen Sr-Isotope. Ich danke Lulzim Haxhiaj, Kirstin Werner, Christelle Not, Andrea Bodenbinder und Fynn Wulf für die Messung der stabilen Kohlenstoff- und Sauerstoffisotope. Vielen Dank an Petra Witte für die Durchführung der REM-Aufnahmen, Nico für Deine Hilfe bei der Vorbereitung der EMP-Präparate und Mario Thöner für die Hilfe und Durchführung der EMP-Messungen.

Vielen Dank an das „B-Team“ vom NOCS, Southampton, speziell an Gavin Foster und Eleni für die herzliche Betreuung während meines Forschungsaufenthaltes in England. Eleni, vielen Dank für Deine Hilfe bei der Vorbereitung und Messung der „boring isotope“-Proben. Ich danke Rosie, Wendy, Tom, Michael, Joe und Miguel für

die hilfreichen Diskussionen und die nette Abendgestaltung. Besonderer Dank gilt Sam, bei Dir habe ich nicht nur eine Bleibe in Southampton sondern auch eine gute Freundin in einer schwierigen Phase gefunden.

Ich danke Dr. Jan Fietzke, nicht nur für die professionelle Hilfe bei den Laserablationsmessungen sondern auch für die intensiven und wertvollen Diskussionen über Wissenschaft im Allgemeinen und im Speziellen. Durch Deine lockere und humorvolle Art hast Du mich oft aufgemuntert.

Ich danke der gesamten Arbeitsgruppe für die zahlreichen Kaffeerunden in der Science Lounge, für die gute Laune, die vielen tollen Gespräche und die nette Freizeit- und Abendgestaltung.

Ich danke meinen (ehemaligen) Bürokollegen Moritz, Daniel und Roland für die gemeinsame Zeit und die lustigen aber auch hilfreichen Gespräche. Vielen Dank speziell an Roland, Du hast mich oft zum Lachen gebracht.

Besonders bedanken möchte ich mich bei Kristin H., Steffie, Kristin D, Clauschi, Patricia und Claudia für die tolle gemeinsame Zeit. Danke für Euer Feedback zu wissenschaftlichen Themen, Eure offenen Ohren, Ratschläge, Ermutigungen, intensive Gespräche und natürlich viel gute Laune. Kristin D., ich danke Dir für die vielen tollen Erlebnisse, unsere gemeinsamen Urlaube in Peru und Barcelona und fürs Zuhören und einfach da sein. Sevi, ich danke dir für die erlebnisreiche gemeinsame Zeit, auch wenn es leider immer relativ kurz war. Danke vor allem fürs Zuhören, mich aufbauen und Mut machen.

Ich danke meinen Freunden Barbara, Silke, Katha, Anja und Carlo sowie meinen Bekannten für Euer Verständnis und Eure Geduld in den letzten Jahren und natürlich für unsere Freundschaft und all die tollen Erlebnisse.

Zu guter Letzt möchte ich meiner Familie danken für all die Unterstützung und auch Geduld. Ihr wart immer für mich da, habt an mich geglaubt, mir zugehört und mich stets unterstützt bei all meinen Vorhaben.